Multiscale Image Based Pore Space Characterisation and Modelling of North Sea Sandstone Reservoirs

A Thesis Presented for the Degree of Doctor of Philosophy in Petroleum Engineering at the School of Engineering University of Aberdeen

Gilbert Scott
BSc Hons University of Bristol
MSc Open University

2020

Declaration

This thesis has been composed by the candidate and has not been accepted in any previous application for a degree. The work has been done by the candidate and all sources of information are specifically acknowledged.

G. Scott

Gilbert Scott

16 April 2020

Abstract

This thesis is about pore scale characterisation and the modelling of multiphase flow in complex natural sandstones. These sandstones typically have been exposed to multiple diagenetic processes, contain substantial cements, clays, secondary porosity and contain a wide range of pore sizes. These issues create challenges in imaging and modelling of these systems.

Multiscale 2D scanning electron microscopy (SEM) and 3D X-ray micro computed tomography (μCT) have been used to image sandstone samples from two North Sea petroleum reservoirs. The pore space was characterised from the imaging data to quantify the pore size and pore coordination number distributions. Despite the combination of multiple complex diagenetic processes, the pore space characterisations show some regular character that can be represented by empirical mathematical models. The pore size distributions can be fitted to modified power law (Pareto) distributions with an exponential cut-off at large radii. The frequency distribution of coordination numbers follows an exponential model; additionally the mean and standard deviation of the coordination number are power law functions of the pore radius. An empirical relationship between 2D and 3D coordination number is proposed based on an analysis of random sections extracted from 3D volumes. This relationship makes it possible to estimate multiscale 3D connectivity from high resolution 2D imaging.

A stochastic algorithm has been developed to generate 3D pore networks from 2D imaging data. The stochastic algorithm has a recursive process that naturally fits into multiscale pore structure hierarchies. The methodology has been validated by calculating single phase permeability, capillary pressure and relative permeability from quasi-static pore network modelling for comparison with measured data and results from μCT pore networks.

Relative permeability and capillary pressure generated from stochastic pore networks have been applied in a field scale continuum model to examine the effect of changing wettability and wettability heterogeneity. The results show that a heterogeneous wettability distribution can yield a lower oil recovery than a homogeneous oil-wet or homogeneous water-wet assumption.

Publications and Presentations

Scott, G., Wu, K. and Zhou, Y. Multiscale Image-Based Pore Space Characterisation and Pore Network Generation: Case Study of a North Sea Sandstone Reservoir, Transp. Porous Med. 129(3) pp 855-884 (2019).
https://doi.org/10.1007/s11242-019-01309-8

Wang, C., Wu, K., Scott, G., Akisanya, A., Gan, Q. and Zhou, Y. A New Method for Pore Structure Quantification and Pore Network Extraction from SEM Images, Energy & Fuels,
https://doi.org/10.1021/acs.energyfuels.9b02522

Scott, G. Stochastic Generation of Pore Networks for Complex Sandstone Petroleum Reservoirs, Presented at the 4th InterPore UK Conference, University of Aberdeen 10-11 September 2018.

Acknowledgements

Contents

List of Figures

Notice

Figure 1.2 originally published by The Geological Society, reproduced under STM publishing guidelines.

Figures 2.1, 2.3 and 2.4 originally published by Elsevier, reproduced under STM publishing guidelines.

Figure 2.6 originally published by the American Physical Society, reproduced under license RNP/20/MAR/023681.

Figure 2.7 originally published by the American Physical Society, reproduced under license RNP/20/MAR/023682.

Figure 2.8 originally published by the American Physical Society, reproduced under license RNP/20/MAR/023684.

List of Tables

Nomenclature

a	Tolerance factor in the pore space characterisation procedure
A	Area of a 2D shape
b_o	Skjaeveland model parameter
b_w	Skjaeveland model parameter
c	Constant in the Katz and Thompson relation
c_o	Skjaeveland model parameter
c_w	Skjaeveland model parameter
C	Land trapping constant
D	Diameter or distance
E	Euclidean distance
$E_{i,j,k}$	Euclidean distance of pixel (i,j,k)
E_o	LET model parameter
E_w	LET model parameter
f	Characteristic function
F	Formation resistivity factor
g	Hydraulic conductance
g_i	Hydraulic conductance of element i
G	Shape factor
H	Hessian matrix
I	Electric current
I_{AH}	Amott-Harvey wettability index
I_{USBM}	USBM wettability index
J	Leverett J-function
k	Permeability
k_r	Relative Permeability
k_{ro}	Oil Relative Permeability
k_{rw}	Water Relative Permeability
l_c	Critical pore diameter
L	Length

L_o	LET model parameter
L_w	LET model parameter
m	Archie's law cementation exponent
n	Archie's law saturation exponent
N	Number of pixels or voxels
N_b	Number of bonds
N_e	Number of pore elements
N_l	Number of pore element links
N_n	Number of nodes
P	Pressure or Perimeter
P_c	Capillary pressure
P_i	Pressure of element i
$\Pr$	Probability
Q	Volumetric flow rate
r	Radius
r_c	Critical pore radius
r_i	Radius of element i
r_{min}	Minimum pore element radius
r_{max}	Maximum pore element radius
r_0	Pore size distribution parameter
r_1	Pore size distribution parameter
$r_{z,mean}$	Pore radius where the mean coordination is 1
$r_{z,sd}$	Pore radius where the standard deviation of the coordination is 1
R	Resistance or Resistivity
R_w	Water Resistivity
s	Two-point correlation function
S	Saturation or Surface area
S_o	Oil Saturation
S_w	Water Saturation
S_w^*	Normalised water Saturation
T_o	LET model parameter
T_w	LET model parameter
V	Volume or Electric potential
w_P	Perimeter weighting factor
w_S	Surface area weighting factor

x	Cartesian coordinate
y	Cartesian coordinate
z	Cartesian coordinate
Z	Coordination number
Z_{mean}	Mean coordination number
Z_{sd}	Standard deviation of coordination number
α	Pore size distribution scaling index
β	Coordination number scaling index
η	Pore size distribution parameter
ϕ	Porosity
Φ	Cumulative probability
λ	Eigenvalue
μ	Viscosity
σ	Interfacial tension
θ	Contact angle
θ_a	Advancing contact angle
θ_r	Receding contact angle
τ	Tortuosity
χ	Euler characteristic
χ_V	Specific connectivity function

Abbreviations

AOC	Anasuria Operating Company
BSE	Back Scattered Electron
CCA	Conventional Core Analysis
CCS	Carbon Capture and Storage
EDM	Euclidean Distance Map
EDX	Energy Dispersive X-ray Analysis
FRF	Formation Resistivity Factor
FWL	Free Water Level
GMM	Gaussian Mixture Model
GWC	Gas-Water Contact
IFT	Interfacial Tension
LBM	Lattice Boltzmann Method
MICP	Mercury Injection Capillary Pressure
MPS	Multi-point Statistics
NDA	National Data Archive
NMR	Nuclear Magnetic Resonance
OGA	Oil and Gas Authority
OWC	Oil-Water Contact
PIF	Peak Interval Fraction
PNM	Pore Network Model
REV	Representative Elementary Volume
RI	Resistivity Index
SCAL	Special Core Analysis
SD	Standard Deviation
SE	Secondary Electron
SEM	Scanning Electron Microscopy
TVDSS	True Vertical Depth Sub-Sea
USBM	United States Bureau of Mines Wettability Test
WPSL	Weighted Planar Stochastic Lattice
μCT	X-ray Micro Computed Tomography

Chapter 1

Introduction

"When you wake up in the morning, Pooh," said Piglet at last, "What's the first thing you say to yourself?"

"What's for breakfast?" said Pooh. "What do you say, Piglet?"

"I say, I wonder what's going to happen exciting today?" said Piglet.

Pooh nodded thoughtfully. "It's the same thing," he said.

— A. A. Milne, Winnie-the-Pooh

1.1 Background

An imperative for the petroleum industry is to maximise oil and gas recovery at minimal cost. It is a stated objective of the UK Oil and Gas Authority (OGA) to maximise economic recovery of hydrocarbons, that is maximise the quantity of oil and gas recovered provided that the required activities are economically viable. Maximising the economic recovery from an oil or gas field requires careful evaluation of options, planning of activities and management of the hydrocarbon reservoir.

Carbon capture and storage (CCS) is a technology that involves injecting carbon dioxide into saline aquifers or depleted hydrocarbon reservoirs for long term storage. The objective of this process is to avoid releasing carbon dioxide into the atmosphere and thereby mitigate the impact of fossil fuel emissions on climate change. The UK government has set a target of net zero atmospheric carbon emissions by the year 2050 and CCS is an important technology that can be deployed to help meet this target.

Many of the world's fresh water resources are located in underground aquifers. Managing these underground water resources is becoming increasingly important as the demand for fresh water supplies increases with the global population and the improvement in living standards.

Developing an understanding fluid flow in natural porous media is important for the effective management and engineering of petroleum reservoirs, CCS projects and fresh water aquifers. The characteristics of the pore space such as pore geometry, pore size and pore connectivity have a strong effect on flow behaviour; therefore our understanding and prediction of single and multiphase fluid flow in porous media can be significantly improved by imaging and modelling at the pore scale.

1.2   Pore Scale Imaging and Modelling

Over the last 20 years there have been substantial advances in many pore scale imaging, characterisation and modelling techniques (Blunt et al., 2013; Fredrich et al., 2014; Bultreys et al., 2016a; Verri et al., 2017). These techniques have two main goals: firstly to characterise the geometry and topology of the pore space of porous media from imaging information and secondly to determine macroscopic properties based on the pore scale information and the physical properties of the fluids and the rock surface.

The most commonly employed pore scale imaging technologies are X-ray Micro Computed Tomography (μCT) and Scanning Electron Microscopy (SEM) (Bultreys et al., 2016a). μCT is a 3-dimensional (3D) imaging technique and SEM is a 2-dimensional (2D) technique. Macroscopic properties generally means continuum scale properties. It is currently not feasible to model an entire petroleum reservoir or natural aquifer at the pore scale; this is beyond the capability of existing computers. Large scale porous media are generally modelled using a continuum approximation i.e. viscous fluid flow is governed by Darcy's Law and its multiphase generalisation (Sahimi, 2011). Models of petroleum reservoirs or natural aquifers typically have a spatial discretisation of the order of 1 to 10 meters; therefore this should be the target scale for pore scale imaging and modelling techniques. However, even a 1 m^3 volume would contains perhaps 10^{15} pore elements and modelling this at the pore scale is beyond the capability of existing computers. The actual target scale for pore scale modelling is generally much smaller and continuum upscaling is required.

Porosity, as the most basic macroscopic property of porous media, is relatively straightforward to determine from imaging data. However, capillary pressure and continuum transport properties such as permeability or formation resistivity factor (FRF) and particularly their multiphase generalisations (relative permeability and resistivity index) are significantly more challenging (Bultreys et al., 2016a; Verri et al., 2017).

There are two main approaches to modelling fluid flow at the pore scale: direct simulation of pore scale voxel images and pore network modelling (Meakin and Tartakovsky, 2009; Golparvar et al., 2018; Ramstad et al., 2019). The most popular direct simulation technique is the Lattice Boltzmann method (LBM) (Chen and Doolen, 1998; Sukop and Thorne, 2006; Ramstad et al., 2010; Liu et al., 2016). Although LBM is popular and well suited to single-phase flow, it has a number of disadvantages for multiphase flow. In particular, it is computationally demanding, a high spatial resolution is required to capture film flow and short timesteps are required to capture certain pore filling events (Ramstad et al., 2019).

In pore network modelling (PNM), the pore space is simplified to an interconnected network of pore bodies (network nodes) and pore throats (network bonds) (Øren et al., 1998; Blunt, 2001; Jackson et al., 2002; Valvatne et al., 2005; Meakin and Tartakovsky, 2009). Network elements have simplified cross-sections such as circular, square or triangular and semi-empirical rules are used to model displacement and pore filling events such as piston-like throat filling, snap-off and cooperative pore body filling (Blunt, 1997; Øren et al., 1998; Valvatne and Blunt, 2004). Fluid flow is modelled using analytical solutions of the Stokes' equation for simplified geometries. Quasi-static PNMs assume that capillary forces dominate; capillary pressure is imposed on the model and the static position of fluid interfaces calculated ignoring any transient pressure or viscous effects. Flow properties are derived assuming that each phase flows independently at an infinitesimal rate with no interface movement. The principal advantages of PNM are the computational efficiency and the freedom from grid resolution effects (Ramstad et al., 2019).

It should be emphasised that the overriding objective of pore scale imaging and modelling techniques should be to determine difficult to measure quantities based on more readily available data (Sorbie and Skauge, 2011; Masalmeh et al., 2015). Multiphase properties such as capillary pressure and relative permeability can be measured in the laboratory typically using core plug samples (a few cm size). These laboratory measurements are a

subset of Special Core Analysis (SCAL) and can be complex, time consuming and expensive. Capillary pressure and relative permeability are known to be dependent on the pore structure (geometry and topology), fluid interfacial tensions, surface wettabilities and saturation history (Sahimi, 2011). Wettability is complex because it is influenced by pore size, mineralogy, oil composition and water salinity (Donaldson and Alam, 2008). It may be difficult to reproduce the in-situ reservoir characteristics (particularly wettability) in the laboratory. Hence laboratory measurements of capillary pressure and relative permeability are not straightforward.

In comparison to SCAL, imaging information such as µCT and particularly SEM can be much faster and lower cost. µCT can be used to construct 3D images of porous media but is limited to a resolution of around 1 µm for laboratory equipment. SEM can image microporosity below the resolution of laboratory µCT scanners which is particularly important for low permeability reservoirs. Recent advances in imaging technology have made more equipment available at lower cost; therefore the technology is becoming more accessible and its use is becoming more routine. Hence, pore scale imaging and modelling is a potentially easier and faster process than SCAL measurement and it becomes practical to address a much larger number of variables or sensitivity cases than is feasible with laboratory experiments.

Having said this, pore scale modelling can never be a complete replacement for laboratory experiments; measured data will always be required to validate models and demonstrate the reliability of the pore scale imaging and modelling process.

1.3   Complex Sandstones

There has been considerable success in the prediction of multiphase properties (capillary pressure and relative permeability) for homogeneous rocks with narrow pore size distributions such as Berea or Fontainebleau sandstones (Øren et al., 1998; Patzek, 2001). However, more complex sandstones containing substantial cements, clays and grain dissolution (secondary porosity) typically have much wider pore size distributions and still remain a significant challenge (Mehmani and Prodanović, 2014; Lai et al., 2018; Tahmasebi and Kamrava, 2018; Wu et al., 2019a).

Complex sandstones typically have a long geological history and have been deeply buried (2000-5000 m). The porosity and pore space topology is

strongly influenced by diagenetic processes such as carbonate cementation, quartz overgrowths and pore filling clays (e.g. kaolinite, illite and chlorite). Porosity is reduced by compaction, cementation and authigenic clays. Diagenesis typically creates smaller and more disconnected pores (Cook et al., 2011). Diagenesis also accentuates primary depositional variations and has a major impact on porosity and permeability heterogeneity (Morad et al., 2010). The combination of multiple, complex processes results in a heterogeneous pore structure with a wide range in pore sizes (Lai et al., 2018). A single core plug sample (1 cm size) could contain significant pores with sizes ranging from 0.1 μm to 100 μm (3 orders of magnitude variation) and the reservoir as a whole might contain 4 or 5 orders or magnitude variation.

1.4 The Multiscale Problem

All imaging technologies have a trade-off between resolution and field of view. Achieving a high resolution naturally requires a small field of view and having a large field of view will always compromise the image resolution. High resolution is important to image the smallest pore features but a large field of view is also important to capture a representative sample of the largest pores.

State-of-the-art μCT imaging can capture length scales spanning about 3 orders of magnitude and state-of-the-art SEM imaging can capture over 4 orders of magnitude (Bultreys et al., 2016a). However, these imaging capabilities are not really sufficient for many natural porous media. Complex sandstones samples can contain over 3 orders of magnitude variation in pore sizes and to capture a representative elementary volume (REV) containing a representative sample of the largest pores, the sample size should be at least 10-100 times larger; therefore it is necessary to capture perhaps 5 orders of magnitude variation in length scale. The first part of the multiscale problem is this combined effect of limited resolution and limited field of view making it difficult to capture the wide range of pore sizes (Tsakiroglou, 2012; Jiang et al., 2013b; Tahmasebi and Kamrava, 2018). This imaging problem leads to a strategy of integrating information from multiple images captured at different scales.

The second part of the multiscale problem relates to the computational demands of handling a wide range of length scales. A 3D volume covering 5

orders of magnitude range in linear scale would contain 10^{15} voxels which is challenging to manipulate and process using existing computers. Direct multiphase flow simulation techniques such as LBM are already computationally demanding for much smaller volumes (e.g. 10^9 voxels); therefore some form of upscaling e.g. PNM, is inevitably required.

1.5   Guillemot A Field
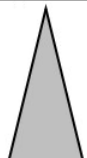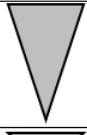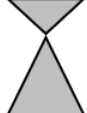
The Guillemot A oil field is located in blocks 21/25 and 21/30 of the United Kingdom Continental Shelf (UKCS) Central North Sea. The field was developed using subsea wellheads and subsea flowlines tied back to the Anasuria Floating Production Storage and Offloading vessel (FPSO). Production started in 1996 and the recovery mechanism has been a partial waterflood with five production wells and two water injectors. The field was originally operated by Shell but is now operated by Anasuria Operating Company (AOC).

The principal reservoir is the Upper Jurassic Fulmar shallow marine sandstone underlain by the Triassic Skagerrak fluvial sands (Evans et al., 2002; Taylor et al., 2015). The reservoir sands are comparable to those in the nearby Kittiwake (Glennie and Armstrong, 1991) and Fulmar (Johnson et al., 1986) oil fields. The reservoirs were deposited in topographic lows created by withdrawal of the underlying Zechstein salt. The present day thickness and distribution of the reservoir formations was controlled by syndepositional structural rifting and halokenesis together with post-Late Jurassic uplift and erosion (Stewart and Clark, 1999).

The Fulmar formation is a highly bioturbated shallow marine sandstone and siltstone. The sands are interpreted as stacked shoreface deposits that have undergone extensive marine reworking due to storms and tidal currents (Howell et al., 1996; Gowland, 1996). There are four main reservoir facies (Cannon and Gowland, 1996). Facies 4, 5 and 6 are moderate to well sorted, bioturbated, silty sandstones of increasing grain size and increasing rate of deposition. Facies 11 is a bioturbated, coarse grained, relatively clean sandstone deposited in a high energy wave/current environment.

The Fulmar formation can be divided into four main intervals (Table 1.1). Interval 1 is a basal transgressive unit and consists predominantly of small upward fining sequences of facies 4, 5 and 6. Interval 2 is an upward coarsening sequence, typically a continuum from facies 4 to 5 to 6. Interval

Table 1.1: Fulmar interval characteristics from Cannon and Gowland (1996)

Reservoir Interval	Depositional Setting	Grain Size Profile	Lithofacies Main	Lithofacies Subordinate	Reservoir Quality
4	Retrograding shallow marine shelf/shoreline (distal → proximal)		1,2,3		Poor
			4	7,12	
			5		
			6		Moderate
3	Aggrading shelf/shoreline complex		6,11		Good
			11	6,7,8,9,10,12	Excellent
			6,11		Good
2	Prograding shallow marine shelf/shoreline (proximal → distal)		6	8,9,10,11	Moderate
			5	7	
			4	7	Poor
1	Basal transgressive/ regressive cycles		4	1,2,3	
			4,5,6	8,9	Moderate/Poor
			12		

3 consists of a series of stacked high energy deposits (facies 6 and 11) interpreted to be a shelf or shoreline complex (Cannon and Gowland, 1996). Interval 4 is an upward fining retrograding sequence, typically a continuum from facies 6 to 5 to 4. Intervals 1 and 2 are informally referred to as Lower Fulmar, interval 3 Middle Fulmar and interval 4 Upper Fulmar.

The Skagerrak consists of red fine grained sandstones and shales deposited in a fluvial and alluvial environment (Akpokodje et al., 2017; Glennie and Armstrong, 1991; Taylor et al., 2015). There are three main reservoir facies: (i) alluvial, sheet flood sandstones with mudstone intraclasts, (ii) overbank red sandstones and siltstones, and (iii) clean, well sorted, cross-bedded fluvial channel deposits.

The Guillemot A reservoir has been buried to a depth of around 8000-8500 ft TVDSS and has been subjected to extensive diagenesis (Stewart, 1986; Burns et al., 2005; Taylor et al., 2015). Figure 1.1 shows SEM images of samples from the Middle Fulmar, Lower Fulmar and the Skagerrak formations. Cements, mica and clays are evident plus secondary porosity created by partial grain dissolution. The Middle Fulmar (facies 11) is coarse grained, relatively clean and displays high porosity and permeability. The Lower Fulmar samples (facies 4 and 5) are clearly finer grained, more silty and more highly cemented. In particular, the Lower Fulmar can be relatively

high porosity but low permeability (compare top left and bottom left images in Figure 1.1. The Skagerrak sample (bottom right Figure 1.1) is from the well sorted fluvial channel facies which is coarser grained than the Lower Fulmar but not as clean as the Middle Fulmar.
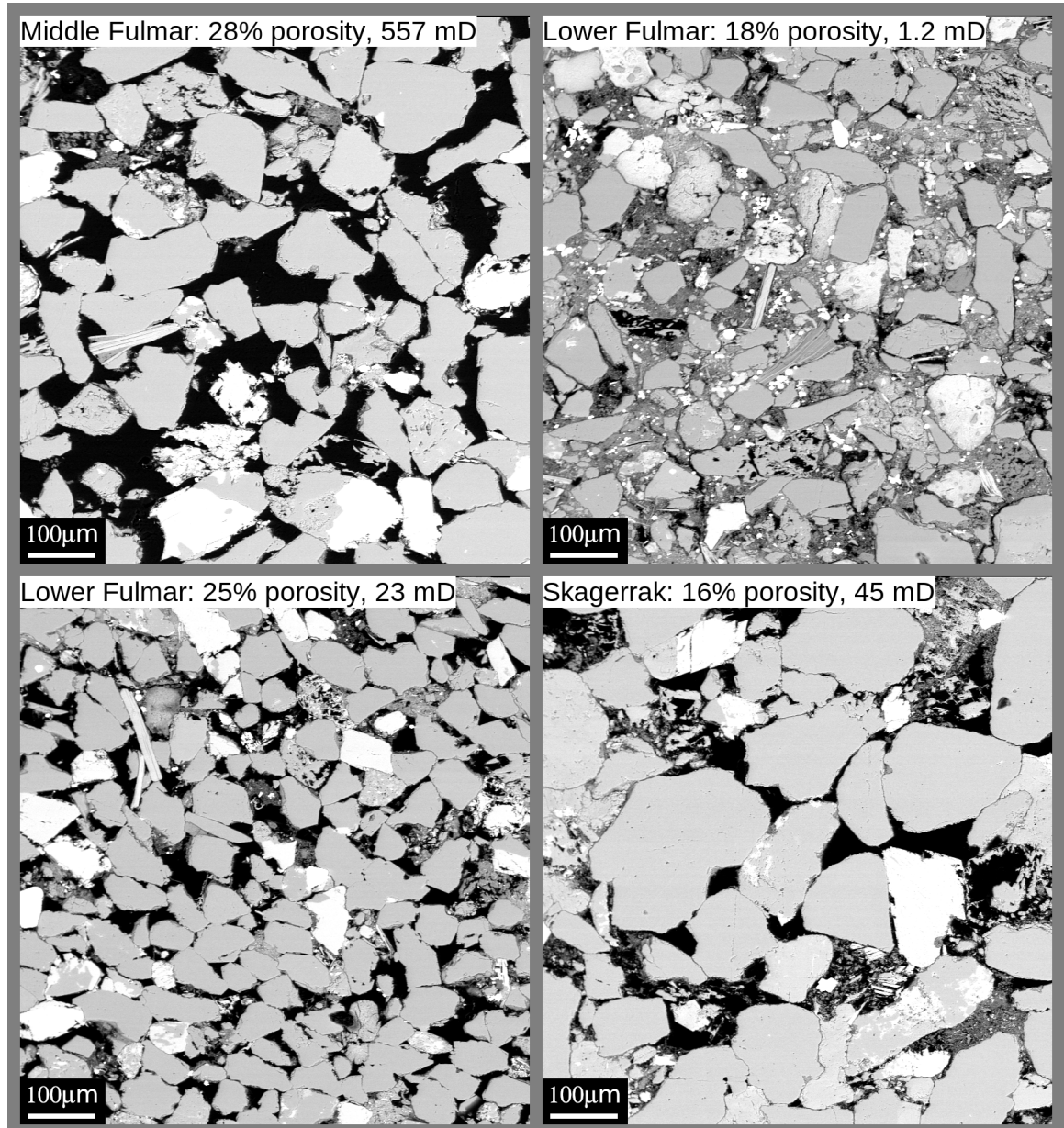
Figure 1.1: SEM images of Guillemot A samples, inset boxes show core plug measured porosity and permeability

The Middle Fulmar is very good quality, has contributed significantly to production and has been effectively waterflooded in many parts of the field. The Lower Fulmar and Skagerrak are generally poorer reservoir quality and contain a significant volume of remaining oil.

An extensive set of Guillemot core and log data were provided by the field

operator, AOC. Some additional data from released wells were also sourced from the Oil and Gas Authority (OGA) UK National Data Archive (NDA)[1]. In addition, AOC provided a number of core plug samples for SEM and μCT imaging.

Appendix A contains a graphical presentation of the convention core analysis (CCA) and special core analysis (SCAL) data. Some key observations from these data are as follows:

- The reservoir is highly heterogeneous with core permeability values varying by more than four orders of magnitude.

- There is a trend of increasing permeability with porosity, but there is not a strong correlation, particularly in the Skagerrak.

- The Middle Fulmar has higher permeability than the Upper and Lower Fulmar at the same porosity. This is a consequence of the larger grain size and lower silt content of the Middle Fulmar (Cannon and Gowland, 1996).

- The capillary pressure data (MICP and air-brine) show that typical samples have 2 to 3 orders of magnitude variation in pore sizes and the reservoir as a whole has a variation of 4 to 5 orders of magnitude.

- Amott wettability data indicates the reservoir is moderately oil-wet. There are no obvious trends in wettability with permeability or depth.

The heterogeneity and complexity of the field has made reservoir management challenging and there is significant scope to optimise production and oil recovery by modelling the multiphase flow, displacement and recovery processes accurately.

1.6   Vanguard Field

The Vanguard gas field is located in block 49/16 of the UKCS Southern North Sea. The field is part of the V-Fields complex of four gas fields operated by ConocoPhillips (Pritchard, 1991). First gas production was in 1988; a total of six development wells were drilled from a small fixed platform and the field has now ceased production.

---

[1]https://www.nda.ogauthority.co.uk

The Vanguard reservoir is the Leman Sandstone Member of the early Permian, Rotliegendes Group (Pritchard, 1991; Lahann et al., 1993; Courtier and Riches, 2003). The reservoir lies over the Eastern margin of the Sole Pit Basin where part of the Carboniferous-Rotliegendes total petroleum system was formed. The reservoir system is a group of evaporites and sands of the Permian age that cover a carbonaceous shale. The creation of the different reservoir facies occurred in dry or semi-dry aeolian, fluvial or lacustrine environments that were interrupted by transgression of the Zechstein sea (Pritchard, 1991). Subsequently, late Permian tectonic movements, uplift and erosion created a complex and highly faulted structure. The field is contained in a completely faulted NW-SE trending anticline, bounded to the NE and SW by major reactivated faults which converge closing the structure to the NW. The gas-water contact (GWC) is 8450 ft TVDSS (Pritchard, 1991).

In the V-Fields area, the Leman sandstone formation has been divided into four main zones, A to D (Figure 1.2), based on lithology and depositional facies, which strongly influence the permeability and porosity of the reservoir (Robertson et al., 1992; Courtier and Riches, 2003). The basal zone D comprises fluvial, aeolian and lacustrine facies of low porosity and permeability. This zone is almost entirely below the GWC. Zone C consists of a sequence of aeolian dune and sandsheet facies that preserve the best reservoir properties in the Vanguard field. Porosity is up to 23% and permeability up to 2000 mD. Zone B comprises interbedded aeolian dune, interdune or sandy sabkha facies. This is the most heterogeneous zone and generally poorer quality than zone C. Zone A comprises aeolian dune facies of generally poor quality due to a combination of fine grain size and diagenesis. The upper part of zone A has been reworked by the Zechstein transgression and is commonly referred to as the Weissliegendes (Courtier and Riches, 2003).

Aeolian dune facies have the best reservoir quality because they consist of coarse well sorted sand grains with little clay. The interdune and sabkha facies generally contain high percent of primary silt and clay due to their semi-dry or lacustrine depositional environments. This results in shales and shaly sands which isolate the better quality dune sands units from one another. Aeolian dunes in zones A and B therefore have much lower production potential than similar quality intervals in zone C (Lahann et al., 1993; Courtier and Riches, 2003).

As discussed by Lahann et al. (1993), diagenesis in the Vanguard reservoir has had significant impact on reservoir quality. The reservoir intervals in two of the development wells (49/16-Q02 and 49/16-Q04) were highly altered by

| Gamma API | Depth Ft. | Neutron Porosity 45 — −15 / Density GM/CC | Porosity % | Permeability mD | Reservoir Zonation |
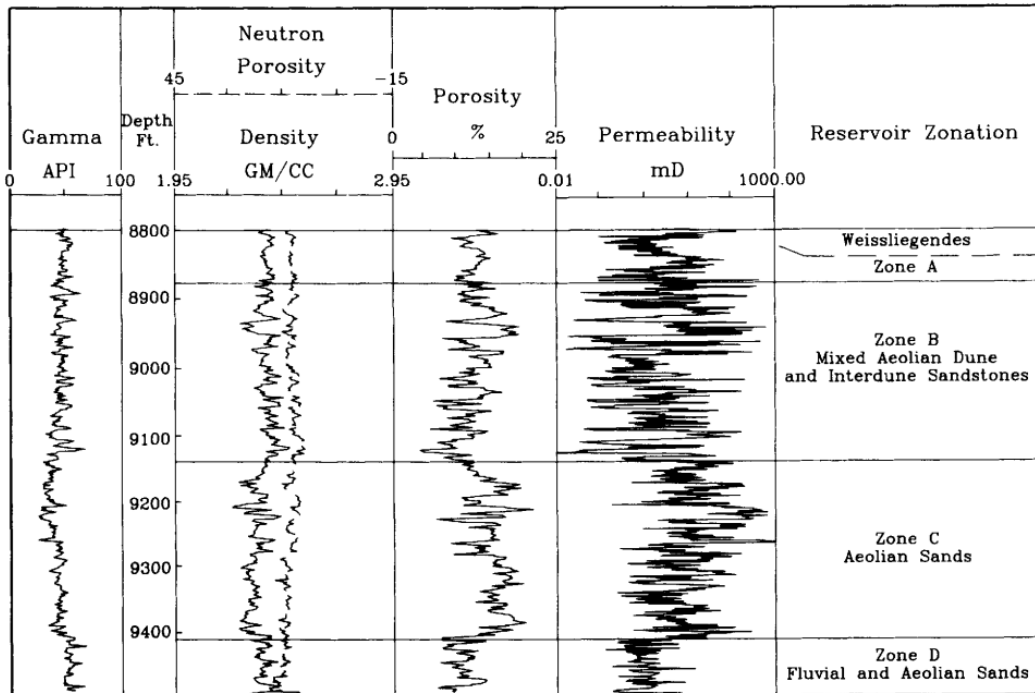
Figure 1.2: Type section for the Leman sandstone in the Vanguard field from Lahann et al. (1993)

migrating fluids and these wells could not be completed economically. There are also significant differences in the productivity of the other wells despite the similarity of the perforated intervals in terms of reservoir zonation. The Vanguard field did not experience the extensive formation of kaolinite from feldspar which characterises the early diagenesis of other Rotliegendes reservoirs. In Vanguard, the principal diagenetic products are quartz cement, illite and chlorite (Lahann et al., 1993; McNeil et al., 1995). Post depositional faults acted as conduits for migrating fluids which altered mineralogy and promoted the dissolution of K-feldspar and the formation of illite. As K-feldspar was removed, the remaining rock fragments were compacted resulting in a significant porosity reduction in the diagenetically altered zones.

Figure 1.3 shows a SEM image of Leman sandstone sample. Quartz cement and extensive fibrous illite are evident in addition to partial dissolution of feldspar grains.

Core and log data for the Vanguard wells have been sourced from the Oil and Gas Authority (OGA) UK National Data Archive (NDA). The operator, ConocoPhillips have donated to the University 135 core plug samples from V-Field wells. The exact source of all these samples is not known, but at least 20 core plug samples are from Vanguard well 49/16-Q03.
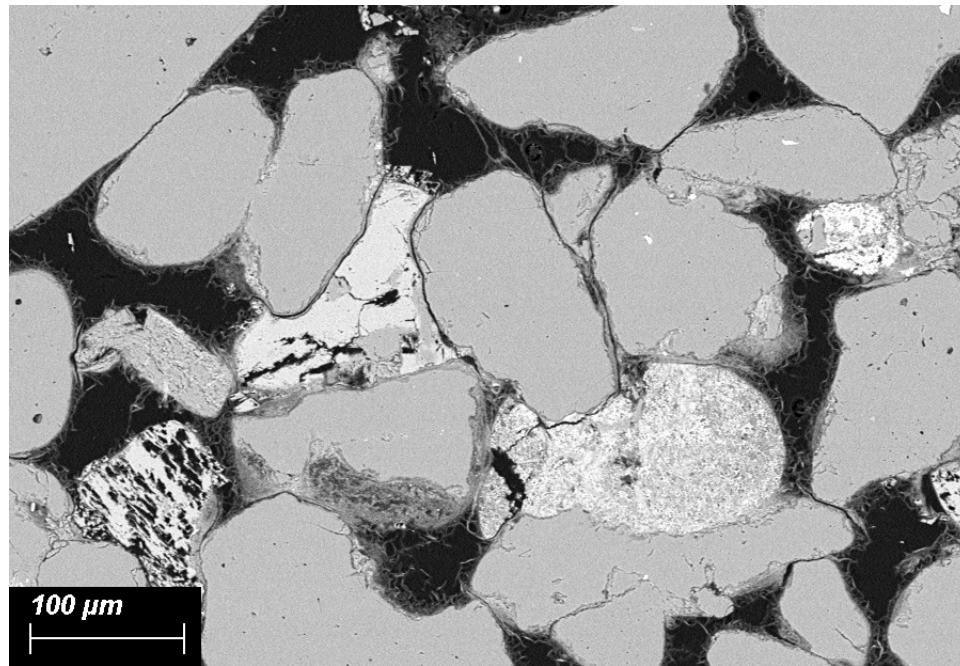
Figure 1.3: SEM image of Leman sandstone sample from Vanguard well 49/16-Q03, porosity 17.7%, permeability 7.5 mD

Appendix B contains a graphical presentation of the Vanguard convention core analysis (CCA) and special core analysis (SCAL) data. These data confirm some key observations:

- The reservoir is highly heterogeneous with core permeability values varying by more than four orders of magnitude.

- There is a weak correlation between permeability and porosity, particularly in zones A, B and D.

- Zone C has the highest reservoir permeability and notably better than zone D at the same porosity.

- The capillary pressure data (MICP and air-brine) show that most samples have 2 to 3 orders of magnitude variation in pore sizes.

Although the field has ceased production, there is still a benefit to understanding the pore scale architecture and multiphase flow characteristics because the UK Southern North Sea area contains many similar Leman sandstone gas fields. Many of these are still in production or could be ideal candidates for CSS at some point in the future.

1.7   Aims and Objectives

The aim of this project is to use advanced imaging technologies at multiple scales to develop an enhanced multiphase modelling flow for petroleum reservoir management and environmental engineering such as CCS projects and water resource management. The workflow should incorporate pore scale imaging and modelling of natural sandstone rocks which have a complex multiscale pore architecture with significant heterogeneity and a wide range in pore sizes.

The key objectives of this project are as follows:

- Obtain pore scale images in 2D and 3D of representative samples from the Guillemot A and Vanguard fields.

- Analyse and quantify the pore space geometry and topology from 2D and 3D imaging information.

- Develop a stochastic algorithm to generate PNMs from statistical pore architecture information.

- Generate multiphase flow functions (relative permeability and capillary pressure) from quasi-static PNM and calibrate with measured SCAL data as appropriate.

- Demonstrate the applicability of the multiphase flow functions through continuum modelling at the field scale.

1.8   Outline of the Thesis

Chapter 2 reviews important literature relating to pore scale imaging and modelling. The first section reviews SEM and µCT imaging techniques, their advantages and disadvantages. The second section reviews documented methods of creating pore scale models from 2D and 3D imaging information. The third section reviews the subject of wettability which has a significant impact on multi-phase flow properties and is an important consideration for oil recovery and CCS projects.

Chapter 3 covers the acquisition and processing of 2D SEM and 3D µCT images of rock samples from Guillemot A and Vanguard fields.

Chapter 4 explains the characterisation of the pore space from the processed images. The methodology is detailed first, followed by the results in terms of pore size, pore coordination and pore shape factor. The final section compares 2D and 3D characterisation results to see if it possible to estimate 3D pore size and connectivity from 2D data.

The stochastic PNM generation algorithm is described in Chapter 5. The algorithm is used to generate a range of models which are used to calculate single and multiphase flow properties for comparison with measured data.

Chapter 6 describes field scale continuum modelling of the Guillemot A field using the relative permeability and capillary pressure functions generated from the stochastic pore networks.

Finally, Chapter 7 summarises the work programme, highlights the key conclusions and presents some suggestions for future investigation.

Chapter 2

Literature Review

"Try this," [Mrs Phelps] said at last. "It's very famous and very good. If it's too long for you, just let me know and I'll find something shorter and a bit easier."

"Great Expectations," Matilda read, "by Charles Dickens. I'd love to try it."

— Roald Dahl, Matilda

2.1 Pore Scale Imaging

2.1.1 SEM Imaging

In SEM, a high energy focused electron beam is scanned across the surface of a sample and signals produced by the electrons are used to construct an image (Figure 2.1). The signals produced by the electron beam include back-scattered electrons, secondary electrons and X-rays (Welton, 2003; Reed, 2005; Zhou et al., 2006; Huang et al., 2013a; Anovitz and Cole, 2015; Bultreys et al., 2016a).

Back-scattered electrons (BSE) are incident beam electrons that are elastically scattered by atoms in the sample. The back-scattering depends strongly on the mean atomic number; typically low density areas of the sample produce a dark image and high density areas are bright (Reed, 2005). If the electron beam is high energy (circa 30 kV), then backscattered electrons can be detected from up to 500 nm below the sample surface (Bultreys et al., 2016a). This results in a large interaction volume which limits the
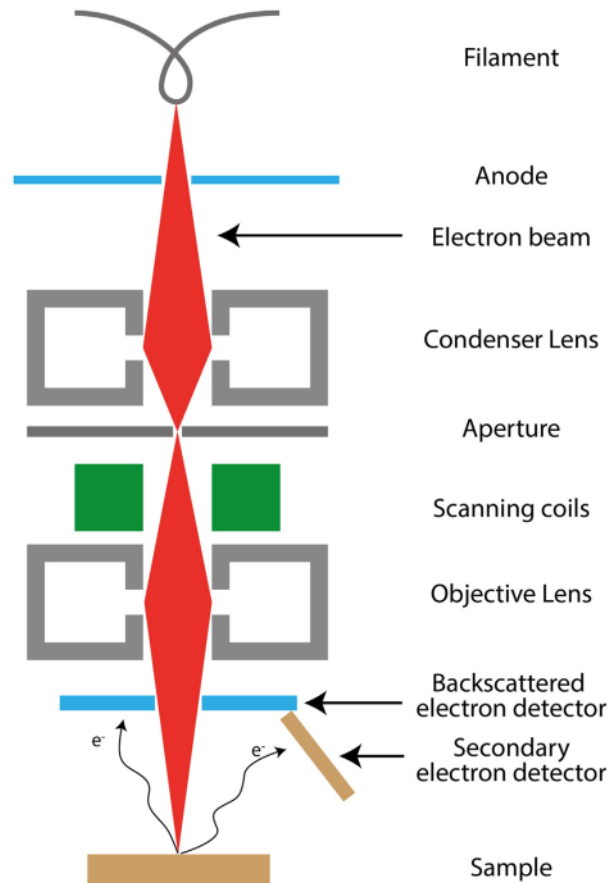
Figure 2.1: Schematic representation of a SEM from Bultreys et al. (2016a)

spatial resolution of the image; the latter is about half the thickness of the interaction volume. Better spatial resolution (50 to 100 nm) can be obtained by limiting the accelerating voltage to around 15 kV (Reed, 2005).

Secondary electrons (SE) are emitted when the primary electron beam excites an electron in the sample. They generally have much lower energy than the primary beam but originate from a much smaller interaction volume and therefore the resolution of SE images can be higher than BSE images (Huang et al., 2013a). The resolution of SE images is effectively the same as the beam diameter which is normally below 10 nm (Bultreys et al., 2016a). Secondary electron are not strongly dependent on sample composition but depend on topography (Figure 2.2); more secondary electrons escape from protruding edges causing them to appear bright relative to flat or concave surfaces (Reed, 2005).

X-rays are emitted when the electron beam excites inner shell electrons within atoms in the sample (Reed, 2005; Bultreys et al., 2016a). Each element has a unique atomic structure and generates X-rays with a characteristic

set of wavelengths. The X-rays can be analysed by Energy Dispersive X-ray analysis (EDX) to identify the elements present and map their distributions within the sample.
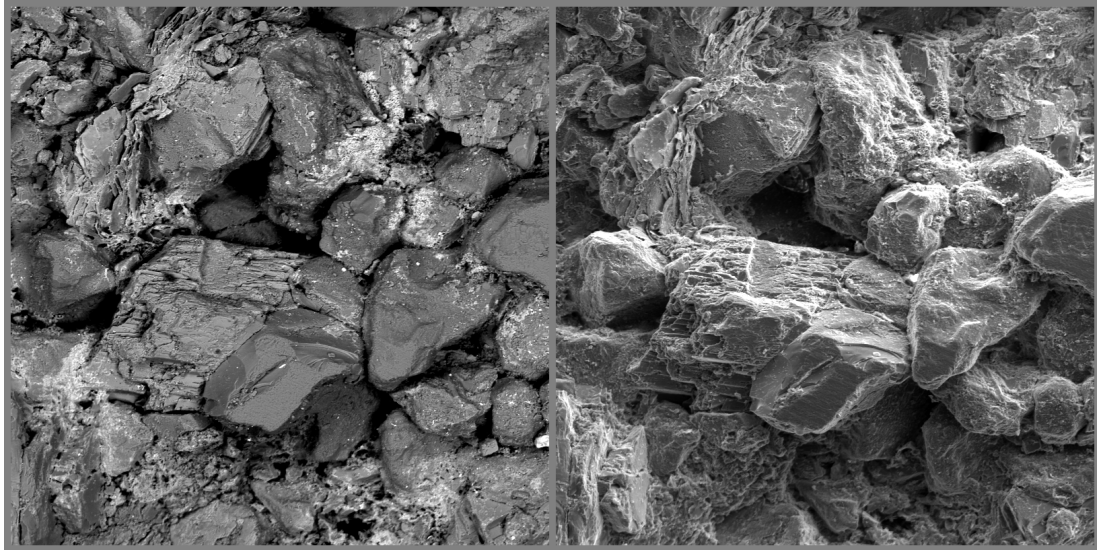
Figure 2.2: SEM images of an unpolished core plug sample from Guillemot A field, left: BSE image, right: SE image

Most geological samples are electrical insulators and require a conductive coating to prevent charge build-up under SEM. Carbon is the most commonly used conductive coating for BSE images but is less suitable for SE because of its low secondary electron yield (Bultreys et al., 2016a).

Unpolished rock surfaces are more commonly imaged by SE as this has high resolution and yields topographic information (Figure 2.2). This type of imaging is ideal for microstructure analysis and morphological identification of minerals (Pittman and Thomas, 1979; Welton, 2003; Huang et al., 2013b), but is less suitable for quantitative pore space characterisation.

The alternative is to create a flat surface by injecting a resin into the pore space, cutting the sample and then highly polishing the exposed surface. Such samples are normally imaged by BSE because there is no topographic contrast and the objective is to differentiate composition; the resin generally has a low density and appears black, minerals have a high density and appear grey to white. This type of image is better for automated rock and pore space characterisation (Ruzyla, 1986; Bultreys et al., 2016a). A disadvantage of polished samples is the possibility of creating artificial pores and fractures during the polishing process. Softer clays can be smeared and stretched and artificial pores can be created at the contact between soft clays and hard quartz or feldspar (Anovitz and Cole, 2015).

SEM is a 2D imaging technology, however it is fast, low cost, high quality, high resolution and covers a wide range of length scales. The trade-off between resolution and field of view is less of a problem for SEM imaging compared with other techniques. Despite the advent of 3D imaging approaches such as μCT, SEM is still popular for characterising the pore space of natural porous media (Wu et al., 2019b).

Clelland and Fens (1991) describe automated rock and pore space characterisation from SEM imaging. They used BSE imaging of polished sandstone samples with a resolution of about 1 μm. They performed grain detection, pore structure analysis from BSE images and automated mineral classification using EDX.

Beckingham et al. (2013) used SEM and μCT to derive pore and pore-throat size distributions of sandstone and reactive sediment samples. The permeability was calculated by constructing regular cubic lattice networks with pore body and pore throat radii randomly assigned from the measured distributions. They found that image resolution affects predicted permeability but SEM and μCT images of comparable resolutions provided comparable estimates of permeability. Low resolution images can over-estimate the size of pore throats leading to an over-estimate of permeability. They also found that high resolution images can under-estimate permeability, but this is most likely related to the pore network construction algorithm which did not incorporate any correlation between pore body and pore throat radii and therefore a higher proportion of smaller pore throats can decrease the connectivity.

Most recently, Wu et al. (2019b) investigated the pore structure of a low permeability sandstone using SEM imaging in addition to MICP, NMR and 3D μCT imaging. The pore radius distribution was quantified from SEM imaging over the range 0.2 to 50 μm and compared with the results from other techniques. They showed that μCT imaging has insufficient resolution to fully characterise low permeability sandstones and tight rocks.

2.1.2   μCT Imaging

X-ray Micro Computed Tomography (μCT) was introduced in the 1980s and the first μCT images of rock samples were generated with synchrotron X-ray sources (Flannery et al., 1987). A modern μCT scanner consists of an X-ray source and a detector placed on opposite sides of the sample. The sample

is rotated and many 2D X-ray images taken from different effective angles are combined through digital processing to create a 3D reconstruction of the rock sample (Herman, 2009).

A number of authors have published excellent reviews of μCT imaging and its application to natural porous media (Werth et al., 2010; Cnudde and Boone, 2013; Blunt et al., 2013; Wildenschild and Sheppard, 2013; Bultreys et al., 2016a; Zhang et al., 2019).
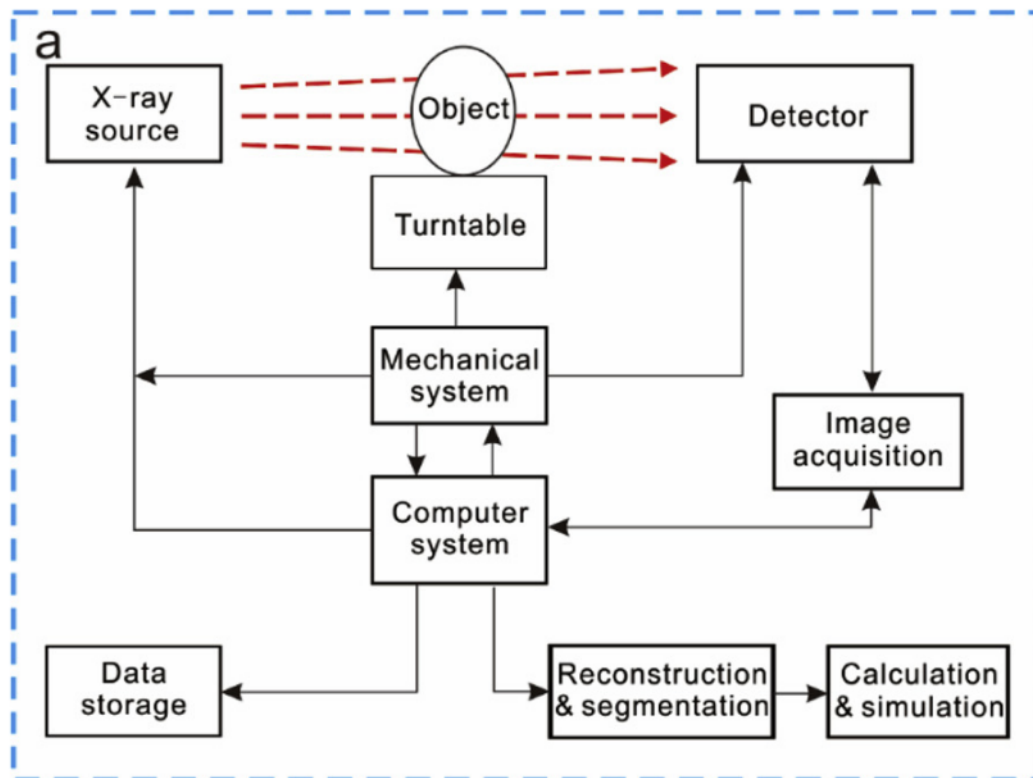
Figure 2.3: Schematic workflow of digital core analysis using lab-based μCT system from Zhang et al. (2019)

In essence, the X-rays produced by the source are attenuated when they pass through the sample and the detector records a sequence of 2D projections (radiographs). Typically, the sample is rotated about a vertical axis over 180° or 360° and several hundred to thousands of radiographs are recorded (Figure 2.3). The radiographs are processed by tomographic reconstruction (Herman, 2009) to create a 3D volume which shows the distribution of the X-ray attenuation coefficient by greyscale values. Generally, dark grey areas are low density and light grey areas are high density. However, the attenuation coefficient also depends on the atomic number of the material; therefore direct information on density or chemical composition of the sample is difficult to obtain (Cnudde and Boone, 2013; Bultreys et al., 2016a).

Using a laboratory μCT scanner is the most common approach to imaging geological materials (Blunt et al., 2013). This type of instrument typically contains a conventional X-ray tube; a device that generates X-rays by accelerating electrons under vacuum and focusing them onto a metal target e.g. tungsten (Wildenschild and Sheppard, 2013). In laboratory μCT scanners the beam is not collimated and is conical (Figure 2.4) or sometimes fan-shaped. The X-rays are also polychromatic i.e. there is range of photon energies, typically 30-160 keV (Blunt et al., 2013). A disadvantage of μCT scanners is the time required for a complete 3D scan, up to 24 hours, because X-ray tubes are relatively low intensity sources (Wildenschild and Sheppard, 2013). Synchrotron X-ray sources are much more powerful and a 3D scan can be completed in 10-30 minutes (Werth et al., 2010), however synchrotron facilities are limited and expensive to use.
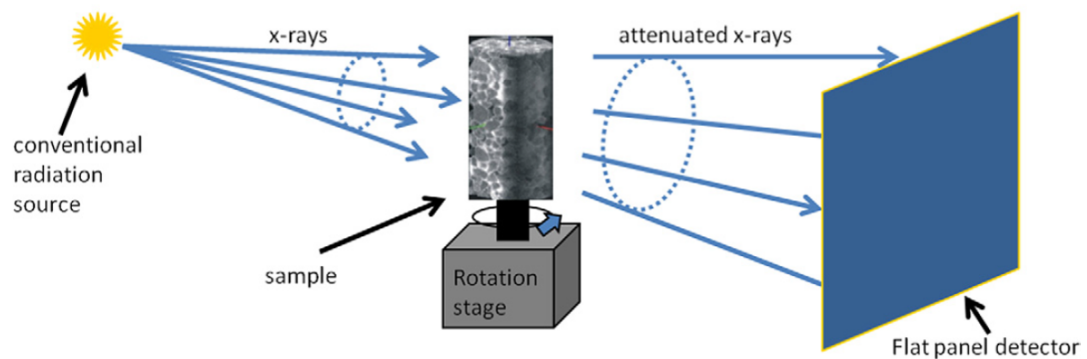
Figure 2.4: Typical tomography setup for a μCT scanner with a cone beam from Wildenschild and Sheppard (2013)

Another disadvantage of μCT scanners is that range of photon energies can introduce image artefacts (Blunt et al., 2013; Cnudde and Boone, 2013). X-ray attenuation coefficients are generally higher for low energy photons; therefore as the X-ray beam progresses through a material it becomes depleted in lower energy photons and there is a relative excess of high energy photons. This is called beam "hardening" (Wildenschild and Sheppard, 2013) and as a result, the beam experiences a higher attenuation coefficient at the beginning of its passage through a homogeneous material than further in. Tomographic reconstruction algorithms do not fully account for this effect and the edges of objects consequently appear more attenuating i.e. brighter (Wildenschild and Sheppard, 2013). The impact of beam hardening can be reduced by filtering out low energy photons from the beam but this reduces the X-ray intensity and thereby increases noise and/or image acquisition time.

Another problem with µCT scanners is the cone-beam artefact (Cnudde and Boone, 2013) which arises because tomographic reconstruction depends on approximations that are only strictly valid at low cone angles. Cone-beam artefacts can be eliminated by helical scanning (Varslot et al., 2011; Sheppard et al., 2014) but this is not generally implemented in laboratory µCT scanners.

One advantage of µCT imaging is that it is non-destructive. Another advantage is the high resolution, typically in the range 1-10 µm, which is generally the best resolution among 3D imaging methods (Werth et al., 2010). For µCT scanners the resolution of the image is determined by the focal spot size of the source and the proximity of the sample to the source (Cnudde and Boone, 2013; Blunt et al., 2013). In a cone-beam set-up, the geometrical magnification can be adjusted by moving the sample towards or away from the source (Cnudde and Boone, 2013). The minimum attainable spot size is about 3 µm for a power of less than 7 W (Elkhoury et al., 2019). Increasing power increases the spot size and a decrease in power results in additional noise.

Normally, the imaged volume is only a few mm across. To maximise image quality, it is desirable to minimise attenuation of the X-rays outside the subject volume; therefore for best results the sample should be cut to a cylindrical shape with a diameter not much larger than the image size (Cnudde and Boone, 2013; Zhang et al., 2019).

Typical images from µCT scanners are 1000^3 to 2000^3 voxels (Blunt et al., 2013). However, it is not possible to capture 3 orders of magnitude range in pore features. Pores generally need to be at least 2-3 voxels across to be imaged reliably and, to avoid an image dominated by a few large pores, the image size needs to be considerably larger than the maximum pore size; therefore typical µCT images will capture at best 2 orders of magnitude range in pore sizes.

The term "image resolution" usually refers to the size of one voxel but this is not the same as "spatial resolution" which is a measure of the resolving power of the complete imaging system. Spatial resolution is complex and depends on the instrument parameters as well as the sample size and the attenuation contrast within the sample (Cnudde and Boone, 2013; Elkhoury et al., 2019). True spatial resolution is seldom evaluated in practice hence the term "resolution" is commonly used to denote the reconstructed voxel size.

Elkhoury et al. (2019) have published a detailed study of the spatial resolution of a Nikon XT H 225 ST µCT scanner measured using a resolution chart consisting of gold lines of known spacing fabricated on a silicon chip. They concluded the smallest resolvable length scale was about 7 µm using a focal spot size of 3 µm. They also found that the measured line width was consistently over-estimated by about 1 pixel even with the smallest pixel size of 2 µm.

A number of studies have shown that the porosity of many geological samples is underestimated by µCT imaging because of the inability to resolve the smallest pores (Soulaine et al., 2016; Garing et al., 2017; Munawar et al., 2018; Thomson et al., 2018).

Boever et al. (2015) analysed a sample of Vosges sandstone containing around 10% clay minerals using µCT, SEM and EDX. A low resolution µCT scan (8.9 µm/voxel) imaged circa 40% of the measured porosity and a high resolution scan (0.89 µm/voxel) of a microplug sub-sample, imaged circa 75% of the porosity. Image registration techniques were used to link the microplug scan to the larger sample and link the SEM and EDX images to the larger sample. This linking enabled a pseudo-3D mapping of the distribution of mineral phases within the sample and a better understanding of the impact of mineralogy on pore structure.

2.2   Pore Scale Modelling

This section reviews methods of constructing pore scale models, firstly voxel models of the pore space and secondly pore network models (PNM). PNMs can be extracted from 3D voxel models or generated from statistical information. Figure 2.5 is a flow chart showing the relationship between data sources and various type of pore scale models. The methodologies are reviewed in the following sections.

2.2.1   Pore Space Reconstruction from 2D Imaging

Although it is possible to study pore space morphology and construct pore space models directly from 3D µCT volumes, such models are limited by the inherent resolution and field of view of the data. As, discussed above, SEM is inherently better quality and higher resolution than µCT imaging and this has motivated a number of workers to develop techniques to reconstruct
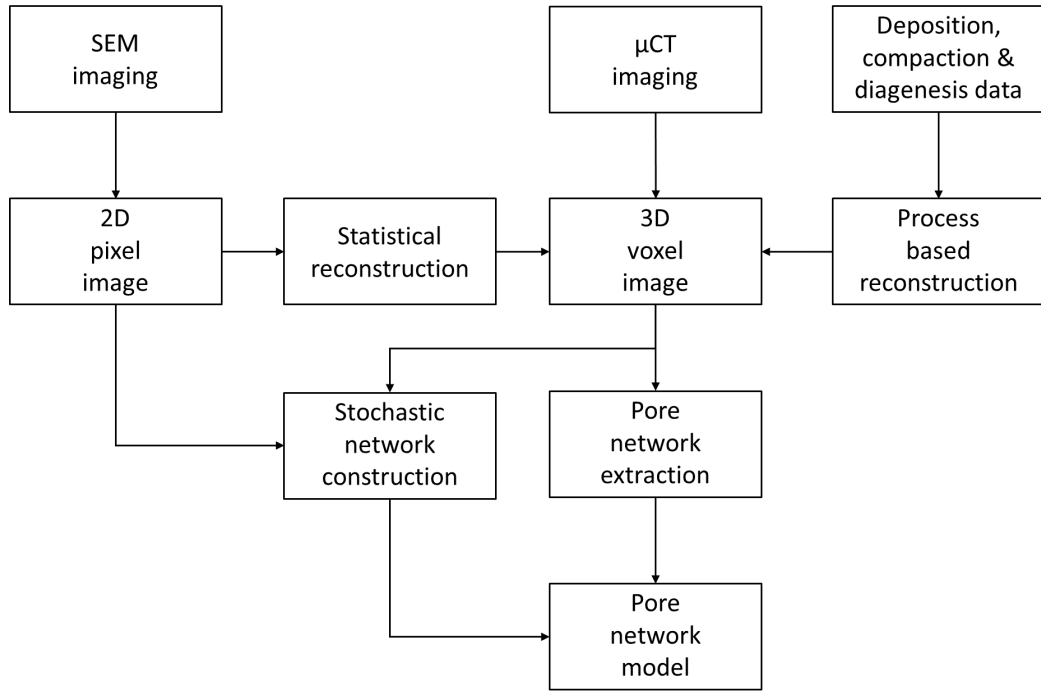
Figure 2.5: Flow chart showing different methods of constructing pore network models

3D voxel volumes from 2D training images. These methods extract patterns, typically multi-point statistics (MPS), to reproduce connectivity of the pore space (Blunt et al., 2013).

The methods generally assume that the pore space is isotropic and the third dimension is statistically equivalent to the other two. However, some algorithms can reconstruct anisotropic media given two or three orthogonal 2D training images.

A binary image of a porous medium can be represented by a characteristic or indicator function:

$$f(\vec{x}) = \begin{cases} 1 & \text{if voxel } \vec{x} \text{ is pore space} \\ 0 & \text{otherwise} \end{cases} \tag{2.1}$$

where $\vec{x} = (i, j, k)$ is a position vector. The porosity is given by:

$$\phi = \langle f(\vec{x}) \rangle \tag{2.2}$$

where $\langle \rangle$ denotes the spatial average.

The two-point correlation function is given by:

$$s(\vec{h}) = \langle f(\vec{x})f(\vec{x}+\vec{h}) \rangle \qquad (2.3)$$

where $\vec{h}$ is a lag vector.

The two-point correlation function satisfies the following relations (Blair et al., 1993; Pyrcz and Deutsch, 2014):

$$s(\vec{0}) = \phi \qquad (2.4)$$

and

$$\lim_{\vec{h}\to\infty} s(\vec{h}) = \phi^2 \qquad (2.5)$$

The semi-variogram, $\gamma(\vec{h})$, commonly used in geostatistical modelling, is given by:

$$\gamma(\vec{h}) = \frac{1}{2}\langle (f(\vec{x}) - f(\vec{x}+\vec{h}))^2 \rangle = s(\vec{0}) - s(\vec{h}) = \phi - s(\vec{h}) \qquad (2.6)$$

Adler et al. (1990) determined the two-point correlation function from binary 2D thin section images and reconstructed 3D models to match the porosity and the two-point correlation function. They calculated permeability from the reconstructions but obtained rather poor agreement with measured data.

Manwart et al. (2000) performed the reconstruction of a Berea sandstone and a Fontainebleau sandstone using a simulated annealing algorithm. The algorithm starts with a random distribution of pore space and rock matrix voxels that honours a given porosity. At each iteration, two voxels of different phases are randomly chosen and they are exchanged with probability given by the Metropolis rule (Yeong and Torquato, 1998):

$$p = \begin{cases} 1 & \text{if } E_i \leq E_{i-1} \\ \exp\left(\frac{E_{i-1}-E_i}{T}\right) & \text{if } E_i > E_{i-1} \end{cases} \qquad (2.7)$$

where E_i is the system "energy" at iteration i given by the squared misfit i.e. the difference between the statistical function and the target statistical function. T is the system "temperature" which starts at a high value and is reduced slightly at each iteration thereby gradually decreasing the probability of accepting an exchange that increases the misfit.

Manwart et al. (2000) extracted the two-point correlation functions from 2D sections of 3D µCT volumes. They also incorporated the lineal-path (Yeong and Torquato, 1998) and the pore size distribution functions into the algorithm, however they found that these did not improve the connectivity of the reconstructions. The results showed that simple morphological quantities agreed well between the reconstructions and the original data but the local percolating probability and the total fraction of percolating cells were under predicted in the reconstructions.

Keehm et al. (2004) investigated the reconstruction of 7 sandstone samples from the Daquing oil field based on thin-section micrographs. They used Sequential Indicator Simulation (SIS) (Journel, 1986) to generate reconstructions honouring the porosity and the two-point correlation function. SIS uses a random walk through the computational grid and indicator kriging is used for each voxel to estimate the conditional probability of pore space or rock matrix based on the previously simulated voxels and the two-point correlation function (Sahimi, 2011; Pyrcz and Deutsch, 2014).

Keehm et al. (2004) calculated the permeability using LBM and obtained a good match with the measured permeabilities. They concluded that SIS generates better connectivity than simulated annealing algorithms.

A number of other workers (Biswal et al., 1999; Hazlett, 1997; Øren and Bakke, 2002) have concluded that low-order statistics (porosity and the two-point correlation function) are insufficient to reproduce the connected long-range geometry, particularly in low porosity systems. Despite this, methods based on low-order statistics have still been employed in some more recent studies (Fullwood et al., 2008; Bodla et al., 2014; Hasanabadi et al., 2016).

Multi-point statistics (MPS) is an extension of low-order statistics. MPS methods attempt to characterise and simulate the spatial continuity between three or more locations at a time. A review of MPS methods for geostatistical modelling is given by Tahmasebi (2018).

To incorporate higher order statistics, Wu et al. (2004, 2006) used a template to capture patterns in the training image and replicated the patterns in the 3D reconstruction using a Monte-Carlo Markov chain algorithm. Okabe and Blunt (2005a,b) extended this approach using a larger template to capture larger scale patterns. They used the single normal equation simulation (SNESIM) method introduced by Strebelle (2002). A search tree is constructed to store multi-point statistical information extracted from a training

image and the algorithm generates a reconstruction by simulating voxels in a random sequence and calculating the probability of void or solid based on the multi-point statistics and conditioning data (previously simulated voxels). To minimise memory requirements, they used a four-stage multi-grid method that starts at the coarsest scale and transfers simulated values to the next level as conditioning data. The results showed that the local percolating probability was much better predicted than other low-order statistical methods. The SNESIM method has also been extended to multiscale modelling (Okabe and Blunt, 2007) and 3D training images (Wu et al., 2018).

Tahmasebi and Sahimi (2012) introduced an MPS algorithm called cross-correlation based simulation (CCSIM). The first layer of the 3D reconstruction volume is given directly by the 2D training image which is used to reconstruct the second layer, which is then used to reconstruct a third layer, etc. They showed that the method is computationally faster and uses less memory than the Okabe and Blunt (2005a) SNESIM approach. In addition, the method better honours large-scale infrequent patterns and consequently reproduces highly heterogeneous systems more reliably (Tahmasebi et al., 2012).

Naraghi et al. (2017) proposed an MPS algorithm called direct patch simulation (DPSIM). The technique constructs a series of 2D images by copying patches from the training image, randomly at first and then by finding patches that best match nearby conditioning data (previously simulated pixels). The sequence of 2D images are then interpolated using a probability perturbation method (Kashib and Srinivasan, 2006) which is essentially a gradual deformation process. They showed that the method is accurate and computationally efficient.

An alternative approach proposed by Ju et al. (2014), uses a simulated annealing algorithm similar to Manwart et al. (2000) and Yeong and Torquato (1998) but incorporates a fractal system control function based on a box-covering fractal measurement. The simulated annealing is accelerated by a multiple interchange process and a novel pre-conditioning procedure. They showed that the reconstructions reproduce the two-point correlation function, the lineal path function and the fractal system control function.

Recently, Mosser et al. (2017, 2018) have used generative adversarial neural networks to reconstruct 3D images from 2D data. This is a type of machine learning that essentially learns to generate new data with the same statistics as a training data set. The authors show the method efficiently reproduces key attributes of the pore space including the Euler characteristic, two-point

statistics and single-phase permeability.

2.2.2 Process Based Reconstruction Methods

An alternative method of constructing a 3D voxel pore scale models is to simulate the principal sandstone formation processes of sedimentation, compaction and diagenesis. Early studies of this type modelled sedimentation by packing simple shapes (e.g. spheres) together. Compaction can be modelled by moving the centres of the shapes closer together in the vertical direction, allowing them to overlap. Diagenesis (essentially cementation) is modelled by expanding the shapes and allowing them to overlap further. In these models, the porosity is primarily controlled by the amount compaction and cementation.

Roberts and Schwartz (1985) used this type of model, excluding compaction, with both regular and random sphere packings. They used the model to calculate the electrical conductivity as a function of porosity and generated some insights into Archie's Law (Archie, 1942).

Random sphere packs with compaction and cementation were simulated by Bryant and Cade (1992) and Bryant et al. (1993). Equivalent networks were constructed and used to simulate single and multiphase flow.

Bosl et al. (1998) used data from a random packing of spheres (Finney and Bernal, 1970) and simulated cementation in various ways: uniform expansion of grains, preferential expansion at grain contacts and random filling of the pore space. They calculated permeability using LBM and found different permeability-porosity relationships depending on the cement deposition pattern.

An algorithm to simulate the packing of spheres of different sizes was developed by Bakke and Øren (1997). The grain size distribution was obtained from analysis of thin-section photomicrographs (Øren et al., 1998; Øren and Bakke, 2002). They incorporated compaction and cementation using existing methods; pore-lining and pore-filling clays were also included in the model (Biswal et al., 1999). They showed that process-based reconstruction algorithms generate more realistic connectivity than pore space reconstruction algorithms based on low-order statistics.

Packing of non-spherical grains was simulated by Coelho et al. (1997) and Pilotti (2000) modelled the deposition of irregular grains in a viscous fluid.

Biswal et al. (2007, 2009) developed a continuum geometrical modelling technique to reconstruct a sedimentary oolitic dolostone. The rock is represented by a random but correlated set of points decorated with crystallites which are polyhedra defined geometrically from image analysis. To simulate sedimentation and compaction, the grains are inserted into the model in sequence from largest to smallest using an overlap rule to control positioning based on the grain size. A texture rule is also used to correlate the location and properties of the grains with the depositional texture. The technique was later adapted to reconstruct a Fontainebleau sandstone using parameters for grain shape, compaction and diagenesis derived from 2D imaging (Latief et al., 2010) and a more complex carbonate system (Roth et al., 2011). The model is constructed in a continuum domain and is therefore capable of representing an arbitrary range of scales. Subsequently, it can be discretised at any convenient resolution to investigate flow and transport properties.

Politis et al. (2008) proposed a hybrid process-based and statistical reconstruction method. The technique uses a shape packing algorithm to create an initial pore space construction which is used as the input to a simulated annealing algorithm to minimise the error between the model and the target two-point correlation function. The authors claim the method is computationally efficient and preserves long-range correlations that are not reproduced in other low-order statistical methods.

2.2.3   Pore Network Modelling

Pore network modelling (PNM) is essentially a simplification or upscaling of the pore space into a network of pore bodies (nodes) and pore throats (bonds) (Blunt, 2001; Blunt et al., 2002; Jackson et al., 2002; Valvatne and Blunt, 2004).

Imaging of real porous media shows that pore bodies and throats in general have a highly irregular geometry which is very difficult to represent exactly. To calculate macroscopic transport properties it is necessary to represent the pores and throats with a simplified geometry such as triangular, square or circular section tubes.

A recent review of PNM is given by Xiong et al. (2016). The references above provide a detailed discussion of how multiphase flow is represented in PNM.

There are three main methods for generating PNMs viz:

- using a regular lattice e.g. cubic,

- extracting a network from a 3D voxel volume (either reconstructed or directly imaged),

- using a stochastic process to generate a non-regular network.

Regular Lattice Networks

Regular lattice networks were used in early studies (Blunt et al., 1992; Blunt, 1997; Fenwick and Blunt, 1998; Dixit et al., 1999). Such simple network models are relatively easy to construct and parameters can be tuned to available data such as MICP and pore coordination number distributions (Dillard and Blunt, 2000; Fischer and Celia, 1999).

A cubic lattice has a basic coordination number of 6 but can be extended with diagonal connections to allow coordination numbers up to 26 (Raoof and Hassanizadeh, 2010) although this will have physically unrealistic over-lapping of bonds. To avoid overlap, pore networks can be constructed from a body-centred cubic lattice using a truncated octahedron unit cell with a maximum coordination number of 14 (Jivkov et al., 2013).

However, simple network models based on regular lattices, with tuned parameters, are likely to have limited predictive capability because the data match is non-unique and essential features of the pore space are missing (Blunt, 2001). To reproduce qualitative trends in behaviour and make credible predictions, a disordered pore network is required containing the appropriate correlation between node and bond radii. In particular, the connectivity function is known to be important for controlling single-phase and multiphase flow behaviour (Vogel and Roth, 2001; Jiang et al., 2013b).

The connectivity function is an extension of the Euler characteristic which is a key topological invariant of a shape or structure. The Euler characteristic of a fully connected network with N_n nodes and N_b bonds, is given by:

$$\chi = N_n - N_b = N_n \left(1 - \frac{Z_{mean}}{2} \right)$$

(2.8)

where Z_{mean} is the mean coordination number (Vogel and Roth, 2001).

The specific connectivity, as a function of radius, is defined as the Euler characteristic per unit volume of the reduced network with elements larger

than the given radius. Hence the specific connectivity function is given by:

$$\chi_V(r) = \frac{N_n(r) - N_b(r)}{V} \qquad (2.9)$$

Where $N_n(r)$ is the number of network nodes with radii greater than r inside a volume V and $N_b(r)$ is the number of bonds which (i) have radii greater that r and (ii) connect nodes which both have radii greater than r. Note that the definition of $N_b(r)$ avoids dangling bonds in the reduced network.

Regular lattice network models with node and bond radii assigned randomly, generally do not reproduce realistic connectivity (Blunt, 2001). Pore networks should either be extracted from realistic imaging data, extracted from a process based reconstruction or generated from a stochastic process that honours connectivity information.

Pore Network Extraction from 3D Images

Three principal methods have been proposed to extract pore networks from 3D images.

Firstly, the medial axis method starts by transforming the pore space into a reduced representation called the medial axis or topological skeleton (Lindquist et al., 1996; Al-Raoush and Willson, 2005; Prodanović et al., 2006). The medial axis is defined as the set of points in the pore space having more than one closest point at equal distance on the pore wall. In continuum space this is a continuous set, however in discretised space, the voxels which satisfy the medial axis criterion are generally disconnected (Silin and Patzek, 2006).

Medial axis methods generally use grassfire or thinning algorithms (Zhang and Suen, 1988; Zhang et al., 2008; She et al., 2009) to generate a connected skeleton which is a superset of the medial axis voxels. Jiang et al. (2007) developed a novel thinning algorithm than checks voxels in ascending order of distance from the pore wall and deletes them if this does not change the image topology. The remaining skeleton preserves topology, preserves "medialness" and is single voxel width. Youssef et al. (2007) describe pore network extraction based on a conceptually similar thinning algorithm by Fouard et al. (2004). Liang et al. (2019) have presented a further improved thinning algorithm specifically for 3D porous media.

In the medial axis method, nodes are associated with junctions of the

skeleton and the node radius is defined as the distance from the junction to the nearest pore wall. Sometimes a second junction occurs within the node radius; this situation can be handled by empirical node merging criteria (Jiang et al., 2007). Network bonds are associated with the residual parts of skeleton not covered by nodes. The medial axis method is a topology based method; the main advantage is that it preserves the topology of the pore space.

The second method is the maximal ball algorithm (Silin and Patzek, 2006; Al-Kharusi and Blunt, 2007) which is a morphology based method that tries to preserve the shape of the pore space. The algorithm finds, for each pore space voxel, the largest inscribed sphere that just touches the pore wall. Those spheres which are included in other spheres are removed and the remaining ones are defined as maximal balls. The centres of the maximal balls define the skeleton of the pore space (Silin and Patzek, 2006).

The method was adapted by Al-Kharusi and Blunt (2007) who developed comprehensive criteria to determine the hierarchy of maximal balls and how to handle equally sized balls. Dong and Blunt (2009) improved the method, introducing a two-step searching algorithm to avoid nodes with very high coordination numbers and other efficiencies to reduce the memory requirements and computing time. Further improvements are discussed by Arand and Hesser (2017); they use a subvoxel accurate distance field and introduced a more efficient data structure called a morphology volume.

In the maximal ball algorithm, the pore bodies and throats are defined from the hierarchy of maximal balls. In general the largest balls define pores and the smallest ones define throats. In particular, a maximal ball with no larger neighbours is defined as an ancestor, its smaller overlapping neighbours are ranked as second generation and their smaller overlapping neighbours are ranked as third generation etc. A throat is defined as a maximal ball that is a common child of more than one ancestor (Figure 2.6). After all pore and throat maximal balls are identified, the pore space is segmented into nodes and bonds. Dong and Blunt (2009) defined a segmentation coefficient which is somewhat arbitrary parameter which determines the proportion of length and volume assigned to bonds relative to nodes.

The third method applies a watershed algorithm (Bieniek and Moga, 2000) to the negative distance map of the pore space. The method was first described by Thompson et al. (2005) and applied by Sheppard et al. (2005, 2006) but has become more popular recently (Rabbani et al., 2014; Homberg et al., 2014).
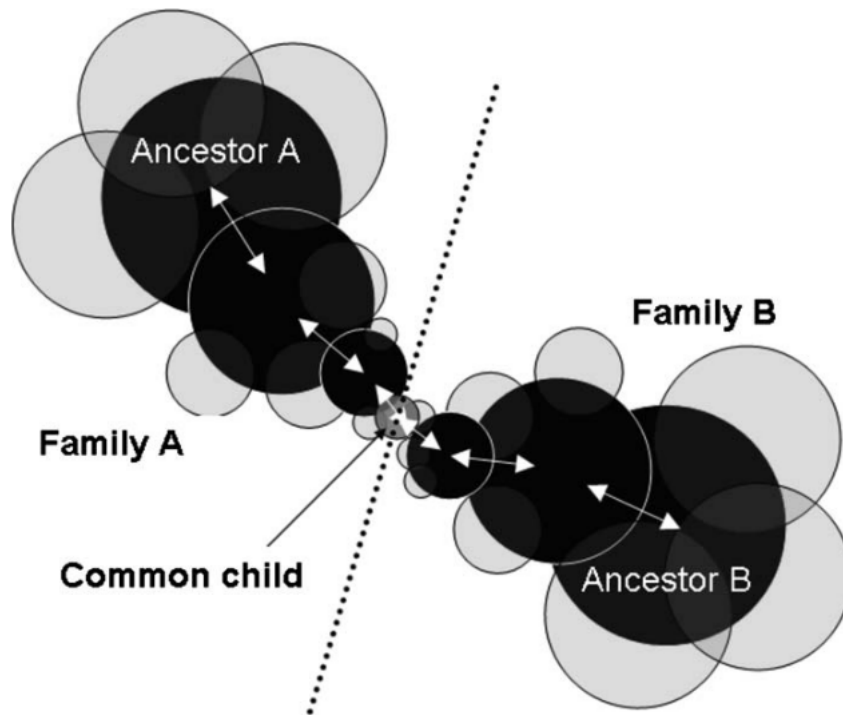
Figure 2.6: Schematic of two families of maximal balls and their common child defining a pore throat from Dong and Blunt (2009)

To understand the watershed algorithm, consider a 2D image interpreted as the topography of a surface i.e. the greyscale value of each pixel represents the height at that point. Water falling on the surface will flow in the direction of steepest descent into a local catchment basin. Each catchment basin has a single local minimum and the watershed lines are the elevated ridges separating adjacent catchment basins.

The concept can be extended to 3D where the catchment basins are connected groups of voxels with a single local minimum and the watersheds are the surfaces separating adjacent catchment basins. The algorithm of Bieniek and Moga (2000) simulates the flooding process and labels each voxel with an index identifying its catchment basin.

For a pore space image, the watershed algorithm is applied to the negative distance map of the pore space e.g. the Euclidean Distance Map (EDM) is the Euclidean distance from each voxel to the nearest point on the pore wall. The algorithm thus divides the pore space into catchment basins which comprise all voxels whose path of steepest ascent terminates at the local maximum of the distance map. The catchment basis become the pore bodies (nodes) with radius equal to the Euclidean distance at the local maximum and the pore throats (bonds) are the watersheds i.e. the

boundaries between catchment basins. All of the volume is assigned to pore bodies as the pore throats are just surfaces.

Homberg et al. (2014) used the Euclidean Distance Map (EDM). However, Rabbani et al. (2014) used the city-block distance (the sum of the absolute differences of the Cartesian coordinates of two points) because they found it creates more angular contours and leads to clearer pore-throat distinction.

A problem with the watershed method is the presence of spurious peaks (local maxima in the distance map) that arise on ridges and saddle points particularly in high porosity materials. These spurious peaks lead to over-segmentation of the pore space. Rabbani et al. (2014) applied a median filter to the distance map to alleviate this problem. Homberg et al. (2014) also observed multiple local maxima but applied node merging criteria based on the radius difference in a post-processing step. Gostick (2017) describes a more complete solution to the problem; firstly a Gaussian blur filter is applied to the EDM, then spurious peaks on saddles and plateaus are eliminated and finally nearby peaks are merged. Having identified all the valid peaks; these are passed as markers to the watershed algorithm which defines the boundaries between catchment basins (Figure 2.7).
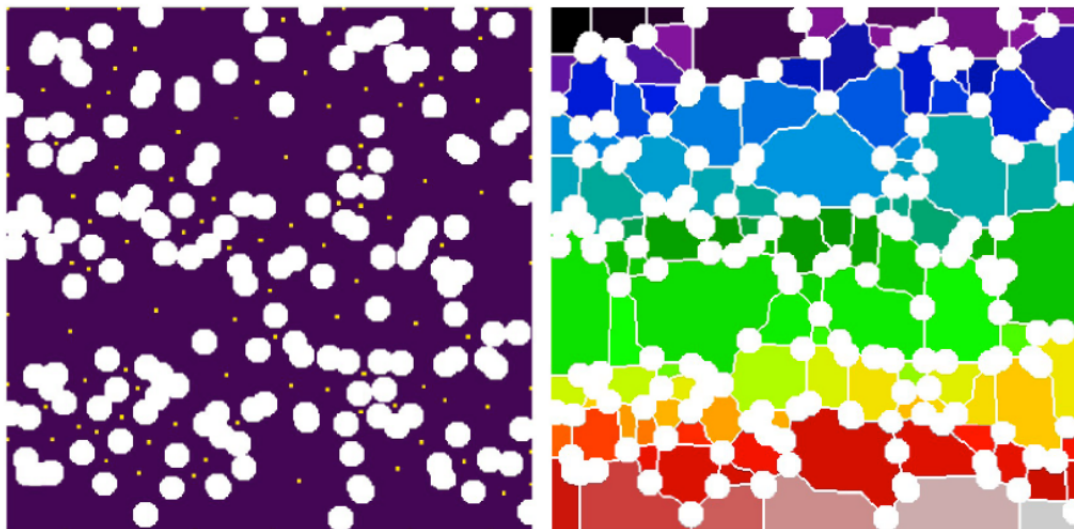
Figure 2.7: Watershed segmentation from Gostick (2017). Left: High porosity medium showing valid peaks of the EDM (markers) as light points, right: watershed catchment basins

Stochastic Pore Network Algorithms

Stochastic pore network generation algorithms generally fall into two categories.

Firstly, there are algorithms that (implicitly or explicitly) assume the pore space is relatively homogeneous and the pore size and pore coordination number distributions are not too wide. For example, Arns et al. (2004) describe a method of generating stochastic networks for a regular lattice that honours both the mean coordination and the coordination number distribution. Idowu and Blunt (2008) proposed a different algorithm that positions nodes randomly (non-overlapping) within the domain, honours node and bond radii distributions and the coordination number distribution. The algorithm also incorporates the correlation between node radius and coordination and the correlation between node and bond radii.

Jiang et al. (2012) present an improved methodology that honours the connectivity function (Vogel and Roth, 2001) as well as the node and bond properties and the coordination number distribution. They analysed networks extracted from μCT images of two sandstones and determined the strong and moderate correlations between node and bond properties. Generally, they found the strongest correlations were between:

- node radius and node volume,

- node radius and coordination,

- node radius and bond radius.

The strong correlations were honoured directly and the moderate correlations were described with conditional probability distributions.

The algorithms of Idowu and Blunt (2008) and Jiang et al. (2012) honour connectivity information and they successfully constructed networks that reproduced multi-phase flow functions for simple homogeneous sandstones. However, they assume that network nodes are uniformly distributed in space which is unlikely to be correct for complex sandstones.

The second group of algorithms are based on the concept of heterogeneous preferential attachment (HPA) (Santiago, 2008; Yakubo and Koroak, 2011) which is an extension of the Barabasi-Albert (BA) model of heterogeneous networks (Barabasi and Albert, 1999). These algorithms are fundamentally modelling heterogeneous networks and they lead to the emergence of scale-free character with a power law behaviour. The HPA concept results in networks where the probability of coordination number Z is $\Pr(Z) \propto Z^{\alpha}$ where α is a scaling exponent. Although these models have been applied to complex soil systems and successfully reproduce observed power-law

behaviour, it has not been demonstrated that they can reproduce experimental relative permeability data. One of the problems with these models is that they are difficult to embed in 3D space; which is essential to calculate continuum properties such as porosity and permeability.

2.2.4 Multiscale Network Models

A number of workers have published multiscale network modelling techniques aimed at both sandstone and carbonate systems. A schematic of the key techniques is given in Figure 2.8.

These methods essentially create networks at different scales from different resolution images and then join them together in some way. Typically, it is assumed that the porous medium consists of two types of pores and has a bimodal pore size distribution. The larger macropores are primary intergranular pores and the smaller micropores are either secondary pores created by dissolution of primary grains or pores within diagenetic products such as cements or clays. In Figure 2.8(a) the original porous medium is shown with the matrix in solid black and the macropore network nodes and bonds are shown by blue circles and blue bars respectively.

Figure 2.8(b) shows a lattice based model of the micropores introduced by Békri et al. (2005). In this model, the micropores are represented by continuum properties: porosity, permeability, capillary pressure and relative permeability, distributed on a regular lattice (yellow in Figure 2.8(b)) with connections to the macropore network (shown red in Figure 2.8(b)). Békri et al. (2005) assumed that the continuum properties were homogeneous, but in principle they could be heterogeneous.

Similarly, Bauer et al. (2011, 2012) represented micropores by continuum properties, but they proposed a dual PNM consisting of two parallel networks, connected at the nodes, where the fluid exchange takes place (Figure 2.8(c)). The main issue with these approaches is the requirement to derive continuum properties either from experiment or from microscale PNM. For example, Bauer et al. (2012) were not able to image the micropores directly and they calculated microscale relative permeability from a cubic lattice network with pore throat radii determined from MICP data. Yao and Al. (2013) followed a similar approach, but calculated continuum properties of microporous regions using high resolution SEM images as input to a 3D reconstruction algorithm.
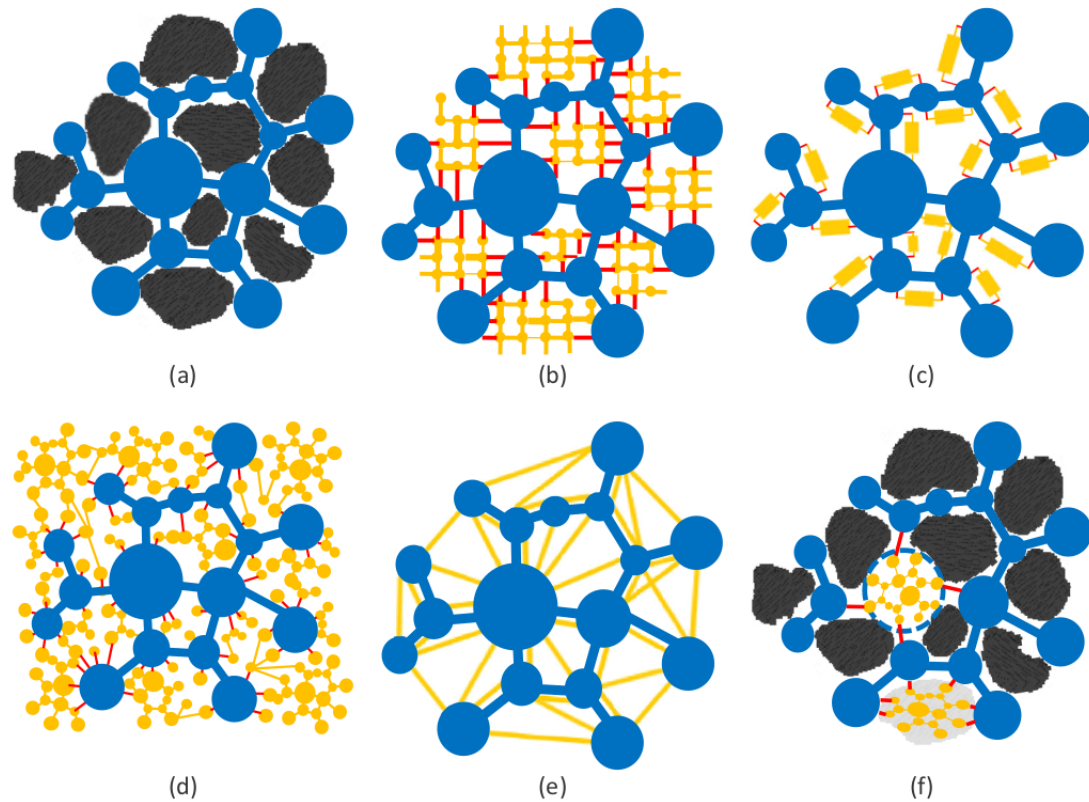
Figure 2.8: Schematic of multiscale network modelling approaches from Tahmasebi and Kamrava (2018): (a) Macropore network, (b) lattice-based model of micropores (yellow) with connections to macropores (red), (c) parallel network of micropores, (d) macroscale and microscale networks joined together, (e) serial and parallel microlinks, (f) microscale networks of grain-filling and pore-filling microporosity

Wu et al. (2011), Roth et al. (2012) and Jiang et al. (2013b) discuss techniques which generate two pore networks at different scales and then join them together (Figure 2.8(d)). Wu et al. (2011) reconstructed 3D voxel volumes from 2D SEM images at multiple scales and generated multiple stochastic networks. Roth et al. (2012) and Jiang et al. (2013b) extracted macroscale networks from 3D μCT volumes and generated microscale networks stochastically using statistical data from high-resolution μCT or SEM images. The microscale networks were distributed uniformly but this was refined later (Jiang et al., 2013a). Pak et al. (2016) extended the technique to three-scale network models using data from multiple resolution μCT images.

Mehmani and Prodanović (2014) used a similar approach to Jiang et al. (2013b) but distinguished between pore-filling microporosity which acts in series with the macropores and intragranular or dissolution microporosity which acts in parallel (Figure 2.8(f)). They used a sphere packing process-

based reconstruction method to generate both macroscale and microscale networks. Within the macroscale network a given fraction of grains are designated as microporous and a given fraction of pore bodies are designated as microporous and these grains and pore bodies are replaced by appropriate microscale networks linked to the macro-network. The model was used to study the behaviour of tight gas sandstones and they showed that serial microporosity produces different effects from parallel microporosity. They also investigated the "permeability jail" phenomenon where both gas and water have very low relative permeability at intermediate saturations when the pore-filling microporosity is water saturated and the macroporosity is gas saturated. The method has been extended to use image-based modelling for the macroscale network (Prodanović et al., 2015; Mehmani et al., 2019).

Tahmasebi and Kamrava (2018) also used a similar approach to Jiang et al. (2013b) but employed high resolution 2D SEM images to reconstruct 3D models of the pore-filling microporosity and the intragranular microporosity using the CCSIM MPS algorithm (Tahmasebi and Sahimi, 2012).

Bultreys et al. (2015a,b) used a continuum modelling approach similar to Bauer et al. (2011) but upscaled the microscale properties into specific serial or parallel network connections called "micro-links" (Figure 2.8(e)). They used a sample of Estailledes carbonate with a clear bimodal pore size distribution, obtained a µCT image and performed a three-phase segmentation to identify pore voxels, solid voxels and microporous voxels. The volume and connectivity of the micro-links in the network were obtained from the morphology and distribution of the microporous voxels. They were not able to derive petrophysical properties of the microporosity from image analysis; they used rough estimates of porosity and permeability and obtained relative permeability for the micro-links from PNM assuming a cubic lattice network. They used finite size scaling laws from percolation theory to calculate the breakthrough capillary pressure sufficient for the non-wetting fluid to percolate through a micro-link. This means the breakthrough capillary pressure is a function of the length and cross-sectional area of a micro-link and not all micro-links will percolate at the same capillary pressure. This modelling approach has been extended to secondary waterflooding in mixed-wettability (Bultreys et al., 2016b).

Ruspini et al. (2016) followed a similar approach to Bultreys et al. (2015a), but used a process-based reconstruction method to generate network models for the microporous regions. They also used EDX/SEM analysis with an

image registration technique to identify minerals and microporous voxels in the μCT image.

All of the techniques above divide the pore space into classes (e.g. macropores and micropores) which are characterised separately and then linked to together in a single model. In sandstones, however, the combination of multiple diagenetic processes can create a wide range of pore sizes without necessarily being multi-modal.

2.3 Wettability

2.3.1 Oil-Brine-Rock Interactions

Wettability is the tendency for one fluid (e.g. water) to adhere to the rock surface in the presence of another fluid (e.g. oil). Consistent with most petroleum industry literature, the contact angle is defined here as the angle at which the water-oil interface meets the rock surface as measured through the water phase. If the angle of contact is small or zero, the rock surface is water wet. If the angle of contact is large or 180°, the rock surface is oil wet.

Direct contact angle measurements in porous media are difficult to perform, although some significant advancements have been made recently (Klise et al., 2016; AlRatrout et al., 2017). Historically, simpler experimental methods were developed to characterise wettability from the capillary characteristics of porous media. The most well know of these methods are the Amott (Amott, 1959) and USBM (Donaldson et al., 1969) tests (Section 2.3.2).

An early milestone study of wettability was conducted by Treiber and Owens (1972). They investigated the wettability of 55 oil reservoirs (most of them onshore USA) using contact angle measurements with reservoir fluids and crystals of reservoir minerals (quartz for sandstones and calcite for carbonates). They found that 50% of the sandstone reservoirs and 84% of the carbonate reservoirs were oil wet (contact angle greater than 105°). They also found no correlation between wettability and reservoir temperature or the oil API gravity.

As stated by Anderson (1986a), most reservoir minerals are intrinsically water wet, but this can be altered by the adsorption of certain compounds from the oil onto the rock surface. These surface active agents are generally considered to be polar compounds that contain oxygen, nitrogen and

sulphur most prevalent in the heaviest crude fractions such as resins and asphaltenes. For example, Crocker and Marchin (1988) obtained a linear relationship between USBM wettability and the concentration of nitrogen and sulphur compounds in the crude oil polar fraction.

Wolcott and Groves (1996) investigated the influence of oil composition on wettability alteration. They used Berea sandstone cores with six different crude oils. After aging the cores, the Amott wettability indices were measured and the results showed significant trends of increasing oil wettability with increasing resin and asphaltene content. In addition to oil composition, the degree of wettability alteration is influenced by the mineral surface, the brine composition and pH (Anderson, 1986a).

Intermediate wettability means that the angle of contact is some intermediate value between 0° and 180° (Anderson, 1986a). However few reservoirs, if any, have a homogeneous intermediate wettability. Fractional wettability is a more realistic concept and means that the large scale wettability is somewhere between water-wet and oil-wet but on the pore scale, some pores are water-wet and some pores are oil-wet (Anderson, 1986a). In a pure sense, some pores have zero contact angle and some have 180° contact angle. The term mixed wettability refers to a type of fractional wettability where the pore scale wettability is controlled by pore size. This concept was first introduced by Salathiel (1973) who postulated that the large pores become oil-wet whilst the small pores remain water-wet.

Subsequently, Kovscek et al. (1993) developed an improved theory that is the basis of mixed wettability in most current PNM simulators. Initially, the pore space is filled with water and the rock surfaces are strongly water-wet. After oil has migrated into the reservoir, a water film remains between the oil and solid pore surfaces of the order of 10 nm thick and is sufficient to prevent components of the oil being adsorbed onto the rock surface. At a critical capillary pressure, the water film collapses to an ultra-thin molecular layer which is not sufficient to prevent adsorption of oil components and the rock surface is able to become oil-wet. Kovscek et al. (1993) give an expression for the critical capillary pressure which is larger for large pores and therefore these pores are more likely to retain protective water films and less likely to become oil-wet (contrary to Salathiel (1973)).

Dubey and Doe (1993) discuss the stability of the water film between the oil and the rock surface as a function of the electric charges that form on the water/rock and water/oil interfaces. If these charges are large and of the same sign, then electrostatic repulsion maintains a thick water film and the

rock surface remains water wet. If the charges are of opposite sign, then the water film is unstable and the rock can become oil-wet. Quartz surfaces are negatively charged above pH 2. To determine the sign of the charge on the water/oil interface, the authors measured the zeta potential (the electric potential at the slipping plane of the interfacial double layer), as a function of pH, for emulsions of 24 crude oils. They found that the crudes had positive zeta potentials at low pH and each oil had an isoelectric pH above which the zeta potential is negative. This suggested that the oils would wet a quartz surface below a certain pH and would not wet the surface at high pH. The authors used a simple bottle test to measure the wetting behaviour of the crudes to clean sand as a function of pH and found that all the oils wetted the sand at low pH but not at high pH, in agreement with the theory. However, there was only a weak correlation between the wetting reversal pH and the isoelectric pH. The authors also measured acid numbers and base numbers of the crudes and found a weak correlation between the wetting reversal pH and the ratio of base number to acid number. This confirms the intuitive idea that surface charges are associated with acids and bases.

Three key mechanisms by which crude oils alter surface wettability are discussed by Buckley et al. (1997, 1998). Firstly, is the mechanism of surface precipitation of destabilised asphaltenes. The addition of asphaltene precipitants such as n-hexane significantly increases the tendency of crude oils to change surface wettability and the addition of asphaltene solvents such as toluene and alpha-methylnapthalene significantly decreases the tendency. They concluded that crudes with high API gravity can promote oil wetting because they are poor asphaltene solvents (in comparison to low API crudes).

Secondly, Buckley et al. (1998) discuss the mechanism of acid/base interactions. In general, the oil/water surface charge depends on the extent of acid/base dissociation reactions, the pH of the brine and ionic strength of the brine. Some combinations of acid/base numbers and brine compositions will stabilise the water film and others do not.

Thirdly, is the mechanism of ion binding. If there are sufficient divalent cations (e.g. Ca^{2+}, Mg^{2+}) in the brine, they can bridge the water film by binding at both the water/rock and the water/oil interfaces leading to film instability and the rock surface becoming oil-wet. For example, Yan et al. (1997) compared the wetting performance of a crude in the presence of NaCl, $CaCl_2$ and $AlCl_3$ brines and found that increased cation valency significantly

promoted oil wetting.

Robin et al. (1995) used cryo-SEM to investigate pore scale wettability. They found that wettability is related to both mineralogy and pore geometry. For a reservoir sandstone, kaolinite booklets ($\sim$10 µm) were oil-wet whilst quartz, feldspar, illite and fine kaolinite ($\sim$1 µm) were water-wet. For a reservoir carbonate, geometry largely affected the wettability with small pores water-wet and large pores oil-wet. The observation that kaolinite can promote oil wetting has been confirmed by other studies. Jerauld and Rathmell (1997) investigated cores from the Prudoe Bay field, they found from cryo-SEM that kaolinite was consistently wet by oil and flooding tests showed higher residual oil saturations in clay rich cores, consistent with the idea that oil sticks to clays. Amott wettability results also showed higher indices (more water wet conditions) for core samples with higher initial water saturations.

Hamon (2000) has published a review of field scale wettability variations in an oil bearing sandstone reservoir. The wettability was measured on 26 core samples using the Amott wettability test. Large variations in wettability were found with the most significant factors being height above the OWC and absolute permeability. Wettability to oil increased with increasing height above the OWC and increasing permeability. Mineralogy data were also available from thin-section and SEM images. These data showed a clear relationship with higher permeability samples having lower total clay plus mica content. There was no clear relationship between mineralogy and wettability. It was expected that increased kaolinite would result in greater oil wettability, however a weak opposite trend was observed. The author concludes that the effect of clays on pore geometry (i.e. permeability) is more significant than the direct effect on wettability.

2.3.2   Effect of Wettability on Oil Recovery

It is generally accepted that wettability has a significant effect on both multiphase flow functions (relative permeability and capillary pressure) and oil recovery (Anderson, 1987a,b,c; Morrow, 1990; Agbalaka et al., 2008).

We adopt the terminology of Morrow (1990): drainage is defined as water saturation decreasing and imbibition is defined as water saturation increasing; irrespective of the actual wetting condition of the rock. Here, the principal recovery mechanism of interest is waterflooding; therefore the

main focus is on imbibition relative permeability and capillary pressure.

The effect of wettability on capillary pressure is the basis of the standard Amott (Amott, 1959) and USBM (Donaldson et al., 1969) wettability measurements. A strongly water-wet core will have a positive imbibition capillary pressure which reaches zero at the residual oil saturation and a strongly oil-wet core will have a negative imbibition capillary pressure which becomes highly negative at the residual oil saturation (Killins et al., 1953; Anderson, 1987a).

The Amott test (Amott, 1959) measures the volumes for spontaneous/forced imbibition and spontaneous/forced secondary oil drainage, where the spontaneous processes correspond to a reduction in capillary pressure to zero and the forced processes correspond to increasing capillary pressure (positive or negative). The Amott water index, I_W, is defined as the ratio of the volume of spontaneous imbibition to the total volume of imbibition and the Amott oil index, I_O, is the ratio of the volume of spontaneous drainage to the total volume of drainage (Figure 2.9). The difference, $I_{AH} = I_W - I_O$, is sometimes used to characterise wettability by a single number called the Amott-Harvey index.

The Amott water index is most relevant to waterflooding; this will be close to unity for a strongly water-wet core and close to zero for a strongly oil-wet core (Anderson, 1986b). The advantage of the Amott test is that it is not necessary to measure capillary pressure, although the test does reflect fundamental characteristics of the capillary pressure.

In contrast, the USBM test (Donaldson et al., 1969) measures the full capillary pressure curves for imbibition and secondary drainage and the index, I_{USBM}, is determined from the logarithm of the ratio of the area under the positive part of the drainage curve to the area under the negative part of the imbibition curve (areas A_1 and A_2 in Figure 2.9). Water-wet cores will have the first area larger than the second and a large positive index. Oil-wet cores will have the second area larger than the first and a large negative index.

In practice, many rocks have mixed or fractional wettability and the imbibition capillary pressure reaches zero at some intermediate saturation (Figure 2.9). In this case, $I_W \approx I_O$, $I_{AH} \approx 0$ and $I_{USBM} \approx 0$.

The relationship between the standard wettability indices and the distribution of contact angles has been investigated by PNM (Dixit et al., 1998, 2000). They showed that the relationship is not straightforward and differ-

$$I_w = \frac{\Delta S_{ws}}{\Delta S_{wt}} \qquad I_o = \frac{\Delta S_{os}}{\Delta S_{wt}}$$

$$I_{USBM} = \log\left(\frac{A_1}{A_2}\right)$$
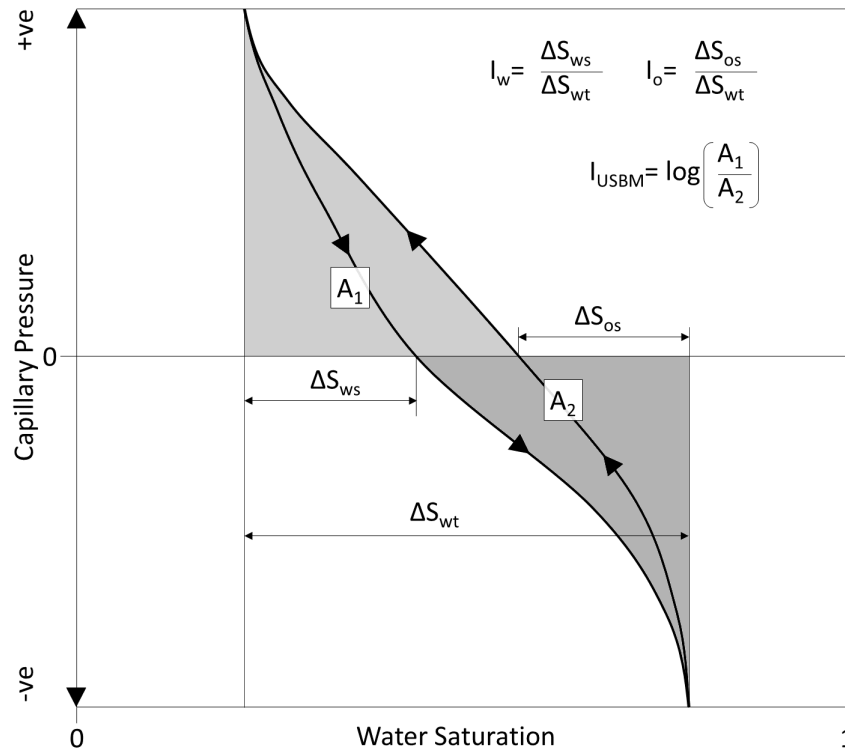
Figure 2.9: Imbibition and drainage capillary pressure curves for a mixed-wet system illustrating Amott and USBM wettability indices

ent relationships are predicted for mixed-wet and fractionally wet systems.

The effect of wettability on relative permeability was investigated by a number of early workers (Owens and Archer, 1971; McCaffery and Bennion, 1974; Wendell et al., 1987). Wettability affects relative permeability because it controls the distribution of the phases within the pore space. As a general rule, in a uniformly wetted core, the oil relative permeability decreases and the water relative permeability increases as the core becomes more oil-wet. The rules of thumb presented by Craig (1971) state that:

- The water saturation at which the oil and water relative permeabilities are equal is generally greater than 50% in water-wet cores and less than 50% in oil-wet cores.

- The relative permeability at residual oil is generally less than 0.3 in water-wet cores and greater than 0.5 in oil-wet cores.

However, it is dangerous to rely on Craig's rules to evaluate wettability because relative permeability is influenced by other factors such as initial saturation and pore geometry (Anderson, 1987b).

For example, Caudle et al. (1951) showed that the cross-over point (where

the oil and water relative permeabilities are equal) in water-wet sandstones is a function of the initial water saturation. Also, Morgan and Gordon (1970) found that the cross-over point is at a significantly lower water saturation and the relative permeability at residual oil is larger in sandstones with large well connected pores compared with rocks containing smaller less well connected pores.

Early studies of laboratory waterfloods generally showed decreasing oil recovery with increasing oil wettability (Kyte and Naumann, 1961; Donaldson and Crocker, 1977). However, later it was shown that oil recovery for a fractional or mixed wetting state can be higher than for strongly oil-wet or water-wet states in the same core sample (Morrow et al., 1986; Dullien et al., 1990).

Jadhunandan and Morrow (1995) used Berea sandstone cores aged with crude oil at a range of temperatures and various brine compositions. They found the waterflood recovery at breakthrough and after 3 pore volumes of injection was largest for those samples with Amott-Harvey index close to zero.

McDougall and Sorbie (1993) used a cubic lattice PNM to investigate trends in relative permeability and waterflood oil recovery in mixed-wet and fractionally wet systems. They showed the oil recovery at breakthrough was maximised in a pore network where half the pore space was oil-wet. However, oil recovery after many pore volumes of injection was greater in more oil-wet networks (circa 75% oil-wet for 20 pore volumes of injection).

Dixit et al. (1999) used a cubic lattice PNM with bonds randomly removed to achieve a target average coordination number. They considered mixed-wet and fractionally wet systems and allowed for water film flow for contact angles less than 45° and oil film flow for contact angles greater than 135°. They simulated flooding cycles and calculated Amott wettability indices. From the results they found maximum oil recovery for "moderate aging" corresponding to $I_{AH} \approx 0$, but also highlighted more complex non-monotonic behaviour and developed a theory based on aging regimes to explain experimental results.

Zhao et al. (2010) used pore networks extracted from μCT images to investigate the effect of wettability on waterflood oil recovery. For a mixed-wet system, their model reproduced the experimental results of Jadhunandan and Morrow (1995). For a uniformly wet system, they found the oil recovery increases with the contact angle and reaches a plateau for contact angles

greater than approximately 100°. In water-wet systems oil recovery decreases as initial water saturation increases, however in oil-wet systems oil recovery initially increases and then decreases.

Waterflood recovery, particularly from water-wet systems, is strongly influenced by capillary trapping and the residual oil saturation. Land (1968) developed an empirical model for the so-called trapping curve which expresses the residual oil saturation, S_{or}, as a function of the initial oil saturation, S_{oi}. His work was originally developed to model gas trapping by water, but it is readily extended to oil trapping in the water-wet case. The residual oil saturation in the Land model is given by:

$$S_{or} = \frac{S_{oi}}{1 + C\frac{S_{oi}}{1-S_{wc}}} \qquad (2.10)$$

where S_{wc} is the connate water saturation and C is the Land constant which can be determined from the maximum trapping which occurs at $S_{oi} = 1 - S_{wc}$. Al Mansoori et al. (2010) have compiled trapping curve data from published experimental studies on water-wet porous media. The data show the Land constant varies from ≈ 0.25 for highly consolidated (low porosity) rocks up to ≈ 4 for unconsolidated (high porosity) sand packs.

For oil-wet systems, Salathiel (1973) showed that oil saturations can be decreased below 10% by continued flooding for a long time (more than 100 pore volumes). Data compiled by Alyafei and Blunt (2016) show that oil-wet and mixed-wet systems display significantly less trapping than water-wet systems.

Spiteri et al. (2008) used a PNM to investigate trapping in uniformly wetted systems. They showed that the trapping curve is non-monotonic if the contact angle is greater that approximately 30°. Subsequent experimental studies also showed non-monotonic behaviour for mixed-wet cores (Pentland et al., 2013; Tanino and Blunt, 2013). As an alternative to the Land (1968) model, Spiteri et al. (2008) proposed a trapping model where S_{or} has a quadratic dependence on S_{oi} with two free parameters.

The effect of wettability on recovery has primarily been investigated by core scale flooding experiments and PNM, whilst the number of published field scale studies is limited. However, a number of studies have shown that both relative permeability and imbibition capillary pressure behaviour are important at the field scale, particularly in heterogeneous and mixed-wet or heterogeneous wetting reservoirs.

Angert and Begg (1993) published a case study of the Prudhoe Bay field which showed that modelling imbibition capillary pressure had a significant impact on recovery, particularly in poor quality zones.

van Lingen et al. (1996) showed that wettability and its heterogeneity play an important role in capillary trapping in cross-bedded sands with alternating high and low permeability laminae.

Namba and Hiraoka (1995) introduced the concept of capillary force barriers which are subtle low permeability layers in certain oil-wet carbonate reservoirs. These layers act as capillary barriers to water movement and thereby have a major effect on waterflooding performance. The concept has been extended to incorporate wettability heterogeneity (Muneta et al., 2004).

Shams et al. (2013) have published a study of capillary effects in conventional and fractured reservoirs. They concluded that imbibition capillary pressure is more significant in depletion rather that displacement recovery processes. They also found no clear correlation between capillary effects and the degree of heterogeneity although it is not clear if they considered oil-wet and mixed-wet systems or wettability heterogeneity.

Chapter 3

Image Acquisition and Processing

She took out from the empty bag a starched white apron and tied it round her waist. Next she unpacked a large cake of Sunlight Soap, a toothbrush, a packet of hairpins, a bottle of scent, a small folding armchair and a box of throat lozenges.

— P. L. Travers, Mary Poppins

3.1   Sample Selection

For the Guillemot A field, a set of 76 core plugs from wells 21/25-2 and 21/30-8 were made available by AOC. From this, a subset of 10 core plugs were selected for analysis. The samples were selected to capture a representative range of porosity and permeability and a representation from each of the main geological layers. Additional samples were chosen from the Skagerrak and Lower Fulmar because these zones are thicker and more complex than the Upper and Middle Fulmar. No rigorous statistical analysis was performed to select the samples.

For the Vanguard field, a set of 135 core plugs have been donated by Cono-coPhillips. Not all of these samples have routine porosity and permeability measurements available. From the subset of core plugs with CCA data, five core plugs were selected to capture a representative range of porosity and permeability. One sample was selected from zone C and two samples were selected from each of the more heterogeneous zones B and D.
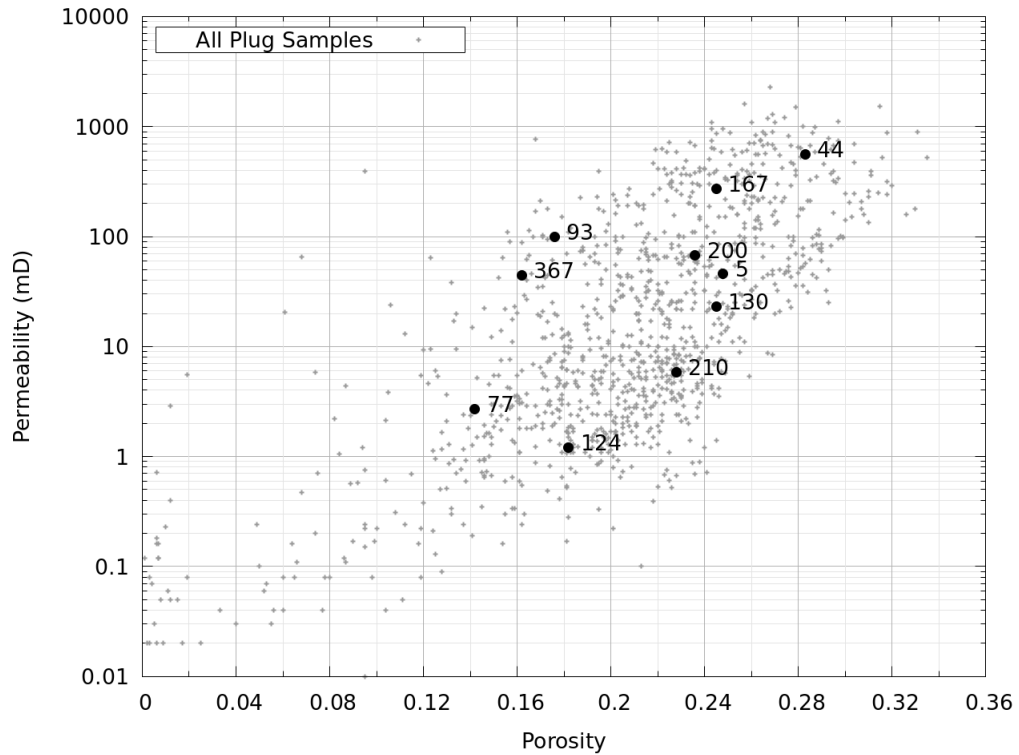
Figure 3.1: Guillemot A measured core plug permeability versus porosity showing selected samples
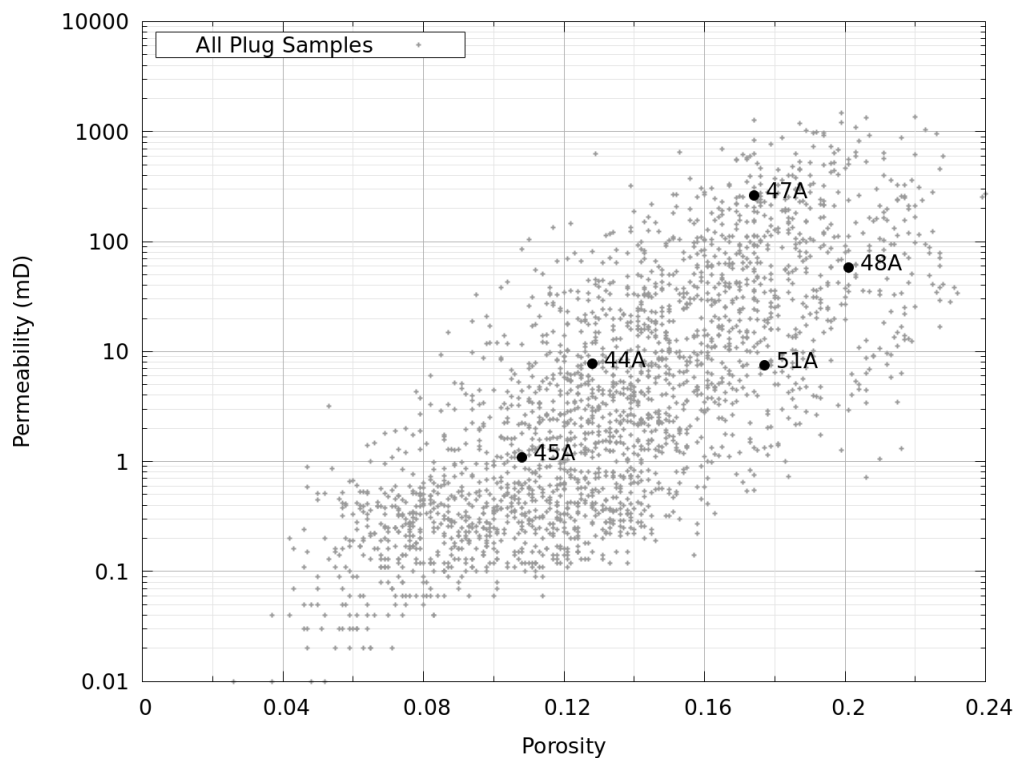
Figure 3.2: Vanguard measured core plug permeability versus porosity showing selected samples

The selected core plug samples are shown on cross-plots of permeability versus porosity in Figures 3.1 and 3.2.

The Guillemot A core plugs are nominally 25 mm diameter and 38 mm in length. The Vanguard core plugs are nominally 38 mm diameter and 50 mm in length. Some photographs of Guillemot A plug samples are shown in Figure 3.3.
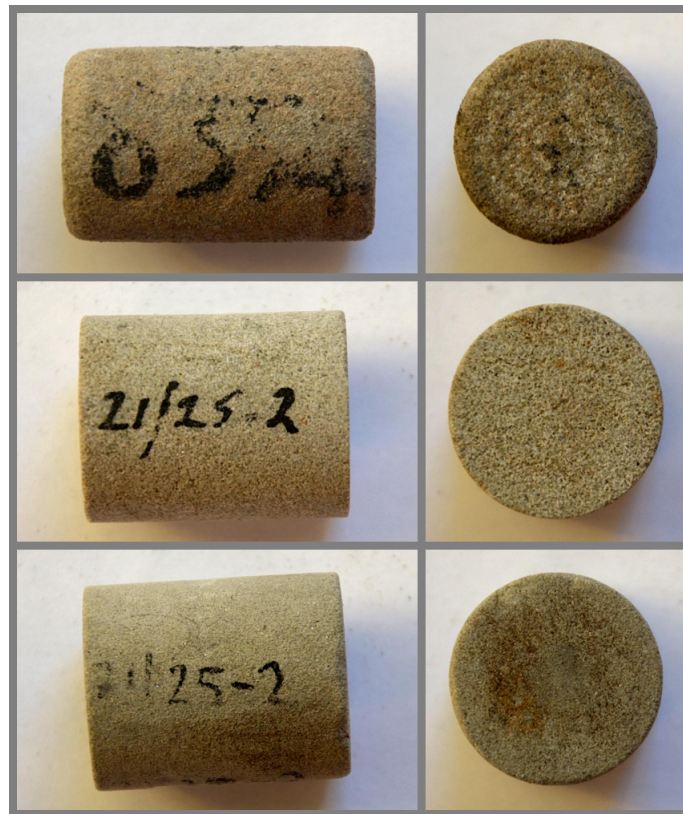
Figure 3.3: Guillemot A example core plugs, top: plug 44, middle: plug 93, bottom: plug 130

The samples selected for analysis are given in Tables 3.1 and 3.2. Macroporosities were obtained from air-brine capillary pressure or MICP measurements where macropores (micropores) are defined as those with a radius larger (smaller) than 0.1 μm.

The distinction between macropores and micropores is based on the potential for hydrocarbon charge. The maximum oil column in the Guillemot A field is approximately 800 ft which corresponds to an oil-water capillary pressure of circa 100 psi equivalent to a pore radius of about 0.1 μm assuming an oil-water interfacial tension (IFT) of 38 dyn/cm. Similarly, in the Vanguard field, the maximum gas column is approximately 500 ft which corresponds to a gas-water capillary pressure of circa 200 psi, also equivalent to radius of about 0.1 μm assuming the gas-water IFT is 72 dyn/cm. Hence macropores

will be charged with hydrocarbons at the maximum structural elevations and micropores will everywhere be water filled.

Table 3.1: Guillemot A rock sample properties

Well	Sample	Zone	Helium Porosity	Macro Porosity	Perm- eability (mD)	Formation Resistivity Factor
21/30-8	5	Upper Fulmar	24.8%	16.2%	45.8	11.19
21/30-8	44	Middle Fulmar	28.3%	22.7%	557	8.30
21/30-8	77	Lower Fulmar	14.2%	5.3%	2.7	25.0
21/25-2	93	Middle Fulmar	17.6%	13.6%	100	19.17
21/30-8	124	Lower Fulmar	18.2%	5.3%	1.2	18.18
21/25-2	130	Lower Fulmar	24.5%	16.7%	23	10.92
21/30-8	167	Skagerrak	24.5%	19.1%	270	10.23
21/30-8	200	Skagerrak	23.6%	15.8%	68	12.73
21/25-2	210	Skagerrak	22.8%	12.5%	5.8	12.35
21/30-8	367	Skagerrak	16.2%	10.4%	44.5	21.46

Table 3.2: Vanguard rock sample properties

Well	Sample	Zone	Helium Porosity	Macro Porosity	Permeability (mD)	Formation Resistivity Factor
49/16-Q3	44A	B	12.8%	7.9%	7.7	35.2
49/16-Q3	45A	B	10.8%	4.2%	1.1	50.3
49/16-Q3	47A	C	17.4%	14.2%	263	21.4
49/16-Q3	48A	D	20.1%	14.8%	58	25.6
49/16-Q3	51A	D	17.7%	12.2%	7.5	28.7

3.2   SEM Imaging

3.2.1   Acquisition

For the purposes of SEM imaging, polished blocks were created from a subsample cut from each core plug. The polished blocks were made at Petrolab[1] by injecting a low density epoxy resin into each sample under vacuum and then polishing one surface with diamond abrasives until optically flat. The polished blocks are nominally 30 mm diameter and 12 mm thick. The blocks were low-vacuum sputter coated with carbon graphite, to ensure

[1]https://www.petrolab.co.uk

the polished surfaces were electrically conducting and copper tape applied to provide a conductive path from the surface to the SEM sample holder (Figure 3.4).
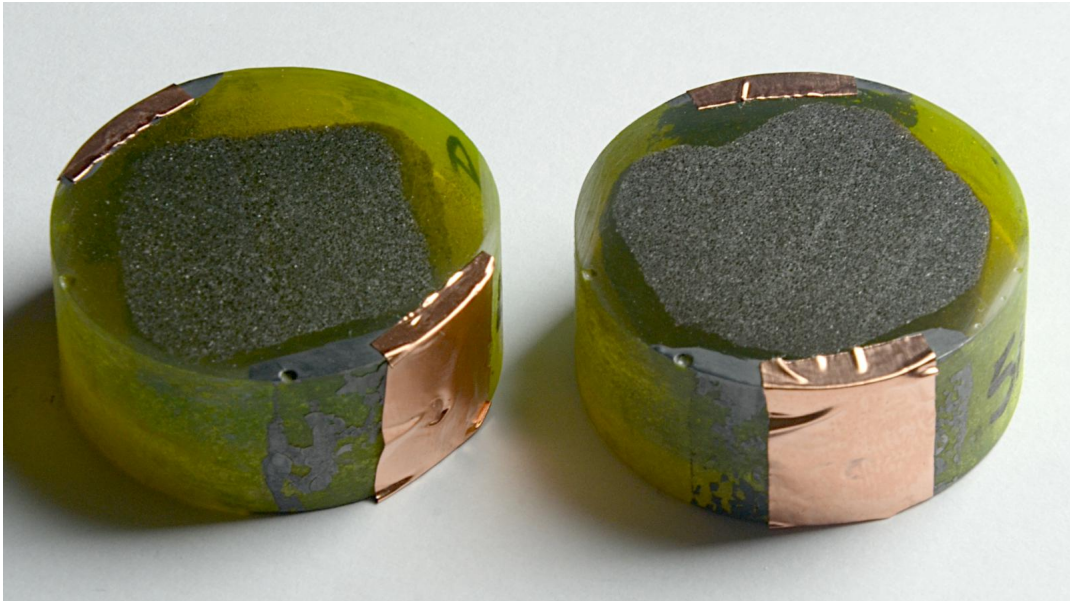
Figure 3.4: Polished blocks for SEM imaging

The polished blocks were imaged with two instruments belonging to the University: Topcon ABT-60 SEM and Carl Zeiss GeminiSEM 300. All SEM images were acquired from the backscattered electron (BSE) detector.

The number of SEM images is given in Table 3.3.

Two SEM imaging strategies were used in this work.

Firstly, all ten Guillemot A samples were imaged using the Topcon ABT-60 SEM at a range of magnifications with the same image size (1400 × 862 pixels). Typically, four images were captured at each of four magnifications, corresponding to spatial resolutions of 2.12, 1.06, 0.53 and 0.27 μm/pixel. This is a rapid process as each image can be captured in less than two minutes. These images were used in the downscaling algorithm (Section 3.2.4) which progressively adds detail from higher magnification images into the lowest magnification image to result in a final image with a high spatial resolution and a wide field of view. The procedure was applied twice for each sample to generate two final images based of different intermediate images. The final downscaled images have a spatial resolution of 0.27 μm/pixel and an image size of 8800 × 6400 pixels. Downscaling requires segmented images; therefore the details of the downscaling procedure are presented after segmentation.

Table 3.3: Number of SEM images acquired by sample and instrument

Well	Sample	Topcon ABT-60 SEM	Carl Zeiss GeminiSEM 300
21/30-8	5	17	-
21/30-8	44	17	12
21/30-8	77	17	3
21/25-2	93	17	-
21/30-8	124	18	-
21/25-2	130	17	13
21/30-8	167	17	-
21/30-8	200	17	-
21/25-2	210	17	19
21/30-8	367	18	18
49/16-Q3	44A	-	4
49/16-Q3	45A	-	4
49/16-Q3	47A	-	3
49/16-Q3	48A	-	4
49/16-Q3	51A	-	4
Total		172	84

Secondly, a wide field, high resolution image was acquired for each of five samples from Guillemot A and all five samples from Vanguard using the Carl Zeiss GeminiSEM 300. These images have a spatial resolution of 0.17 μm/pixel and an image size of 16384 × 12288 pixels. The field of view of each image is 2.785 mm × 2.089 mm. The acquisition time for each image was about 3 hours as they have a large size.

Further acquisition parameters for the Carl Zeiss GeminiSEM 300 were as follows:

- accelerating voltage 15 kV

- beam current 80 pA

- image capture scan speed 9

- working distance 23 mm

Figure 3.5 shows example images of Guillemot A plug 367 acquired with the Topcon ABT-60 SEM. The high resolution image of the same sample acquired with the Carl Zeiss GeminiSEM 300 is shown in Figure 3.6.
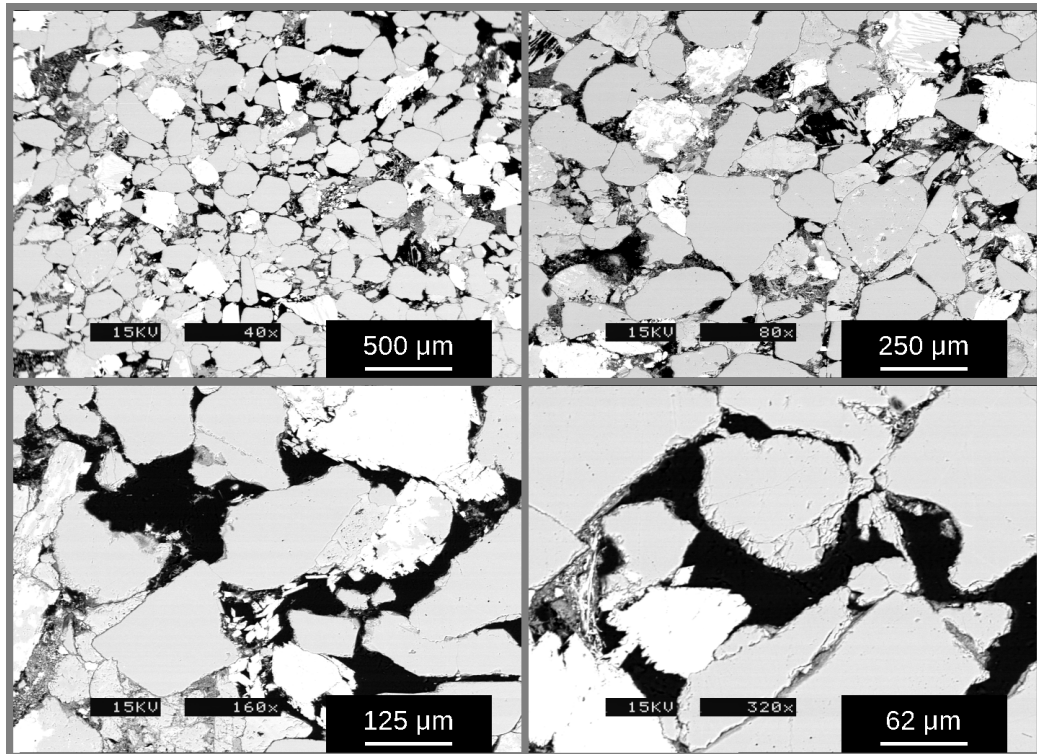
Figure 3.5: Topcon ABT-60 SEM multiscale images of plug 367, top left: 2.12 μm/pixel, top right: 1.06 μm/pixel, bottom left: 0.53 μm/pixel, bottom right: 0.27 μm/pixel

3.2.2 Segmentation

Segmentation, filtering and downscaling of the SEM images was performed using the imagenet program written for this project (Appendix C).

The objective of segmentation is to classify each greyscale pixel in an SEM image as rock matrix or pore space.

Figure 3.7 and 3.8 show grey level intensity distributions for the high resolution images from Guillemot A and Vanguard. The grey level peaks corresponding to pore space (near black) and quartz (light grey) are well defined in all cases. The images from both SEM instruments have high contrast range and good signal to noise ratio. Accordingly, it was decided to segment the images by applying a simple global grey level threshold.

Three methods were investigated to select the threshold value.

Firstly, Otsu's method as originally formulated (Otsu, 1979), selects a single threshold to divide an image into two classes of pixels such that the inter-class variance is maximised. The method can be generalised to multiple thresholds (Liao et al., 2001) with three or more classes of pixels, by maximising the variance given by:
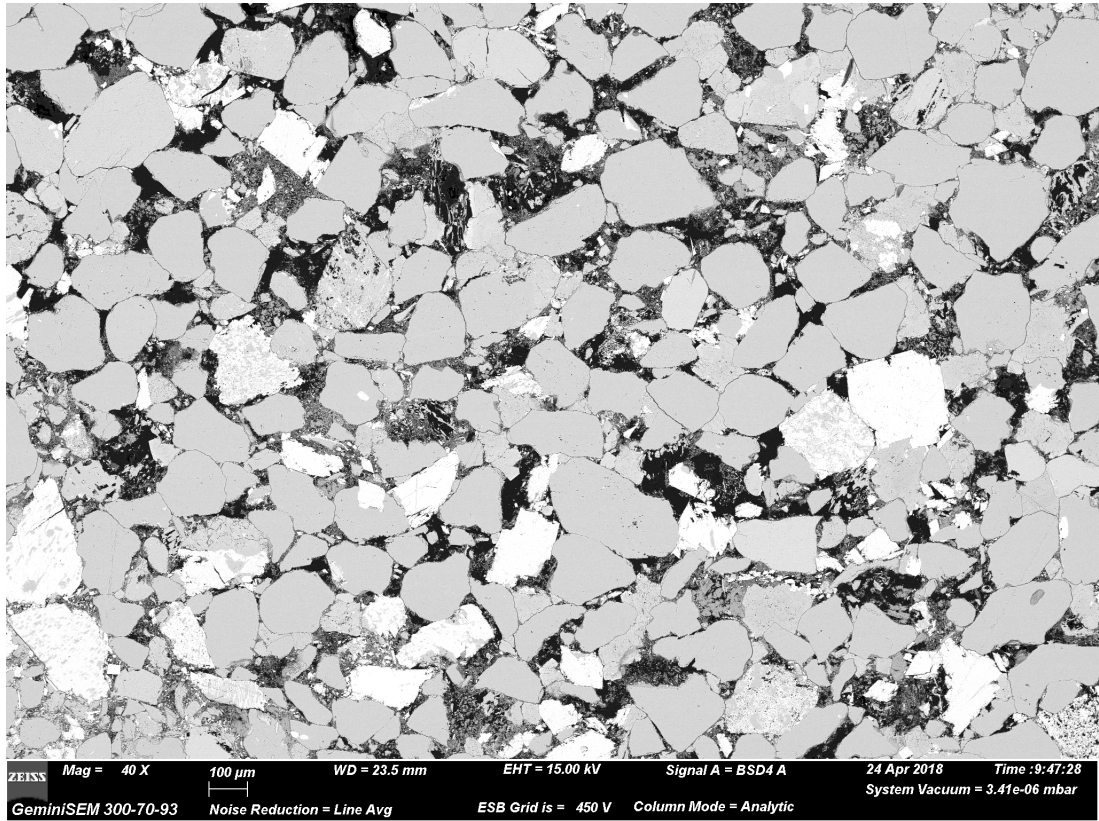
Figure 3.6: Carl Zeiss GeminiSEM 300 image of plug 367, 16384 × 12288 pixels at 0.17 μm/pixel

$$\mathrm{Var} = \sum_{i=1}^{M} \omega_i (I_i - I_T)^2 \qquad (3.1)$$

where M is the number of classes, ω_i is the fraction of pixels in class i, I_i is the mean grey level intensity of class i and I_T is the mean grey level intensity of the whole image. In this generalisation, the number of classes is given and the method determines the optimum thresholds.

Secondly, a Gaussian Mixture Model (GMM) was used to identify threshold values (Huang and Chau, 2008). In this approach, the grey level intensity distribution of the image is represented by a combination of Gaussian distributions. Typically, the number of components (Gaussian distributions) is chosen to equal the number of modes in the overall distribution under the assumption that each mode corresponds to a sub-population of pixels representing a different image feature. Each component of the GMM has three parameters viz: the mean and variance of the Gaussian distribution plus a mixture weighting; therefore a GMM with M components has $3M$ independent parameters. Here, the parameters are determined using a non-linear least-squares Gauss-Newton algorithm. Having determined the
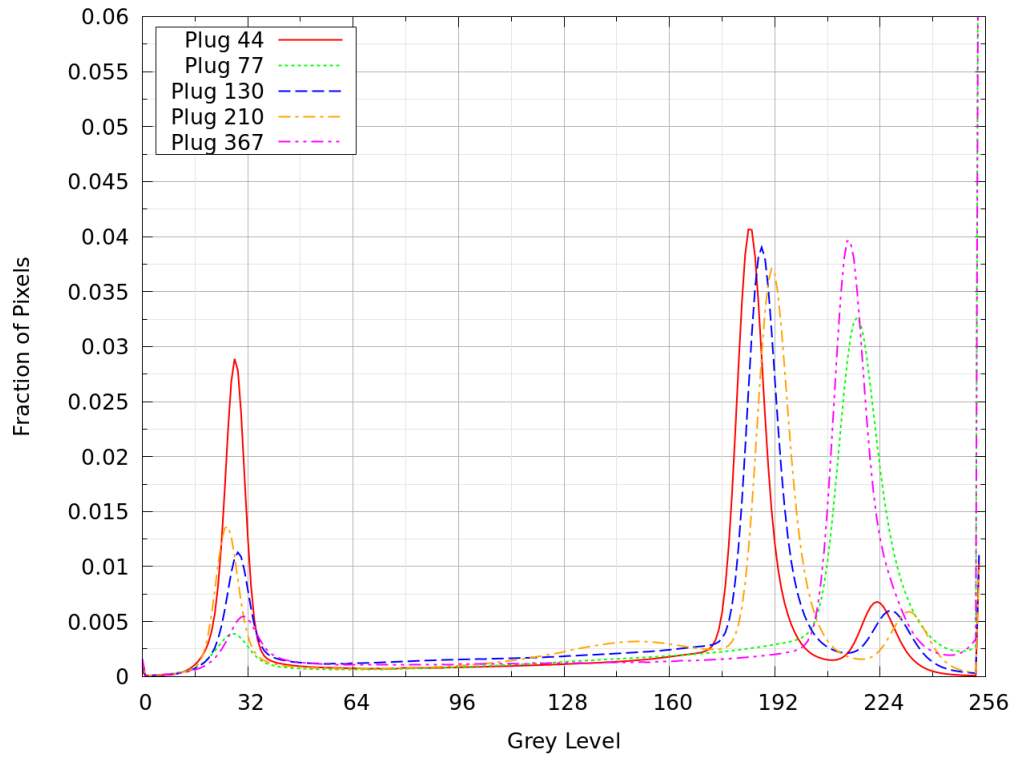
Figure 3.7: Grey level distributions for Guillemot A high resolution SEM images
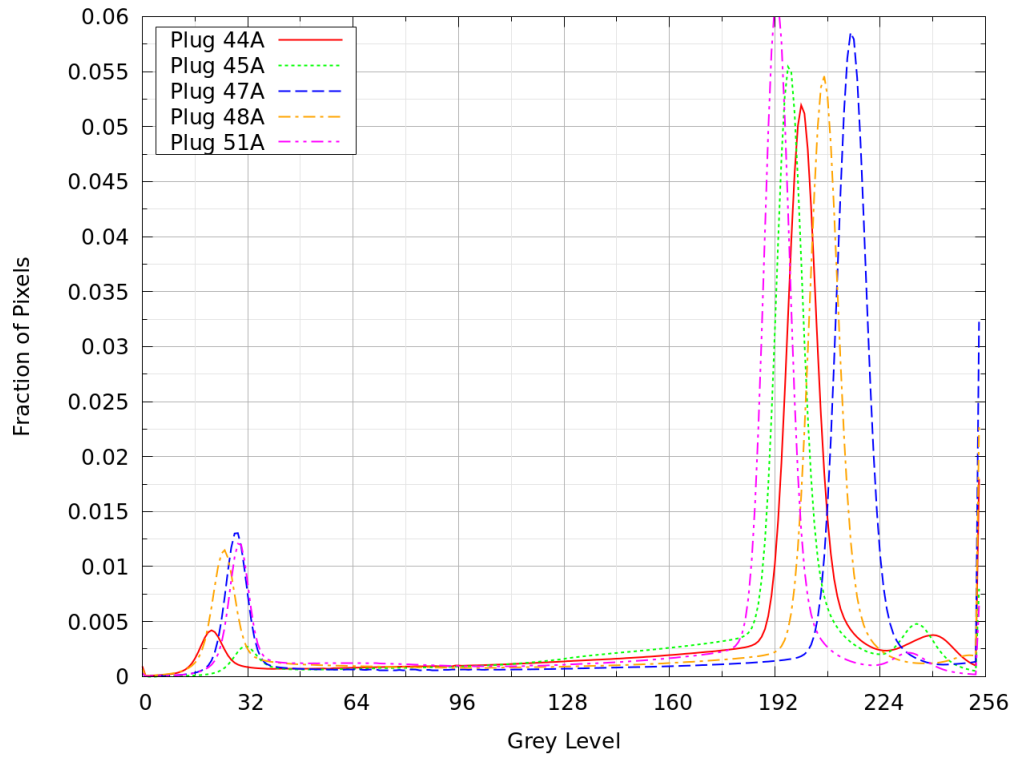
Figure 3.8: Grey level distributions for Vanguard high resolution SEM images

mixture components, the thresholds are given by the intensity values where the component probability densities are equal.

In the third method, the segmentation threshold was selected from a given peak interval fraction (PIF). The pore space peak and the quartz matrix peak of the grey level distribution (Figures 3.7 and 3.8) are identified and the threshold is equal to the grey level of the pore space peak plus a given fraction of the interval between the peaks.

Table 3.4 shows the thresholds and resulting porosities from the three methods applied to the high resolution SEM images from Guillemot A plug 367 and Vanguard plug 51A. In the case of the multi-level Otsu and GMM methods, Table 3.4 shows the lowest identified threshold.

Table 3.4: SEM images: results from three segmentation threshold selection methods

Method	Plug 367 Threshold	Plug 367 Porosity	Plug 51A Threshold	Plug 51A Porosity
Otsu: 2 Classes	141	19.8%	121	19.6%
Otsu: 3 Classes	90	13.7%	81	15.7%
Otsu: 4 Classes	87	13.3%	79	15.5%
GMM: 2 Components	176	24.6%	181	29.0%
GMM: 3 Components	180	25.3%	39	10.6%
GMM: 4 Components	46	8.7%	37	10.3%
PIF 10%	49	9.2%	45	11.4%
PIF 20%	67	11.2%	61	13.3%
PIF 30%	86	13.2%	78	15.3%
PIF 40%	104	15.2%	94	17.0%
PIF 50%	123	17.4%	111	18.5%

Generally, Otsu's method and the GMM method with two classes give thresholds and resulting porosities which are too high. In some cases, the porosity is greater than the measured helium porosity. This is unrealistic given the finite resolution of the images. Microporosity (below image resolution) will not be fully resolved and therefore the image porosity should be closer to the macroporosity (Tables 3.1 and 3.2). Increasing the number of classes results in lower porosity values but Otsu's method requires an unreasonably large number of classes to give credible porosity values. The GMM method with 4 or more classes results in one or more very wide components being assigned to the grey level interval 50-175 (Figures 3.7 and 3.8). This makes the threshold and resulting porosity too low.

It was found that peak interval method with PIF 50% typically gives porosities close to the measured helium porosities whereas PIF 10% to 30% gives

porosity close to the macroporosity. On this basis, it was decided to segment all the SEM images using the peak interval method with PIF 20%.

3.2.3   Filtering

There was some residual noise after segmentation; therefore a decluster filter was applied to remove isolated pixel clusters (islands) of 4 pixels or less. The filter removes both small black areas (isolated porosity) and small white areas (floating particles). Small pores which are connected are retained. The filter substantially reduces the number of isolated pixel clusters with minimal impact on the porosity. Note that the filter preserves information below 1 μm and is not equivalent to removing pores of diameter 4 pixels or less because those features are likely to be rounded and will consist of more than 4 pixels.

3.2.4   Downscaling

A downscaling procedure was applied to the Topcon ABT-60 SEM images of Guillemot A samples. In this context, downscaling is defined as a procedure to progressively incorporate information from high magnification (high resolution and small field of view) SEM images into a low magnification (low resolution and large field of view) SEM image. The resulting image has a high spatial resolution and a large field of view.

The objective of downscaling is to reduce the time required to characterise a complex pore space from SEM imaging. Images with a high spatial resolution and a large field of view can be acquired directly, but the acquisition time is typically several hours. The alternative is to acquire a sequence of images of progressively higher magnifications, with the same number of pixels, and then apply the downscaling algorithm to add information from the later (higher magnification) images into the first (lowest magnification) image. The lower magnification images capture large scale features and large pores and higher magnification images capture small scale features and small pores.

In this work, a sequence of images is captured where each image has twice the magnification of the previous one. Each image can typically be acquired in a few minutes and therefore this process is significantly faster than acquiring a single high resolution image. The underlying assumption is that

the pore structure detail (e.g. distribution of fine structure clays or cements) captured in the high magnification images is homogeneously distributed in the lowest magnification image.

Each stage of the downscaling process refines each pixel in the target binary image into 2×2 pixels based on the neighbourhood of 3×3 pixels. One stage is illustrated in Figure 3.9.
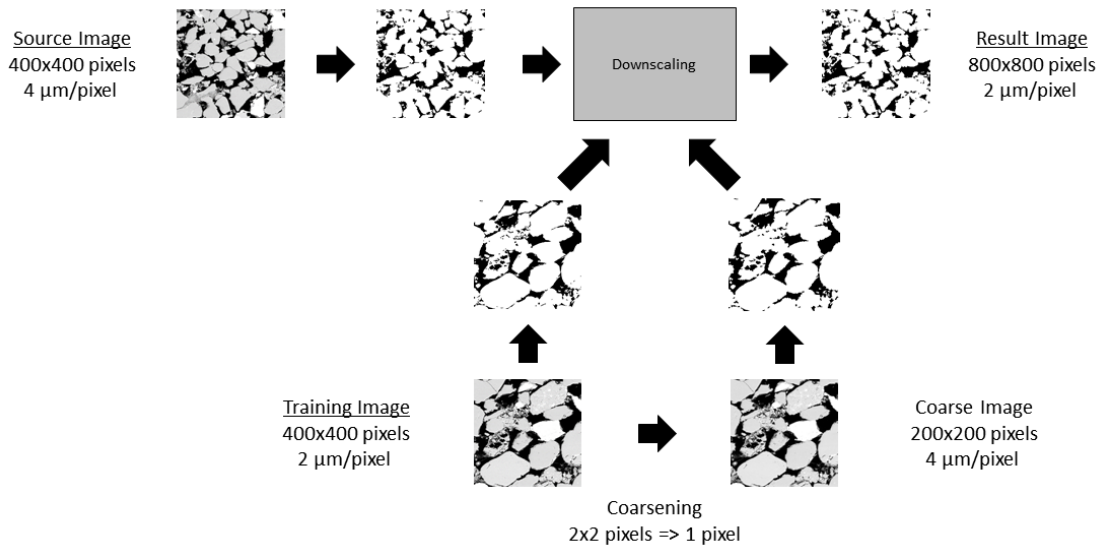
Figure 3.9: One stage of the image downscaling process. The source image is downscaled using higher spatial resolution information from the training image

Two images are required as input for each downscaling stage. The first is the source image which covers the required field of view but at a low spatial resolution. The second is a training image which has twice the spatial resolution of the source image but does not cover the field of view. The training image is coarsened by taking the arithmetic mean of each 2×2 pixel group to generate an image of the same spatial resolution as the source. The original and the coarsened training images are then segmented as described in Section 3.2.2 using the same threshold value to generate binary images. The two binary images are compared to calculate a probability matrix $\{p_{ij}\}$ where p_{ij} is the probability of the fine scale 2×2 state i conditional on the coarse scale 3×3 state j (for $i = 0, 1, 2, 3, ...2^4 - 1$ and $j = 0, 1, 2, 3, ...2^9 - 1$). The probability p_{ij} is conditional of the state, j; therefore this must satisfy:

$$\sum_{i=0}^{15} p_{ij} = 1 \quad \forall j \tag{3.2}$$

For example, on the left in Figure 3.10 is part the coarse scale training image

and the equivalent part of the fine scale training image is on the right. With pixels ordered in rows starting from the top left, taking black=1 and white=0, the left hand state, j, is 000100111 (binary) = 39 (decimal) and the right hand state of the middle 2×2 pixels, i, is 0010 (binary) = 2 (decimal). The probability $p_{ij} = p_{2,39}$ is calculated from the number of occurrences of these patterns in the training images.
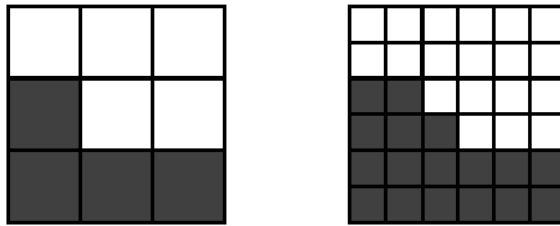
Figure 3.10: Left: part of the coarse training image showing state $j = 39$, right: equivalent part of the fine training image showing state $i = 2$

The probability matrix $\{p_{ij}\}$ has $2^4 \times 2^9$ = 8192 elements; however the number of independent elements is only 1236 due to symmetry. The statistics for mirror symmetric and rotational symmetric states are combined in the algorithm.

It is possible that not all of the 1236 patterns are present in the training image. If a certain pattern is not present in the training image, then the value of the central pixel in the 3×3 group in the source image is used to determine all four of the pixels in the downscaled image. If the central pixel is black, then $p_{ij} = 1$ for $i = 15$ and $p_{ij} = 0$ otherwise. If the central pixel is white, then $p_{ij} = 1$ for $i = 0$ and $p_{ij} = 0$ otherwise.

Having calculated the probability matrix from the training image, it is applied to the source binary image to generate the result image. The state, j, of each 3×3 pixel neighbourhood in the source image is calculated and then one of the states for the central pixel 2×2 refinement is randomly chosen where the probability of choosing each state i is p_{ij}.

Finally, the downscaling is repeated using a sequence of training images of progressively higher spatial resolution. For the Guillemot A plug sample images, the downscaling was applied three times using a sequence of four images with spatial resolution of 2.12, 1.06, 0.53 and 0.27 µm/pixel. The overall result is a single binary image with a resolution of 0.27 µm/pixel and a wide field of view.

For the Guillemot A images, the procedure was applied twice for each

plug sample to generate two final images based of different intermediate images. The final output is two high resolution images for each of the 10 plug samples. Each final image has a spatial resolution of 0.27 μm/pixel and an image size of 8800 × 6400 pixels.

An example of downscaling is shown in Figure 3.11.

Figure 3.11: Downscaling example, top: extract from coarse scale SEM image at 2.12 μm/pixel, middle: segmented image, bottom: downscaled image at 0.27 μm/pixel

3.2.5   Image Porosity

Figures 3.12 and 3.13 compare the porosity from SEM imaging with the macro porosity from capillary pressure data. Generally, there is agreement within ±3 porosity units (PU). The capillary pressure data were measured on whole core plug samples whereas the SEM images cover a much smaller area, therefore the differences in porosity estimates may indicate some heterogeneity at the core plug scale.
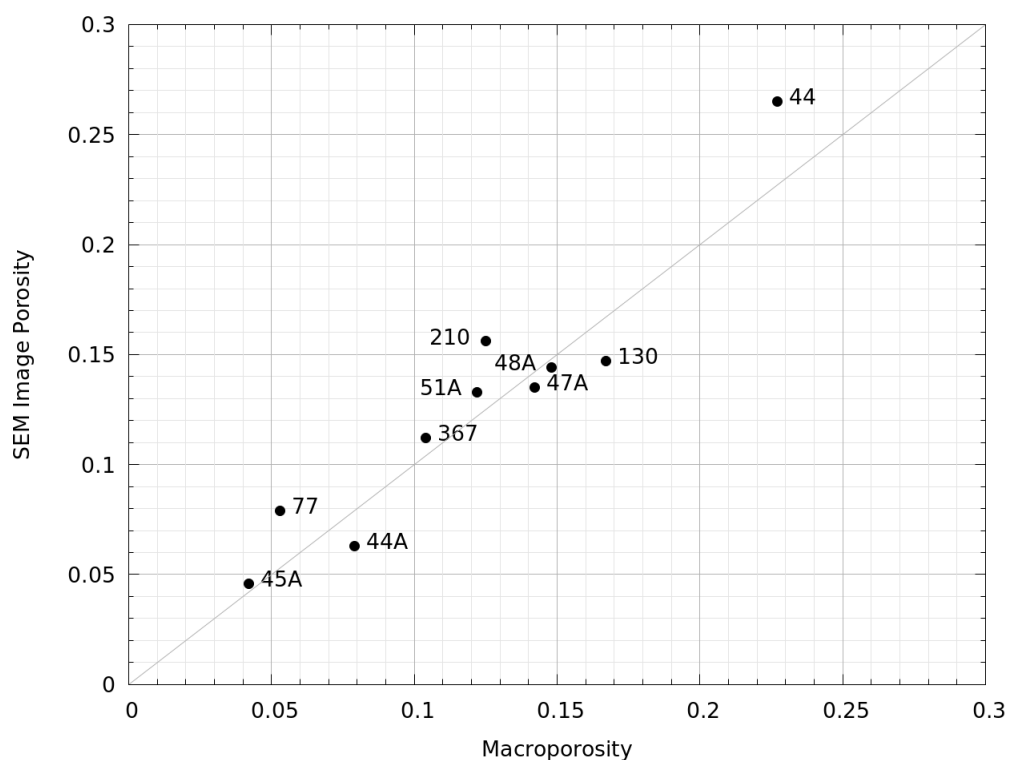
Figure 3.12: Carl Zeiss GeminiSEM images: porosity from image analysis versus macroporosity from capillary pressure data

3.3   μCT Imaging

3.3.1   Acquisition

Four samples from Guillemot A were imaged using Zeiss Xradia Versa 3D microscopes. Three samples were imaged using the microscope belonging to the University and one samples was imaged at the Saudi-Aramco facility. For μCT imaging, a subsample of approximately 5 mm × 5 mm × 20 mm was cut from each core plug. Key acquisition parameters were as follows:
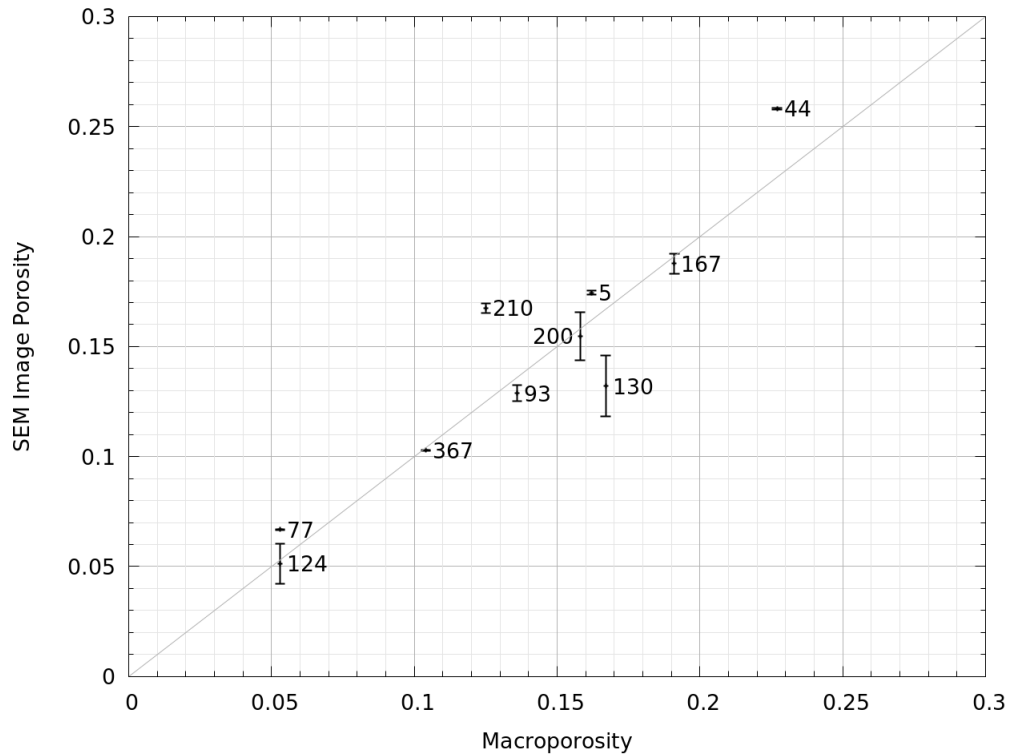
Figure 3.13: Downscaled images from Topcon ABT-60: porosity from image analysis versus macroporosity from capillary pressure data

- Voltage 90 kV

- Power 10 W

- Exposure time 55 s

- Number of projections 2880

A summary of the μCT volumes is given in Table 3.5.

Table 3.5: Summary of Guillemot A μCT volumes

Plug Sample	Voxel Size (μm)	Volume (voxels)	Volume (μm)
44	1.0	980×1014×993	980×1014×993
77	1.0	976×1014×993	976×1014×993
130	1.5	1908×2030×1991	2862×3045×2987
367	1.0	976×1014×992	976×1014×992

Figure 3.14 shows example extracts from the μCT volumes.
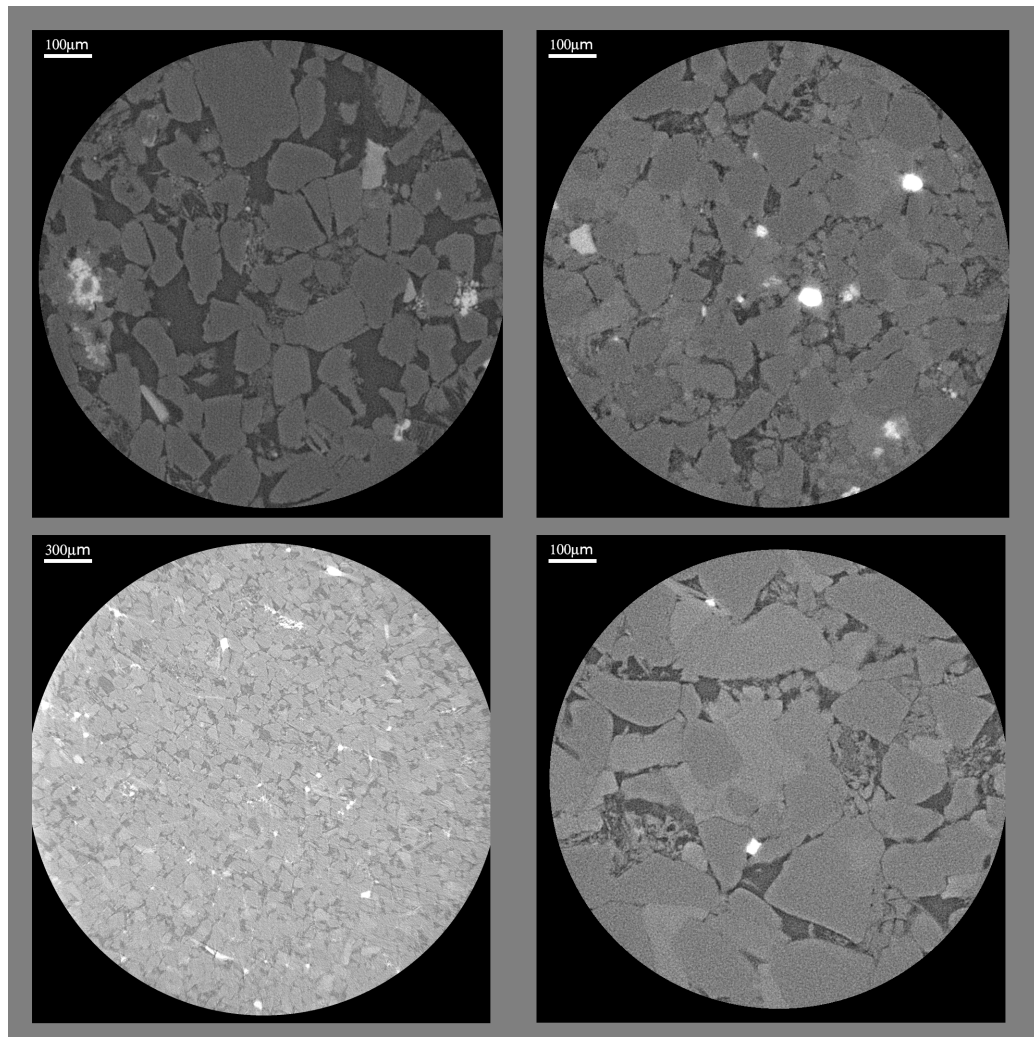
Figure 3.14: Extracts from Guillemot A µCT volumes, top left: plug 44, top right: plug 77, bottom left: plug 130, bottom right: plug 367

3.3.2 Image Processing

The processing sequence applied to the µCT volumes consisted of:

1. Cropping

2. Contrast enhancement

3. Bilateral filtering

4. Segmentation

5. Decluster filtering

All processing steps were performed using the imagenet program (Appendix C).

Cropping

The images were cropped to remove obvious edge artefacts and generate a suitable cuboid volume.

Contrast Enhancement

Visual inspection shows that all datasets have low contrast and most of the grey level values are concentrated over a narrow range. Contrast enhancement applies a mapping of grey levels to spread the intensity distribution over the full range (0-255). In this case, a simple linear mapping was applied. Contrast enhancement improves the quality of the segmentation and makes the segmentation algorithm more robust, particularly if global thresholding is applied (Iassonov et al., 2009; Schlüter et al., 2014).

Filtering

Bilateral filtering was applied to reduce noise and improve the signal to noise ratio of the volumes. Filtering essentially replaces each voxel value with some average of values within a neighbourhood. A disadvantage of filtering is that it can smooth out edges, reduce fine detail and remove information. To mitigate the loss of detail, a bilateral edge-preserving filter was used (Tomasi and Manduchi, 1998; Eibenberger et al., 2008).

A bilateral filter combines domain filtering with range filtering. The filter replaces each voxel value with a weighted average of values within its neighbourhood where the weighting is the product of two Gaussian functions. The first (domain function) depends on the distance between pixels and the second (range function) depends on the difference in the grey level intensities. This second function reduces the averaging across large grey level differences i.e. at the edges of image features. Hence the bilateral filter helps to preserve edge detail.

The filter requires two parameters as input viz: the standard deviations (SD) of the domain function and the range function. The parameters were optimised after some testing. It was found that the optimum SD for the domain function is between 1 to 2 voxels and the optimum SD for the range function is close to the grey level difference between the principal peaks of the distribution.

Figure 3.15 shows example grey level intensity distributions before contrast enhancement, after contrast enhancement and after bilateral filtering. The highest peak corresponds to quartz matrix and peak at lower grey level values corresponds to the pore space. The width of the peaks is a measure of noise and the distance between peaks is a measure of the signal. It is clear that the signal to noise ratio is much poorer than that of SEM images (Figures 3.7 and 3.8), but it is substantially improved by filtering.
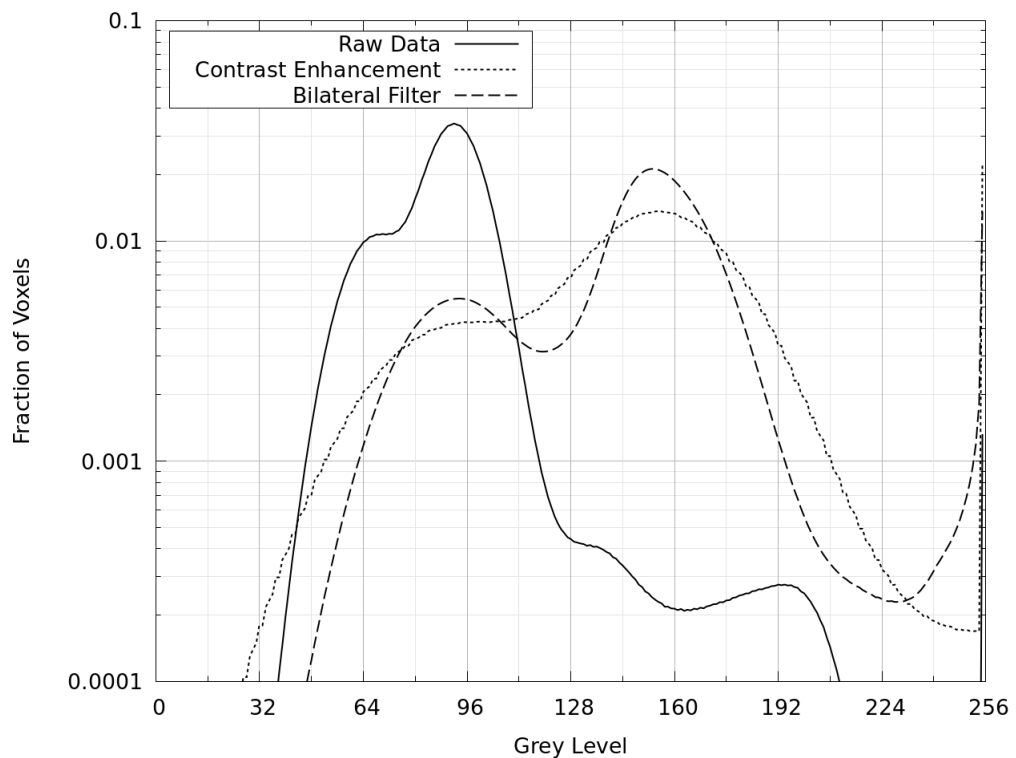
Figure 3.15: Grey level distributions for plug 44 µCT data: raw data, after contrast enhancement and bilateral filtering

Segmentation

As with the SEM images, three methods were investigated to select a segmentation threshold, viz: Otsu's method, the GMM method and the PIF method. Table 3.6 shows the results for plug 44 µCT data. It can be seen that Otsu's method and the GMM method are broadly consistent and give reasonable results. The grey level distribution for plug 44 does not have more than 3 obvious modes and therefore it does not make sense to consider more than 3 classes or components.

For all µCT volumes, it was found that the modes of the grey level distributions are well represented by Gaussian components. Accordingly, the GMM

Table 3.6: Plug 44 µCT data: results of segmentation threshold selection methods

Method	Threshold	Porosity
Otsu: 2 Classes	128	25.8%
Otsu: 3 Classes	125	24.8%
GMM: 2 Components	123	23.8%
GMM: 3 Components	122	23.7%
PIF 10%	100	15.4%
PIF 20%	106	18.2%
PIF 30%	112	20.5%
PIF 40%	118	22.5%
PIF 50%	124	24.4%

method was used to segment all the datasets.

The GMM components representing pore space and quartz matrix for the µCT data are shown in Figure 3.16. Note that the optimum threshold is selected where the principal component probability densities are equal and this threshold is slightly higher than the local minimum of the overall distribution.
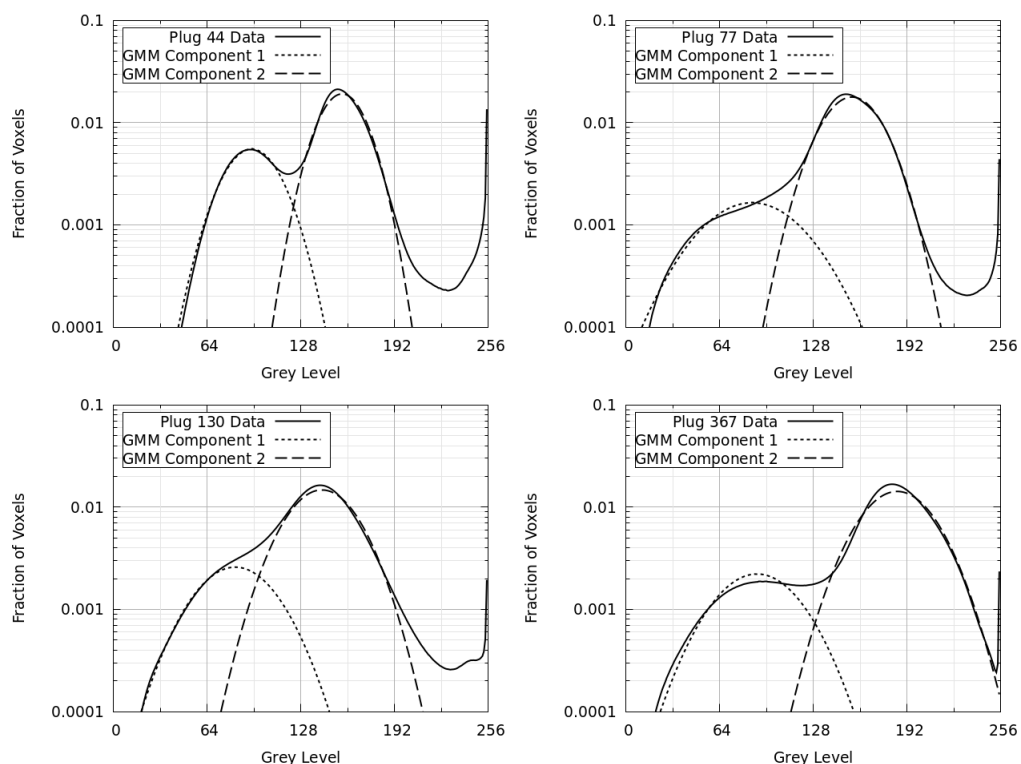
Figure 3.16: Grey level distribution for Guillemot A µCT data showing principal GMM components

Decluster Filter

A declustering filter was used to remove residual noise in the form of isolated pixel clusters. The procedure was the same as that applied to the SEM images to remove isolated porosity and floating particles except that no cluster size limit was applied.

After application of the declustering filter, the pore space in each µCT dataset consists of one single connected voxel cluster.

3.3.3   Porosity

The decluster filter results in some slight changes to porosity as shown in Table 3.7.

Table 3.7: Porosity of Guillemot A µCT volumes

Plug Sample	Helium Porosity	Segmentation Porosity	Decluster Porosity
44	28.3%	23.9%	23.7%
77	14.2%	8.6%	8.1%
130	24.5%	14.1%	13.3%
367	16.2%	13.9%	13.6%

Figure 3.17 shows a comparison of the final µCT volume porosities with macroporosities derived from capillary pressure data. Macropores are defined as those larger than 0.2 µm as discussed in Section 3.1. In all cases, the micro-CT imaging underestimates the total porosity because of the inability to resolve the smallest pores. We observe better agreement with the macro porosity numbers even though these are determined from capillary pressure equivalent to a pore size which is still significantly below micro-CT resolution. However, capillary pressure is controlled by pore throat sizes and the pore bodies invaded at a given pressure are likely to be larger.

3.4   Additional Datasets

Four additional data sets were used for the pore space characterisation described in Chapter 4.
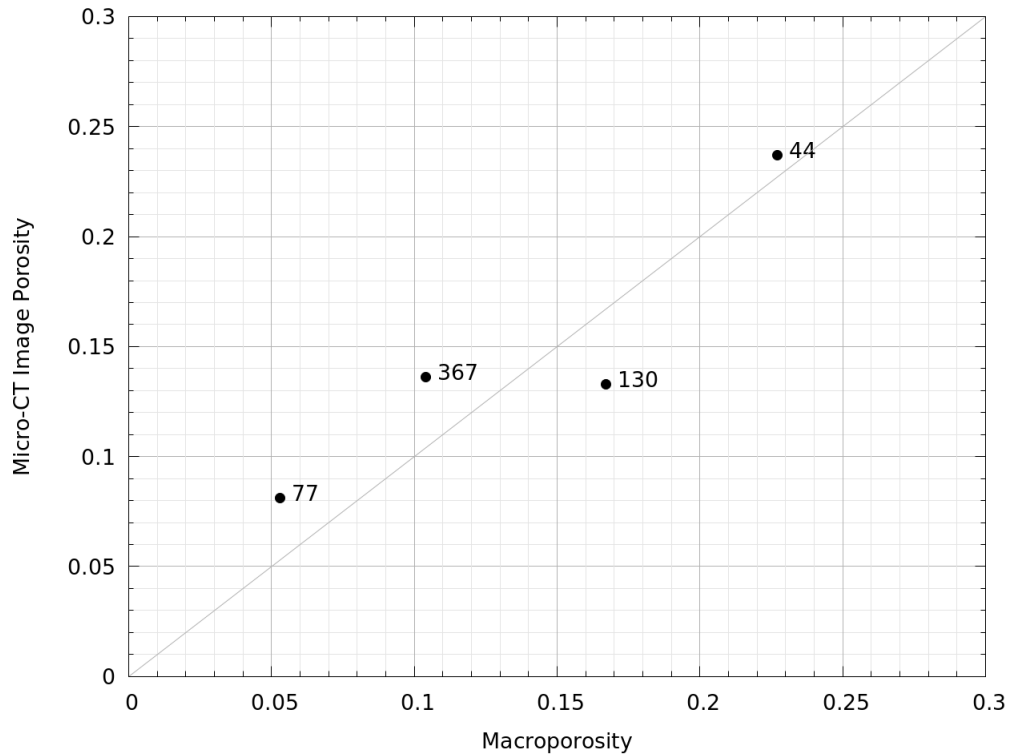
Figure 3.17: Guillemot A µCT volume porosities versus macroporosities from capillary pressure data

- Bentheimer sandstone µCT volume (Ramstad et al., 2012; Ramstad, 2018)

- Gildehauser sandstone µCT volume (Berg et al., 2016, 2018)

- Random sphere pack from Finney and Bernal (1970)

- Fontainebleau sandstone volume reconstructed by Hilfer and Zauner (2011)

The first three volumes were obtained from the digital rocks portal[2] (Prodanovic et al., 2015).

The Fontainebleau sandstone volume was obtained from Hilfer et al. (2012) and is only part of the complete reconstruction. The part volume used in this work is the one labelled a4_x0_y0_z0 in Hilfer and Zauner (2011).

The properties of these volumes are given in Table 3.8.

Example sections from these volumes are shown in Figure 3.18.

The Bentheimer and Gildehauser greyscale volumes were processed and segmented in the same way as the Guillemot A µCT volumes except that the

---

[2]http://www.digitalrocksportal.org

Table 3.8: Summary of additional data volumes

Volume	Voxel Size (μm)	Volume (voxels)	Volume (μm)
Bentheimer	7.0	601×594×1311	4207×4158×9177
Gildehauser	4.4	893×897×570	3939×3947×2508
Sphere Pack	1.0	500×500×500	500×500×500
Fontainebleau	3.66	1024×1024×1024	3750×3750×3750
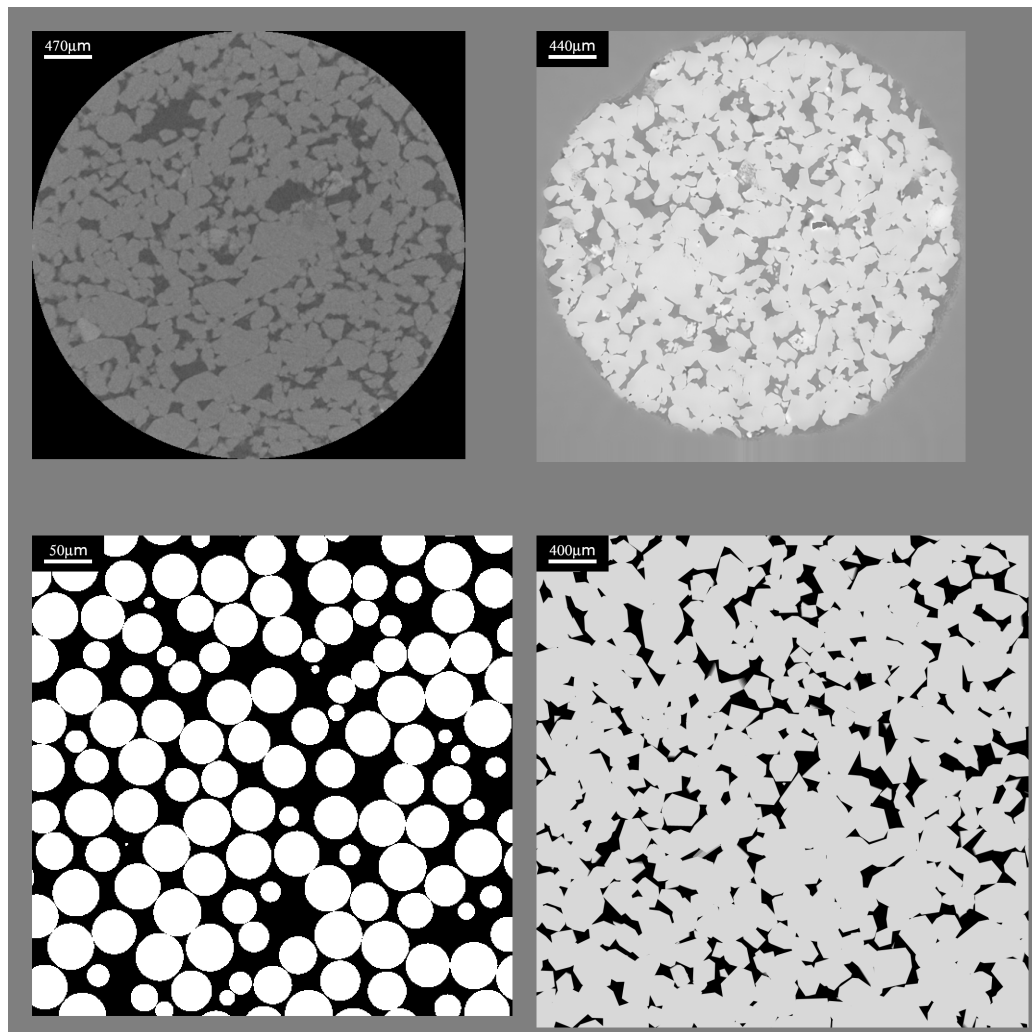
Figure 3.18: Extracts from additional volumes, top left: Bentheimer, top right: Gildehauser, bottom left: sphere pack, bottom right: Fontainebleau

grey level distributions could not be adequately represented by Gaussian components; therefore Otsu's method was used to segment the volumes.

The random sphere pack was generated experimentally by recording the positions of a large number of packed spherical balls. This dataset is available as a binary volume where each sphere is digitised with a radius of 25 voxels (Finney, 2016).

The Fontainebleau dataset was generated using a stochastic process based reconstruction method (Latief et al., 2010) and is available as a greyscale volume at a range of resolutions (Hilfer et al., 2012). The dataset at a resolution of 3.66 µm/voxel is used in this work. This dataset is very high quality and required minimal processing to generate a segmented volume.

Porosities of these datasets are given in Table 3.9.

Table 3.9: Porosity of additional data volumes

Volume	Calculated Porosity	Reference Porosity	Reference
Bentheimer	21.8%	23.7%	Ramstad et al. (2012)
Gildehauser	20.1%	20%	Berg et al. (2016)
Sphere Pack	36.3%	36%	Finney and Bernal (1970)
Fontainebleau	13.2%	13.4%	Hilfer and Zauner (2011)

The reference porosity for the Bentheimer sandstone is an experimental value and includes a minor amount of clay porosity which is below the resolution of the µCT data.

The reference porosity for the Fontainebleau volume is for the complete reconstruction whereas the calculated porosity is for the part volume a4_x0_y0_z0.

The permeability of the Bentheimer sandstone is 2860 mD (Ramstad et al., 2012) and the permeability of the Gildehauser sandstone is 1500 mD (Berg et al., 2016).

Chapter 4

Pore Space Characterisation

"What have I, I wonder?" he said to himself, as he panted and stumbled along. He put his left hand in his pocket. The ring felt very cold as it quietly slipped onto his groping forefinger.

— J.R.R. Tolkein, The Hobbit

4.1 Methodology

4.1.1 Summary

This chapter describes the methods used to characterise the pore space of rock samples from both 2D and 3D images. The pore space characterisation algorithm is implemented in the imagenet program (Appendix C).

The procedure for 3D images is a straightforward extension of the 2D procedure; therefore the overall methodology is described and the differences between 2D and 3D are highlighted as appropriate. Word(s) in brackets indicate the 3D procedure where it differs from 2D.

The pore space is characterised by discretising it into elements and performing a statistical analysis of the elements. The definition of a pore space element is a little arbitrary, but each element is based on an inscribed circle (sphere) which touches the pore wall in at least two (three) separate places. Generally, the inscribed circle (sphere) will touch opposite sides of the pore wall. For efficient characterisation of the pore space it is desirable to minimise both overlaps and gaps between the inscribed circles (spheres).

71

The Euclidean Distance Map (EDM) is the Euclidean distance from each point in the pore space to the nearest point on the pore wall and the medial axis is the set of points which have two (three) or more closest points on the pore wall. Note that the 3D medial axis is required to have at least three closest points on the pore wall and therefore medial surfaces are not included (Silin and Patzek, 2006).

A circle (sphere) centred on the medial axis with radius equal to the Euclidean distance at its centre will touch the pore wall in at least two (three) separate places. Therefore the centres of the pore elements are constrained to the medial axis and the pore element radius is defined from the value of the EDM at the centre of the element. Such circles (spheres) are comparable but not identical to maximal balls (Silin and Patzek, 2006; Al-Kharusi and Blunt, 2007).

The boundaries between pore elements are approximately perpendicular to the medial axis of the pore space and the links between element centres capture the pore space topology. Links between elements are important because an objective is to characterise the connectivity of the pore space for flow modelling. The methodology assumes that the principal direction of flow is parallel to the medial axis. The elements are identified in sequence from largest to smallest such that largest pore bodies are captured first and represented by a minimal number of elements.

The process of discretising the pore space is conceptually equivalent to extracting a pore network from imaging data. Therefore, it would be possible to use an existing pore network extraction algorithm such as the maximal ball method (Silin and Patzek, 2006), a medial axis method (Lindquist et al., 1996) or a watershed algorithm (Sheppard et al., 2005). However, there are potentially large and complex images to analyse, therefore the discretisation algorithm incorporates elements from existing methodologies but most importantly is pragmatic and efficient. One of the objectives is to compare 2D and 3D pore space characterisation; therefore the 2D and 3D algorithms should be equivalent.

Starting from a segmented binary image, the algorithm is summarised as follows:

1. Calculate the EDM of the pore space.

2. Calculate the ridge points of the EDM.

3. Construct a set of inscribed circles (spheres) centred on the ridge

points.

4. Assign each pixel (voxel) to a pore space element.

5. Identify the connections between pore space elements.

The algorithm for a simple 2D example is shown in Figure 4.1.
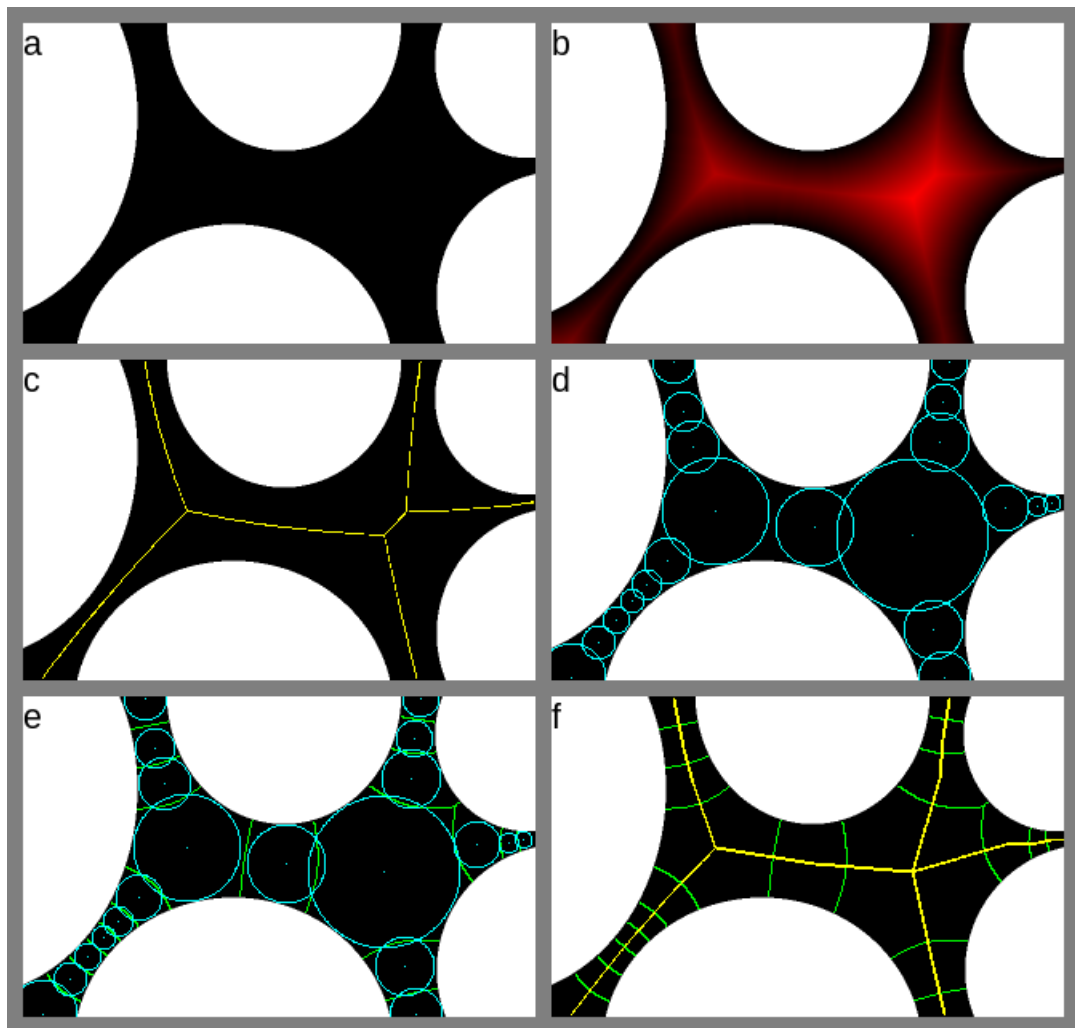
Figure 4.1: Pore space discretisation: (a) binary image with pore space in black (b) EDM in red shading (c) ridge points of the EDM in yellow (d) inscribed circles centred on the EDM ridge (e) boundaries between pore space elements in green (f) element boundaries in green and links between elements in yellow

4.1.2 Euclidean Distance Map

The EDM (Figure 4.1b) is calculated using an efficient algorithm due to Borgefors (1984). The EDM calculation requires 4 scans of the image in 2D

and 8 scans in 3D. At this stage, it is assumed that all pixels (voxels) are square (cubic) with unit side length. The transformation to real units of length is applied later.

Next the ridge points of the EDM are determined which amount to an approximation of the skeleton or medial axis of the pore space (Figure 4.1c).

A very efficient criterion is used which defines a ridge point based on approximating the curvature or second derivative of the EDM. The criterion is a local calculation which determines whether or not a pixel (voxel) is a ridge point based on the EDM of the pixel (voxel) and its 8 (26) immediate neighbours.

Generally, the ridge points are where the EDM has a large negative curvature, in particular, the curvature is less than –1 (Serra, 1983). More specifically, it is necessary to consider the principal components of the curvature which are equal to the eigenvalues of the Hessian matrix, where the Hessian matrix of the EDM in 2D is given by:

$$H = \begin{pmatrix} \dfrac{\partial^2 E}{\partial x^2} & \dfrac{\partial^2 E}{\partial x \partial y} \\ \dfrac{\partial^2 E}{\partial x \partial y} & \dfrac{\partial^2 E}{\partial y^2} \end{pmatrix} \tag{4.1}$$

and the Hessian matrix of the EDM in 3D is given by:

$$H = \begin{pmatrix} \dfrac{\partial^2 E}{\partial x^2} & \dfrac{\partial^2 E}{\partial x \partial y} & \dfrac{\partial^2 E}{\partial x \partial z} \\ \dfrac{\partial^2 E}{\partial x \partial y} & \dfrac{\partial^2 E}{\partial y^2} & \dfrac{\partial^2 E}{\partial y \partial z} \\ \dfrac{\partial^2 E}{\partial x \partial z} & \dfrac{\partial^2 E}{\partial y \partial z} & \dfrac{\partial^2 E}{\partial z^2} \end{pmatrix} \tag{4.2}$$

The elements of the Hessian matrix are calculated using standard central difference formulae using the 9 pixel (27 voxel) neighbourhood of each point. For example, for voxel (i, j, k):

$$\frac{\partial^2 E}{\partial x^2} = E_{i-1,j,k} + E_{i+1,j,k} - 2E_{i,j,k} \tag{4.3}$$

$$\frac{\partial^2 E}{\partial x \partial y} = \frac{1}{4}(E_{i+1,j+1,k} + E_{i-1,j-1,k} - E_{i+1,j-1,k} - E_{i-1,j+1,k}) \tag{4.4}$$

$$\frac{\partial^2 E}{\partial x \partial z} = \frac{1}{4}(E_{i+1,j,k+1} + E_{i-1,j,k-1} - E_{i+1,j,k-1} - E_{i-1,j,k+1}) \tag{4.5}$$

with analogous formulae for the other partial derivatives.

In 2D, the two eigenvalues ($\lambda_1 < \lambda_2$) of the Hessian matrix are computed for each pixel and the pixel is classified as a ridge point if $\lambda_1 \leqslant -1$. The eigenvector corresponding to the most negative eigenvalue, λ_1, is perpendicular to the medial axis and the eigenvector corresponding to the other eigenvalue, λ_2, is parallel to the medial axis.

In 3D, the three eigenvalues ($\lambda_1 < \lambda_2 < \lambda_3$) of the Hessian matrix are computed for each voxel and the voxel is classified as a ridge point if $\lambda_2 \leqslant -1$. In this case, the two eigenvectors corresponding to λ_1 and λ_2 are perpendicular to the medial axis and the eigenvector corresponding to λ_3 is parallel to the medial axis.

The elements of the Hessian matrix are coordinate dependent but the eigenvalues, representing the principal components of the curvature, should be independent of any coordinate transformation. Accordingly, the estimate of the ridge points can be improved by applying a coordinate transformation and calculating the average of the smallest and largest eigenvalues. In 2D, this does not make a significant difference. But in 3D, the estimate of the ridge points can be significantly improved by considering a 45° rotation about each of the three coordinate axes and re-formulating the expressions for the partial derivatives. For example, a 45° rotation about the z-axis gives for voxel (i, j, k):

$$\frac{\partial^2 E}{\partial x^2} = \frac{1}{2}\left(E_{i-1,j-1,k} + E_{i+1,j+1,k} - 2E_{i,j,k}\right) \tag{4.6}$$

$$\frac{\partial^2 E}{\partial x \partial y} = \frac{1}{2}\left(E_{i,j+1,k} + E_{i,j-1,k} - E_{i+1,j,k} - E_{i-1,j,k}\right) \tag{4.7}$$

$$\frac{\partial^2 E}{\partial x \partial z} = \frac{\sqrt{2}}{4}\left(E_{i+1,j+1,k+1} + E_{i-1,j-1,k-1} - E_{i+1,j+1,k-1} - E_{i-1,j-1,k+1}\right) \tag{4.8}$$

with analogous formulae for the other partial derivatives.

In 3D, λ_1, λ_2 and λ_3 are each calculated from the average of four eigenvalues i.e. using the untransformed coordinates and using 45° rotations about each of the three coordinate axes. Also, numerical experiments show that a more continuous set of voxels is obtained using the modified criterion $\lambda_1 \leqslant -1$ AND $\lambda_2 \leqslant \frac{4}{7}\lambda_1$.

Figure 4.1c shows the ridge points for the simple 2D example. In general, the ridge points are not necessarily continuous and single pixel width.

4.1.3   Pore Elements

Each pore element is based on an inscribed circle (sphere) which is centred on the EDM ridge and touches the pore wall in at least two (three) separate places. Generally, the inscribed circle (sphere) will touch opposite sides of the pore wall. It is desirable that pore elements have approximately the same extent in all directions and are not highly elongated; therefore it is necessary to cover the pore space with inscribed circles (spheres) with minimal gaps between them and minimal overlaps.

To identify the pore elements, it is only necessary to consider the identified EDM ridge points. The algorithm finds the maximum value of the EDM, constructs a circle (sphere) of radius equal to that Euclidean distance and then removes those ridge points inside the circle plus an extra tolerance. The tolerance for a circle (sphere) of radius r is defined as ar where a is a tolerance factor discussed below.

The algorithm finds the next largest value of the EDM and repeats the process until there are no remaining ridge points. Each circle (sphere) defines a pore space element with radius equal to the EDM at its centre.

At this point the pore space is covered by elements although there can be both gaps and overlaps between the circles (spheres) (Figure 4.1d). The balance between overlap and gaps is controlled by the tolerance factor, a. Considering two pore elements of radii $r_1 > r_2$, it is straightforward to show that the maximum overlap is $r_2 - (a-1)r_1$ and the maximum gap is $(r_1 + r_2)(a-1)$. If $a \geqslant 2$, there is guaranteed to be no overlap (even if $r_2 = r_1$) and if $a \leqslant 1$ there will be no gaps. A reasonable criterion is to equate the maximum overlap to the maximum gap because this will tend to make the overlaps and gaps small. It follows that:

$$\frac{r_2}{r_1} = \frac{2(a-1)}{2-a} \tag{4.9}$$

Typically, r_2 is between 50% and 90% of r_1 and taking $\frac{r_2}{r_1} = \frac{2}{3}$ gives $a = 1.25$. Based on the 2D and 3D images analysed here, a value of $a = 1.25$ achieves a reasonable compromise with, on average, the distance between element centres being close to the sum of the radii.

Now the pore space is partitioned and each pixel (voxel) is assigned to a pore space element. To do this the algorithm start at the centre of each element and searches all connected pixels (voxels) to a maximum distance of three times the element radius. Each pixel (voxel) is assigned to the

element with the smallest value of $E_{ijk,m} - r_m$ where $E_{ijk,m}$ is the Euclidean distance from pixel (voxel) (i, j, k) to the centre of element m and r_m is the radius of element m. This criterion ensures that:

1. where circles (spheres) overlap, the boundary between elements passes through the intersection points, and

2. where there is a gap, the boundary between elements passes through the mid point of the shortest line connecting the circles' circumferences (spheres' surfaces).

Boundaries of 2D pore space elements are shown in Figure 4.1e.

The area (volume) of each pore space element is computed from the number of pixels (voxels) comprising the element.

Finally, the algorithm identifies links between pore space elements based on the interface between pixel (voxel) regions belonging to different elements. Consider two interfacing elements of radius r_l and r_m. In 2D, a link is created between the two elements if the interface length is greater than the harmonic mean of r_l and r_m. In 3D, a link is created between the two elements if the interface area is greater that one third of the harmonic mean of πr_l^2 and πr_m^2. These criteria ensure that small interfaces do not create spurious links that would not honour the topology.

Example links between 2D elements are shown in Figure 4.1f.

A larger example is shown in Figure 4.2. This shows the pore element discretisation for a 2D image of a glass-etched micro model from Pei et al. (2011).

A 3D example is shown in Figure 4.3. This shows the pore space discretisation of part of the Finney random sphere pack (Section 3.4).

In summary, each pore space element in 2D (3D) is characterised by the following (Figure 4.1):

- a position in space,

- a radius,

- an area (volume),

- a coordination number and a set of other linked elements.

In addition, it is necessary to determine the shape factor of pore elements and links.
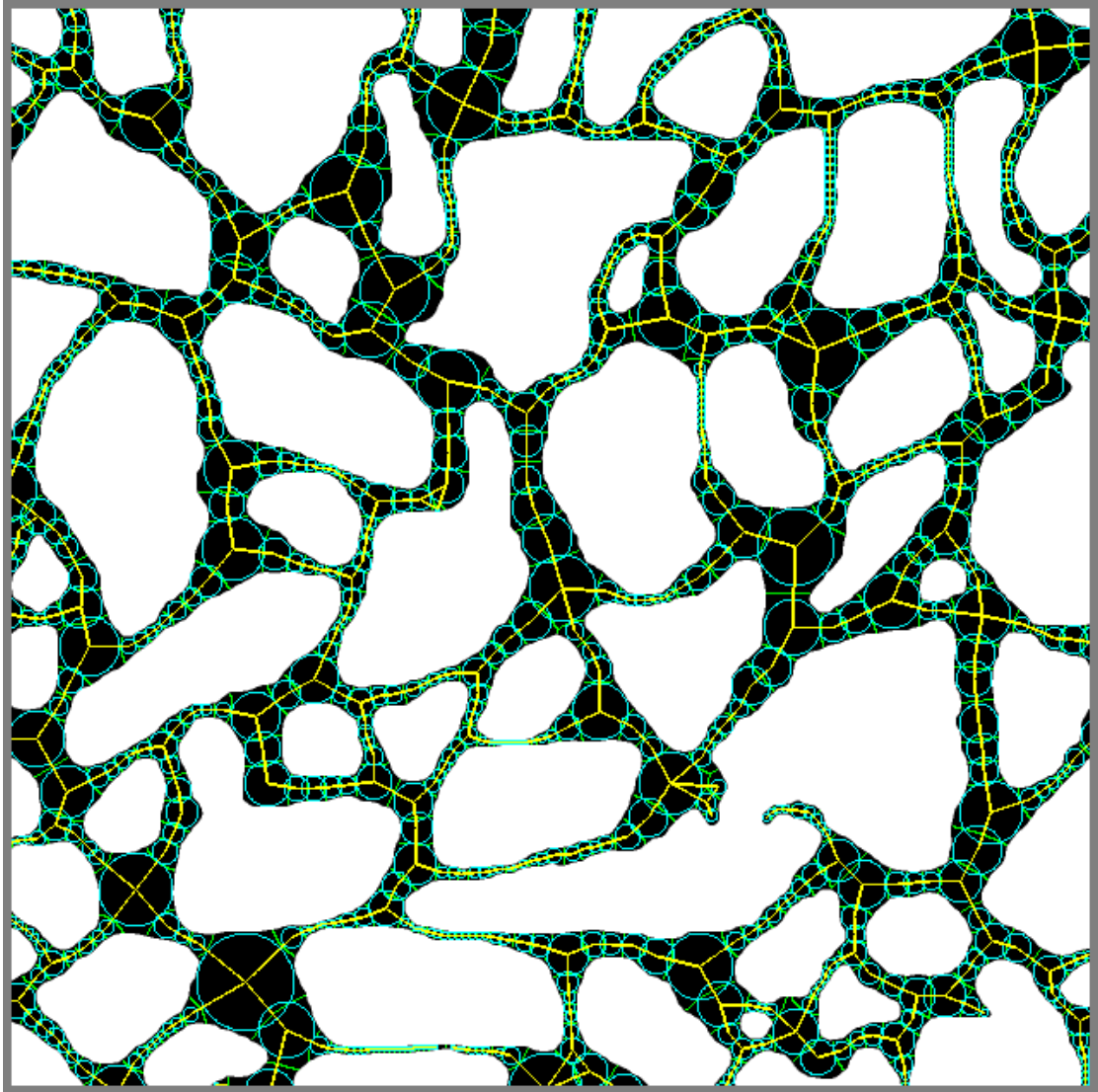
Figure 4.2: Pore space discretisation of a glass-etched micro model image

4.1.4 Shape Factor

The shape factor $G = A/P^2$ was introduced by Mason and Morrow (1991) to characterise the cross-section of irregular pores. The shape factor of pore elements is important because PNM simulators (Jackson et al., 2002; Valvatne and Blunt, 2004) use it to characterise the shape of pore bodies and pore throats. PNM simulators typically consider each pore throat cross-section to have an idealised geometry (e.g. triangular) which has the same shape factor as the actual pore throat.
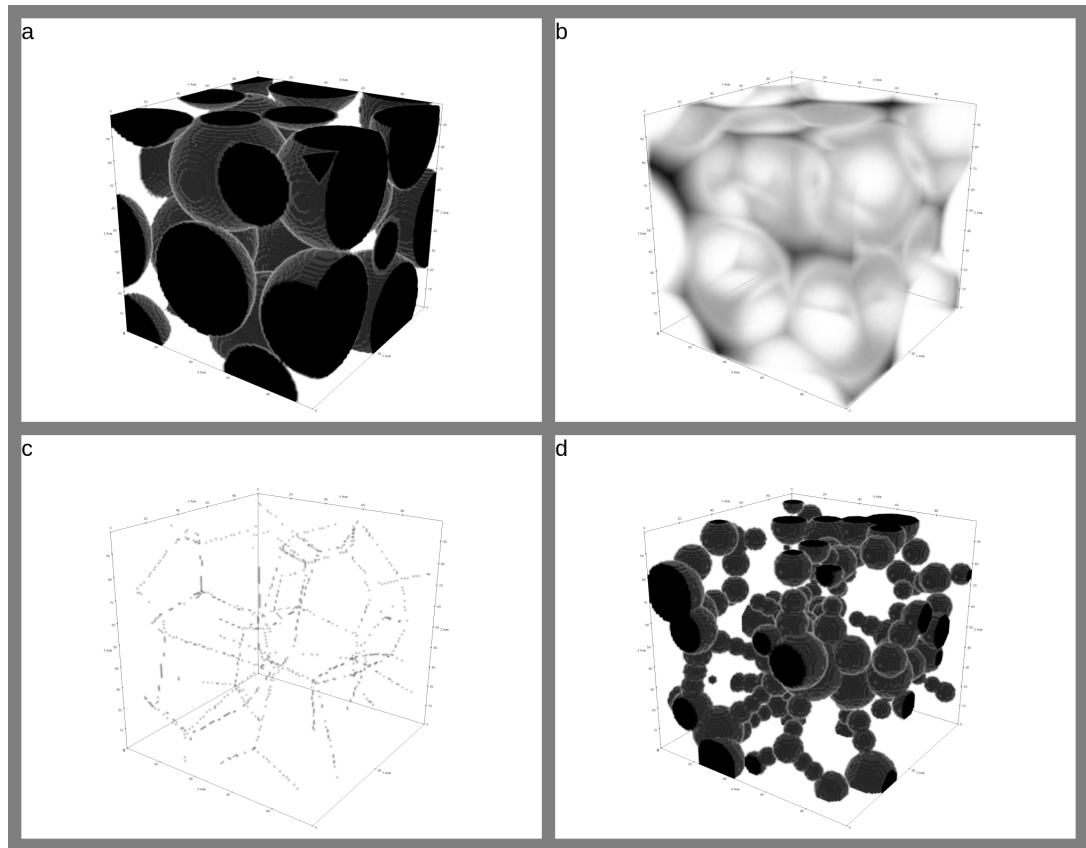
Figure 4.3: Pore space discretisation of 3D random sphere pack: (a) spheres in black and pore space transparent (b) EDM of the pore space in grey shading (c) ridge points of the EDM (d) inscribed spheres of the pore space elements

2D Elements

In 2D, the shape factor of each pore element is calculated from

$$G = A/P^2 \tag{4.10}$$

where A is the element area (calculated from the number of pixels) and P is its perimeter. The nature of pixelated images means that the boundaries of pore elements will be zig-zag lines and a naive calculation of the perimeter will generally be an over-estimate. The largest error occurs for an edge at 45° to the coordinate axes, where the zig-zag length over-estimates the true length by approximately 41%.

To address this issue, a simple algorithm is used to determine the perimeter by calculating the contribution of each pixel to the perimeter and then summing over all pixels in the element. The contribution of each pixel to the perimeter, w_P, is a function of the number of immediate neighbours of

the pixel which are outside the element, N. This function is a simple look-up given in Table 4.1.

Table 4.1: Perimeter contribution of a pixel as a function of its neighbour pixels

Number of neighbour pixels outside the element N	Perimeter contribution $w_P(N)$
0	0.000
1	0.421
2	0.476
3	0.985
4	1.30
5	1.83
6	2.36
7	2.70
8	3.54

The perimeter contribution factors in Table 4.1 for $1 \leqslant n \leqslant 4$ were determined by considering a straight edge at various angles and constructing a system of simultaneous equations to be satisfied. Consider a straight edge at angle of arctan(1) = 45° to the coordinate axes, then the edge pixels will have either 1 or 3 neighbours which are outside the element and it follows that:

$$w_P(1) + w_P(3) = \sqrt{2} \tag{4.11}$$

Similarly, considering a straight edge at an angle of arctan(2), gives:

$$w_P(1) + w_P(2) + w_P(4) = \sqrt{5} \tag{4.12}$$

and a straight edge at an angle of arctan(3), gives:

$$w_P(1) + w_P(2) + w_P(3) + w_P(4) = \sqrt{10} \tag{4.13}$$

In total, 11 equations were formulated considering different angles from 0° to 45° and the 4 perimeter factors calculated to minimise the sum of the square of the residuals.

The perimeter contribution factors for $N \geqslant 5$ were determined by considering a small number of simple pixel groups which are assumed to represent simple shapes with rounded corners. For example, a single isolated pixel represents a circular feature with unit area and it follows that

$w_P(8) = \sqrt{4\pi} \approx 3.54$. Similarly, a 2×2 block of four pixels represents a rounded corner feature of the same area and it follows that $w_P(5) = 1.832$.

	Area	Perimeter	Shape Factor		Area	Perimeter	Shape Factor
■	1	3.54	0.0796	▬	2	5.40	0.0687
▭	3	7.75	0.0499	▭	4	10.11	0.0391
⌐	3	7.07	0.0600	⊥	4	8.38	0.0570
■	4	7.33	0.0745	⌐	4	8.38	0.0570
✚	5	8.63	0.0672	⌐	6	10.13	0.0585
⊥	6	9.91	0.0611	⊥	6	12.91	0.0360
✚	10	11.83	0.0714	⊥	10	13.32	0.0564

Figure 4.4: Shape factor calculated from the proposed method for various 2D shapes

Figure 4.4 shows the area, perimeter and shape factors for some simple 2D shapes calculated from Equation 4.10 and the methodology above. It should be clear that the calculated perimeters are less than would be obtained by measuring the zig-zag length and therefore the shape factors are larger. Hence these pixel arrangements would be represented by more regular PNM elements thereby avoiding unrealistic corner effects.

3D Elements

In 3D, the shape factor of a pore element is calculated from its volume and surface area.

Consider a 3D pore element with volume V and surface area S. The element is modelled as an irregular base right prism of length L where the direction of flow is along the prism axis. Let the area of the base be A and the

perimeter of the base be P. Then:

$$V = LA \qquad (4.14)$$

$$S = 2A + LP \qquad (4.15)$$

$$G = \frac{A}{P^2} = \frac{V^2}{A(S - 2A)^2} \qquad (4.16)$$

From the pore space discretisation algorithm, it should be clear that pore elements will not be highly elongated and will have approximately the same extent in each direction. The tolerance factor of 1.25 (Section 4.1.3) implies that elements will not be elongated by more than 25% of their width. For a cube, $A = S/6$ and the same relationship holds for a triangular based prism of length $2r$ where r is the inradius of the triangle. Assuming $A = S/6$ gives:

$$G = \frac{27V^2}{2S^3} \qquad (4.17)$$

which is the formula used here to calculate the shape factor of 3D pore elements. Note that the formula is not very sensitive to the elongation assumption. For example, assuming $A = S/8$ gives a factor of 128/9 = 14.222 rather than 27/2 = 13.5.

Table 4.2 shows the shape factors calculated from Equation 4.17 for some simple 3D shapes.

Table 4.2: Example shape factors computed from volume and surface area using the proposed formula

Shape description	Volume	Surface area	Shape factor
Cylinder, radius=1, length=1	3.14	12.57	0.0671
Cylinder, radius=1, length=2	6.28	18.85	0.0796
Cylinder, radius=1, length=3	9.24	25.13	0.0755
Cube, side length=1	1	6	0.0625
Cuboid, side lengths=1,1,2	2	10	0.0540
Cuboid, side lengths=1,2,3	6	22	0.0456
Cuboid, side lengths=3,4,5	60	94	0.0585
Equilateral triangle based prism side length=1, length=1	0.433	3.866	0.0438
3,4,5 triangle based prism length=4	24	60	0.0360

The surface area, S, of a pore element is determined in an analogous way to the 2D perimeter calculation. In particular, the contribution of each voxel to the surface area, w_S, is given by a look-up table function of the number

of immediate neighbours of the voxel which are outside the element, N, (Table 4.3).

Table 4.3: Surface area contribution of a voxel as a function of its neighbour pixels

Number of neighbour voxels outside the element N	Surface area contribution $w_S(N)$	Number of neighbour voxels outside the element N	Surface area contribution $w_S(N)$
0	0.000	15	1.83
1	0.150	16	2.08
2	0.306	17	2.33
3	0.424	18	2.58
4	0.434	19	2.83
5	0.479	20	3.14
6	0.476	21	3.45
7	0.691	22	3.76
8	0.765	23	4.07
9	0.985	24	4.38
10	1.14	25	4.69
11	1.19	26	5.54
12	1.30		
13	1.31		
14	1.59		

The surface area contribution factors in Table 4.3 for were determined by considering a number of planar surfaces at various angles to the coordinate axes. Firstly, considering a surface which is parallel to one coordinate axis, then by examining a 2D cross-section perpendicular to that axis, it should be clear that $w_S(3) = w_P(1)$, $w_S(6) = w_P(2)$, $w_S(9) = w_P(3)$ and $w_S(12) = w_P(4)$. The remaining factors for $0 \leqslant N \leqslant 14$ were determined by considering a planar surface at various angles and constructing a system of simultaneous equations. For example, considering a surface at 45° to all three coordinate axes, the edge voxels will either have 1, 4 or 10 neighbouring voxels outside the element and it follows that:

$$w_S(1) + w_S(4) + w_S(10) = \sqrt{3} \qquad (4.18)$$

The surface area contribution factors for $N \geqslant 15$ were determined by considering a number of voxel groups which are assumed to represent simple shapes with rounded corners. For example, a single isolated pixel represents a cylindrical feature with unit volume and it follows that $w_S(26) = 2 + \sqrt{4\pi} \approx 5.545$. Similarly, a 2×2×2 block of 8 pixels represents a rounded

corner prism of the same volume and it follows that $w_S(19) = 2.832$.

	Length	Volume	Surface Area	Shape Factor		Length	Volume	Surface Area	Shape Factor
	1	1	5.54	0.0792		1	2	9.38	0.0654
	1	3	13.76	0.0466		1	4	18.14	0.0362
	2	6	20.71	0.0547		2	8	25.13	0.0544
	2	8	22.66	0.0743		2	8	25.13	0.0544
	2	10	27.32	0.0662		2	12	32.47	0.0568
	2	12	32.47	0.0568		2	12	38.94	0.0329
	3	30	54.30	0.0759		3	30	59.57	0.0575

Figure 4.5: Shape factor calculated from the proposed method for 3D prisms of various lengths and cross-sections

Figure 4.5 shows the volume, surface area and shape factors for a set of 3D prisms calculated by the proposed methodology. Comparison with Figure 4.4 shows that the 3D shape factors generally agree with the 2D section shape factors within ±5%.

4.2 Results

4.2.1 Pore Size Distribution

Figures 4.6, 4.7 and 4.8 show pore size distributions from SEM images. Pore size distributions from µCT images are shown in Figure 4.9. The plots show the complementary cumulative probability distribution $\Phi(r) = \Pr(R > r)$ as a function of element radius r, i.e. the fraction of pore elements larger than a given radius.

Figure 4.10 shows a comparison between SEM and µCT pore size distributions for Guillemot A plug 367.
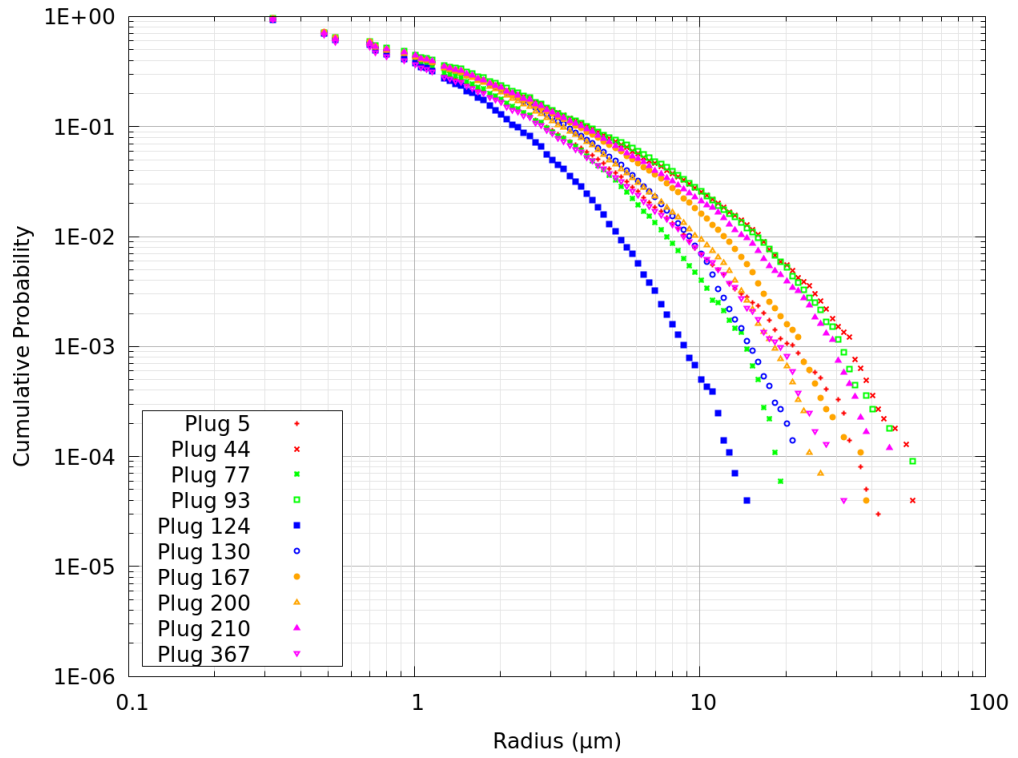
Figure 4.6: Cumulative pore size distribution from Guillemot A downscaled SEM images
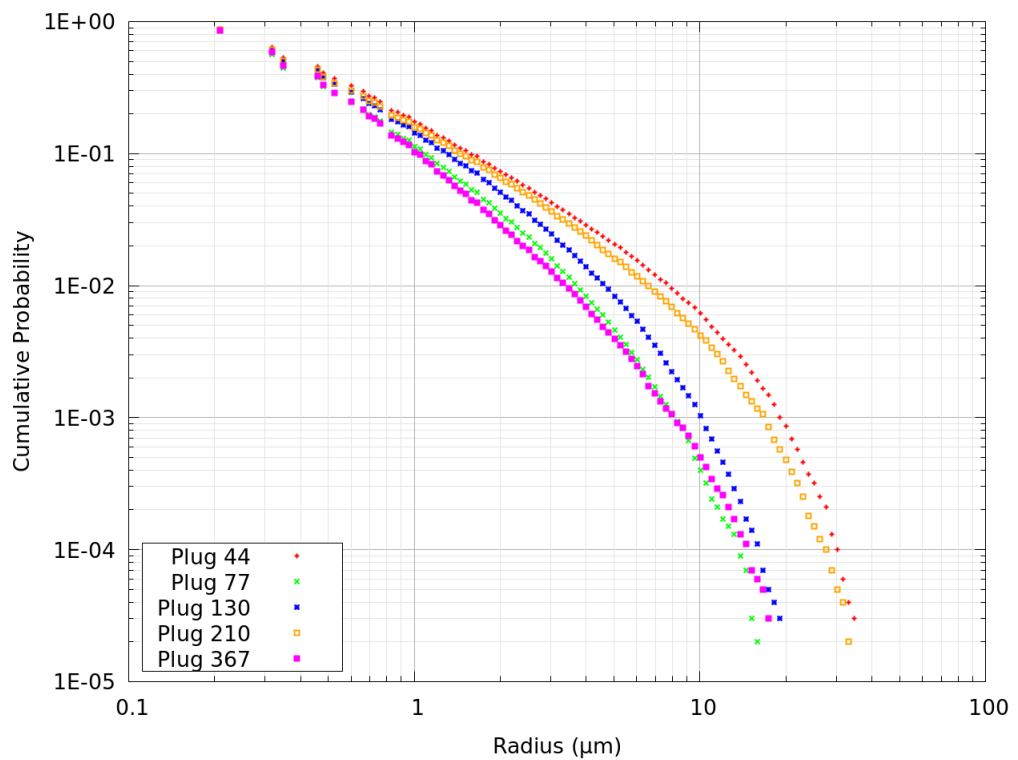
Figure 4.7: Cumulative pore size distribution from Guillemot A Carl Zeiss GeminiSEM images
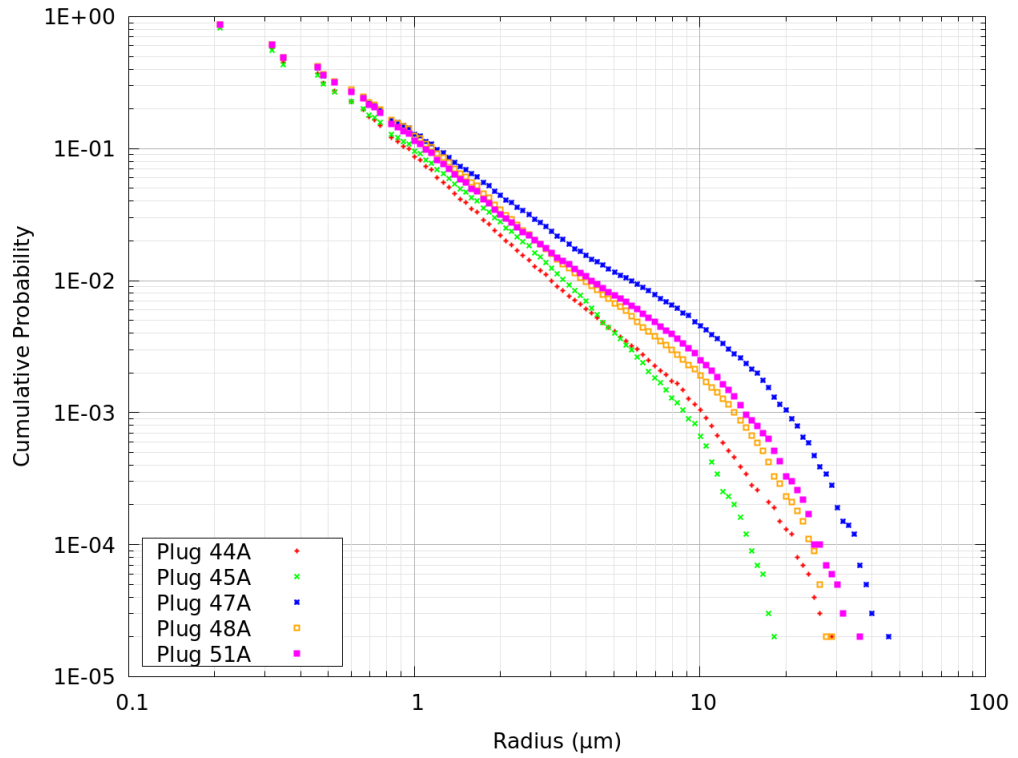
Figure 4.8: Cumulative pore size distribution from Vanguard Carl Zeiss GeminiSEM images
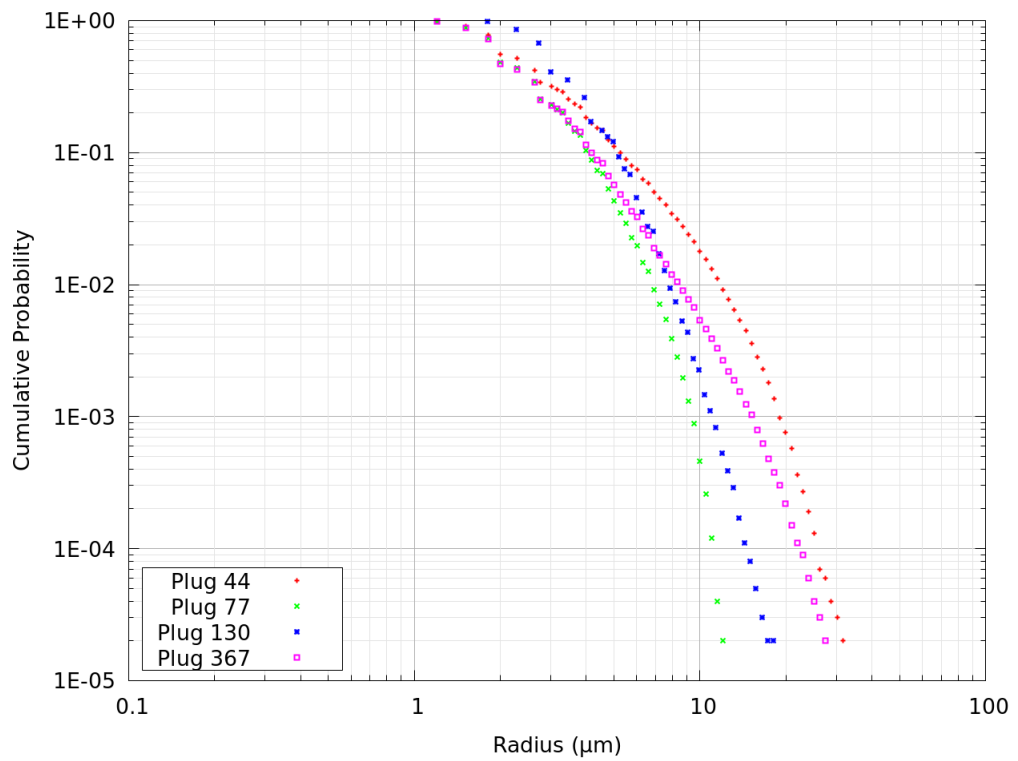
Figure 4.9: Cumulative pore size distribution from µCT data
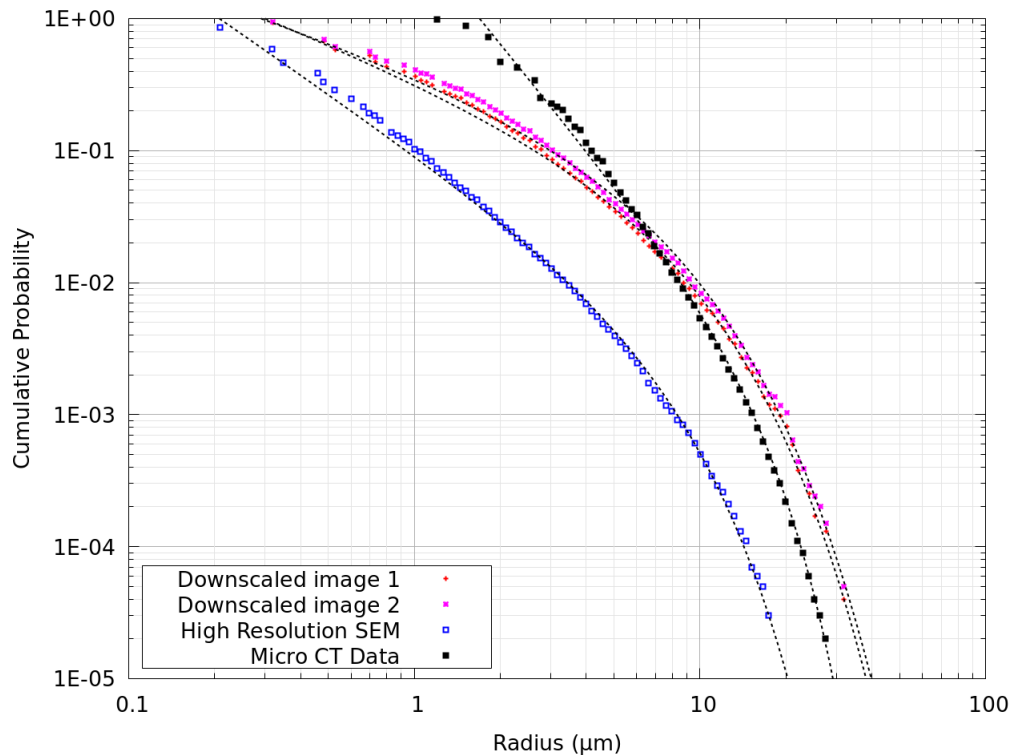
Figure 4.10: Comparison of pore size distribution from SEM and μCT images: Guillemot A plug 367

The SEM images have higher resolution than the μCT images and therefore they provide information for the small pores (less than circa 2 μm). The high resolution SEM images also have a better spatial resolution than the downscaled SEM images, the minimum resolved pore size is smaller and therefore we see the pore size distributions shifted to the left. Accounting for this effect, there is qualitative agreement between distributions from the two SEM imaging strategies. However, pore radii are imperfectly defined from SEM images because they are only 2D and therefore there could be some bias in the pore size distributions.

The μCT images have much poorer spatial resolution than the SEM and accordingly the distributions are narrower and shifted to the right. However, μCT images are 3D and pore radii are defined more reliably. Therefore μCT images provide the best information for large pores (greater than circa 10 μm) and SEM provides the only information for small pores (less than circa 2 μm).

In all cases, we observe a near linear relationship between $\log(\Phi(r))$ and $\log(r)$ at small radii (Pareto Type I distribution) with an exponential cut-off at larger radii. For all images, the data have been fitted to a cumulative

probability distribution function of the form:

$$\Phi(r) = \left(\frac{r}{r_0}\right)^{-\alpha} \exp\left(-\left(\frac{r}{r_1}\right)^{\eta}\right) \tag{4.19}$$

using a nonlinear least-squares Marquardt-Levenberg algorithm.

The parameter α is the slope or scaling index which is related to the fractal dimension of the pore space, r_0 is a parameter controlling the lower limit of the distribution, r_1 controls the position of the cut-off and η controls the shape of the cut-off. The parameter r_0 is defined from the image resolution and was not used as a variable in the fitting algorithm. For the SEM image data, the other three parameters were varied in the fitting algorithm. The μCT image data have narrower pore size distributions and preliminary testing showed evidence of overfitting i.e. a model with three free parameters cannot be justified by the data. Accordingly, the parameter η was fixed at the value $\eta = 2$ and the remaining two parameters were adjusted in the fitting algorithm.

The fitted parameters are given in Tables 4.4, 4.5 and 4.6. An example of fitted curves are shown in Figure 4.10.

The differences between the pore size distributions of different samples are due to geological variations in grain size, silt content, cementation and clay content.

In Guillemot A, grain size is a primary control on permeability and porosity is controlled by cementation and silt content (Cannon and Gowland, 1996; Gowland, 1996; Akpokodje et al., 2017). Within the Fulmar, the Middle unit was deposited in the highest energy environment and has the largest grain size. Samples 44 and 93 from the Middle Fulmar exhibit larger pore sizes consistent with lower silt and clay content. Samples 77 and 124 from the Lower Fulmar have smaller pore sizes consistent with smaller grain size, higher silt content and a lower energy depositional environment (Gowland, 1996).

For Vanguard, sample 47A from zone C has the largest pore size consistent with large grain size and clean aeolian dune facies (Lahann et al., 1993; Courtier and Riches, 2003). Samples 44A and 45A from zone B have the smallest pore size consistent with interdune or sandy sabkha facies with smaller grain size and higher primary silt content. Samples 48A and 51A from zone D have intermediate pore size consistent with fluvial or lacustrine facies.

Table 4.4: Downscaled images: pore size distribution parameters

Sample	Image	r_0 μm	r_1 μm	α	η
5	1	0.318	8.0	0.98	1.05
5	2	0.318	10.4	1.08	1.14
44	1	0.318	13.9	0.84	1.24
44	2	0.318	13.0	0.81	1.29
77	1	0.318	4.4	0.78	1.22
77	2	0.318	4.0	0.74	1.15
93	1	0.318	13.6	0.85	1.27
93	2	0.318	12.6	0.95	1.23
124	1	0.318	2.3	0.71	1.10
124	2	0.318	3.2	0.92	0.96
130	1	0.318	6.5	0.84	1.50
130	2	0.318	4.9	0.77	1.23
167	1	0.318	10.6	0.89	1.44
167	2	0.318	11.9	0.94	1.56
200	1	0.318	8.0	0.90	1.46
200	2	0.318	5.8	0.74	1.01
210	1	0.318	10.4	0.81	1.16
210	2	0.318	13.8	0.89	1.30
367	1	0.318	5.5	0.87	1.03
367	2	0.318	4.7	0.74	0.97

Table 4.5: High resolution images: pore size distribution parameters

Field	Sample	r_0 μm	r_1 μm	α	η
Guillemot A	44	0.209	14.2	1.16	1.68
Guillemot A	77	0.209	3.0	1.17	0.98
Guillemot A	130	0.209	5.6	1.22	1.34
Guillemot A	210	0.209	11.0	1.18	1.39
Guillemot A	367	0.209	6.4	1.49	1.34
Vanguard	44A	0.209	14.0	1.63	1.22
Vanguard	45A	0.209	8.8	1.58	1.78
Vanguard	47A	0.209	22.0	1.34	1.68
Vanguard	48A	0.209	16.2	1.51	1.91
Vanguard	51A	0.209	16.9	1.47	1.50

In all cases, the downscaled images give systematically lower slope parameter. This is most likely due to imaging limitations and some residual noise in the highest magnification images. These effects perhaps result in erroneous extension of the pore size distribution to the smallest radii i.e. parameters r_0 and α should both be larger. There is more confidence in the high resolution images because they were obtained with the more modern

Table 4.6: µCT images: pore size distribution parameters

Sample	r_0 µm	r_1 µm	α	η
44	1.7	14.5	2.06	2.0
77	1.7	4.4	1.60	2.0
130	2.6	7.9	3.21	2.0
367	1.7	14.6	2.64	2.0

Carl Zeiss GeminiSEM.

4.2.2 Pore Link Size Distribution

The radius of a link between two pore elements is defined as the minimum of the two connected element radii. The distribution of pore link sizes is important because it is related to the pore space connectivity function.

From Equation 2.9 it follows that:

$$\chi_V(r) = \frac{N_e \Phi_e(r) - N_l \Phi_l(r)}{V} \tag{4.20}$$

or

$$\chi_V(r) = \frac{N_e}{V} \left(\Phi_e(r) - \frac{1}{2} Z_{mean} \Phi_l(r) \right) \tag{4.21}$$

where subscripts e and l indicate pore elements and links respectively and

$$Z_{mean} = \frac{2 N_l}{N_e} \tag{4.22}$$

is the mean coordination number.

Figures 4.11 and 4.12 show the pore link radius distributions compared with the pore element radius distributions for four SEM images and the Guillemot A µCT images. The distributions are similar but the pore link radius distributions are consistently shifted to the left (smaller radii) compared with the pore element radius distributions. The sizes for pore elements and pore links are close because the link radius is defined as the minimum of the connected element radii as discussed above.

To quantify the difference between distributions, the link radius distributions were fitted to the same cumulative probability distribution function (Equation 4.19) by adjusting the parameter r_1 and fixing the parameters α and η from the pore element radius distribution analysis. The results (Tables

4.7 and 4.8) show that the parameter r_1 for the link radius distributions is approximately 70% to 80% of the value from the pore element radius distributions. This result is consistent between the Guillemot A and Vanguard samples and consistent between the SEM (2D) and μCT (3D) analysis.
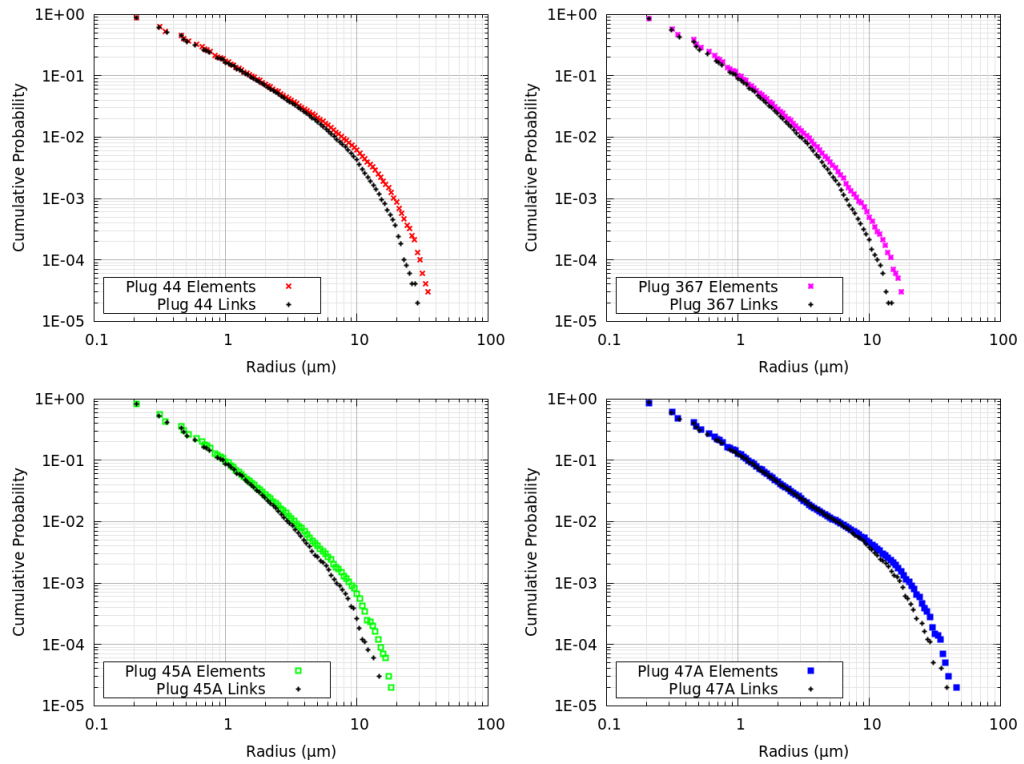
Figure 4.11: Cumulative pore size and pore link size distribution from SEM images

Table 4.7: High resolution SEM images: pore link size distribution parameters

Field	Sample	r_0 μm	r_1 μm	α	η
Guillemot A	44	0.209	11.3	1.16	1.68
Guillemot A	77	0.209	2.3	1.17	0.98
Guillemot A	130	0.209	4.2	1.22	1.34
Guillemot A	210	0.209	8.3	1.18	1.39
Guillemot A	367	0.209	4.7	1.49	1.34
Vanguard	44A	0.209	10.3	1.63	1.22
Vanguard	45A	0.209	6.8	1.58	1.78
Vanguard	47A	0.209	17.2	1.34	1.68
Vanguard	48A	0.209	12.9	1.51	1.91
Vanguard	51A	0.209	11.2	1.47	1.50
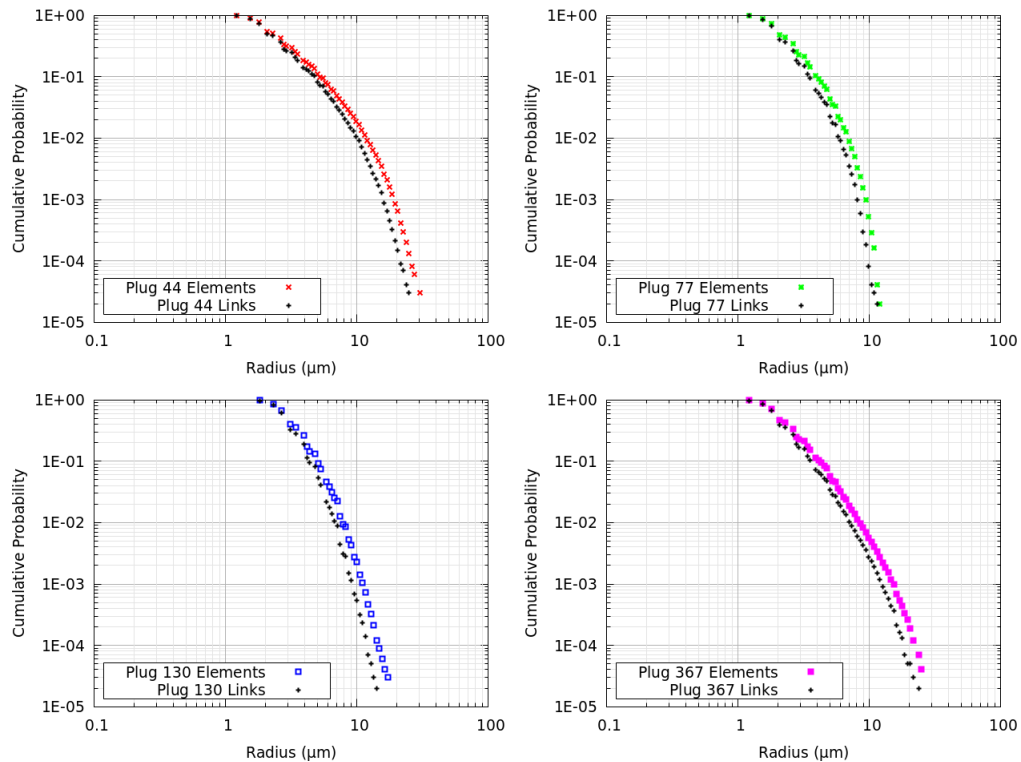
Figure 4.12: Cumulative pore size and pore link size distribution from μCT data

Table 4.8: μCT images: pore link size distribution parameters

Sample	r_0 μm	r_1 μm	α	η
44	1.7	10.9	2.06	2.0
77	1.7	3.9	1.60	2.0
130	2.6	5.9	3.21	2.0
367	1.7	10.7	2.64	2.0

4.2.3 Pore Coordination

The frequency distribution of coordination numbers for the SEM images is shown in Figure 4.13, 4.14 and 4.15. The frequency distribution for the μCT images is shown in Figure 4.16.

For coordination numbers greater than 2, we observe an exponential behaviour where the probability of coordination number Z is $\Pr(Z) \propto \exp(-aZ)$ and the constant a is 0.5 to 0.7. This is contrary to the HPA type model proposed by Santiago (2008) for soil pore structures, which has a power law behaviour with scale free character.

A comparison between SEM and μCT coordination number frequency distri-
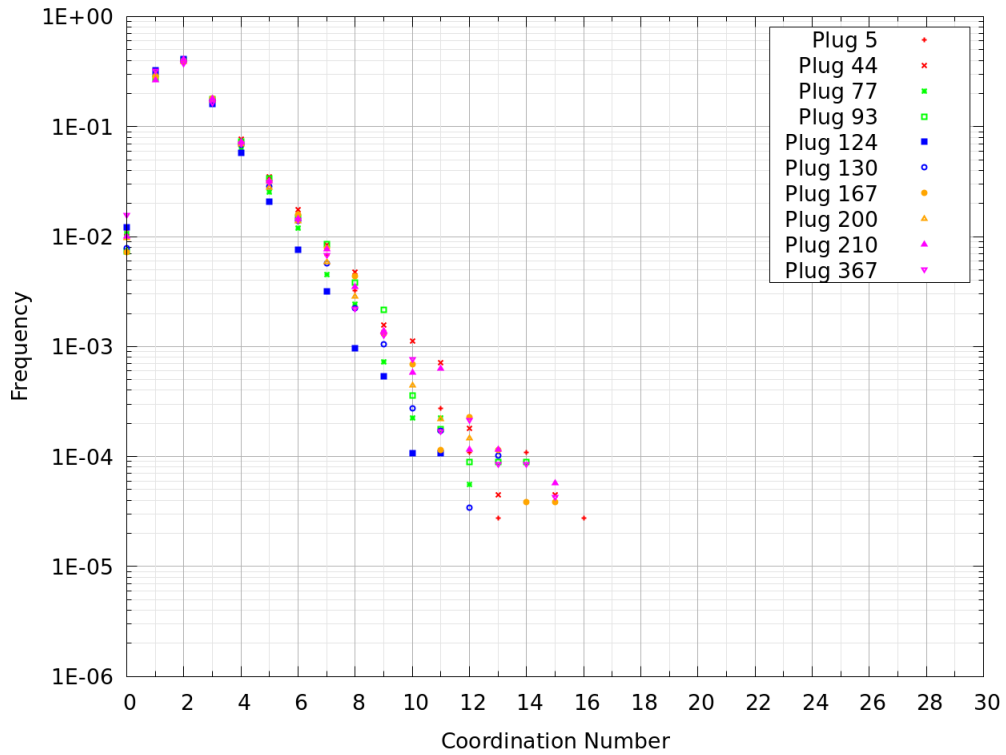
Figure 4.13: Coordination number frequency distributions for Guillemot A downscaled SEM images
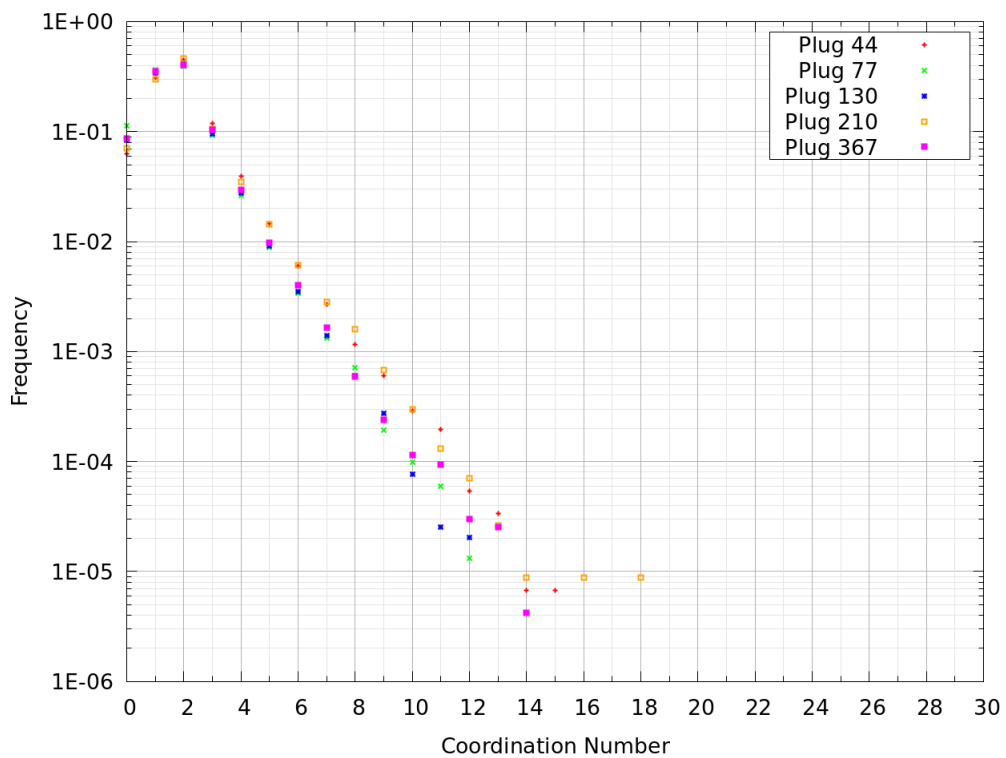
Figure 4.14: Coordination number frequency distributions for Guillemot A high resolution SEM images
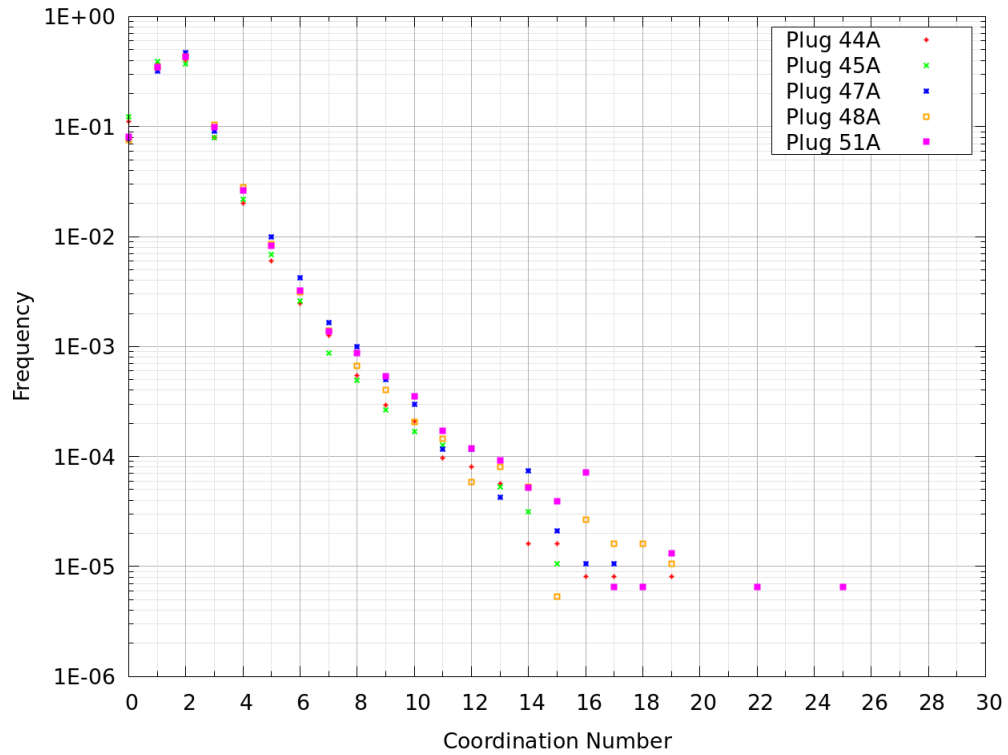
Figure 4.15: Coordination number frequency distributions for Vanguard high resolution SEM images
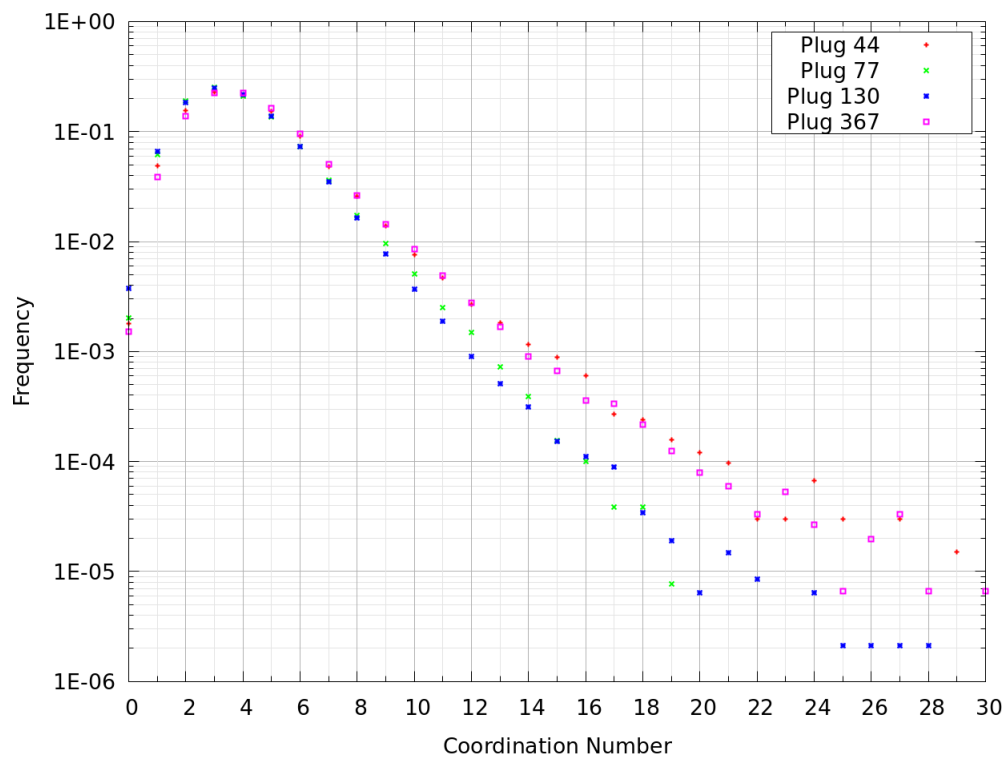
Figure 4.16: Coordination number frequency distributions for Guillemot A µCT images

butions for Guillemot A plug 367 is shown in Figure 4.17.
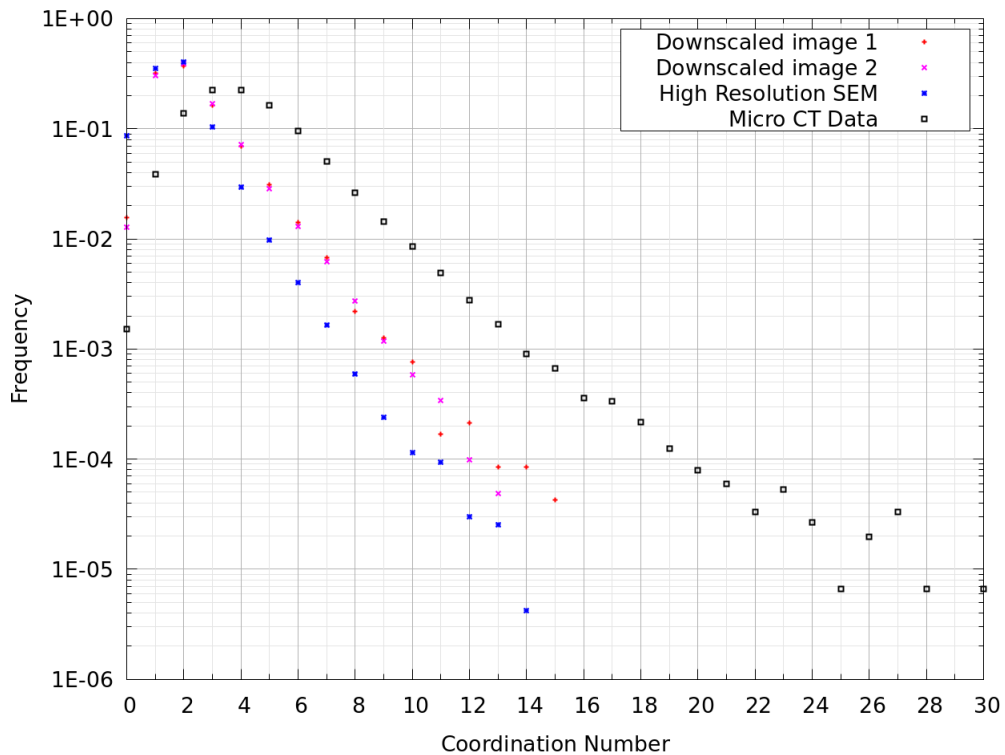
Figure 4.17: Comparison of coordination number frequency distributions from SEM and µCT images: Guillemot A plug 367

For a given element radius, the coordination number from the pore space discretisation is close to a normal distribution. The mean coordination number increase with radius as shown in Figure 4.18. The standard deviation (SD) of the coordination number also increases with radius and is approximately one third of the mean in all cases.

The mean and SD of the coordination number have been fitted to power law relationships of the form:

$$Z_{mean}(r) = \left(\frac{r}{r_{z,mean}} \right)^{\beta} \tag{4.23}$$

and

$$Z_{sd}(r) = \left(\frac{r}{r_{z,sd}} \right)^{\beta} \tag{4.24}$$

using a nonlinear least-squares Marquardt-Levenberg algorithm. Note that the parameter β is common to both equations i.e. the coordination number distribution at a given element radius is a function with three parameters. The parameters $r_{z,mean}$ and $r_{z,sd}$ represent the radii where the mean coordination and SD of the coordination respectively are 1.
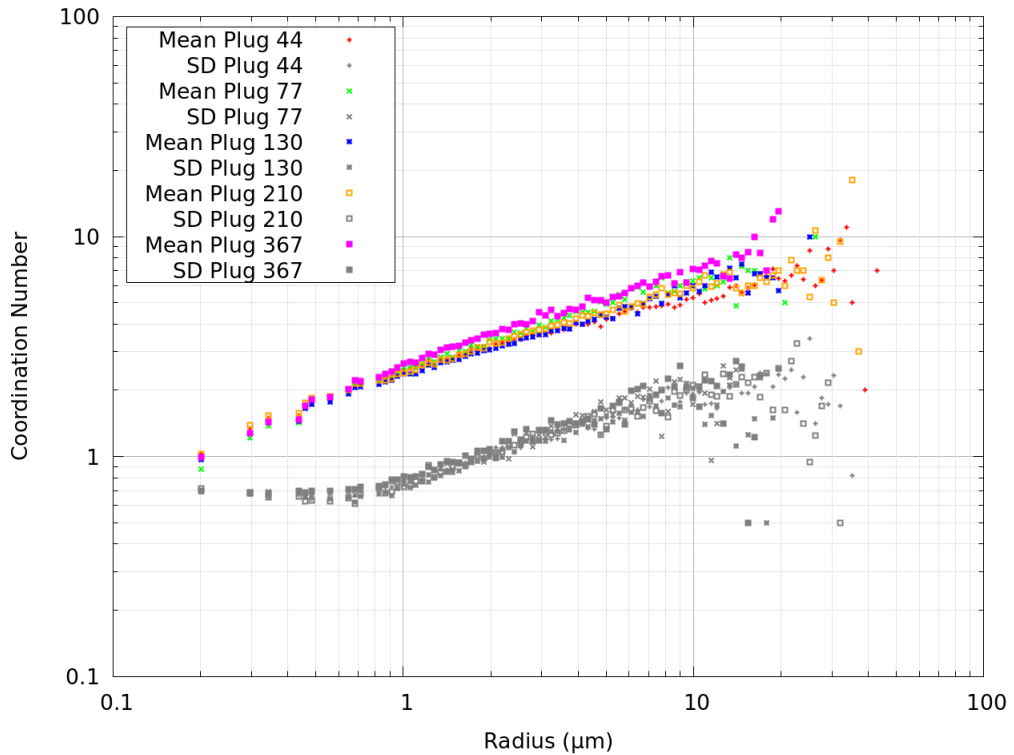
Figure 4.18: Mean and SD of the coordination number as a function of element radius for Guillemot A high resolution images

The overall mean coordination number Z_{mean}, the parameters $r_{z,mean}$, $r_{z,sd}$ and β are given in Tables 4.9, 4.10 and 4.11.

A comparison between the SEM and µCT images for plug 367 is shown in Figure 4.19.

There are differences between images firstly because of the differences in resolution and secondly because of the differences between 2D and 3D characterisation. For the largest pores (greater than 10 µm) the 3D µCT images should be most reliable. However, for the pores less than circa 3 µm, the coordination number distribution must be estimated from SEM images.

For the SEM image data, the mean and SD coordination number distributions are shifted to the left for the higher resolution images. This is reflected in the parameters $r_{z,mean}$ and $r_{z,sd}$ which are smaller for the high resolution SEM compared with the downscaled SEM images. For both high resolution and downscaled SEM images, the parameter $r_{z,mean}$ is about half of r_0 and the parameter $r_{z,sd}$ is about 8 times r_0 i.e. r_z, sd is around 16 times $r_{z,mean}$. The effect of image resolution on coordination number distribution is examined further in Section 4.3.

The relationship between $r_{z,mean}$ and $r_{z,sd}$ is reasonable. Combining Equa-

Table 4.9: Downscaled images: coordination number parameters

Sample	Image	Z_{mean}	$r_{z,mean}$ μm	$r_{z,sd}$ μm	β
5	1	2.1895	0.187	2.43	0.46
5	2	2.1941	0.169	2.44	0.45
44	1	2.3052	0.149	2.52	0.40
44	2	2.3029	0.135	2.51	0.39
77	1	2.1291	0.187	2.72	0.45
77	2	2.1206	0.188	2.49	0.45
93	1	2.2801	0.180	2.83	0.42
93	2	2.2253	0.184	2.55	0.44
124	1	2.0490	0.203	2.64	0.48
124	2	2.0383	0.144	2.75	0.42
130	1	2.1947	0.210	2.72	0.45
130	2	2.1678	0.219	2.82	0.46
167	1	2.2666	0.162	2.64	0.42
167	2	2.2367	0.149	2.66	0.40
200	1	2.1969	0.184	2.65	0.44
200	2	2.2261	0.166	2.65	0.42
210	1	2.2806	0.160	2.67	0.41
210	2	2.2776	0.130	2.70	0.38
367	1	2.1692	0.159	2.29	0.44
367	2	2.1841	0.190	2.44	0.45

Table 4.10: High resolution images: coordination number parameters

Field	Sample	Z_{mean}	$r_{z,mean}$ μm	$r_{z,sd}$ μm	β
Guillemot A	44	1.8575	0.061	1.76	0.33
Guillemot A	77	1.6083	0.107	1.80	0.41
Guillemot A	130	1.6945	0.120	2.06	0.40
Guillemot A	210	1.8379	0.104	1.85	0.39
Guillemot A	367	1.6955	0.107	1.67	0.43
Vanguard	44A	1.5682	0.144	1.96	0.47
Vanguard	45A	1.5295	0.181	1.71	0.49
Vanguard	47A	1.7376	0.092	1.82	0.37
Vanguard	48A	1.7200	0.123	1.79	0.42
Vanguard	51A	1.7047	0.135	1.76	0.44

tions 4.23 and 4.24 gives:

$$\frac{Z_{sd}}{Z_{mean}} = \left(\frac{r_{z,mean}}{r_{z,sd}} \right)^{\beta} \tag{4.25}$$

and taking $Z_{sd} = 0.333 Z_{mean}$ and $\beta = 0.4$ implies $r_{z,sd} = 15.63 r_{z,mean}$.

Table 4.11: µCT images: coordination number parameters

Sample	N_e	N_l	Z_{mean}	$r_{z,mean}$ µm	$r_{z,sd}$ µm	β
44	133442	274711	4.1173	0.213	1.92	0.56
77	128985	241215	3.7402	0.431	2.40	0.77
130	468488	868464	3.7075	0.845	3.68	0.95
367	151147	317749	4.2045	0.227	1.70	0.63
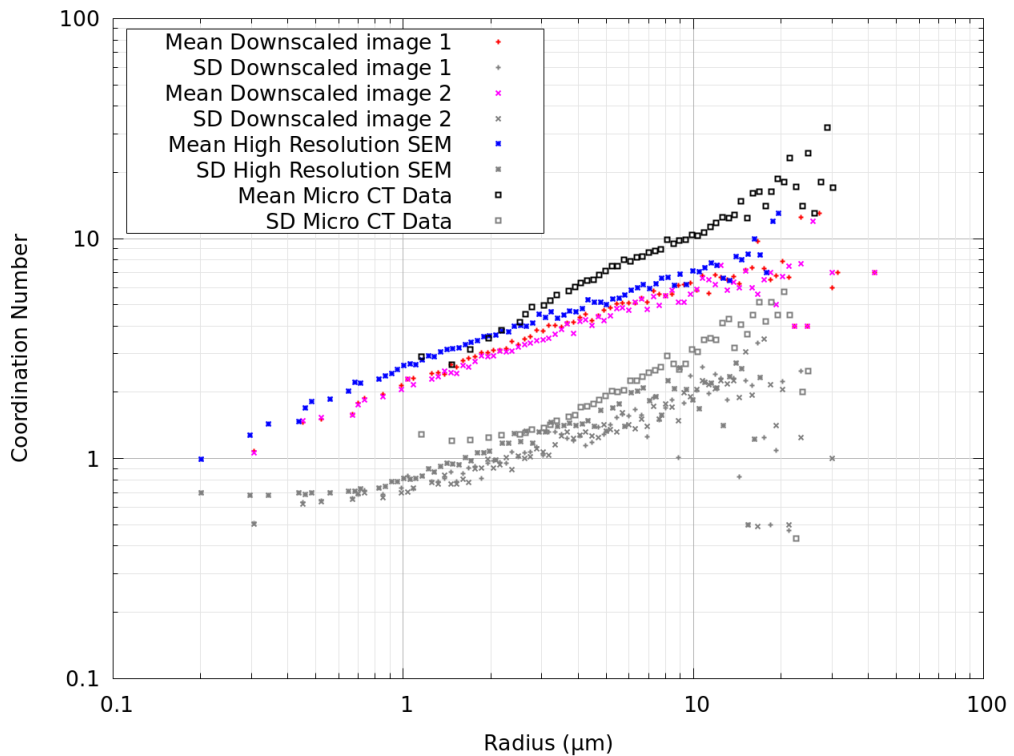
Figure 4.19: Mean and SD of the coordination number as a function of element radius for Guillemot A plug 367 images

The µCT data show different relationships. In particular, the parameter β is approximately 50% larger than for the SEM data and the parameters $r_{z,mean}$ and $r_{z,sd}$ are smaller in comparison with r_0. The difference in the parameter β is clear in Figure 4.19 where the µCT data show a steeper slope in comparison with the SEM data. These differences are due to the difference between 2D and 3D pore space characterisation and will be addressed further in Section 4.4.

4.2.4   Shape Factor

The shape factor (Section 4.1.4) is close to a normal distribution for all images. Figure 4.20 shows the shape factor distributions for the SEM images and μCT data from plug 367. The other samples are not significantly different.

The downscaled SEM images have mean shape factors approximately 5% lower than the high resolution SEM images. The reason for this is not immediately obvious but it may be due to imaging limitations of the Topcon ABT-60 SEM at the highest magnification images.
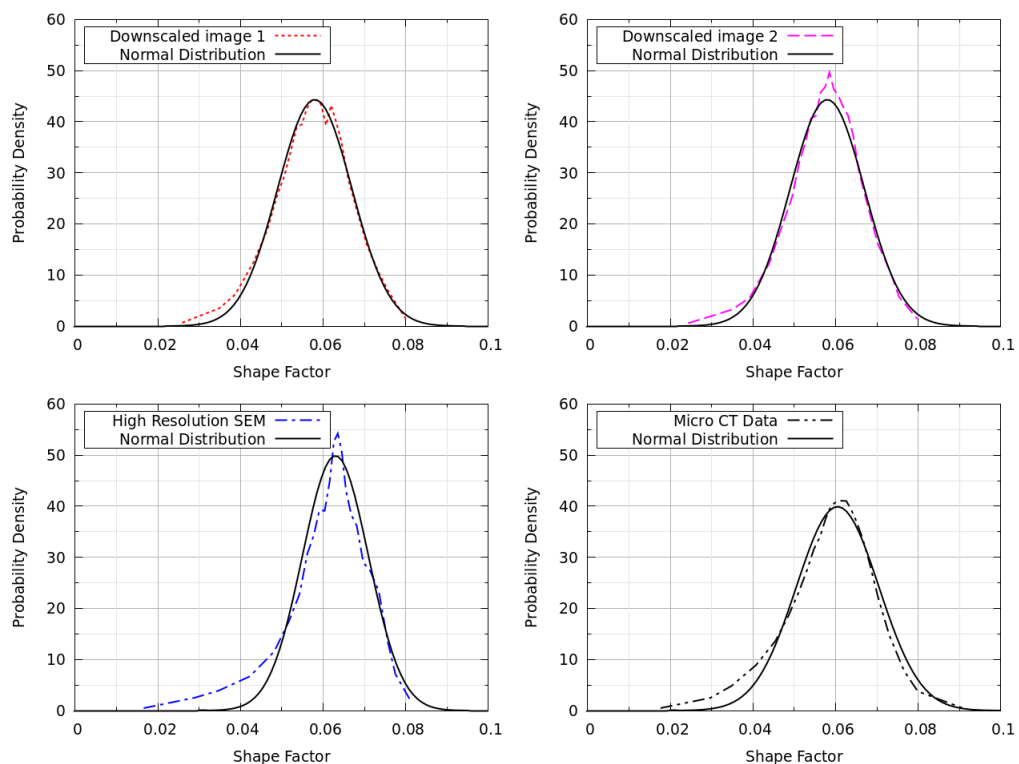
Figure 4.20: Shape factor probability distributions for Guillemot A plug 367 images

The mean shape factor shows a small variation with element radius (Figure 4.21). SEM images display a slightly higher shape factor at smaller radii which is consistent with the reduction in imaging information for small pore features i.e. they are more likely to be characterised as rounded because there is less image information available to capture their detailed shapes. The μCT data show the same effect but less obviously.

Overall, there is good agreement between the 2D SEM and 3D μCT shape factors. The mean shape factor is from 0.057 to 0.062 and the SD is from 0.008 to 0.011.
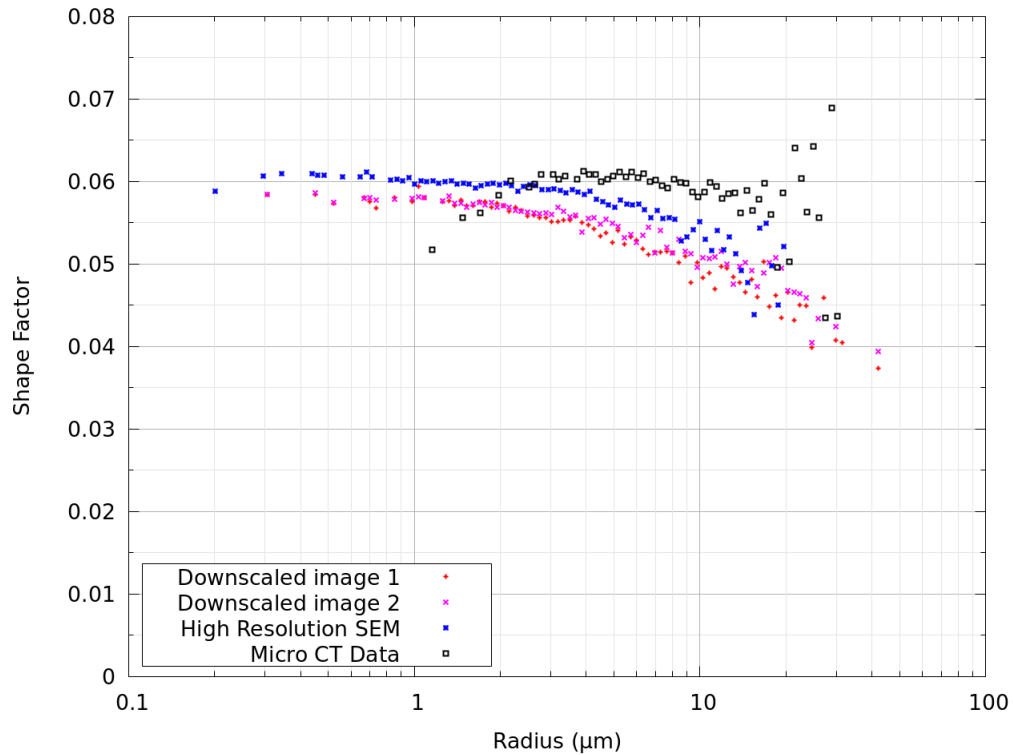
Figure 4.21: Mean shape factor as a function of element radius for Guillemot A plug 367 images

4.2.5 Connectivity

The connectivity function, Equation 2.9, is important for single-phase and multiphase flow behaviour. If $\chi_V(r) < 0$ then the sub-network of radii greater than r is well connected on a large scale and if $\chi_V(r) > 0$ then it is not. The critical radius, r_c such that $\chi_V(r_c) = 0$, is the point where the network becomes connected which corresponds to the macroscopic capillary entry or threshold pressure for an invading non-wetting phase in a sufficiently large sample.

The connectivity function was calculated for the Guillemot A μCT volumes and is shown in Figure 4.22. All the volumes are well connected for small radii and display a critical radius above which the pore space becomes disconnected.

The critical radii, $\chi_V(r_c) = 0$ and the equivalent capillary pressures from the Young-Laplace equation are given in Table 4.12 in comparison with the measured air-brine capillary entry pressures. There is qualitative agreement between the datasets.
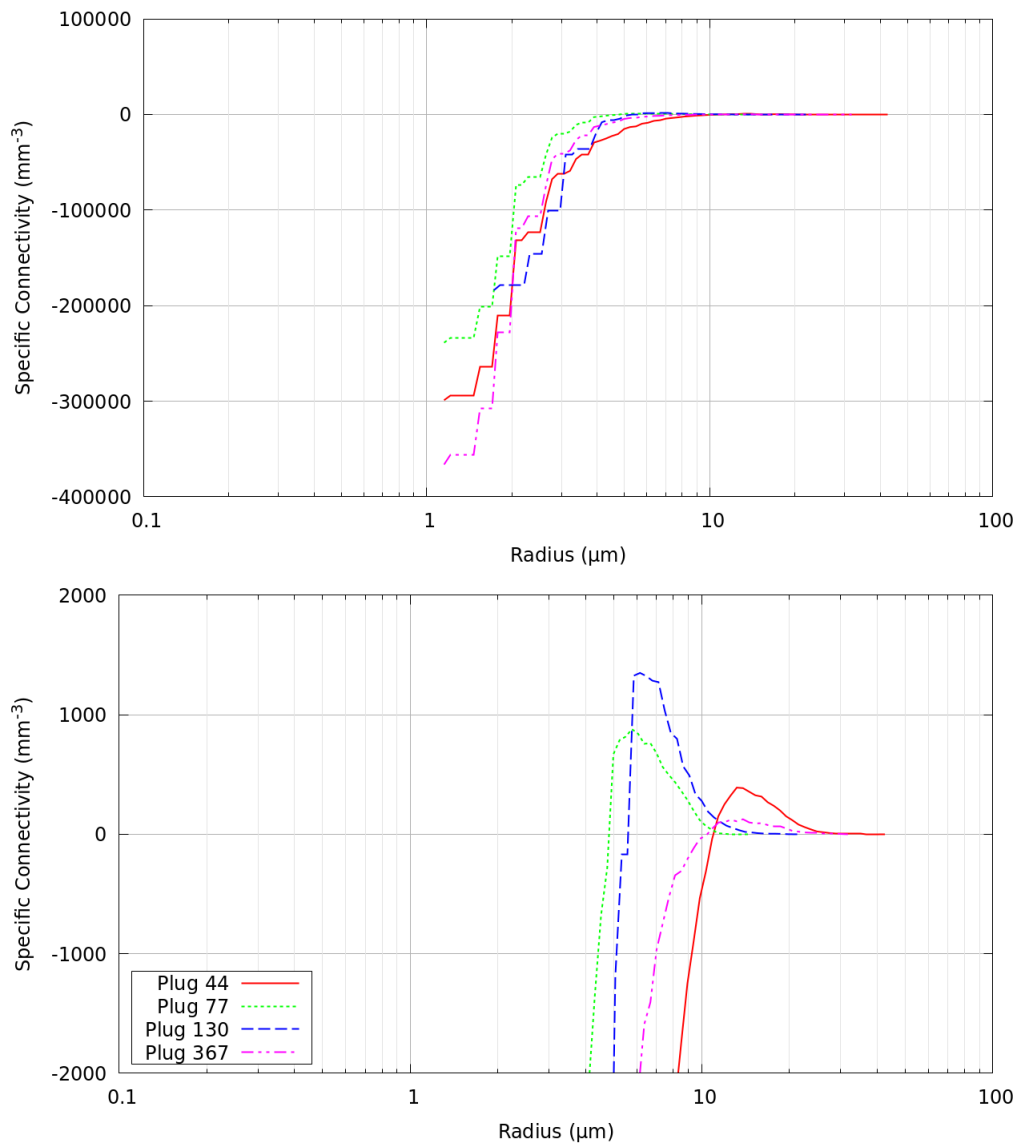
Figure 4.22: Specific connectivity function of Guillemot A μCT volumes; lower plot shows expanded vertical scale

Table 4.12: Critical connectivity radii and equivalent capillary pressures from μCT volumes compared with laboratory measured capillary entry pressures

Volume	Critical Radius (μm)	Equivalent Air-Brine P_c (psi)	Lab Air-Brine Entry Pressure (psi)
Plug 44	10.9	1.9	0.5
Plug 77	4.8	4.4	9.0
Plug 130	5.6	3.7	1.5
Plug 367	10.6	2.0	1.0

4.2.6 Permeability

SEM Images

Single phase permeability has been estimated from the SEM images by calculating a radius which is characteristic of the pores which control permeability. Katz and Thompson (1987) show that permeability is related to the square of a characteristic length, l_c, which can be obtained from the inflection point on the capillary pressure curve.

$$k = \frac{cl_c^2}{F} \tag{4.26}$$

Based on percolation theory, l_c is the size of the smallest pore on the connected path of pores containing the largest pores (Thompson et al., 1987). F is the formation resistivity factor (FRF) and c is a constant with the value $1/226 \approx 0.00442$.

The characteristic radius could be estimated from the critical connectivity radius, $\chi_V(r_c) = 0$, i.e. Equation 4.21 gives:

$$\Phi_e(r_c) = \frac{1}{2} Z_{mean} \Phi_l(r_c) \tag{4.27}$$

However, this procedure requires an estimate of the mean 3D coordination number. The relation between 2D and 3D pore space characterisation is addressed later (Section 4.4). In the mean time, a characteristic radius is obtained from the fitted pore size distribution which includes an exponential cut-off which characterises the tail of the distribution. The parameter r_1 is not suitable for this purpose because it depends on the cut-off shape parameter η. Instead, r_x is chosen to be the radius where the exponential cut-off reduces the cumulative probability to one half of the value it would have without the cut-off.

$$\exp\left(-\left(\frac{r_x}{r_1}\right)^\eta\right) = 0.5 \tag{4.28}$$

Thus:

$$r_x = r_1(-\log(0.5))^{1/\eta} \tag{4.29}$$

The factor of one half does not have any physical basis. This is essentially a tuning factor which has been adjusted to obtain permeability estimates of the right order.

For the FRF, measured data are used where available, otherwise $F = \phi^{-m}$ where $m = 1.75$ (Figures A.4 and B.4).

Figures 4.23 and 4.24 show the calculated permeability from images against the measured air permeability. A trend is evident with higher measured permeability samples having a higher image permeability.

Plugs 210, 51A, 44A and 45A are all outliers; the SEM image analysis would suggest that the permeability is higher than has been measured. For plug 210 the image porosity is also higher than expected (Figure 3.9), therefore we suspect there is some low porosity/permeability heterogeneity within the core plug which is not captured by the SEM imaging.

The other three outliers are all low permeability samples from Vanguard. Plug 51A in particular has a low permeability for its porosity (Figure 3.2) and therefore the discrepancy could be explained by core plug heterogeneity. Another possibility is that clays (e.g. fibrous illite) have been damaged or smeared by the sample preparation process (Anovitz and Cole, 2015) thereby increasing the apparent permeability.
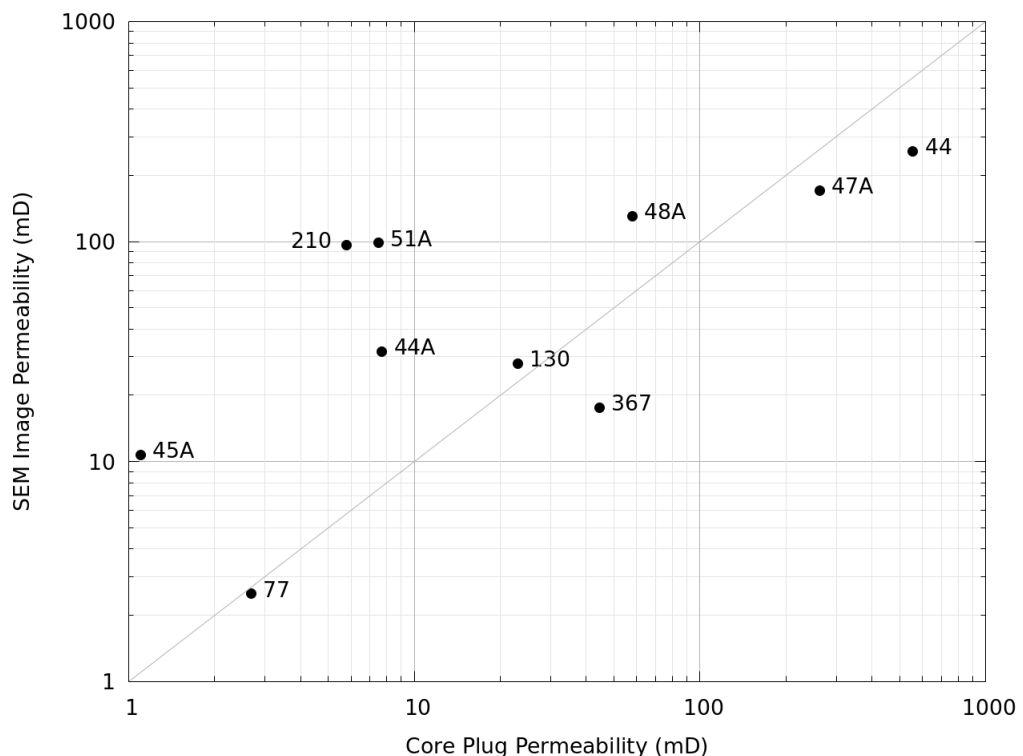
Figure 4.23: Image permeability versus measured permeability for high resolution SEM images
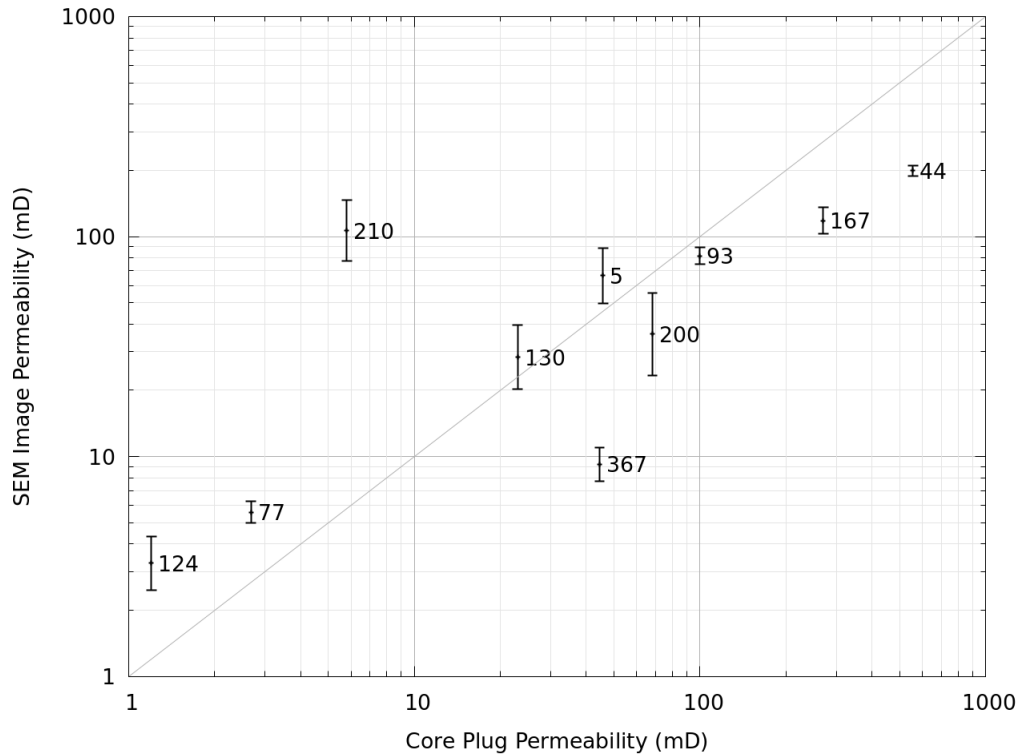
Figure 4.24: Image permeability versus measured permeability for down-scaled SEM images

μCT Images

The permeability is calculated assuming single phase incompressible laminar flow. The pore space characterisation is used to construct a network of pore elements and a single pressure solution node is assigned to each element. Two opposite faces of the model are designated the inlet and outlet with arbitrary constant pressures differing by ΔP. The other four faces of the model are no-flow boundaries.

The flow rate between two connected pore elements, i and j with pressures P_i and P_j, is given by:

$$Q_{ij} = \frac{g_{ij}(P_i - P_j)}{\mu} \tag{4.30}$$

where g_{ij} is the hydraulic conductance between the two elements, given by:

$$g_{ij} = \frac{g_i g_j}{g_i + g_j} \tag{4.31}$$

The hydraulic conductance, g_i, of a single element connection is given by

Valvatne and Blunt (2004). For near circular elements ($G_i \geqslant 0.07$):

$$g_i = \frac{r_i^4}{32 G_i L_i} \tag{4.32}$$

For near square elements ($0.0481 < G_i < 0.07$):

$$g_i = \frac{2 r_i^4}{57 G_i L_i} \tag{4.33}$$

For other elements ($G_i \leqslant 0.0481$):

$$g_i = \frac{3 r_i^4}{80 G_i L_i} \tag{4.34}$$

Where:

$$L_i = \frac{L_{ij} r_i}{r_i + r_j} \tag{4.35}$$

and L_{ij} is the distance between the element centres.

Imposing a volumetric balance constraint at each element implies that the sum of the flows to all its connected elements must be zero and this leads to a system of simultaneous linear equations to be solved for the pressures at each element. The system of equations is solved using a conjugate gradient algorithm with an incomplete Cholesky factorisation pre-conditioner. The total inlet (or outlet) flux, Q_T, is calculated and the permeability follows from Darcy's law:

$$k = \frac{Q_T \mu L_T}{A_T \Delta P} \tag{4.36}$$

where L_T is the total length of the model in the direction of flow and A_T is the cross-sectional area of the model perpendicular to the direction of flow.

To validate the permeability calculation, the pore space of the Finney random sphere pack and the Fontainebleau sandstone reconstruction (Section 3.4) have been characterised and the permeability calculated. The Finney sphere pack was characterised assuming 1 μm/voxel and all spheres have a radius of 25 μm.

The results are given in Table 4.13.

Bosl et al. (1998) calculated a permeability of 1693 mD for the Finney sphere pack using LBM and Mattila et al. (2016) quote a permeability of 1169 mD for the Fontainebleau sandstone reconstruction at a resolution of 3.66 μm/voxel. Note that the latter figure is for the complete reconstruction, not the a4_x0_y0_z0 subvolume used here (Hilfer et al., 2012).

Table 4.13: Calculated permeability for the Finney sphere pack and the Fontainebleau sandstone reconstruction

Volume	Permeability X-direction (mD)	Permeability Y-direction (mD)	Permeability Z-direction (mD)	Permeability Average (mD)
Sphere pack	1697	1687	1692	1692
Fontainebleau	1046	1104	1093	1081

Also, the Kozeny-Carman relation (Carman, 1956):

$$k = \frac{\phi^3}{180(1 - \phi)^2} D^2 \qquad (4.37)$$

gives a permeability of 1659 mD for the Finney sphere pack (sphere diameter D = 50 μm) and a permeability of 972 mD for the Fontainebleau sandstone assuming a mean grain diameter of 232 μm (Mattila et al., 2016).

The permeabilities of the μCT images calculated from the pore space characterisation and the network of pore elements are given in Table 4.14. For the Guillemot A samples, X-direction means along the axis of the core plug which is a direction parallel to the bedding plane, however Y- and Z-directions are arbitrary and are not necessarily parallel or perpendicular to the bedding plane. Accordingly, the X-direction might be expected to have the highest permeability but this is not the case for any of the samples. In fact, the variation between the permeability calculated in different directions increases from ±15% at high permeability to ±45% at low permeability. This suggests that the μCT volumes may not capture a representative elementary volume (REV) and this issue is most serious for plug 77.

Table 4.14: Calculated permeability for μCT volumes

Volume	Permeability X-direction (mD)	Permeability Y-direction (mD)	Permeability Z-direction (mD)	Permeability Average (mD)
Plug 44	491	572	445	503
Plug 77	2.0	5.2	3.6	3.6
Plug 130	26.6	27.7	36.0	30.1
Plug 367	56.7	50.5	96.1	67.8
Bentheimer	3980	3150	3330	3490
Gildehauser	1840	1810	1370	1670

Figure 4.25 shows a cross-plot of the calculated and measured permeability data. Despite the REV issue, there is reasonable agreement between the

average permeability from µCT imaging and the measured permeabilities.
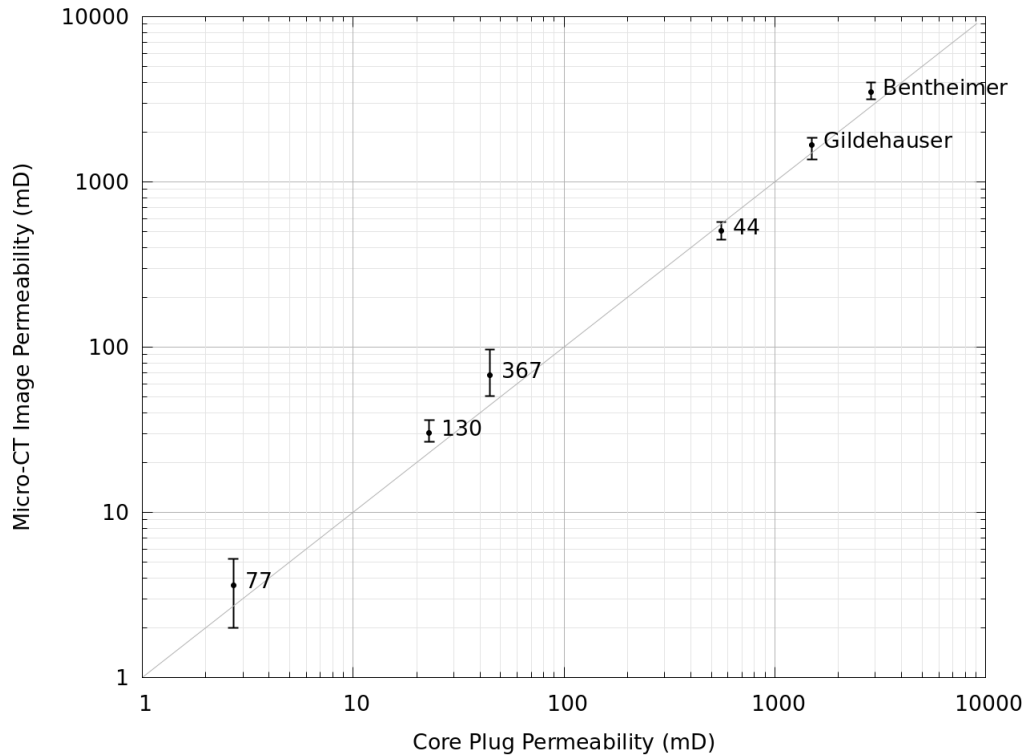
Figure 4.25: µCT image permeability versus measured permeability, error bars indicate permeability range of X, Y and Z directions

4.2.7   Formation Resistivity Factor

Here, the Formation Resistivity Factor (FRF) is examined because this is a transport property which is related to tortuosity (Paterson, 1983; Walsh and Brace, 1984):

$$F = \frac{\tau}{\phi} \tag{4.38}$$

where τ is the tortuosity of the porous medium:

$$\tau = \left(\frac{L_a}{L}\right)^2 \tag{4.39}$$

L_a is the average tortuous path length and L is the macroscopic length of the sample.

The FRF of the µCT volumes is calculated in an analogous way to the single phase permeability. The pore space is assumed to be fully saturated with a conducting brine with resistivity R_w. Fluid flow is replaced by electrical current, pressure is replaced by electric potential and Darcy's Law is replaced

by Ohm's Law. The pore space characterisation is used to construct a network of pore elements and a single solution node is assigned to each element. Two opposite faces of the model are designated the inlet and the outlet with arbitrary constant potentials differing by ΔV. The other four faces of the model are zero-current boundaries.

The electric current between two connected pore elements, i and j, with potentials V_i and V_j is given by:

$$I_{ij} = \frac{V_i - V_j}{R_i + R_j}$$ (4.40)

where R_i is the resistance of a single element connection:

$$R_i = \frac{4G_i L_i R_w}{r_i^2}$$ (4.41)

where G_i is the shape factor of element i of radius r_i and L_i is given by Equation 4.35.

Imposing electric current balance (Kirchhoff's first law) at each node leads to a system of simultaneous linear equations to be solved for the electric potential at each element. The total inlet (or outlet) current, I_T, is calculated and the FRF follows from Ohm's law:

$$F = \frac{\Delta V A_T}{I_T R_w L_T}$$ (4.42)

where L_T is the total length of the model in the direction of flow and A_T is the cross-sectional area of the model perpendicular to the direction of flow.

The FRF of the μCT volumes are shown in Table 4.15.

Table 4.15: Calculated formation resistivity factor for μCT volumes

Volume	FRF X-direction	FRF Y-direction	FRF Z-direction	FRF Average
Plug 44	10.4	10.5	11.5	10.8
Plug 77	449	229	311	330
Plug 130	72	71	57	67
Plug 367	39	48	31	39
Bentheimer	14.7	18.0	16.2	16.3
Gildehauser	14.3	14.7	19.0	16.0

Figure 4.26 shows FRF versus porosity with the μCT volumes (calculated FRF versus model porosity) and the measured data (lab measured FRF versus total helium porosity). Also shown is the straight line for a cementation

exponent $m = 1.75$ (Archie, 1942), consistent with the trend for the Guillemot A data (Figure A.4). It can be seen that most of the data lie close to this line. Although the FRF is too high in all models, in most cases this can be explained by insufficient porosity i.e. the inability of μCT to capture microporosity. Microporosity or clay-bound water can make a significant contribution to electrical conductivity and therefore its omission will significantly increase the resistivity. The μCT volumes of plug 130 and plug 77 have a more serious discrepancy as these data lie closer to $m = 2.0$ and $m = 2.2$; inconsistent with the Guillemot A cementation exponent. This suggests these volumes have excessive tortuosity and insufficient connectivity which is not entirely due to the lack of porosity.
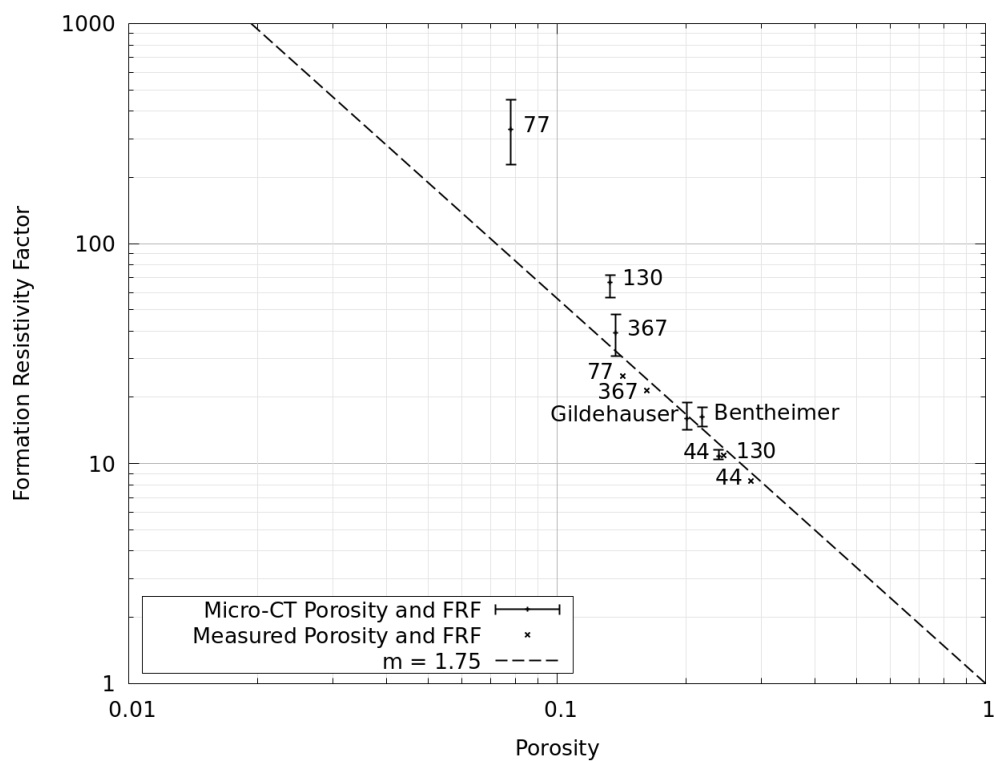
Figure 4.26: Formation resistivity factor versus porosity for μCT volumes; error bars indicate FRF range of X, Y and Z directions

4.2.8   Relative Permeability

Relative permeabilities were generated from the μCT networks using the poreflow[1] quasi-static PNM simulator described by Valvatne and Blunt (2004); Valvatne (2004).

---

[1]https://www.imperial.ac.uk/earth-science/research/research-groups/perm/research/pore-scale-modelling/software

Network nodes correspond to the model pore elements with radius, volume and shape factor as described above. Network bonds correspond the links between pore elements with radius equal to the minimum of the connected element radii and zero volume. Each bond has four lengths viz: bond length, length first node, length second node and total length. Bond length is zero, lengths first node and second node are given by Equation 4.35 and total length is the distance from node centre to node centre.

The simulation does not include any viscous or gravity effects; therefore nominal values are used for fluid densities and viscosities.

Figures 4.27, 4.28, 4.29 and 4.30 show the calculated drainage relative permeabilities where the receding contact angle is assumed to be 0°. Some variation between X, Y and Z directions is apparent, particularly for plug samples 77 and 367 suggesting that these µCT volumes do not capture REVs. This result is consistent with the single phase permeability and FRF results which showed the greatest variation between X, Y and Z directions for plug samples 77 and 367.

Comparing plugs 44 and 130; the water relative permeabilities are quite similar whereas the oil relative permeability is significantly lower for plug 130. In general, the relative permeabilities for plugs 77 and 130 are lower which is a consequence of the poorer connectivity (Figure 4.22) and lower porosity of these samples.

For plugs 77, 130 and 367, the variation in relative permeability between different directions makes it difficult to judge whether the differences between samples are significant.

Relative permeabilities, including a comparison of modelling results with measured SCAL data, are addressed further in Chapter 5.

4.3   Effect of Image Resolution

4.3.1   Methodology

The comparison between 2D and 3D pore space characterisation is complicated by the differences in resolution between the SEM and µCT images. To explore this further, the high resolution SEM images have been upscaled and the pore space characterisation repeated. Two upscalings were performed: 2×2 pixels and 4×4 pixels.
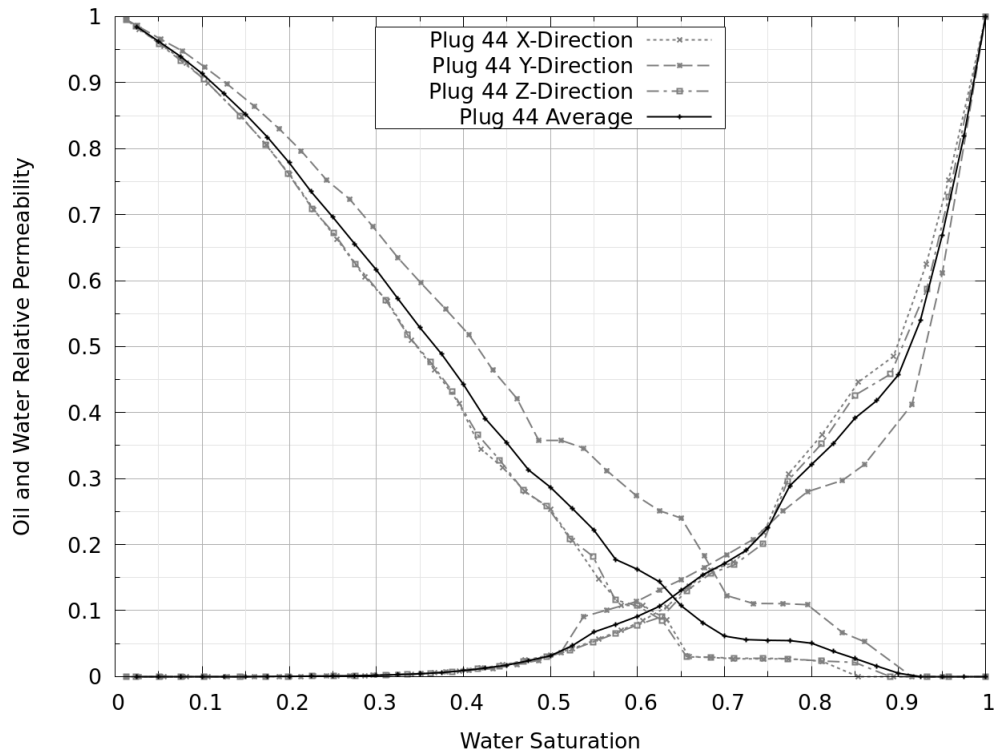
Figure 4.27: Drainage oil-water relative permeability from Guillemot A plug 44 µCT network
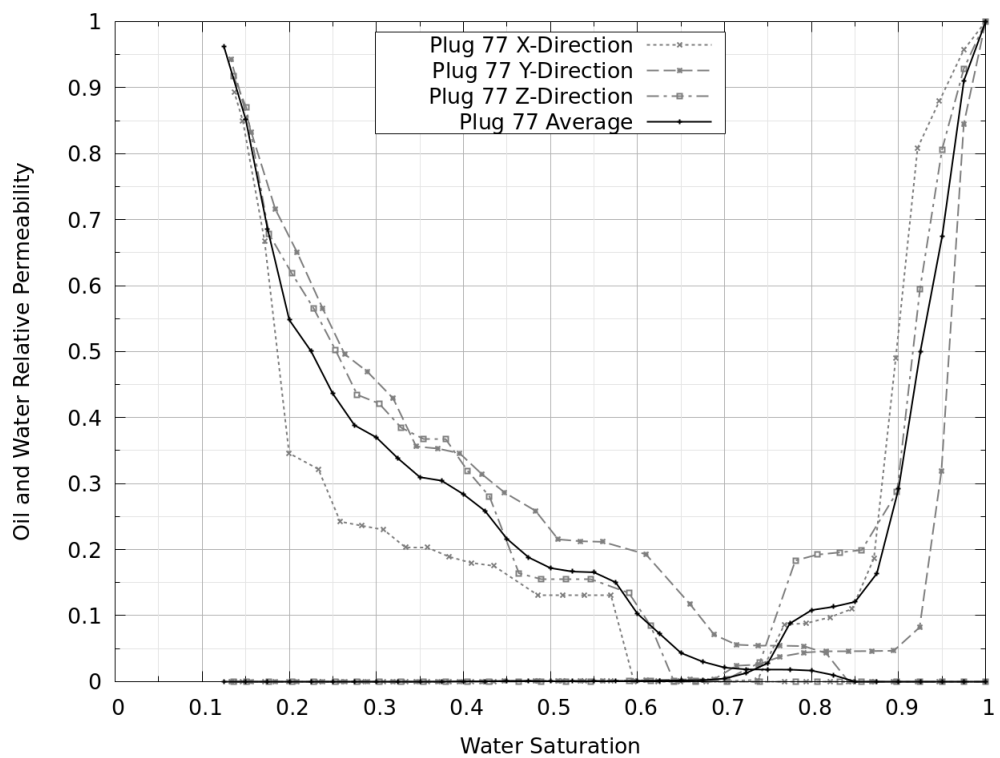
Figure 4.28: Drainage oil-water relative permeability from Guillemot A plug 77 µCT network
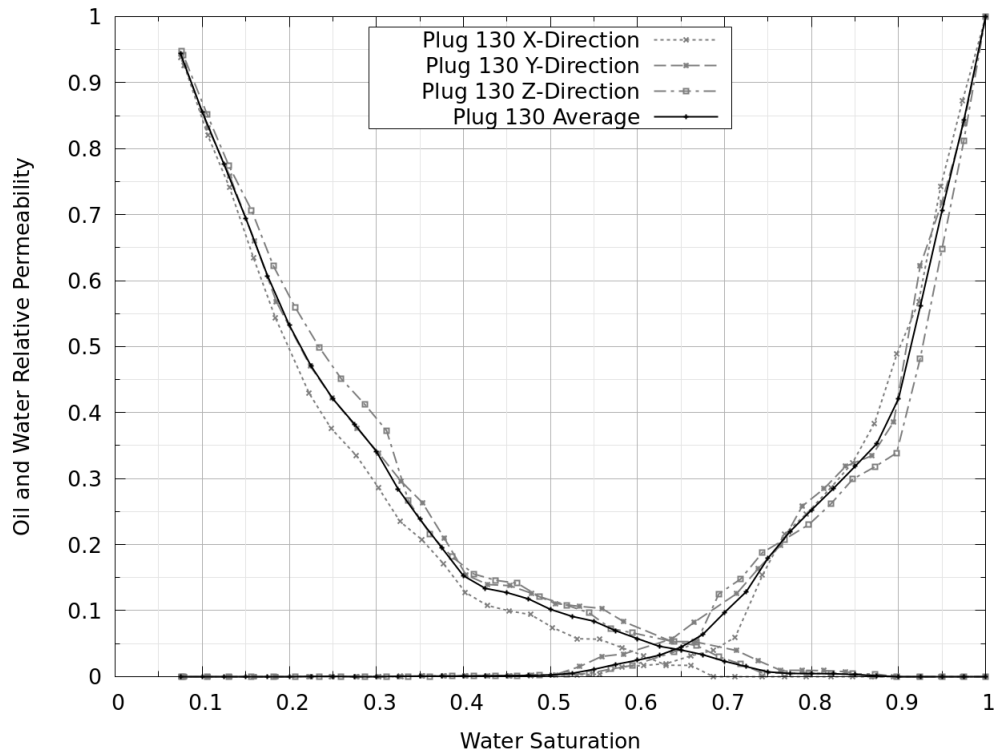
Figure 4.29: Drainage oil-water relative permeability from Guillemot A plug 130 μCT network
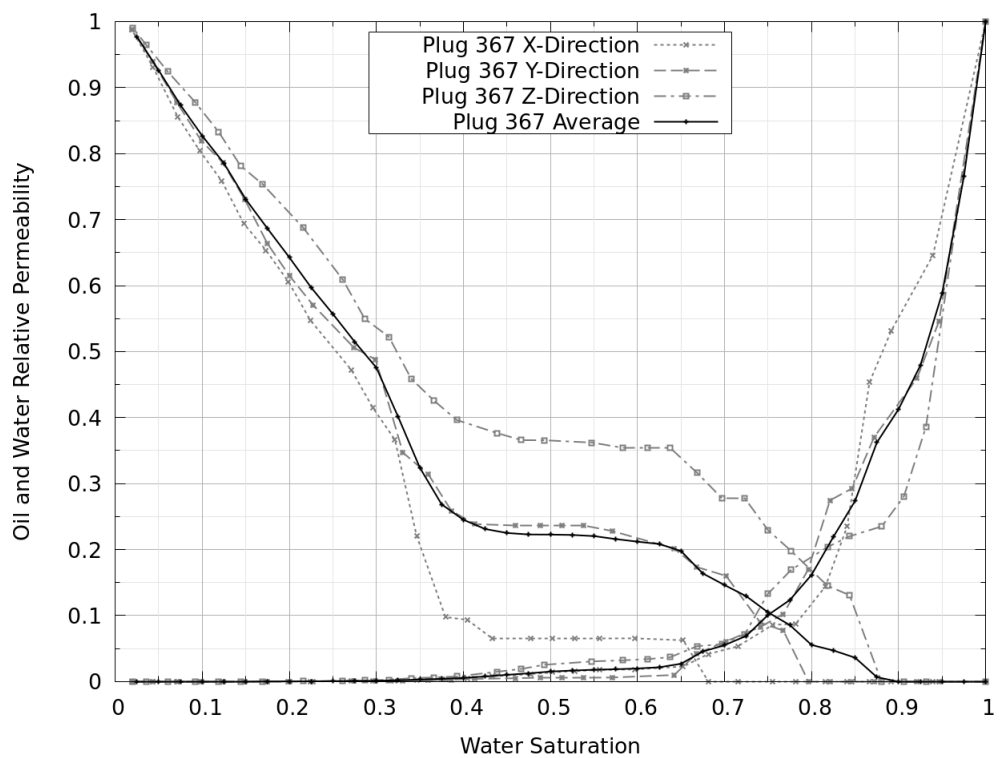
Figure 4.30: Drainage oil-water relative permeability from Guillemot A plug 367 μCT network

The upscaling generates a coarser image with poorer resolution by computing the average greyscale value for each 2×2 or 4×4 group of pixels. This is followed by an identical image processing sequence i.e. the same segmentation threshold (Section 3.2.2), the same declustering filter (Section 3.2.3) and the pore space characterisation algorithm.

4.3.2 Pore Size

Figure 4.31 shows the cumulative pore size distribution for the original and upscaled SEM images of Guillemot A plug 367. Also shown is the empirical model (Equation 4.19) with parameter r_0 increased consistent with the image resolution and parameter r_1 adjusted to fit the data with no change to α and η. It is clear that the main effect of changing image resolution is to increase the lower limit of the distribution, r_0.
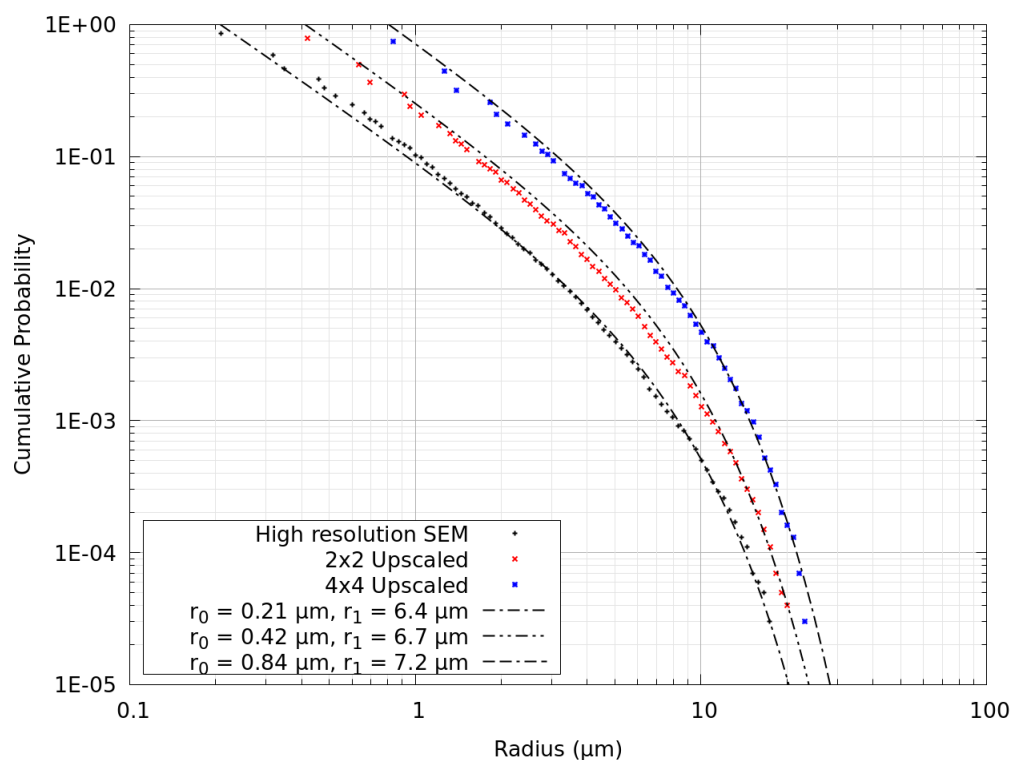
Figure 4.31: Cumulative pore size distribution for Guillemot A plug 367; high resolution and upscaled SEM

In addition, there is a small increase on the parameter r_1 for the coarser images i.e. an extension of the distribution to larger radii. This is caused by some pore elements which are over-estimated by the upscaled images because convex protruding corners of the rock matrix tend to be smoothed out. An example is shown in Figure 4.32, where the radius of the largest

pore element is increased by about 8%. This effect suggests that single phase permeability would be over-estimated by low resolution images.
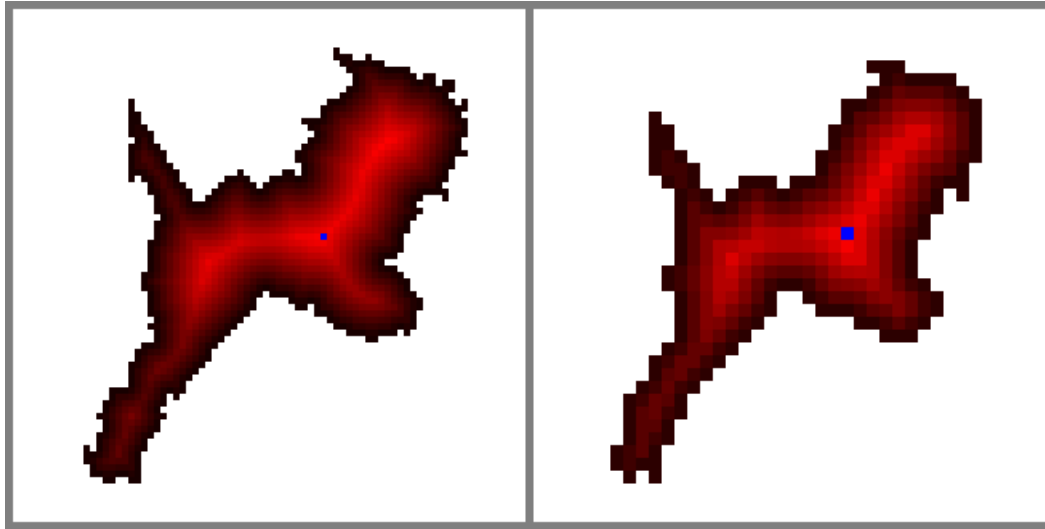
Figure 4.32: Segmented SEM image showing EDM in red shading; left: original image, the blue pixel has a Euclidean distance of 10.77 pixels = 1.83 µm, right: upscaled image, the blue pixel has a Euclidean distance of 5.83 pixels = 1.98 µm

4.3.3 Pore Coordination

Figure 4.33 shows the mean coordination number for the original and upscaled SEM images of plug 367. Also shown is the empirical power-law relationship between the mean coordination number and pore radius (Equation 4.23) with $r_{z,mean}$ increased for the upscaled images and β adjusted to fit the data.

It is reasonable that $r_{z,mean}$ and $r_{z,sd}$ are dependent on image resolution because higher resolution information will reveal smaller pores which may be connected to any larger pores; therefore the coordination number of large pores will be a function of the size of the smallest resolvable pore. This effect tends to reduce the connectivity for low resolution images and therefore the single phase permeability would be under-estimated, in contrast to the pore size effect above.
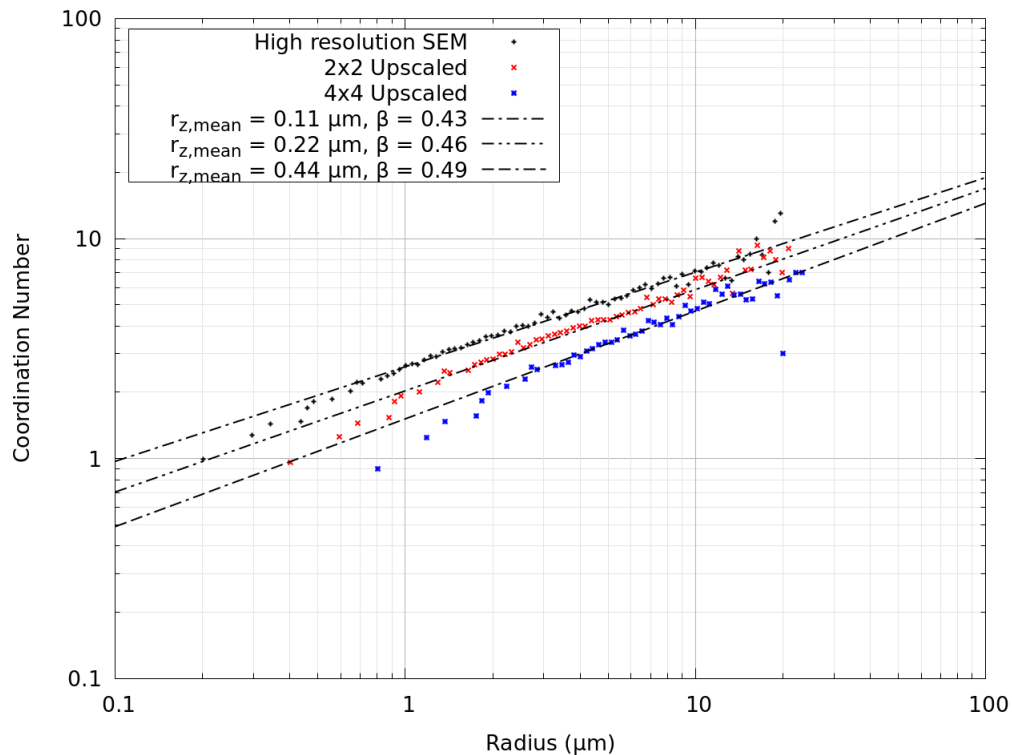
Figure 4.33: Mean coordination number as a function of element radius for Guillemot A plug 367; high resolution and upscaled SEM

4.4 Comparison Between 2D and 3D Characterisation

4.4.1 Methodology

To address the multiscale problem, it is desirable to determine 3D pore space geometry and topology from 2D data such as SEM imaging. To see if this is possible, the 2D and 3D pore space characterisations of the same sample need to be compared. Some conclusions can already be drawn from the comparison between SEM image characterisation and µCT volume characterisation as discussed above. However there are some artefacts due to the differences in image resolution. A more valid comparison can be obtained by comparing 3D characterisation with the characterisation of a representative 2D section extracted from the same volume. More specifically, a series of 2D sections in various directions are extracted and the combined statistics for all 2D analyses compared with the 3D statistics. The approach is similar to that of Rabbani et al. (2016) except the methodology in Section 3.1 is used to characterise the pore space rather than a watershed algorithm.

Here, 20 random sections in each direction (XY, XZ and YZ planes) are extracted from each 3D volume, making a total of 60 2D sections. A total of eight 3D volumes have been used, viz: the four µCT volumes from Guillemot A samples plus the four additional volumes described in Section 3.4.

4.4.2 Pore Size

The pore size distributions from the random 2D sections are compared with complete 3D volume distributions in Figures 4.34 and 4.35. In all cases, the 3D pore size distributions are narrower and have a steeper slope or larger scaling index α. This is consistent with the comparison between SEM and µCT pore size distributions (Figure 4.10).
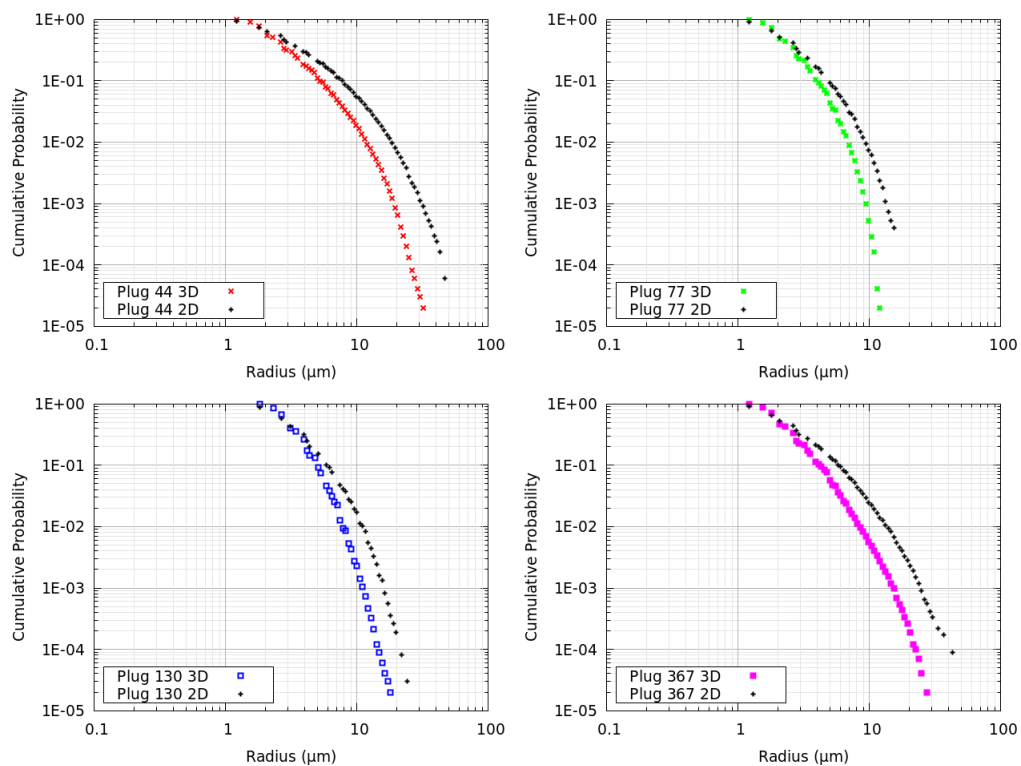
Figure 4.34: Comparison between 3D and 2D pore size distribution from Guillemot A µCT volumes

The 2D pore size distributions have been fitted to a cumulative probability distribution function (Equation 4.19) using the same procedure as before. Again, the parameter r_0 is fixed from the image resolution and η is fixed at the value $\eta = 2$. The Finney sphere pack was not included in this process because it has a narrow pore size distribution which is not well represented by this type of function. The results for the Guillemot A and the other three µCT volumes are given in Table 4.16.
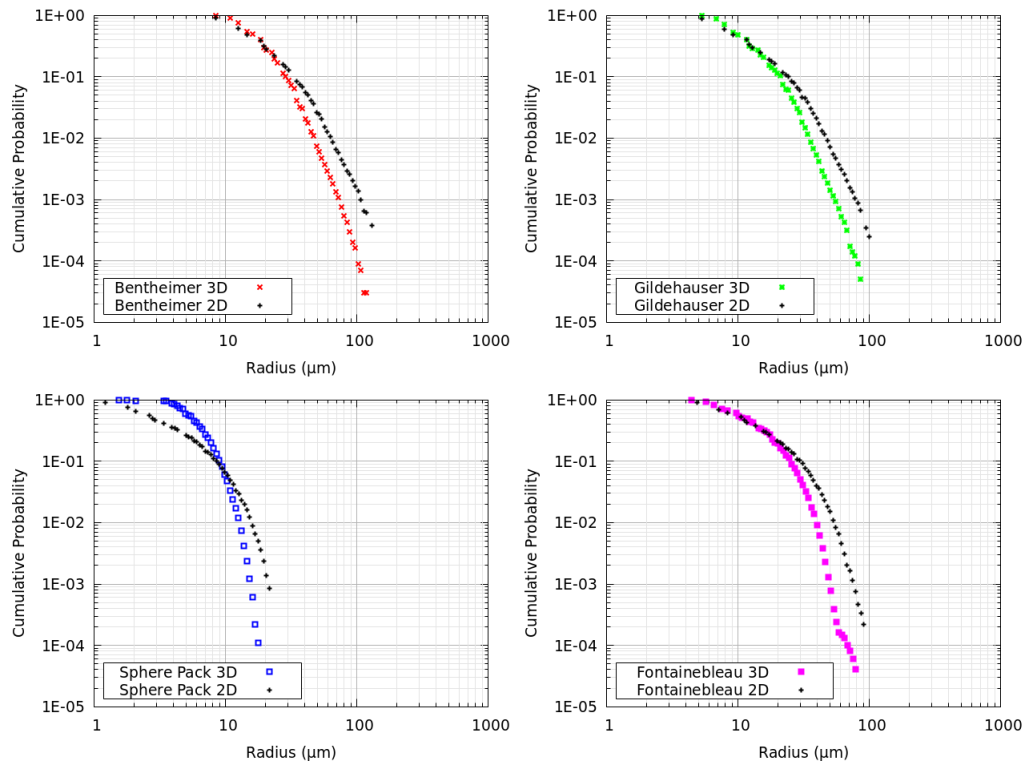
Figure 4.35: Comparison between 3D and 2D pore size distribution from additional volumes

Table 4.16: 3D and 2D pore size distribution parameters

Volume	3D r_0 μm	3D r_1 μm	3D α	3D η	2D r_0 μm	2D r_1 μm	2D α	2D η
Plug 44	1.7	14.5	2.06	2.0	1.7	21.4	1.57	2.0
Plug 77	1.7	4.4	1.60	2.0	1.7	7.7	1.83	2.0
Plug 130	2.6	7.9	3.21	2.0	2.6	10.4	2.40	2.0
Plug 367	1.7	14.6	2.64	2.0	1.7	22.4	2.04	2.0
Bentheimer	11.9	54.0	2.68	2.0	11.9	76.0	2.25	2.0
Gildehauser	7.5	40.7	2.41	2.0	7.5	53.4	2.00	2.0
Fontainebleau	6.2	27.2	1.29	2.0	6.2	37.6	1.13	2.0

The r_1 parameters are plotted in Figure 4.36. This shows that the r_1 parameters of the 3D distributions are close to 70% of the parameter of the 2D distributions. Plug 77 does not lie on the same trend most likely because the mean pore size is smaller and accordingly there is more difficulty in fitting the distribution model and more uncertainty in the fitted parameters.

The α parameters are plotted in Figure 4.37. The α parameters from the 3D distributions are around 25% greater that those from the 2D distributions. Plug 77 is also off-trend for the same reason as above.
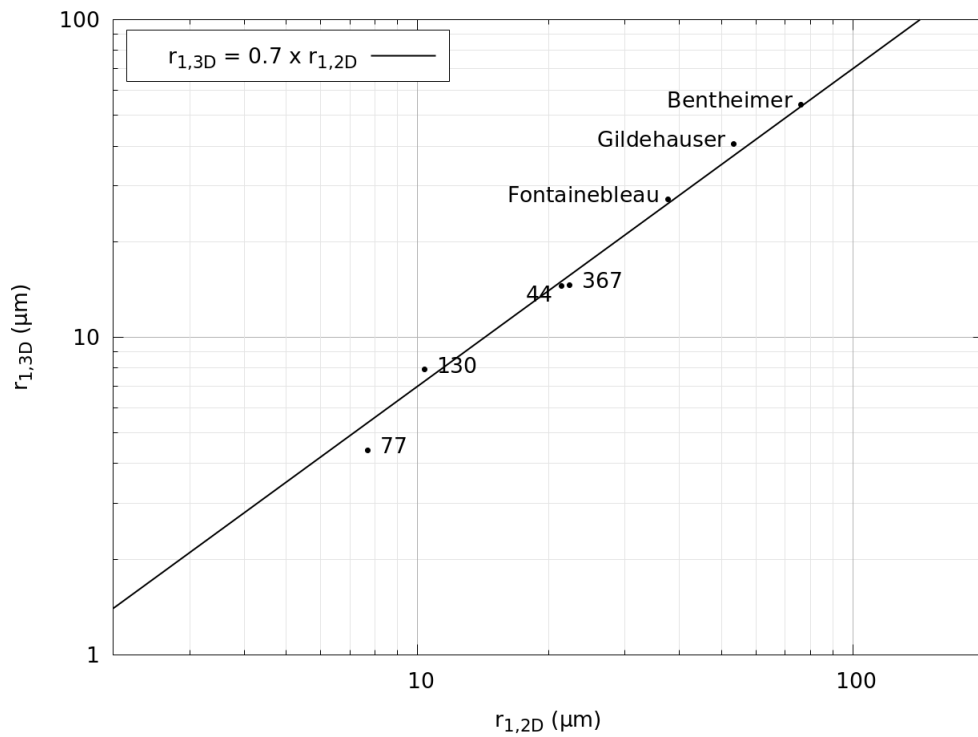
Figure 4.36: 3D versus 2D r_1 pore size distribution parameters
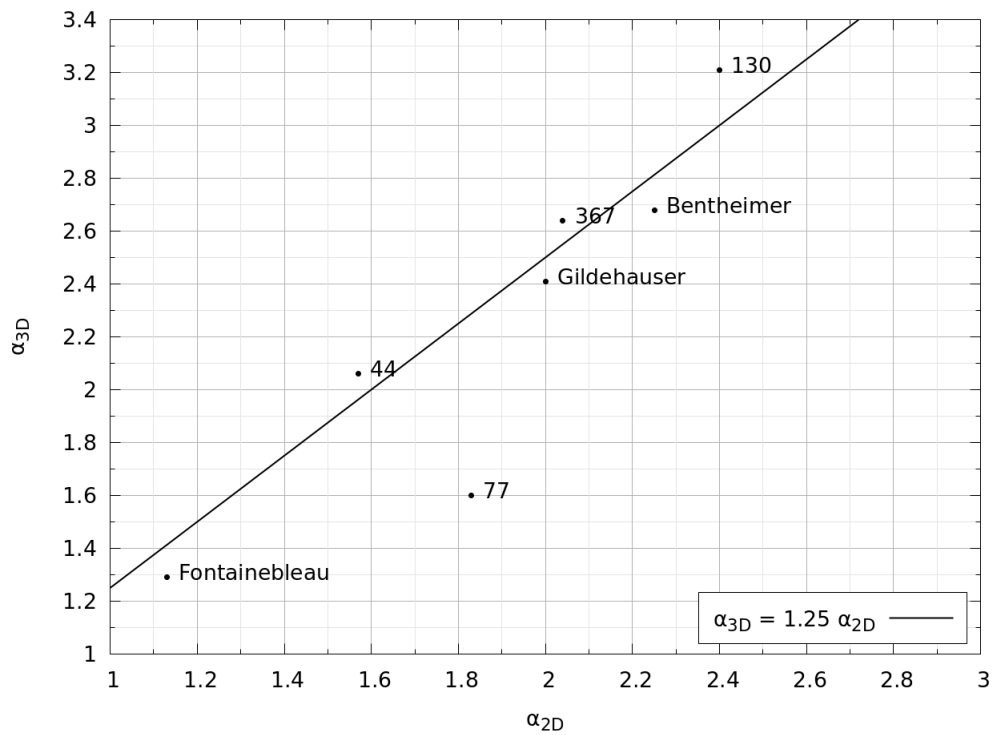
Figure 4.37: 3D versus 2D α pore size distribution parameters

4.4.3 Pore Coordination

Figure 4.38 shows the mean coordination numbers from 3D volumes and the random 2D sections as a function of element radius. At small radii, the mean 3D coordination number is about twice the 2D coordination number and at large radii the difference increases to about four times.

Figures 4.39 and 4.40 show cross-plots of the 3D and 2D mean coordination numbers. Each point plotted here is the mean 3D coordination number for a given radius versus the mean 2D coordination number at the same radius.

The data suggest a relationship of the form:

$$Z_{mean,3D}(r) \propto Z_{mean,2D}(r)^{3/2} \tag{4.43}$$

where the proportionality factor varies from circa 1 to 2 depending on the complexity of the pore space. The Guillemot A μCT volumes have complex pore architecture and a proportionality factor of circa 1.9. The Bentheimer, Gildehauser and Fontainebleau sandstones are less complex and have a proportionality factor of circa 1.6. The Finney sphere pack has a much simpler pore architecture with a narrower pore size distribution and the proportionality factor is about 1.

The standard deviation (SD) of the 3D and 2D coordination numbers is shown in Figure 4.41. The data suggest a relationship of the form:

$$Z_{sd,3D}(r) \propto Z_{sd,2D}(r)^{3/2} \tag{4.44}$$

where the proportionality factor is approximately 2.5.

Using a proportionality factor of 1.9 in relation 4.43 and substituting twice from Equation 4.23 gives:

$$\left(\frac{r}{r_{z,mean,3D}}\right)^{\beta_{3D}} = 1.9 \left(\frac{r}{r_{z,mean,2D}}\right)^{3\beta_{2D}/2} \tag{4.45}$$

Where the subscripts $2D$ and $3D$ distinguish 2D and 3D characterisation parameters. Now, relation 4.43 indicates that:

$$\beta_{3D} = \frac{3}{2}\beta_{2D} \tag{4.46}$$

so re-arranging Equation 4.45 gives:

$$r_{z,mean,3D} = 1.9^{-1/\beta_{3D}} r_{z,mean,2D} \tag{4.47}$$

and similarly for the coordination number SD:

$$r_{z,sd,3D} = 2.5^{-1/\beta_{3D}} r_{z,sd,2D} \qquad (4.48)$$

Equations 4.46, 4.47 and 4.48 can be used to estimate the 3D coordination number distribution parameters from 2D characterisation data.
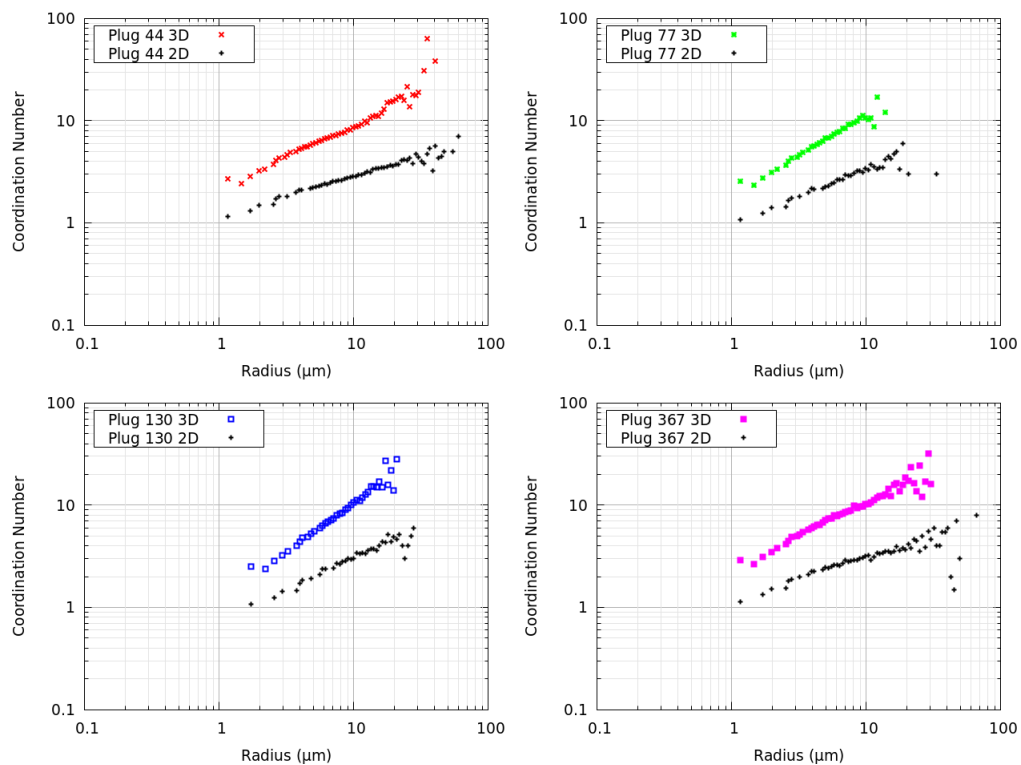
Figure 4.38: Comparison between 3D and 2D mean coordination numbers

4.4.4   Shape Factor

A comparison between the mean shape factor from 3D volumes and the random 2D sections as a function of element radius is given in Figure 4.42. This shows that the 2D characterisation slightly over-estimates the shape factor in some cases, particularly at small radii. However, as discussed in Section 4.2.3, the minor shape factor variation with pore size could be explained by image resolution effects; therefore it is reasonable to assume the shape factor is independent of element radius. The standard deviation of the shape factor (Figure 4.43) shows similar behaviour and therefore we concluded it is feasible to infer the 3D shape factor distribution from 2D imaging data.
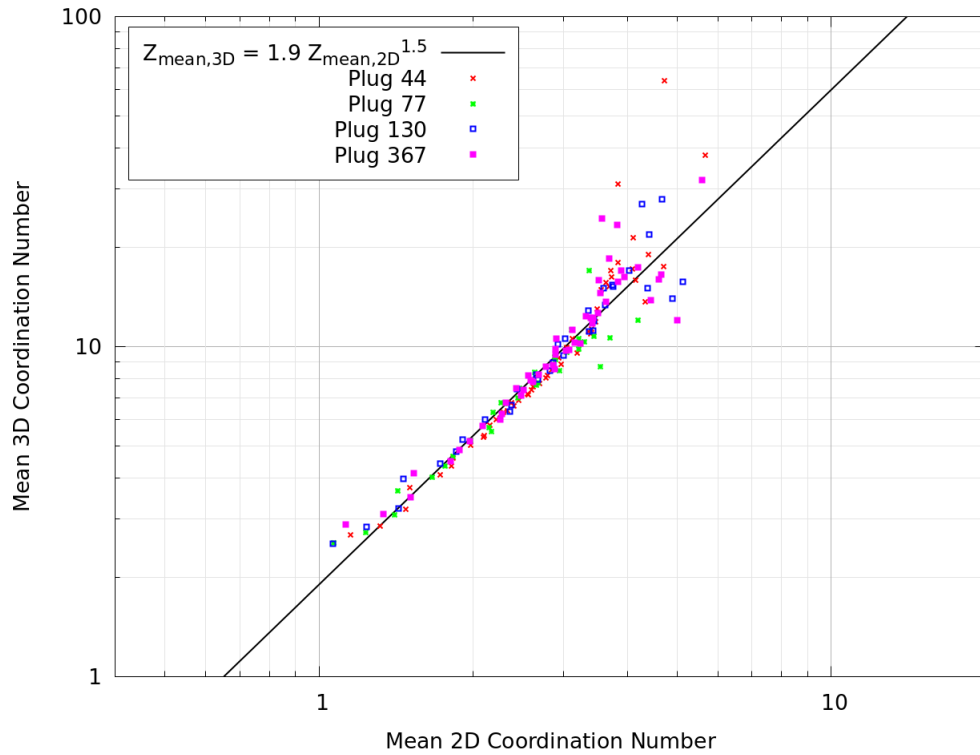
Figure 4.39: Mean 3D coordination number versus mean 2D coordination number from μCT volumes
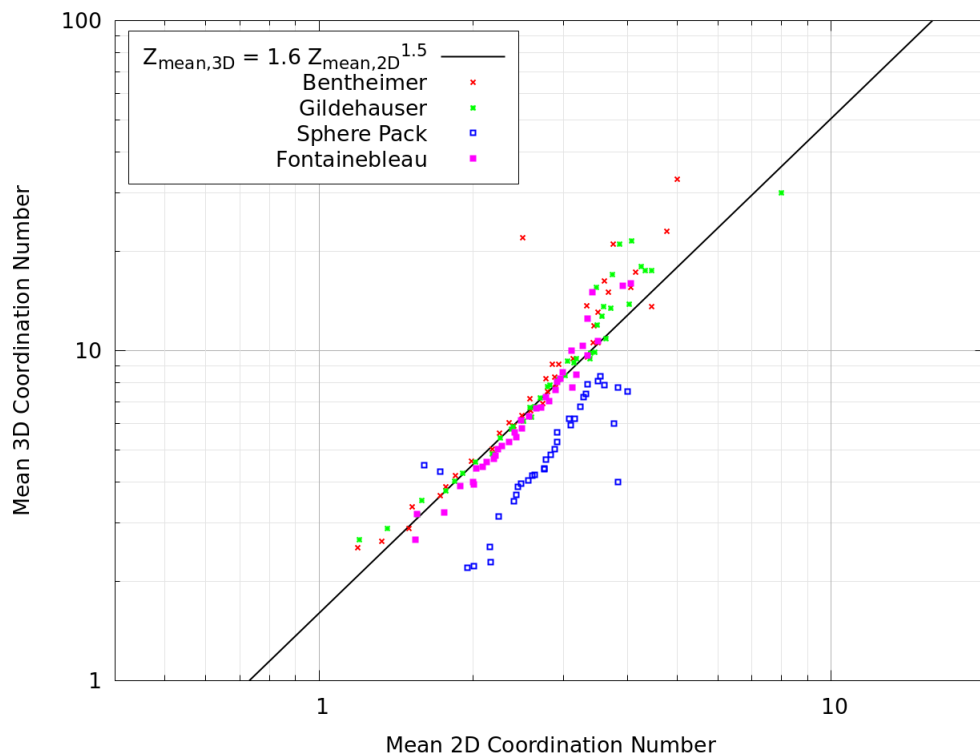
Figure 4.40: Mean 3D coordination number versus mean 2D coordination number from additional volumes
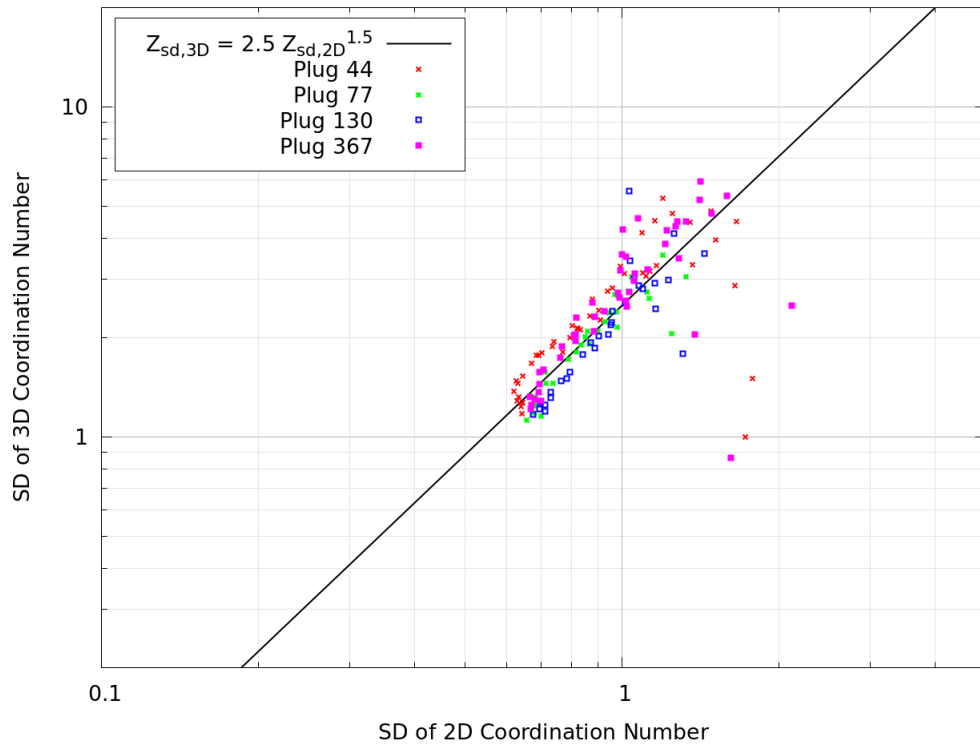
Figure 4.41: SD of 3D coordination number versus SD of 2D coordination number from µCT volumes
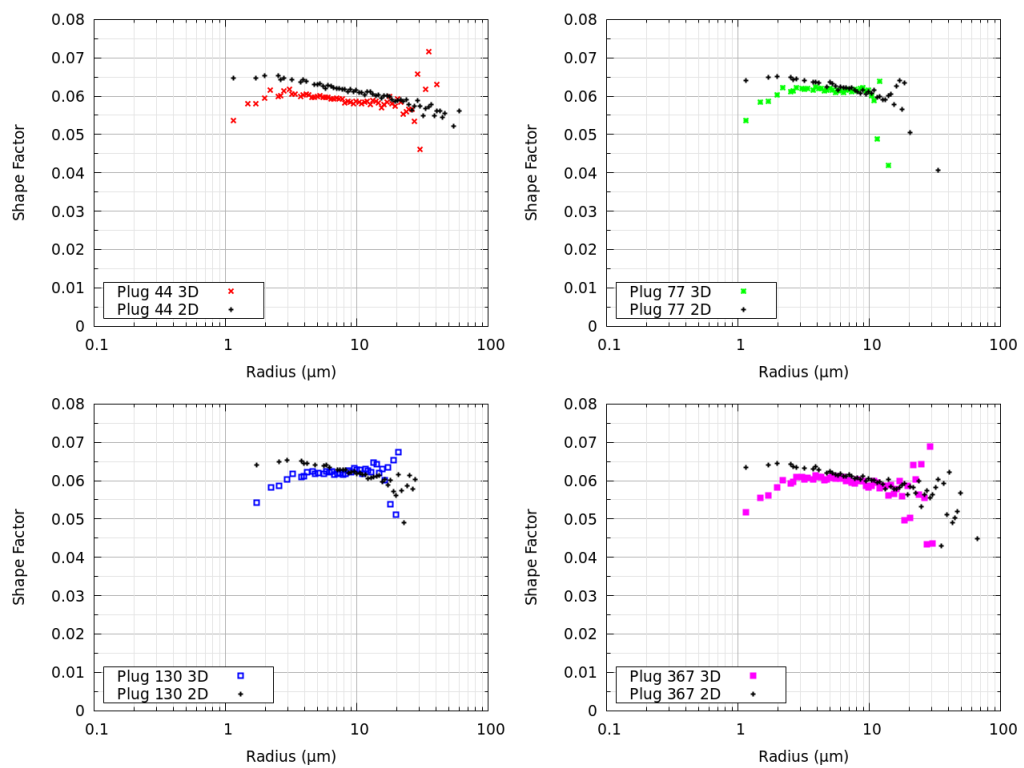
Figure 4.42: Mean 3D and 2D shape factor from µCT volumes
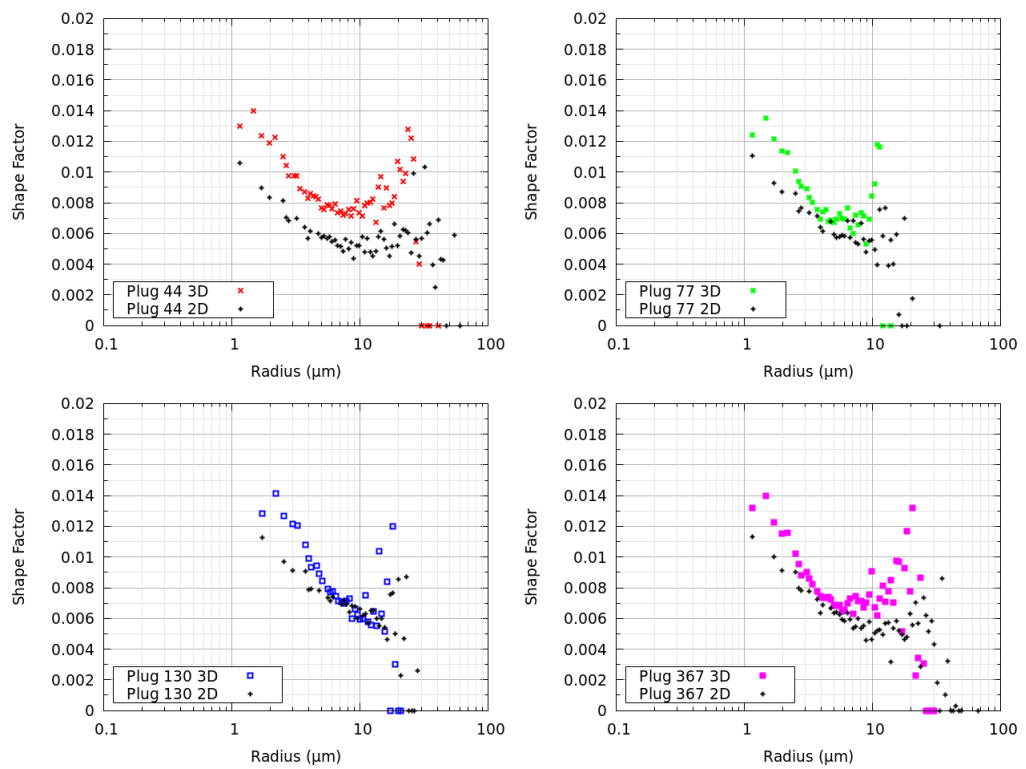
Figure 4.43: Standard deviation of the 3D and 2D shape factor from µCT volumes

Chapter 5

Pore Network Modelling

"I have never tried that before, so I think I should definitely be able to do that."

— Astrid Lindgren, Pippi Longstocking

5.1 Summary

This chapter describes a stochastic algorithm to generate pore networks based on pore space characterisation information from imaging. The motivation for this approach is firstly to overcome the trade-off between resolution and field of view in µCT imaging by incorporating information on small pores below 2 µm from SEM imaging and secondly to generate multiple stochastic networks with larger domain sizes to capture appropriate REVs.

The stochastic pore network algorithm is described followed by the results from applying the algorithm in 2D and 3D. Stochastically generated 3D networks are used to calculate single phase and multiphase flow properties for comparison with the networks extracted from µCT images and measured SCAL data. The results show that stochastic pore networks match the range of single phase permeability in the Guillemot A field indicating that the algorithm reproduces realistic 3D connectivity of the pore space. The relative permeability calculated from stochastic pore networks has good agreement with relative permeability from higher porosity µCT networks but poorer agreement for the lower porosity and more poorly connected samples.

5.2 Methodology

5.2.1 Stochastic Lattice

The stochastic algorithm incorporates some ideas from the weighted planar stochastic lattice (WPSL) (Hassan et al., 2010). A WPSL is a space filling cellular structure on a 2D rectangular domain. A WPSL is constructed by starting with a rectangle and applying a generator that randomly divides it into four smaller rectangles. The generator is then repeatedly applied to one of the available rectangles chosen preferentially with respect to their areas.

The general WPSL can result in many rectangles with extreme aspect ratios, therefore we consider the more specialised construction which is limited to squares. The starting point is a square domain and on each iteration one square is chosen at random and divided it into four equal squares (Figure 5.1). It is clear that the number of squares increases by 3 on each iteration. After any number of iterations a network can be constructed from the dual graph i.e. by placing a node at the centre of each square and constructing a bond between any two squares which share a common border.

Figure 5.2 shows an example after 1000 iterations.

In this work, the WPSL is extended from 2D squares to 3D cubes in a straightforward way.

The WPSL construction has three key properties that make is attractive as a model for porous media. Firstly, large cubes naturally have high coordination numbers and small cubes have low coordination numbers. Secondly, the coordination numbers of the general WPSL obey a power law distribution $\Pr(Z) \propto Z^{-\gamma}$ with $\gamma = 5.66$ (Hassan et al., 2010). Thirdly, the recursive process naturally fits into multiscale pore structure hierarchies. These, properties of the WPSL are similar to but do not perfectly match pore space characterisation information; therefore a further modification is considered where not all cubes are occupied by nodes. This enables the coordination number of pore elements and the resulting pore space connectivity to be modified to match characterisation data from real rock samples.

To generate a network representing the pore space of a real complex sandstone, it is necessary to honour some key information: the pore element size distribution and the connectivity information in the form of the pore element coordination number distribution as a function of pore radius.
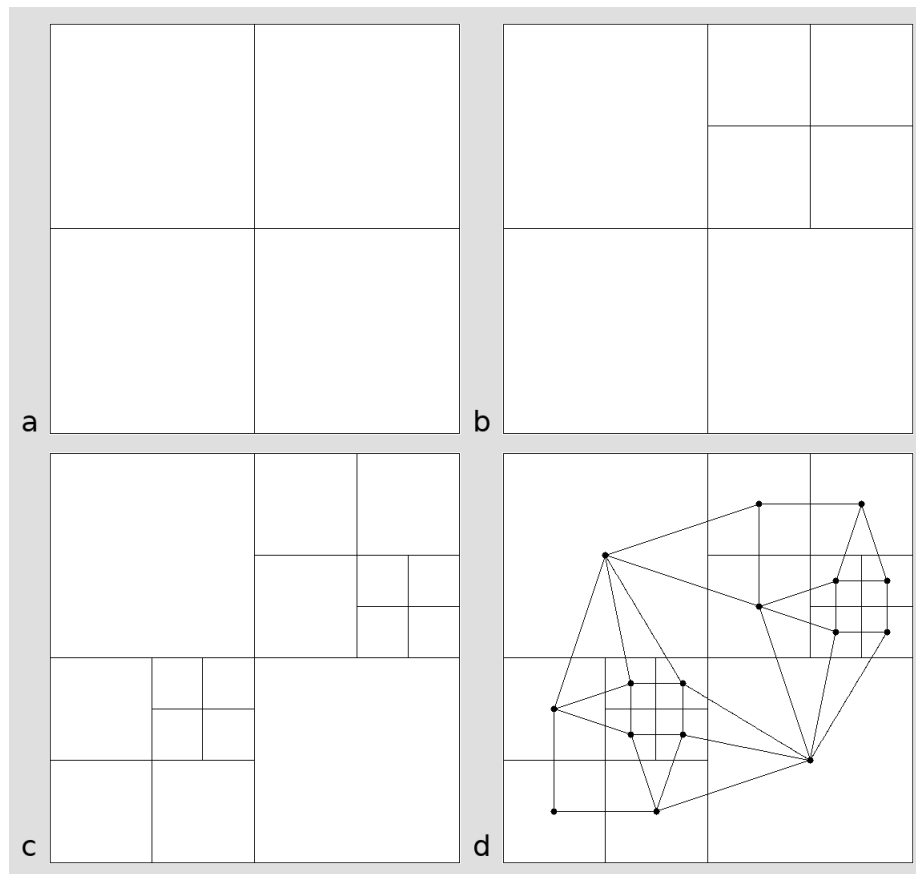
Figure 5.1: WPSL limited to square structures: (a) domain divided into four squares (b) after the second iteration (c) after five iterations (d) the resulting network or dual graph

From 2D and 3D image analysis, the links between elements have been determined (Section 4.1.3) and the radius of a link is defined as the minimum of the two connected element radii.

The connectivity function (Equation 4.20) is important for controlling multiphase flow behaviour and therefore it should be honoured in the stochastic network. The definition of link radius means that a link with radius greater than r will always be connected to two elements with radii greater than r. This means that a straightforward algorithm can be constructed that honours the connectivity function as well as the coordination number information.

The algorithm starts with domain of a given size and inserts a given total number of elements into the domain. If the objective is to generate a stochastic reproduction of a given µCT volume, then the total number of elements is known. Alternatively, the number of elements can be determined from a target porosity because the distribution of element radii is given and the volume of an element is proportional to the cube of its radius. If an
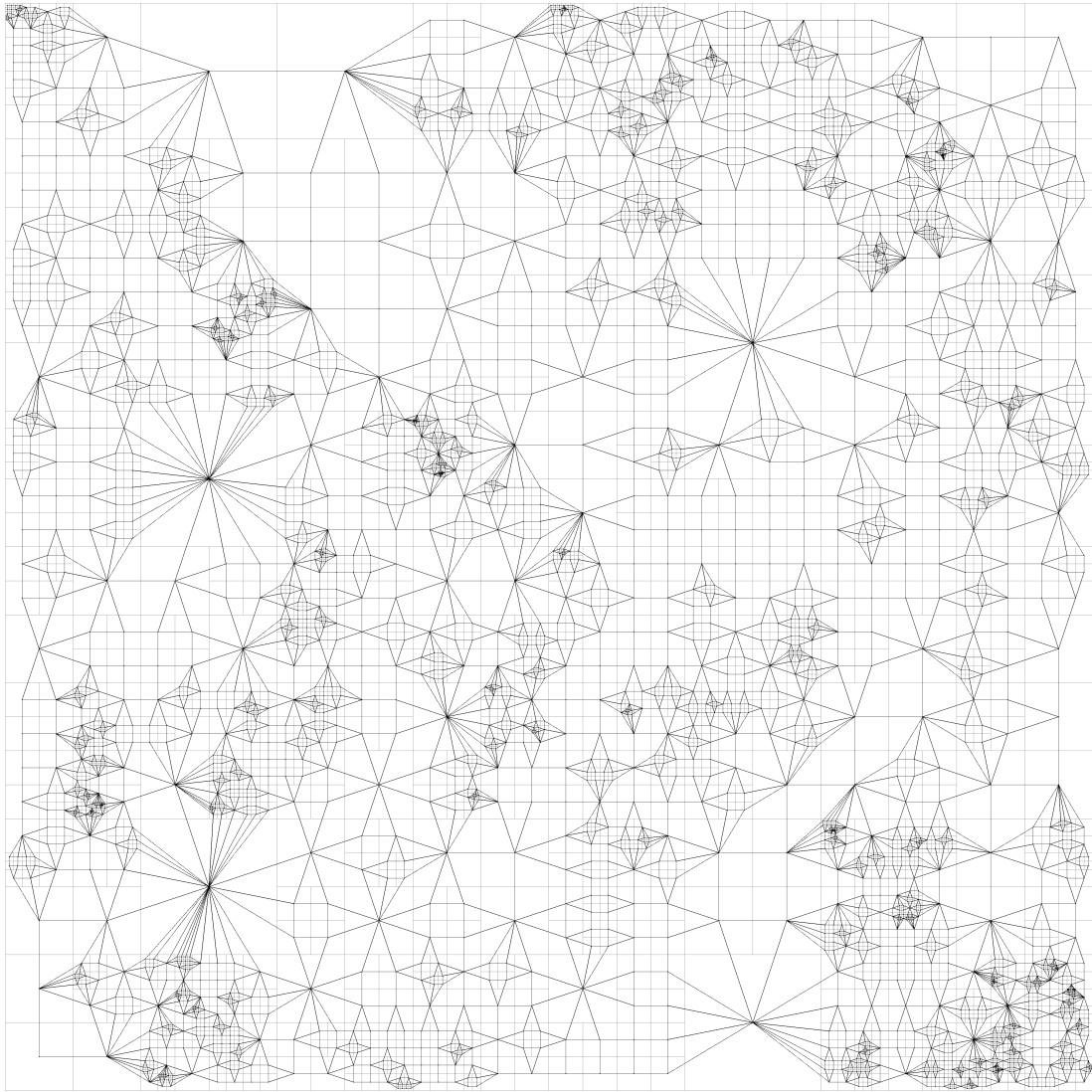
Figure 5.2: WPSL with square structures after 1000 iterations

element is modelled as an irregular base right prism of length $2r$ (Section 4.1.4), where r is the inscribed radius of the cross-sectional area A, then:

$$V = 2Ar \tag{5.1}$$

For circular, square and triangular cross-sections:

$$A = \frac{r^2}{4G} \tag{5.2}$$

where G is the shape factor (Equation 4.10), and it follows that:

$$V = \frac{r^3}{2G} \tag{5.3}$$

The algorithm takes some ideas from published stochastic pore network

generation algorithms. In particular, we start at the largest pore size and progressively add elements into the network in a way that honours the connectivity function as per Jiang et al. (2012). We also assign a target co-ordination number to each element and decrement the target each time the element is linked to another one as per Idowu and Blunt (2008). Unlike these existing algorithms, we do not assume that pore elements are uniformly randomly distributed in space. As shown below, this is a poor assumption for complex sandstones because the pore elements are actually spatially clustered. This is a key motivation for using the WPSL construction because the WPSL enables smaller pore elements to be located in the proximity of existing (larger) pore elements and linked to them in a systematic way.

5.2.2 Algorithm

The complete stochastic algorithm in 2D (3D) is as follows:

1. Start with a rectangular (cuboid) domain of given size.

2. Calculate the minimum and maximum pore radii of interest, r_{min} and r_{max}.

3. Let the given total number of elements be $N_{e,total}$. Construct an array of $N_{e,total}$ elements where each element has a radius sampled from the distribution and a target coordination number Z_i sampled from the distribution based on its radius.

4. Calculate the total number of links $N_{l,total} = \frac{1}{2} \sum_{i=1}^{N_{e,total}} Z_i$ and construct an array of links where each link has a radius sampled from the distribution.

5. Divide the domain into squares (cubes) of side length $L_{max} > r_{max}$.

6. Set $r = r_{max}$.

7. Calculate the number of elements and links with radii between r and $r/2$; $N_e = N_e(r/2) - N_e(r)$ and $N_l = N_l(r/2) - N_l(r)$.

8. Position the N_e elements and N_l links in order of radius, starting with the largest. For each element, if there exists a link with a radius smaller than the element but larger than the next smallest element then position this element at the centre of a square (cube) adjoining an

existing (i.e. larger) element chosen at random and assign the link to the pair of elements. If there is no such link, then position the element at the centre of a randomly selected square (cube) that does not adjoin any existing elements.

9. In the previous step, when an element needs to be positioned adjoining an existing one, the probability of choosing each one of the existing elements is proportional to its target coordination number and when a link is created, the target coordination numbers of the two linked elements are each decreased by one.

10. If the target coordination number of an element is reduced to zero then place an exclusion zone in the lattice sites around that element to prevent any further elements being located close to it.

11. Divide each of the unoccupied squares (cubes) into four (eight) equal squares (cubes).

12. Set $r = r/2$.

13. If $r > r_{min}$ go to step 7.

A 2D illustration of the procedure is shown in Figure 5.3.
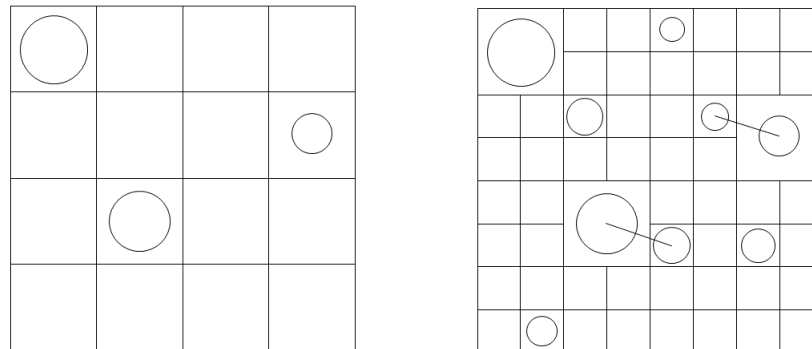
Figure 5.3: Stochastic pore network generation in 2D: (a) divide the domain into squares and insert elements with radii between r_{max} and $r_{max}/2$ (b) divide each of the unoccupied squares into four and insert elements with radii between $r_{max}/2$ and $r_{max}/4$, if there exists a link with radius larger than the next smallest element, then position the element adjacent to an existing one and link them

In step 5 it is necessary to choose a value of L_{max}. It should be clear that the ratio L_{max}/r_{max} controls the average overlap or gap between element radii. The maximum overlap is $2r_{max} - L_{max}$ which occurs when the largest

pore elements on step 8 are being positioned and the maximum gap is $L_{max} - 2\frac{r_{max}}{2}$ which occurs when the smallest pore elements on step 8 are being positioned. Similar to the pore space characterisation (Section 4.1.3), a reasonable approach is to equate the maximum gap to the maximum overlap as this will tend to make the gaps and overlaps small. It follows that:

$$2r_{max} - L_{max} = L_{max} - r_{max} \tag{5.4}$$

or

$$L_{max} = \frac{3}{2}r_{max} \tag{5.5}$$

Hence, Equation 5.5 is used to define L_{max} in step 5.

The algorithm proceeds by dividing the pore size distribution into a geometric progression with a common ratio of a half. At each iteration elements of appropriate radii are inserted into cubes of similar size. Step 8 tries to insert N_e elements and N_l links at each iteration. For the first few iterations, generally N_e is much greater than N_l and therefore most large elements are positioned in randomly selected cubes not adjoining existing elements. These elements will be linked to smaller elements in later iterations. In the last few iterations, generally N_e is less than N_l and therefore most small elements are positioned adjacent to existing (larger) elements and linked to them. If an element is, by chance, positioned adjacent to two or more existing elements then links are inserted between all the adjacent elements. In all cases the largest radius unassigned link is used. This could result in the link array being exhausted before the element array. However, the algorithm tends to result in the element and link arrays being assigned in parallel which ensures that the connectivity function is honoured. Throughout the process, the radius of the largest unassigned element is close to the radius of the largest unassigned link. This means that the radius of a link will be close to the minimum of the two connected element radii, which is consistent with the definition of the link radius given above. If the connectivity is high enough, then there could be two or more links with a radius smaller than a given element but larger than the next smallest element. In this case, the algorithm relies on elements, by chance, being positioned adjacent to two or more existing elements. This is not guaranteed in all cases and therefore it is possible for the element array to be exhausted before the link array.

If the link array is exhausted before the element array then the last elements are positioned without linking to any existing elements. If the element array

is exhausted before the link array then the last links are discarded.

Step 9 tries to honour the coordination number distribution as a function of element radius. Generally, the target coordination numbers are satisfied. If an element has its target coordination number reduced to zero then it cannot be chosen as an adjoining element in step 8. However it could, by chance be linked to a new element which is positioned randomly or positioned adjacent to another element. To prevent this, step 10 places an exclusion zone around elements which have their target coordination number reduced to zero. The effect of this is that elements inserted later will tend to be positioned closer to other elements which have unsatisfied coordination.

The process is complete when the minimum radius is reached and the element array is exhausted. At this point, not all lattice sites will be occupied and there may be some elements which are not connected to any others.

In summary, the inputs to the stochastic lattice algorithm are as follows:

- size of the domain,

- total number of elements or target porosity,

- pore element radius distribution,

- pore link radius distribution,

- mean and standard deviation of the coordination number as a function of element radius,

- pore element shape factor distribution.

The link radius is defined as the minimum of the two connected element radii, consistent with the pore space characterisation (Section 4.2.2). The algorithm inputs enable the total number of pore element links to be calculated and the connectivity function can be honoured (Equation 4.21).

In the algorithm, the pore element shape factors are assigned by sampling from a supplied distribution and the shape factor is assumed to be uncorrelated with all other parameters.

5.3   2D Modelling Results

To illustrate the algorithm, 2D networks were generated for comparison with SEM images. The networks represent the pore space of Guillemot A plug 130 and Vanguard plug 51A from the Carl Zeiss GeminiSEM 300 images (Section 3.2). The key inputs for this process are the parameterised pore element radius distributions (Table 4.5), the mean and standard deviation of the coordination number as a function of radius (Figure 4.18 and Table 4.10) and the shape factor distributions (Figure 4.20). Lastly, a rectangular domain is defined the same size as the source SEM image and the total number of pore elements is the same number as identified from the SEM image.
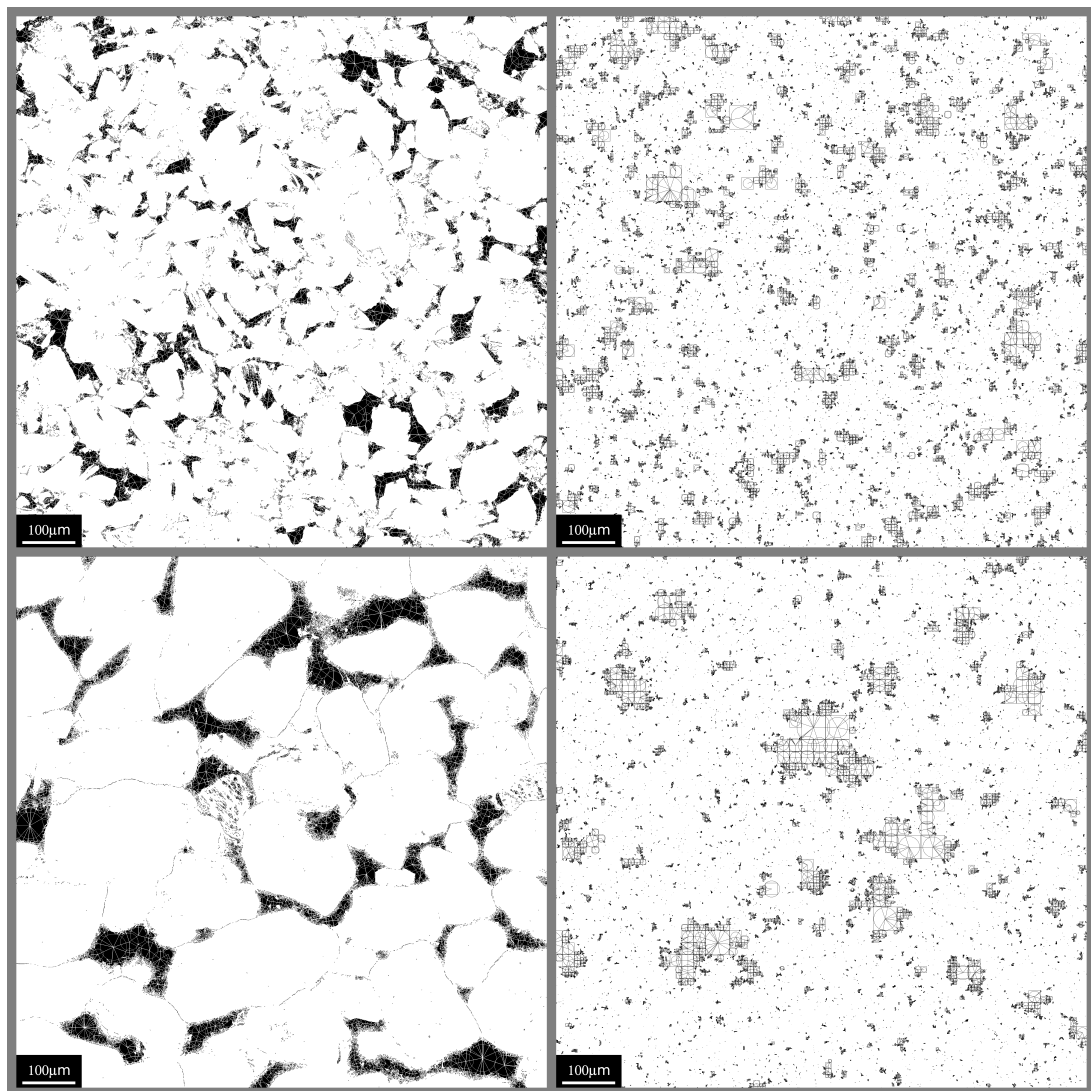
Figure 5.4: Comparison of 2D stochastic pore networks and pore element discretisation of SEM images: plug 130 (top) and plug 51A (bottom)

Figure 5.4 compares extracts of the 2D stochastic networks and the pore element discretisation of the SEM images on the same scale.

Key statistics from the stochastic networks have been analysed in comparison the pore element networks extracted from SEM.

Firstly, Figure 5.5 compares the frequency distribution of coordination numbers for plugs 130 and 51A. There is a good match with data from the SEM images. This is not surprising because the stochastic algorithm uses the element radius distribution and the mean coordination number as a function of element radius; therefore the frequency distribution of coordination numbers should be reproduced.
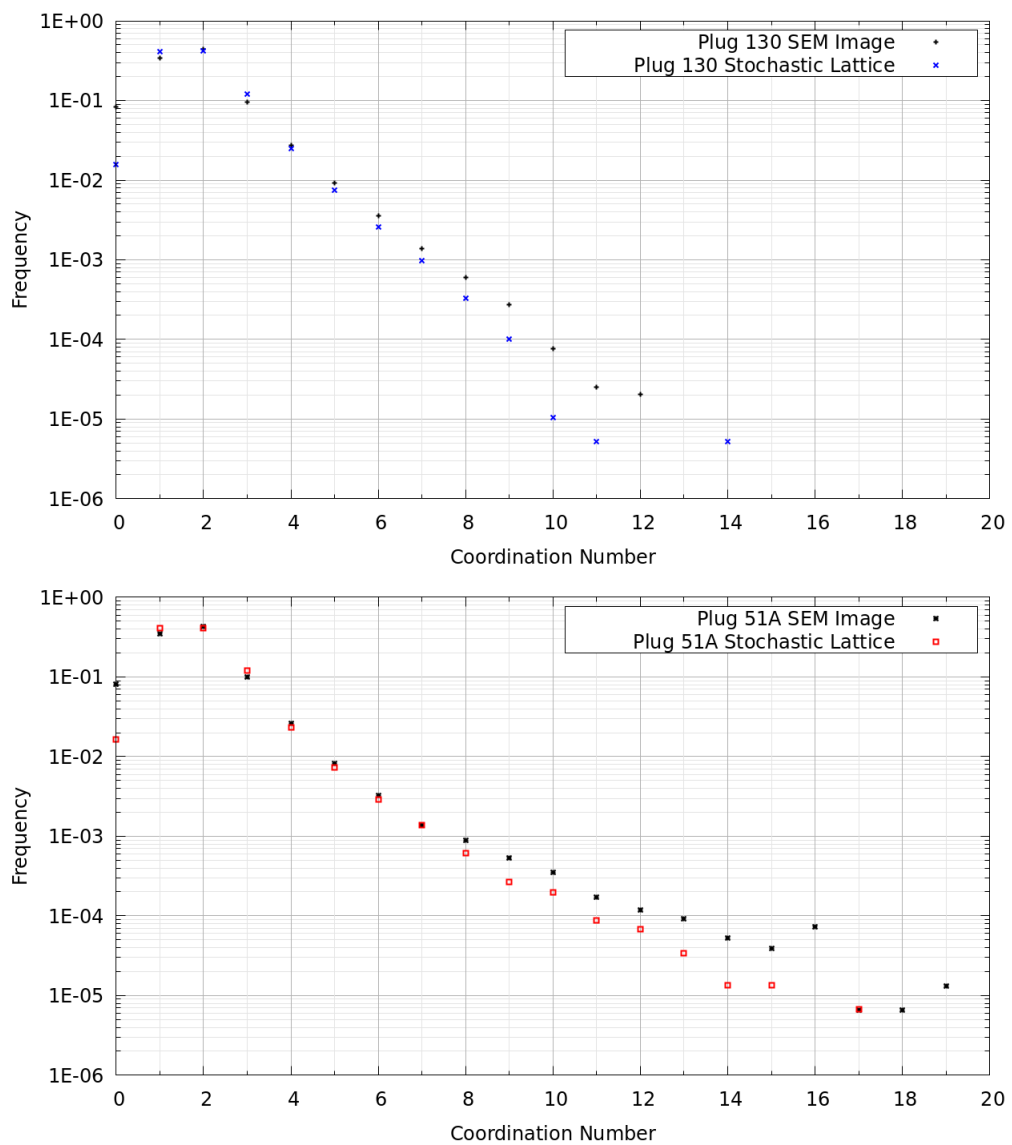
Figure 5.5: Coordination number frequency distribution, comparison between stochastic lattice network and SEM image network for plugs 130 and 51A

Secondly, it is desirable to analyse a measure of network connectivity. As the networks are 2D and the mean coordination number is around 2, there is no large scale connectivity. However, smaller scale connectivity is determined by the clustering of elements. As a proxy for connectivity, Figure 5.6 shows the number of element clusters of a given size as a function of the cluster size. This shows a power law behaviour with a scaling exponent of about 2. The stochastic network shows a discrepancy for very small cluster sizes, in particular there are more isolated elements (cluster size = 1) in the stochastic network. Otherwise, the stochastic network agrees well with the SEM image analysis.
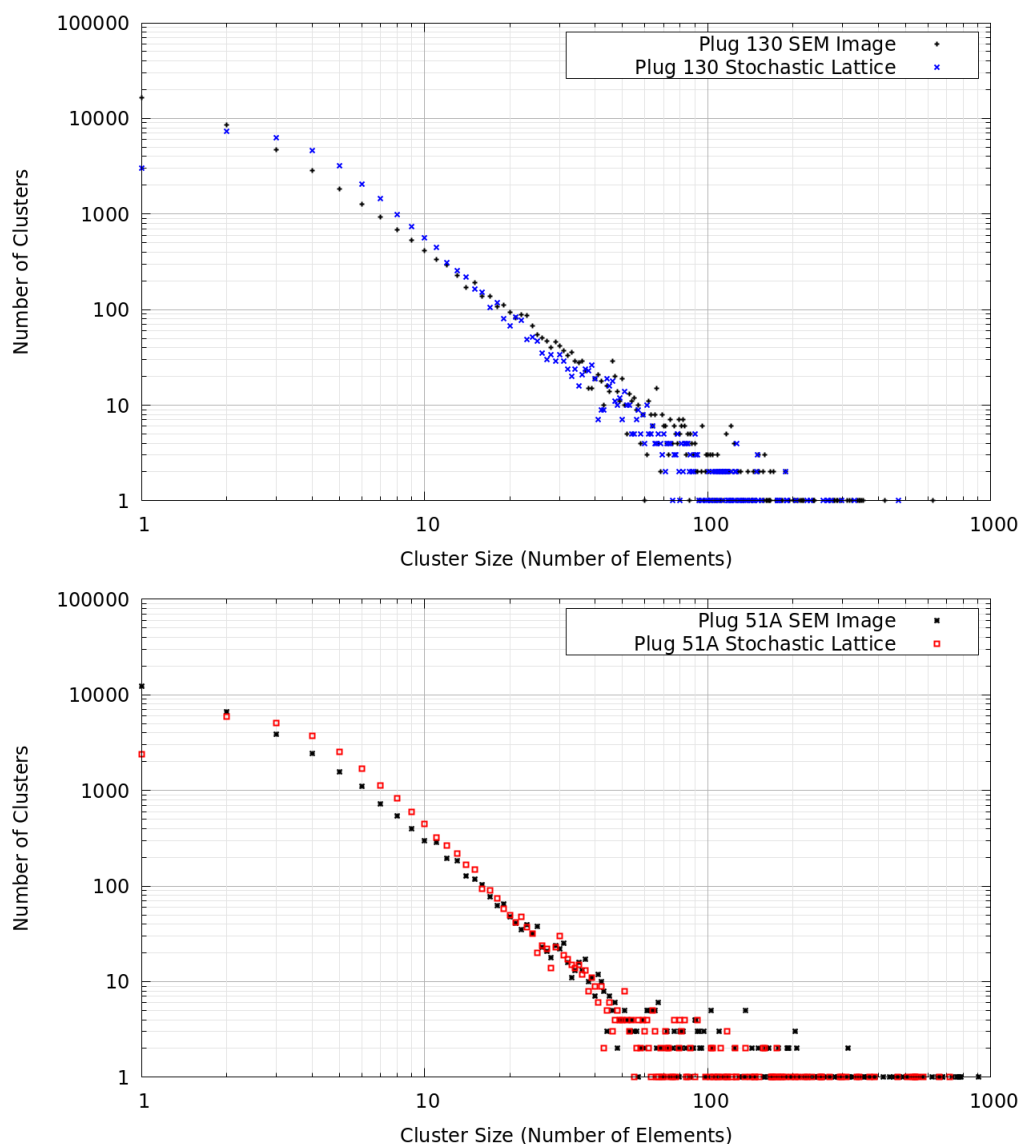
Figure 5.6: Element cluster analysis, comparison between stochastic lattice network and SEM image network for plugs 130 and 51A

Finally, the spatial distribution of pore elements is examined. The domain

is divided into square tiles or subregions such that the average number of elements per subregion is 5. Then the actual number of element in each subregion is counted and plot is made of the number of subregions containing a given number of elements (Figure 5.7). If the elements were uniformly randomly distributed, then this should be very close to a Poisson distribution with a mean of 5. Previous stochastic pore network algorithms presented by Idowu and Blunt (2008) and Jiang et al. (2012) assume that network nodes are uniformly randomly distributed in space, however Figure 5.7 shows that this is not a good assumption for complex sandstones. In particular, the number of subregions which contain zero elements is about 100 times larger than would be expected if the elements were uniformly randomly distributed. The stochastic algorithm achieves a much more realistic spatial distribution of pore elements.

5.4   3D Modelling

5.4.1   Model Construction

In 3D, a cuboid domain is used rather than a 2D rectangular domain.

To demonstrate the stochastic network algorithm in 3D, four models were generated to reproduce the Guillemot A µCT networks. As for the 2D stochastic networks, the key inputs for this process are the pore element radius distributions, the mean and standard deviation of the coordination number as a function of radius and the shape factor distributions.

The input parameters for these models are identical to the pore space characterisation for each µCT volume, as described in Chapter 4 and summarised in Table 5.1. The pore link radius distribution is assumed to be defined by Equation 4.19 with parameter r_1 equal to 75% of the value from the pore element radius distribution (Section 4.2.2). All of these models have a domain size of 800 µm × 800 µm × 800 µm.

In addition to networks representing specific µCT volumes, a suite of models were generated representing the range of pore size and pore connectivity observed in Guillemot A and Vanguard from the µCT and SEM image analysis. The parameters for these models are shown in Table 5.2. The ranges given in the table are not intended to be absolute minimum and maximum from the available data, rather they are intended to represent reasonable sensitivity ranges for illustrative purposes.
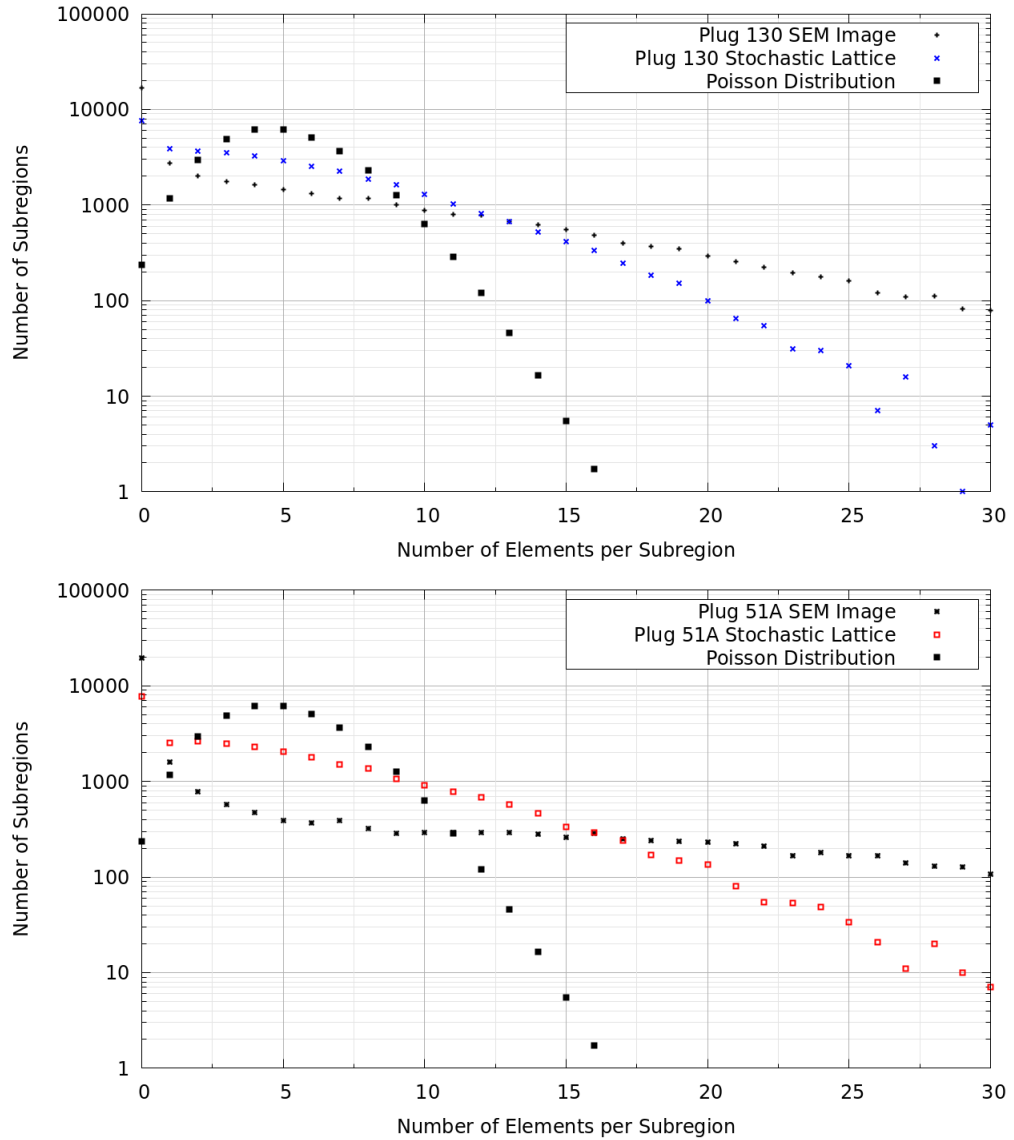
Figure 5.7: Spatial distribution of elements, comparison between stochastic lattice network and SEM image network for plugs 130 and 51A

Table 5.1: Summary of µCT pore space characterisation parameters

Parameter	Units	Plug 44	Plug 77	Plug 130	Plug 367
Porosity	-	23.8%	7.8%	13.3%	13.7%
r_0	µm	1.7	1.7	2.6	1.7
r_1	µm	14.5	4.4	7.9	14.6
α	-	2.06	1.60	3.21	2.64
η	-	2.0	2.0	2.0	2.0
β	-	0.56	0.77	0.95	0.63
$r_{z,mean}$	µm	0.213	0.413	0.845	0.227
$r_{z,sd}$	µm	1.92	2.40	3.68	1.70

The pore radius distribution parameter r_0 is somewhat arbitrary but, as

Table 5.2: 3D stochastic pore network model parameters

Parameter	Units	Minimum	Maximum
Porosity	-	10%	30%
r_0	μm	0.4	1.6
r_1	μm	5.0	15.0
α	-	1.8	3.0
η	-	2.0	2.0
β	-	0.6	0.8
$r_{z,mean}$	μm	0.08	0.32
$r_{z,sd}$	μm	0.38	1.54

discussed in Section 3.1, the smallest pore radius containing hydrocarbons is around 0.1 μm. The μCT data have a maximum resolution of 1.0 μm and the SEM data have a maximum resolution of 0.17 μm; therefore a range was defined to demonstrate the effect of extending the pore size distribution below μCT resolution towards the maximum SEM resolution.

The pore size distribution parameter r_1 was selected from the high resolution SEM data (Table 4.1) taking into account the 70% scale factor observed from 2D to 3D (Section 4.4.2). Similarly, the range of the parameter α was selected from the μCT data (Table 4.6) and the SEM data (Table 4.5) taking into account the factor of 1.25 observed from 2D to 3D characterisation (Section 4.4.2). Parameter η was fixed at $\eta = 2$ consistent with the characterisation of the μCT data (Section 4.2.1).

The mean and SD of the coordination number as a function of pore element radius were defined from Equations 4.23 and 4.24. The parameter β was selected from the μCT data (Table 4.11) and the SEM data (Tables 4.9 and 4.10) considering the factor of $3/2$ between 2D and 3D characterisation as shown in Equation 4.43. The parameter $r_{z,mean}$ was obtained from Equation 4.47 assuming that the 2D parameter is half the value of r_0 as discussed in Section 4.2.2. The parameter $r_{z,sd}$ was obtained from Equation 4.25 on the basis that the SD coordination number is one third of the mean (Section 4.2.2).

The majority of models have $r_0 = 0.8$ μm and a domain size of 800 μm × 800 μm × 800 μm. The models with $r_0 = 0.4$ μm have a smaller domain in order to limit the total number of pore elements and the corresponding computational demands. The number of model elements was determined from a set of target porosities as a function of the pore size distribution and the model domain size. Table 5.3 shows the number of pore elements in the models with $r_0 = 0.8$ μm.

Table 5.3: Stochastic pore network models: number of pore elements as a function of target porosity and pore size distribution

Porosity	$r_1 =$ 5 µm	$r_1 =$ 10 µm	$r_1 =$ 15 µm
10%	1213000	688000	510000
15%	1820000	1032000	768000
20%	2427000	1376000	1024000
25%	3033000	1720000	1280000
30%	3640000	2064000	1536000

5.4.2   Single Phase Permeability

Single phase permeability was calculated in the manner described in Section 4.2.6.

Table 5.4 shows the calculated permeability for the stochastic networks equivalent to the Guillemot A µCT networks. Ten realisations were generated of each model and the table shows the average of X, Y and Z direction permeabilities over all models. This effectively increases the REV of the models to address the issue discussed in Section 4.2.6.

There is reasonable agreement between the permeabilities although the stochastic network permeability for plug 77 is rather low.

Table 5.4: Calculated permeability for stochastic pore networks

Volume	CCA Permeability (mD)	µCT network Permeability (mD)	Stochastic network Permeability (mD)
Plug 44	557	503	690
Plug 77	2.7	3.6	1.3
Plug 130	23	30.1	21.6
Plug 367	44.5	67.8	48.3

Figure 5.8 shows the calculated permeability with the sensitivity to porosity and the pore size distribution parameter r_1. Figure 5.9 shows the sensitivity to the pore size distribution parameter α with $r_1 = 10$ µm. All figures show the average of three directional permeabilities for ten realisations. Also shown is the core plug permeability and porosity data from the Guillemot A field. This demonstrates that the stochastically generated network models reproduce a realistic range of permeability commensurate with the range observed in Guillemot A. Note however that the porosity comparison is not strictly fair because the core plug data show the measured helium porosity

which is interpreted as the total macro plus micro porosity whereas the stochastic model porosity is the porosity above a pore radius of 0.8 µm.

The stochastic modelling also shows that the permeability is most sensitive to the porosity and the pore size distribution parameter r_1 which defines the upper limit of the distribution (Equation 4.19). This is consistent with theoretical models such as Katz and Thompson (1987) (Equation 4.26) which indicate that permeability is related to the size of the smallest pore on the connected path of pores containing the largest pores.

Figure 5.9 shows that smaller values of α result in wider pore size distributions which increase the permeability. The parameter α is significant in controlling permeability although less so than the parameter r_1.

Figure 5.10 shows the sensitivity to the coordination number parameter β with $\alpha = 2.4$ and $r_1 = 10$ µm. The results indicate that the stochastic model permeability is insensitive to the coordination number distribution.
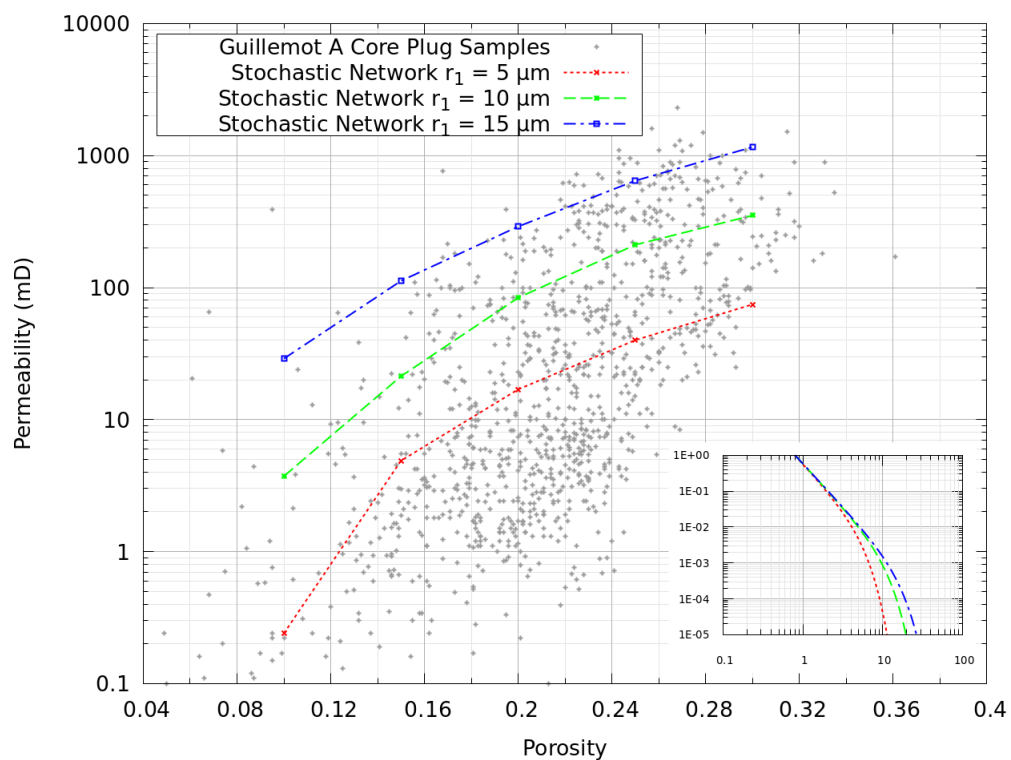
Figure 5.8: Permeability versus porosity for stochastic network models with sensitivity to parameter r_1; inset graph shows corresponding pore size distributions, cumulative probability versus radius (µm)
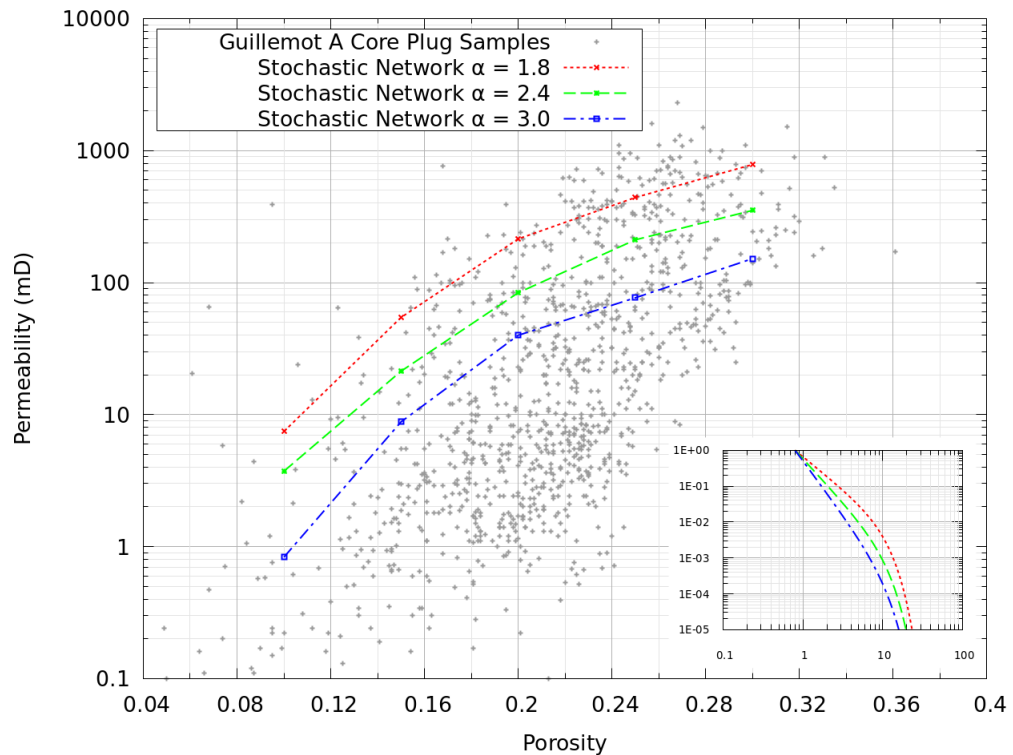
Figure 5.9: Permeability versus porosity for stochastic network models with sensitivity to parameter α; inset graph shows corresponding pore size distributions, cumulative probability versus radius (µm)

5.4.3 Formation Resistivity Factor

The FRF was calculated as described in Section 4.2.5. FRF is primarily dependent on porosity and not a strong function of other parameters. Figure 5.11 shows an example sensitivity to porosity and the parameter α which shows a similar trend to the FRF calculated from the µCT volumes (compare with Figure 4.26). The lower porosity models demonstrate a cementation exponent larger than 1.75 similar to the µCT volumes of core plugs 130 and 77. Hence these models may have insufficient connectivity which is not entirely due to lower porosity. Note also that the stochastic model for plug 77 has low permeability (Table 5.4).

FRF is generally over-predicted because the models do not include sufficient microporosity. To illustrate this point, the FRF was calculated for three models with decreasing values of the pore size distribution parameter r_0. The results are shown in Table 5.5. Note that the models were designed to show the effect of incrementally adding smaller pore elements; therefore there is an increase in porosity. The results show a significant decrease in FRF, consistent with increased porosity but also a decrease in the effective
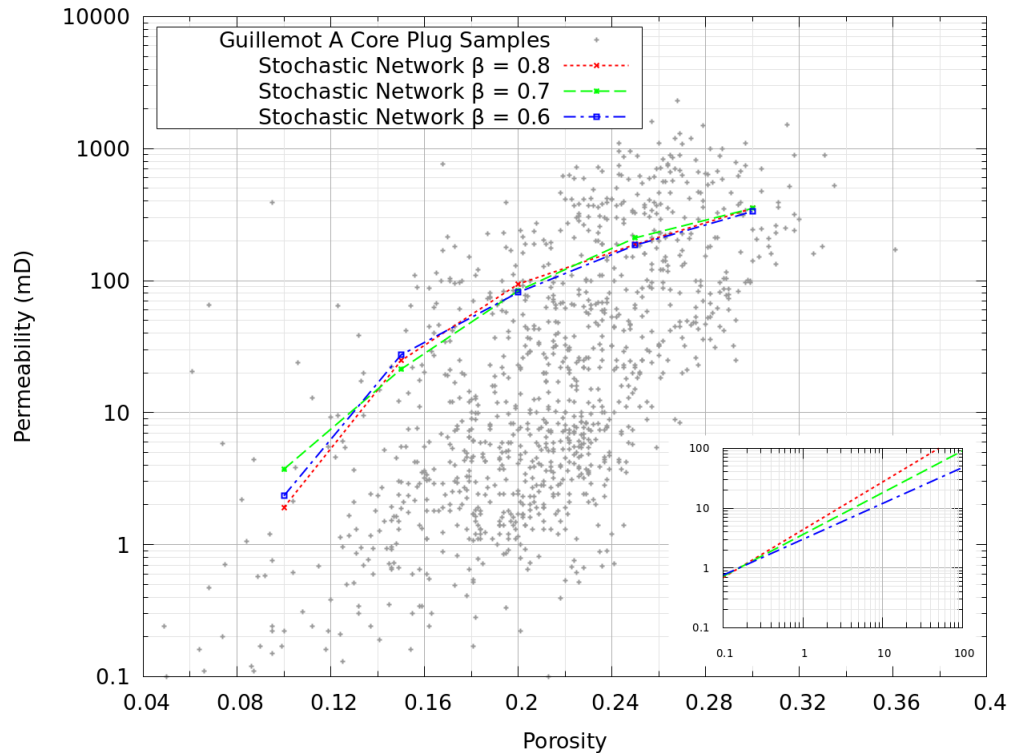
Figure 5.10: Permeability versus porosity for stochastic network models with sensitivity to parameter β; inset graph shows corresponding mean coordination number versus pore radius (µm)

cementation exponent.

Table 5.5: Stochastic pore network models: permeability and FRF for models with decreasing minimum pore size

r_0 (µm)	Number of Pore Elements	Model Porosity	Average X,Y,Z Permeability (mD)	Average X,Y,Z FRF	Cementation Exponent m
1.6	265500	17.5%	85	40.4	2.12
0.8	1410000	20.0%	82	29.8	2.11
0.4	7488000	21.9%	98	19.9	1.97

5.4.4 Multiphase Properties

Multiphase properties were generated from the stochastic networks using the poreflow PNM simulator as in Section 4.2.8. Network nodes correspond to the model pore elements with radius and shape factor as described above and volume given by Equation 5.3. Network bonds correspond the links between pore elements with radius equal to the minimum of the
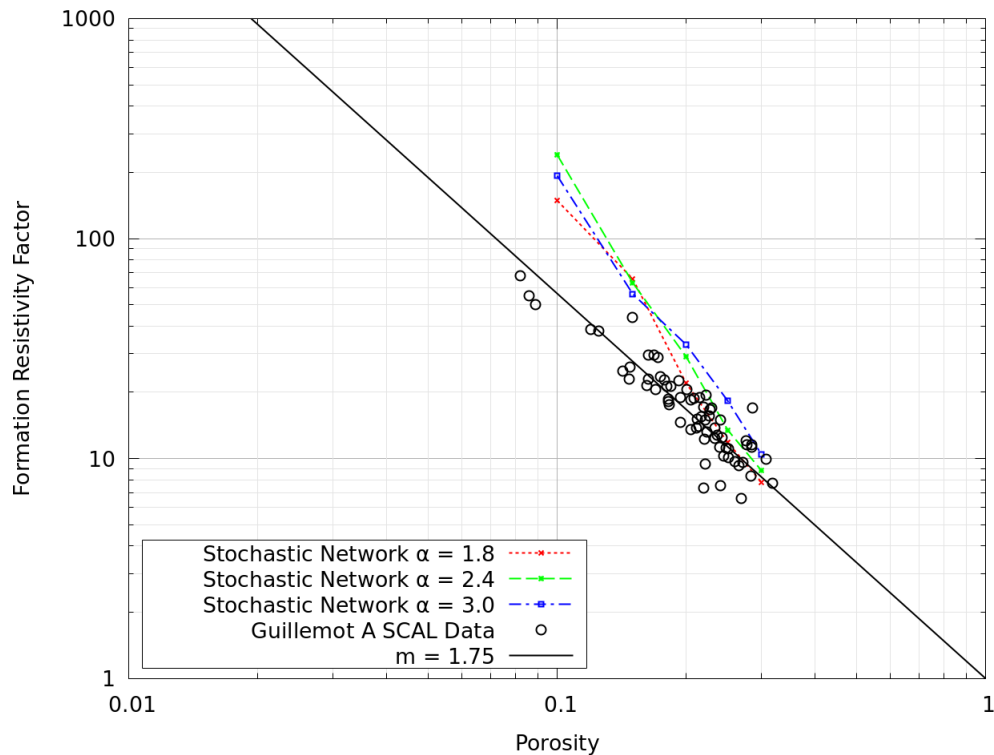
Figure 5.11: Formation resistivity factor versus porosity for stochastic network models with sensitivity to porosity and parameter α

connected element radii and zero volume. Each bond has four lengths viz: bond length, length first node, length second node and total length. Bond length is zero, lengths first node and second node are given by Equation 4.35 and total length is the distance from node centre to node centre.

The simulation does not include any viscous or gravity effects and the capillary pressure comparison below is in terms of the J-function (Leverett, 1941); therefore nominal values are used for fluid density, viscosity and interfacial tension.

The simulation models a drainage process where the receding contact angle is assumed to be 0°, followed by imbibition (water saturation increasing) under a variety of wettability conditions as discussed below.

For most cases, three generic networks designed to investigate the effect of decreasing the minimum pore size (Table 5.6) are shown. For relative permeability, the four networks equivalent to the Guillemot A µCT networks (Table 5.1) are also considered. Some further relative permeability sensitivities are also discussed below. As with single phase properties, the graphs below show the average results from ten stochastic realisations.

Table 5.6: Stochastic models used in multiphase pore network simulations

Model	#1	#2	#3
r_0 (µm)	1.6	0.8	0.4
r_1 (µm)	10.0	10.0	10.0
α	2.4	2.4	2.4
β	0.7	0.7	0.7
Domain (µm^3)	1000^3	800^3	500^3
Number of Pore Elements	594500	1376000	167000
Porosity	20.0%	20.0%	20.0%
Permeability (mD)	130	80	45

5.4.5 Capillary Pressure

Figure 5.12 shows the Leverett J-function from the generic stochastic network drainage capillary pressure simulations ($\cos\theta = 1$) compared with the Guillemot A Fulmar MICP data (Appendix A) and the µCT networks from plug 44 and plug 130 (Section 4.2).

At low wetting phase saturations the modelled J-functions are too low compared to the measured data primarily because the models do not contain sufficiently wide pore size distributions, in particular there is insufficient microporosity. Comparing the three generic stochastic models, it is clear that extending the pore size distribution by decreasing parameter r_0 improves the match to the measured data, as expected. Comparing the µCT networks, plug 130 has the poorest match at low saturations because this µCT volume has the largest voxel size (1.5 µm) and the largest deficiency of microporosity.

At high wetting phase saturations there is a mis-match with the measured data particularly for the stochastic model #3 (r_0 = 0.4 µm). This is most likely related to the system size which has an impact on the effective capillary entry pressure. The MICP data were measured on whole core plugs and a significant reduction in saturation only occurs when the non-wetting phase connects across the entire system. The smallest model is #3 and here a significant saturation change can occur if only a few large pore elements are invaded.
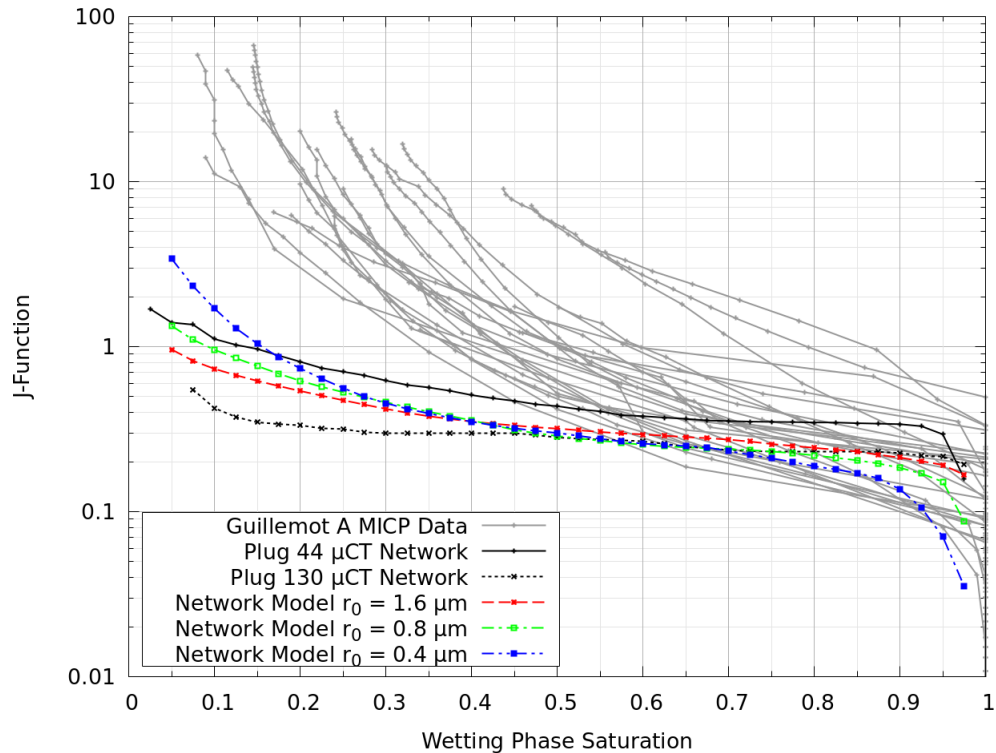
Figure 5.12: Leverett J-function from drainage capillary pressure; stochastic pore network models, µCT networks and field data

5.4.6 Resistivity Index

Figure 5.13 shows the drainage resistivity index from the generic stochastic models compared with the Guillemot SCAL data and the µCT networks from plug 44 and plug 130.

The plug 44 µCT network displays the best match to the measured data consistent with a saturation exponent n of 1.75 (Archies Law, Equation A.1). Plug 130 has a much higher resistivity index, particularly at intermediate and high water saturations, which is not reflected in measured SCAL data. The explanation for this is not known, however it may be related to the discrepancy in FRF (Figure 4.26) and the low drainage relative permeability (Figure 4.29).

The stochastic networks display a higher effective saturation exponent, $n \approx$ 2.2, and generally lie between the plug 44 and plug 130 network results. Model #3 has a large increase in resistivity index at low saturations, this could be due to poor connectivity even though this model has smaller pore size compared with models #1 and #2.
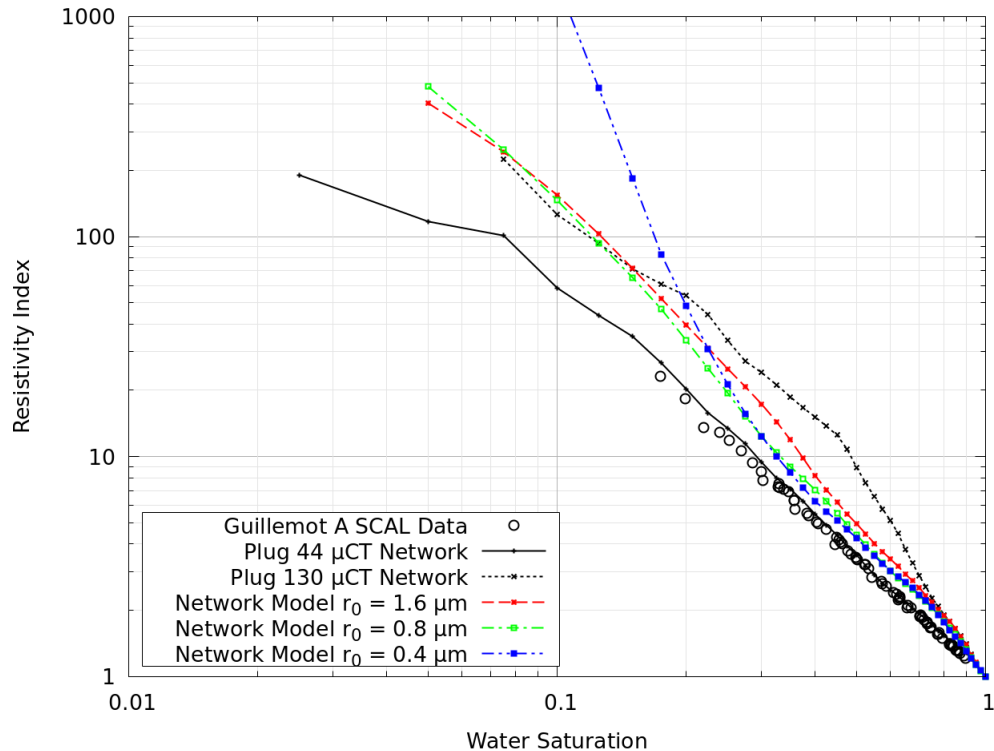
Figure 5.13: Resistivity index from drainage simulation; stochastic pore network models, µCT networks and field data

5.4.7 Relative Permeability

Figures 5.14 to 5.17 show the drainage relative permeability ($\theta_r = 0°$) for each of the stochastic models equivalent to the µCT volumes (Table 5.1) compared with the relative permeability calculated directly from the µCT networks (Section 4.2.8). There are no drainage relative permeability measurements for the Guillemot A field, but comparisons with the measured data from Vanguard and the imbibition data from Guillemot A are discussed below.

Both oil and water relative permeability show a good match for plug 44 (Figure 5.14) demonstrating that the stochastic algorithm generates realistic pore networks in this case.

The comparison of the stochastic and µCT models for the other plugs is less good, but the general character of the relative permeability and some key trends are reproduced. For example, the µCT relative permeabilities for plug 77 (Figure 5.15) and 130 (Figure 5.16) are significantly lower than for plug 44 and this behaviour is reproduced in the stochastic modelling results. In particular, the cross-over relative permeability ($k_{rw} = k_{ro}$) is well matched by all stochastic models with the possible exception of plug 367 (Figure 5.17).
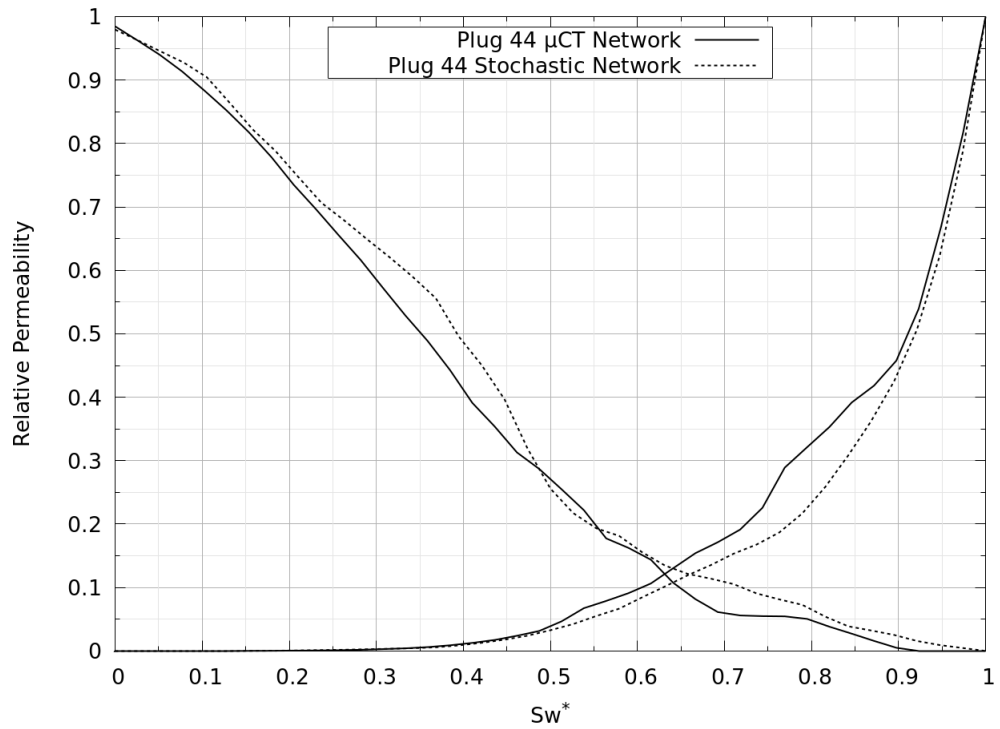
Figure 5.14: Drainage relative permeability; plug 44 stochastic network and µCT network
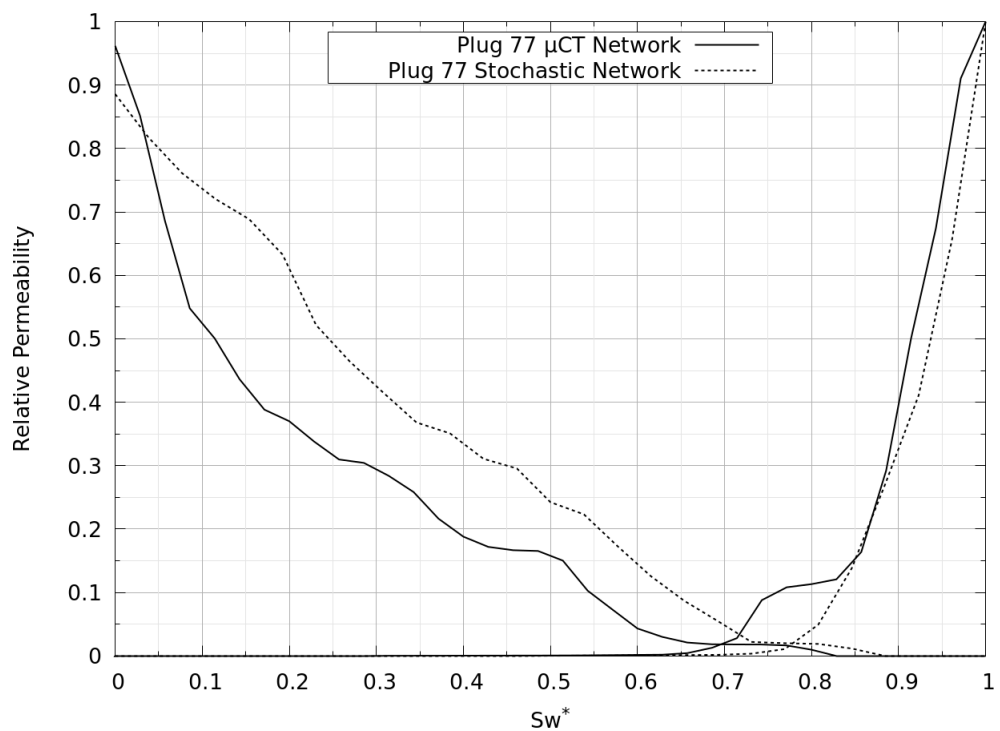
Figure 5.15: Drainage relative permeability; plug 77 stochastic network and µCT network
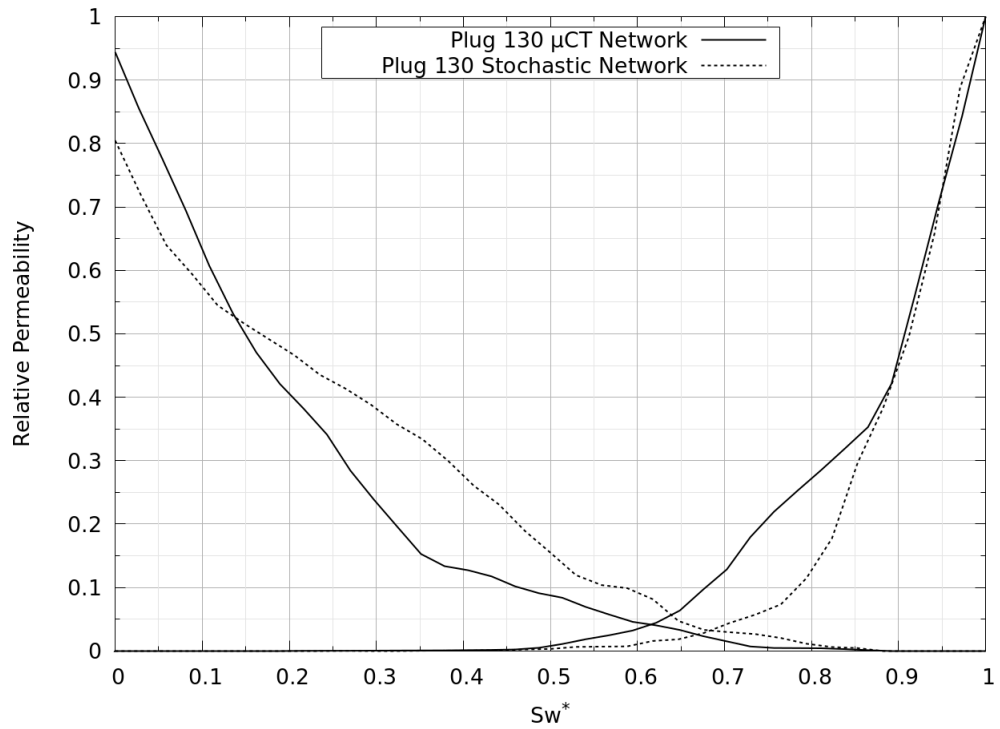
Figure 5.16: Drainage relative permeability; plug 130 stochastic network and μCT network
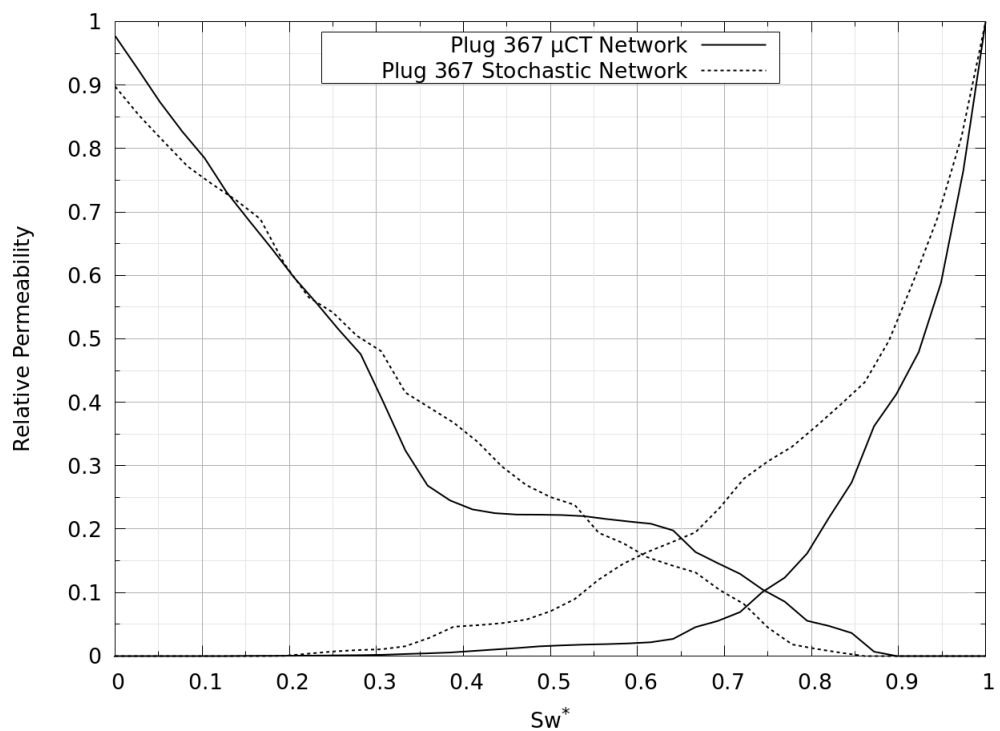
Figure 5.17: Drainage relative permeability; plug 367 stochastic network and μCT network

Plugs 77, 130 and 367 have lower porosity and poorer connectivity. A sensitivity to the model porosity is discussed below.

Figure 5.18 shows drainage relative permeability from stochastic models #1, #2 and #3 (Table 5.1) compared with the Vanguard SCAL data and the µCT network from plug 44.

Comparing the relative permeability calculated from stochastic and µCT networks, it should be noted that there is some statistical uncertainty in the results. An illustration of this is the difference between the X, Y and Z direction relative permeabilities for the µCT networks (Figures 4.27 to 4.30). For the stochastic networks, Figure 5.18 shows the average relative permeability and the 10 model realisations are show in Figure 5.19.
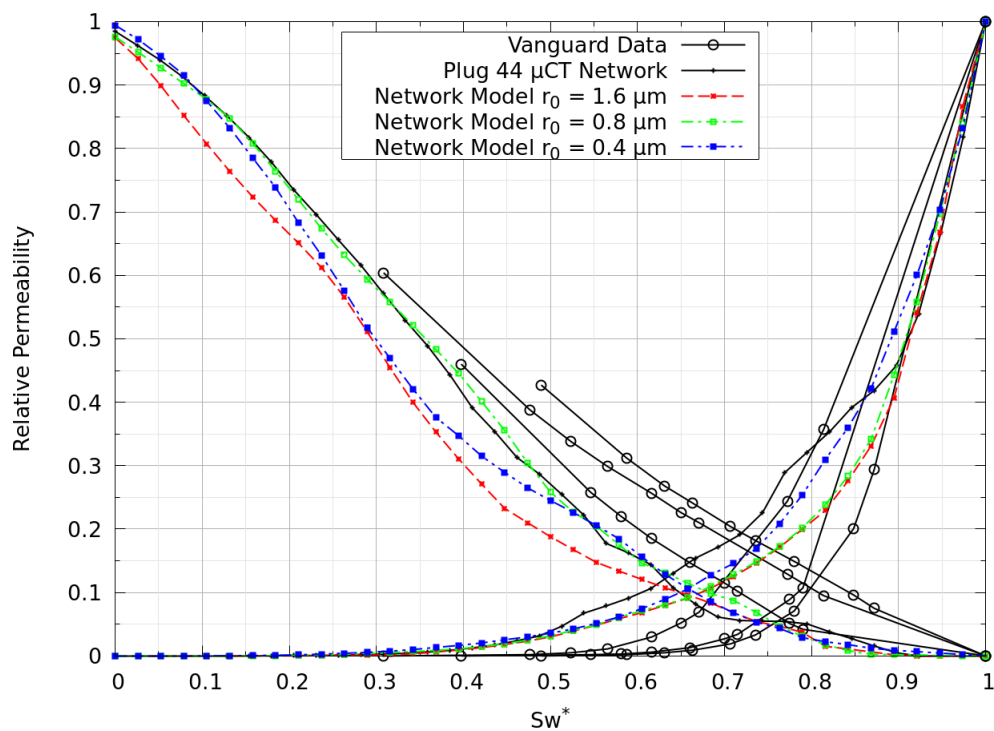
Figure 5.18: Drainage relative permeability; stochastic pore network models and Vanguard data

Both the oil and water relative permeability from the stochastic models is close to that from the plug 44 µCT network.

Neither the stochastic networks nor the µCT networks have a very good match to the Vanguard measured drainage relative permeability data. To remove the effect of micropores below 0.2 µm and make a fair comparison,
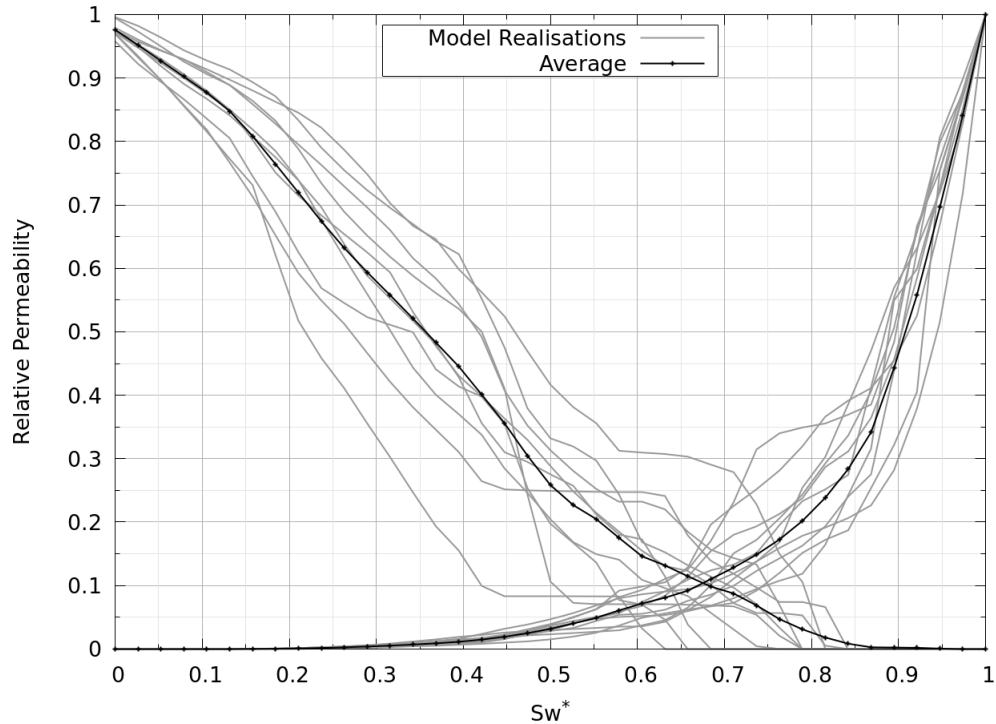
Figure 5.19: Drainage relative permeability; 10 stochastic realisations of pore network model #2

the horizontal axis plots the normalised water saturation given by:

$$S_w^* = \frac{S_w - S_{wmin}}{1 - S_{wmin}} \tag{5.6}$$

where S_{wmin} is the water saturation corresponding to maximum hydrocarbon i.e. 500 ft gas column (Section 3.1). However, the SCAL measurement programme did not reach a sufficiently high capillary pressure and there is considerable uncertainty in the correct values of S_{wmin}.

Figures 5.20 to 5.23 show imbibition relative permeability for a variety of wettability conditions. The water-wet case assumes the advancing contact angle is 40° and the oil-wet case assumes the advancing contact angle is 180°. In general the relative permeabilities from the stochastic models are close to those from the plug 44 μCT network, validating the stochastic algorithm in this case.

Wettability data from the Guillemot A field (Appendix A) indicates the reservoir is moderately oil-wet and accordingly the match of both the oil and water relative permeability to the Guillemot A measured data is better in the oil-wet case (Figure 5.21) than the water-wet case (Figure 5.20). Note that the Guillemot A measured data are from different plug samples (Table

A.1 and Figure A.9) but they show consistent trends.

A close examination shows that the Guillemot A measured data generally lie between the extreme oil-wet and water-wet results from the PNM. In addition, the measured Amott water wettability indices (Figures A.10 and A.11) are approximately 0.1 indicating there is a small spontaneous imbibition of water and therefore a small fraction of pores have retained water-wet character ($\theta < 90°$) despite being contacted by oil.

Figures 5.22 and 5.23 show two sensitivity cases motivated by the previous observations. Here, a fractional wettability model is used where 10% (Figure 5.22) or 20% (Figure 5.23) of the pores contacted by oil are assumed to remain water-wet. For simplicity, the pore elements remaining water-wet are chosen at random and not correlated with size. The results generally show a better match to the measured oil relative permeability compared with Figure 5.21. However, the water relative permeability is a poorer match to the Guillemot A measured data.

The difficulty of matching imbibition water relative permeability in oil-wet and fractionally wet cases is a known limitation of quasi-static PNM. Quasi-static models assume that pores and throats are filled in the order of the local capillary entry pressure (Blunt, 2001). Furthermore, for imbibition in an oil-wet medium, quasi-static models assume that large poorly connected pores can be filled through layer flow i.e. the connected path of water retained in the crevices and corners of the pore space. In reality, the timescale for filling via such layer flow is very large because the hydraulic conductance of layers scales with the fourth power of the radius of the arc meniscus (Blunt, 2017). In practice, the low conductance of layers changes the order in which elements are filled to favour a connected pathway of smaller pores and throats. At low water saturations this results in higher water relative permeability from laboratory experiments than predicted by a strict quasi-static assumption (Blunt, 2017).

Figures 5.24 and 5.25 show imbibition relative permeability for oil-wet conditions with sensitivities to the parameter α and the porosity.

The results show that the oil relative permeability is lower for smaller values of α. This is consistent with the pore space being less well connected because the pore size distribution has greater variance at smaller values of α and the models have fewer pore elements at the same porosity.

Figure 5.25 shows the water relative permeability is higher at higher porosity. This is also consistent with a better connected network and higher absolute
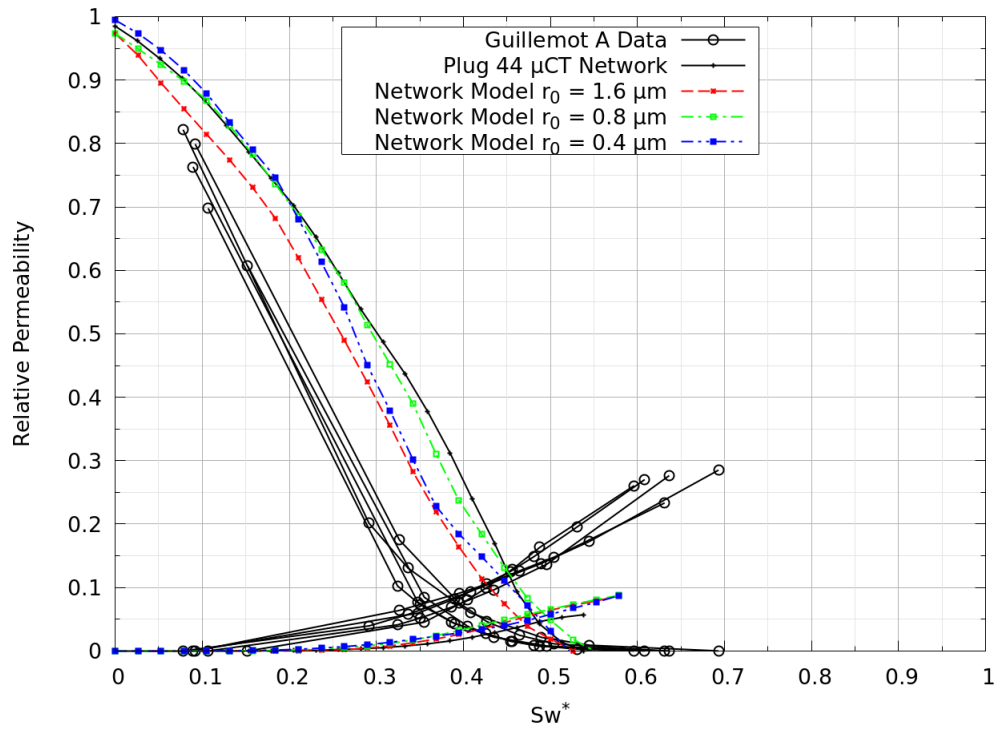
Figure 5.20: Imbibition relative permeability for water wet conditions ($\theta_a = 40°$); stochastic pore network models and Guillemot A data
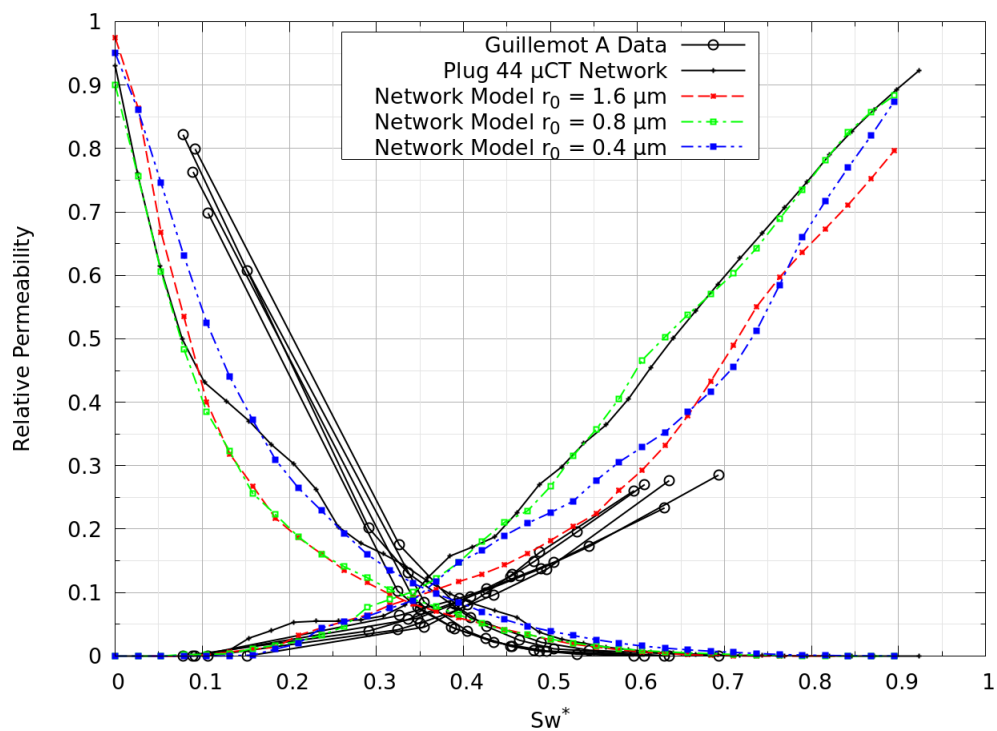
Figure 5.21: Imbibition relative permeability for oil wet conditions ($\theta_a = 180°$); stochastic pore network models and Guillemot A data
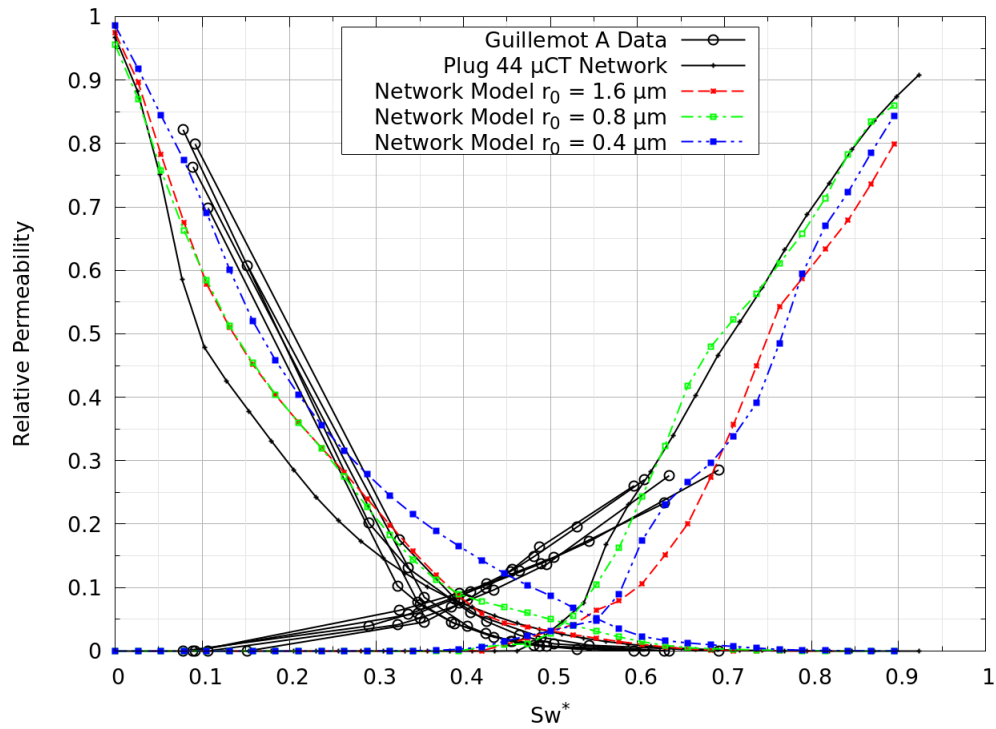
Figure 5.22: Imbibition relative permeability for 90:10 oil:water fractionally wet conditions; stochastic pore network models and Guillemot A data
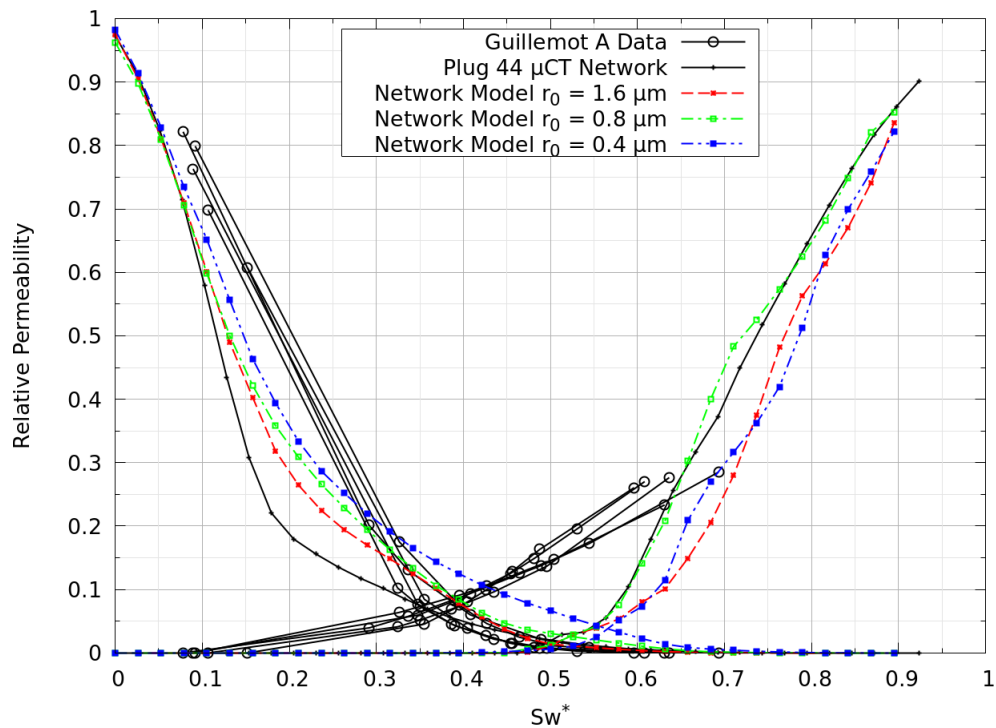
Figure 5.23: Imbibition relative permeability for 80:20 oil:water fractionally wet conditions; stochastic pore network models and Guillemot A data

permeability at higher porosity.
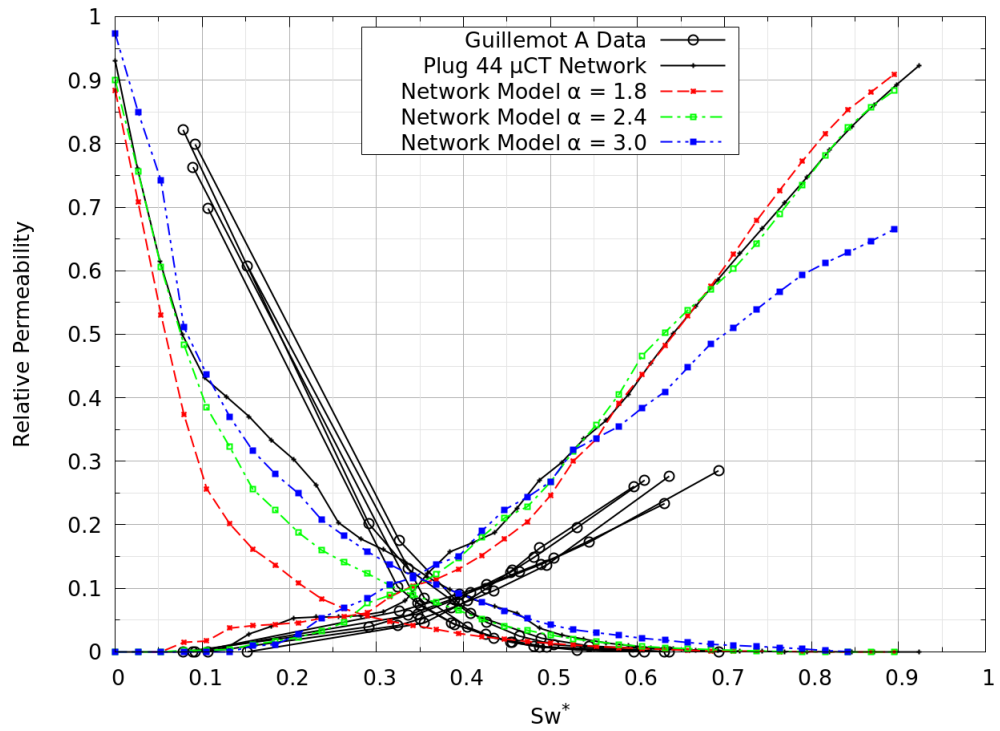
Figure 5.24: Imbibition relative permeability for oil wet conditions; sensitivity to parameter α
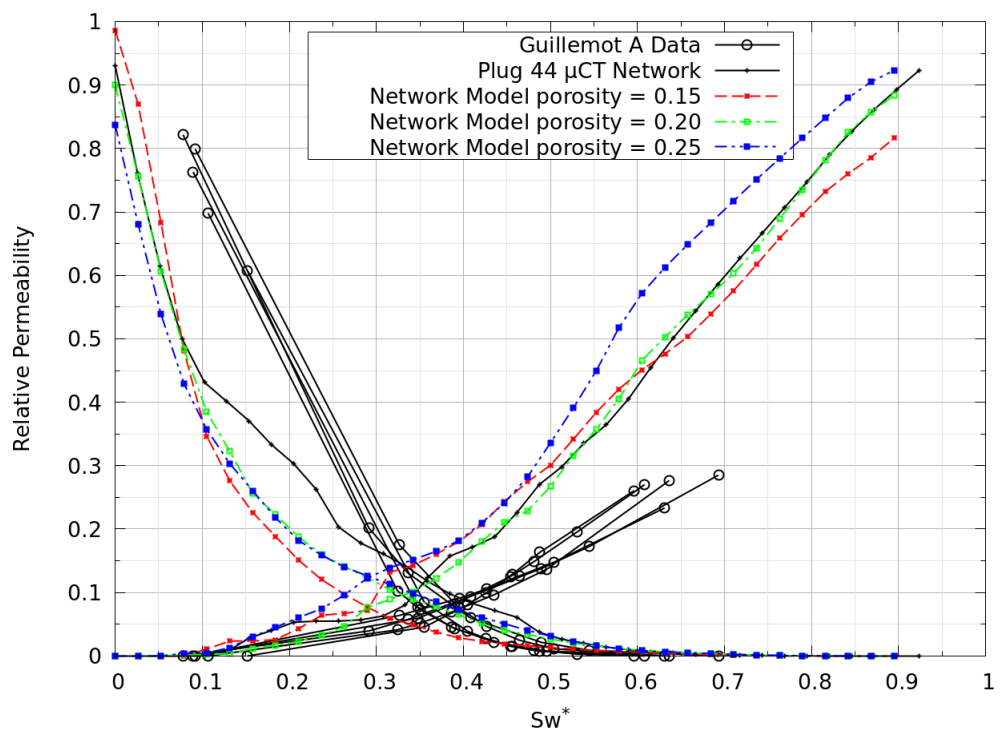
Figure 5.25: Imbibition relative permeability for oil wet conditions; sensitivity to porosity

Chapter 6

Field Scale Modelling

When everything was stirred together in the cauldron, the bubbling liquid was bright pink. Mildred stared at it doubtfully.

"I'm sure it should be green," she said. "In fact I'm sure we should have put in a handful of pondweed-gathered-at-midnight."

— Jill Murphy, The Worst Witch

6.1   Methodology

6.1.1   Summary

This chapter describes a field scale application of image based pore space characterisation and modelling where multiphase flow functions generated from stochastic pore networks are used in field scale continuum simulation model. In particular, through PNM it is possible to generate fully consistent relative permeability and capillary pressure functions which capture a range of key parameters such as wettability, reservoir quality and initial water saturation. The objective is to quantify the impact of different wettability assumptions and the effect of permeability and wettability heterogeneity.

The Guillemot A oil field is used as an example as it has been subjected to partial waterflood and understanding the multiphase flow is a prerequisite for maximising recovery.

The field scale modelling was performed using a commercial reservoir simulator, Eclipse[1].

---

[1] https://www.software.slb.com/products/eclipse

6.1.2   Model Description

The reservoir model is a 2D vertical cross-section of part of the Guillemot A field and represents one production well and one water injection well. The model covers the Fulmar sands only; the Skagerrak is excluded because the sands are lower permeability, more geologically complex and not conformable with the Fulmar. The length of the model is defined from the typical distance between wells and the thickness of the model is equal to the gross Fulmar thickness at well 21/30-8. Figure 6.1 shows the size of the model.
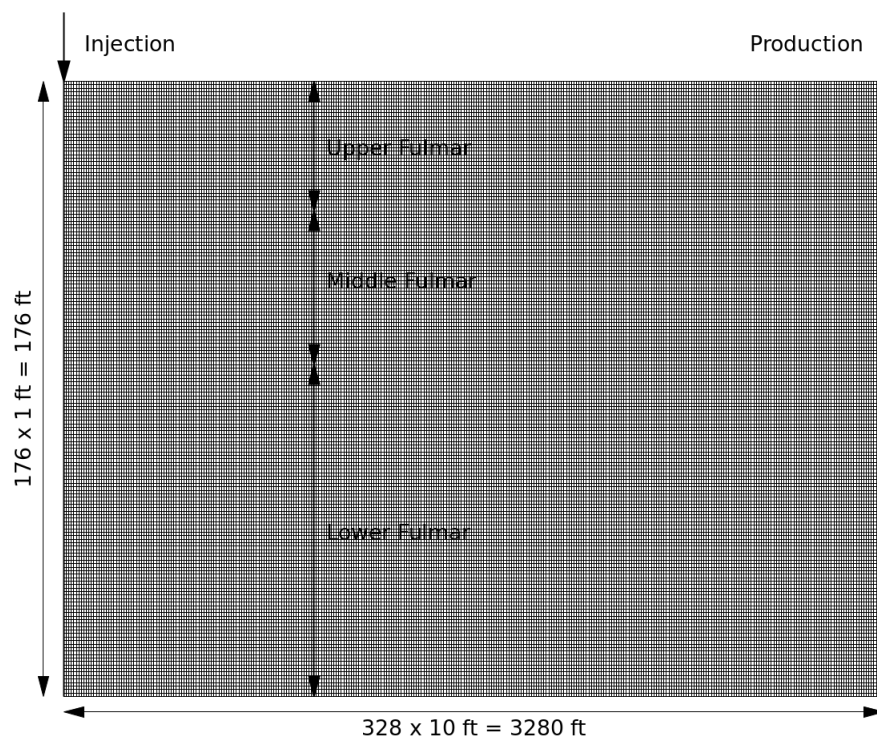
Figure 6.1: Reservoir model grid dimensions

The top 37 model layers represent the Upper Fulmar, 44 layers represent the Middle Fulmar and the bottom 95 layers are the Lower Fulmar. The left side boundary condition is constant rate injection and the right side is constant rate production. The top and bottom sides are no-flow boundaries.

Porosity and permeability are populated using CCA data from well 21/30-8 in three different ways.

Model A has homogeneous properties for each of the four intervals: Upper Fulmar, Middle Fulmar, the main part of the Lower Fulmar and the higher permeability basal transgressive zone. The properties are taken from the arithmetic averages of the CCA data as given in Table 6.1.

Table 6.1: Model A porosity and permeability

Zone	Thickness (ft)	Average Porosity	Average Permeability (mD)
Upper Fulmar	37	24.1%	96
Middle Fulmar	44	24.0%	297
Main Lower Fulmar	81	19.7%	17
Basal Lower Fulmar	14	22.6%	273

Model B has homogeneous porosity and permeability for each of the 176 model layers, taken directly from the 1 ft interval CCA data (Figure A.1).

Model C has the porosity distributed using Sequential Gaussian Simulation (SGS) using exponential variograms (Pyrcz and Deutsch, 2014). The vertical variogram has a range of 3 ft and the horizontal variogram has a range of 300 ft. The vertical variogram was estimated from the CCA data and the horizontal variogram represents an anisotropy ratio of 100:1 which is typical for shallow marine systems. The porosity is modelled separately for the four zones to honour the range of values from the CCA data. The permeability was then calculated from the porosity assuming $\log(k)$ is a linear function of porosity using four different functions generated by fitting the CCA data for each of the four zones.

Figure 6.2 shows the permeability distributions for all models.

Fluid properties are given in Table 6.2. Oil properties were obtained from Sebborn (1983). The Guillemot A formation water has a high salinity of circa 200,000 mg/l (Warren and Smalley, 1994); properties of the water were calculated using empirical correlations from McCain (1991). The oil-water IFT was calculated from the correlation of Firoozabadi and Ramey (1988).

Table 6.2: Guillemot A reservoir and fluid properties

Reservoir pressure	5875 psia
Reservoir temperature	238 °F
Oil density at reservoir conditions	45.3 lb/ft3
Oil viscosity at reservoir conditions	0.721 cP
Water density at reservoir conditions	68.6 lb/ft3
Water viscosity at reservoir conditions	0.375 cP
Oil-water IFT	38 dyn/cm
FWL	8770 ft TVDSS
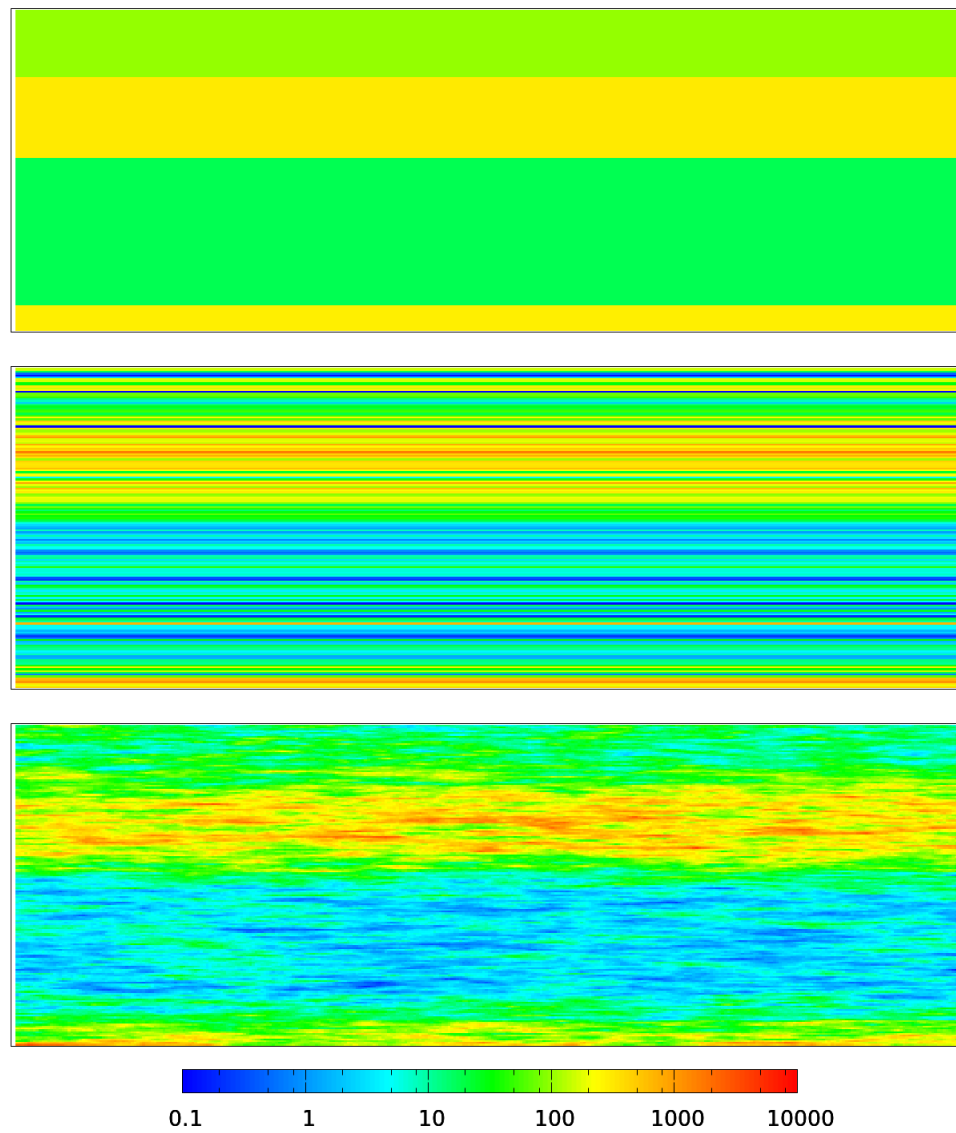
Figure 6.2: Reservoir models, top: model A, middle: model B, bottom: model C, scale bar: permeability (mD)

6.1.3   Relative Permeability and Capillary Pressure

Relative permeability and capillary pressure were calculated from stochastic pore networks. It is assumed that the relative permeability derived from the quasi-static PNM applies at the grid block scale. This assumption introduces two scale issues. The first is the assumption of homogeneity at the grid block scale and the second is the assumption that capillary forces dominate viscous forces at the grid block scale.

The first assumption is difficult to test because the well log data have a vertical resolution of 0.5 ft which is only half the grid block thickness. However, model B uses vertical and horizontal variogram ranges that are larger than the grid block size and therefore it is reasonable to assume some degree homogeneity at the grid block scale.

The second assumption is illustrated by calculating the ratio of viscous to capillary forces at the grid block scale (Barker and Thibeau, 1997):

$$N_{vc} = \frac{dP}{dx}\frac{\Delta x}{P_c} \tag{6.1}$$

where dP/dx is the horizontal viscous pressure gradient and Δx is the length of a grid block. Note that this is not the same as the microscopic capillary number (Hilfer et al., 2015).

Figure 6.3 shows the ratio of viscous to capillary forces for a model grid block (10 ft length) assuming horizontal flow with a typical pressure gradient of 0.1 psi/ft from the Guillemot A field. Here, the capillary pressure is calculated from the J-function using example values (Figures A.6 to A.8) and a range of permeability. Figure 6.3 shows that capillary forces generally dominate for this grid block size ($N_{vc} < 1$) and therefore it reasonable to apply relative permeabilities calculated from quasi-static pore scale simulations.

Based on the results described in Section 5.4, model #2 (Table 5.6) was used to generate imbibition relative permeability and capillary pressures for water-wet and oil-wet conditions. In addition, a series of incomplete drainage processes was simulated to accommodate the heterogeneity of initial water saturation due to variation in rock quality and height above the FWL.

The results from the PNM were fitted to empirical models. The purpose of this was firstly to ensure the relative permeabilities and capillary pressures were smooth functions with a more regular character, secondly to make it
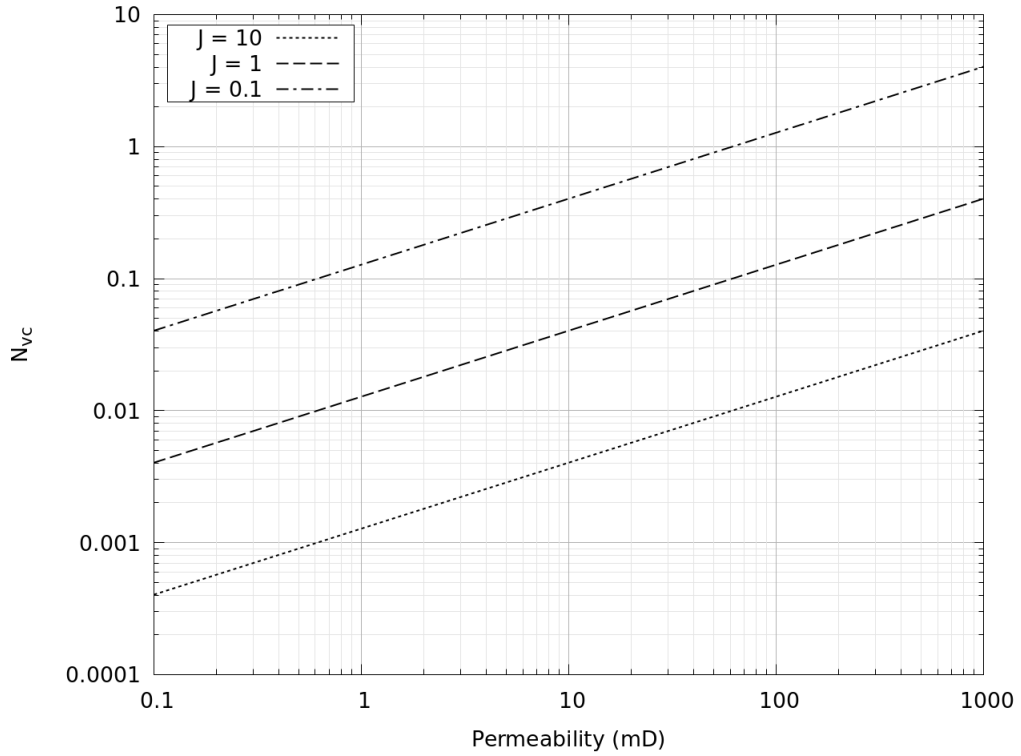
Figure 6.3: Ratio of viscous to capillary forces for horizontal flow in a 10 ft long grid block assuming a constant pressure gradient and reservoir parameters from the Guillemot A field

easier to interpolate between values of initial water saturation and thirdly to incorporate some of the SCAL data to overcome limitations of the PNM.

The relative permeability data were fitted to the LET model (Lomeland et al., 2005; Arief et al., 2016) given by the following equations:

$$k_{rw} = \frac{S_w^{*L_w}}{S_w^{*L_w} + E_w(1 - S_w^*)^{T_w}} \qquad (6.2)$$

and

$$k_{ro} = \frac{(1 - S_w^*)^{L_o}}{(1 - S_w^*)^{L_o} + E_o S_w^{*T_o}} \qquad (6.3)$$

where S_w^* is the normalised water saturation, given by:

$$S_w^* = \frac{S_w - S_{wr}}{1 - S_{wr} - S_{or}} \qquad (6.4)$$

The quantities L, E and T are empirical fitting parameters with no physical meaning; the subscripts w and o indicate water and oil respectively. The

flexibility and utility of the LET correlation is discussed by Lomeland et al. (2005). In particular, the parameter L describes the lower part of the curve, T describes the upper (top) part of the curve and E describes the position (elevation) of the transition between the lower and upper parts of the curve.

The parameter S_{wr} is the maximum water saturations for which the water relative permeability is zero or the oil relative permeability is one. S_{or} is the maximum oil saturations for which the oil relative permeability is zero or the water relative permeability is one. These quantities may be fixed or used as additional fitting parameters.

The fitted parameters are given in Table 6.3. The parameter S_{wi} is the initial water saturation at the end of drainage (the start of imbibition) and is larger than S_{wr} in all cases.

In the water-wet case the PNM shows the imbibition water relative permeability is essentially independent of the initial water saturation; therefore a single set of parameters is used. The residual oil saturation increases with increasing initial oil saturation and a simple linear model is used based on the PNM results.

In the oil-wet case the residual oil saturation S_{or} is essentially independent of initial saturation and a single value is used in all cases. The parameter S_{wr} is used as a fitting parameter with the constraint that the same value is used for the oil and water relative permeabilities. To overcome the issue with quasi-static PNM discussed in Section 5.4.7, the water relative permeability incorporates only the end-point value from PNM. The shapes of the water relative permeability curves in the oil-wet case are defined from the measured SCAL data (Figure A.9). These data are limited and do not justify a three parameter model; therefore L and T are fixed and E is the only fitted parameter.

The relative permeabilities are shown in Figures 6.4 and 6.5.

For capillary pressure, the Skjaeveland model (Skjaeveland et al., 1998) was used to fit $J \cos \theta$ calculated from the PNM, where J is the J-function (Equation A.2):

$$J \cos \theta = c_w S_w^{*-b_w} + c_o S_o^{*-b_o} \qquad (6.5)$$

where

Table 6.3: LET parameters for imbibition oil-water relative permeability under water-wet and oil-wet conditions

Wettability	Phase	S_{wi}	S_{wr}	S_{or}	L	E	T
Water-wet	Oil	0.05	0.0	0.425	1.92	0.23	0.84
Water-wet	Oil	0.15	0.0	0.400	2.06	0.21	0.71
Water-wet	Oil	0.25	0.0	0.375	2.20	0.18	0.59
Water-wet	Oil	0.35	0.0	0.350	2.34	0.15	0.46
Water-wet	Oil	0.45	0.0	0.325	2.48	0.13	0.33
Water-wet	Water	All	0.0	0.0	2.51	7.75	1.00
Oil-wet	Oil	0.05	0.045	0.20	1.90	3.11	0.90
Oil-wet	Oil	0.15	0.12	0.20	2.35	2.50	0.99
Oil-wet	Oil	0.25	0.16	0.20	2.81	1.89	1.09
Oil-wet	Oil	0.35	0.18	0.20	3.26	1.28	1.18
Oil-wet	Oil	0.45	0.20	0.20	3.71	0.67	1.27
Oil-wet	Water	0.05	0.045	0.0	2.0	1.39	1.0
Oil-wet	Water	0.15	0.12	0.0	2.0	2.44	1.0
Oil-wet	Water	0.25	0.16	0.0	2.0	3.48	1.0
Oil-wet	Water	0.35	0.18	0.0	2.0	4.52	1.0
Oil-wet	Water	0.45	0.20	0.0	2.0	5.56	1.0
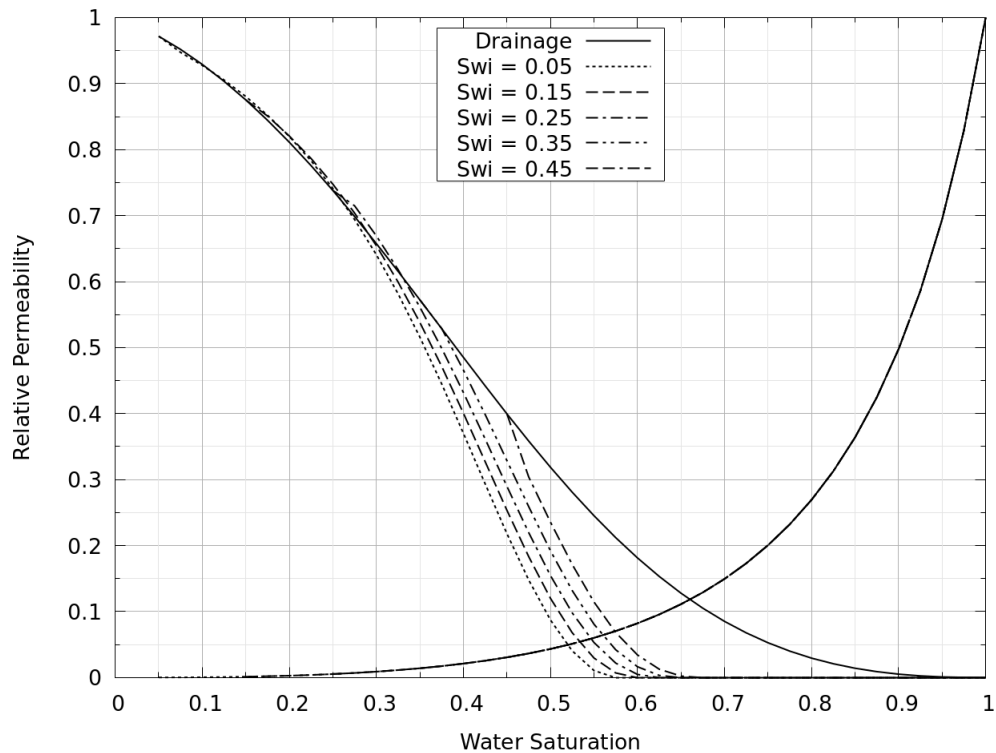
Figure 6.4: Oil-water relative permeability for water-wet conditions

$$S_w^* = \frac{S_w - S_{wr}}{1 - S_{wr}} \tag{6.6}$$
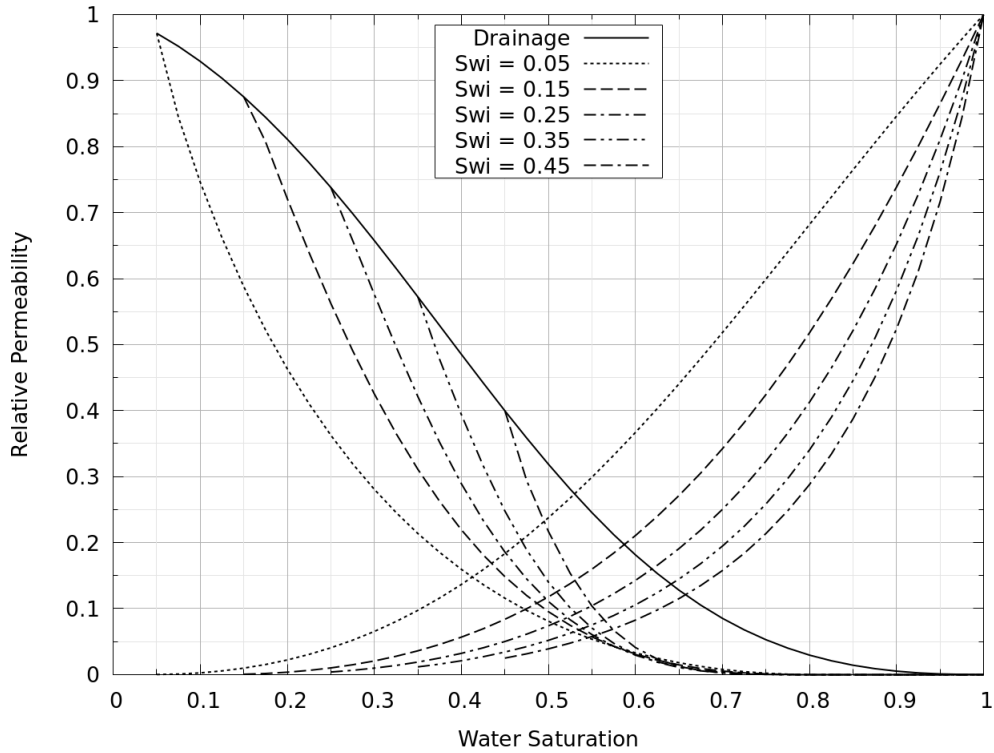
Figure 6.5: Oil-water relative permeability for oil-wet conditions

and

$$S_o^* = \frac{S_o - S_{or}}{1 - S_{or}} \tag{6.7}$$

The capillary pressure is then calculated from:

$$P_c = \sigma\sqrt{\frac{\phi}{k}}\left(c_w S_w^{*-b_w} + c_o S_o^{*-b_o}\right) \tag{6.8}$$

where σ, k and ϕ are the reservoir IFT, permeability and porosity (Section 6.1.2).

For a strongly water-wet system the parameter c_o is zero and the Skjaeveland model reduces to the Brooks and Corey (1964) model where the parameter c_w is given by the capillary entry pressure and b_w is the pore size distribution index which is related to the fractal dimension of the pore space (Angulo et al., 1992; Li, 2004). In an oil-wet or mixed wet system the negative component of the capillary pressure curve is described by the second term in the expression with $c_o < 0$. Note that $c_w \geqslant 0$ and $c_o \leqslant 0$ in all wettability cases.

Here, the quantities c_w, b_w, c_o, and b_o are used as fitting parameters. The

PNM results can be matched using a single value of $b_w = b_o$ independent of S_{wi}. However, as shown in Figure 5.12, the PNM does not have sufficient range of pore throat sizes to fully reproduce the MICP data. Therefore, the measured data are used to define the pore size distribution parameter $b_w = b_o$ and the parameters c_w, c_o are chosen to maintain the same ratio between the imbibition and drainage capillary pressure as given by the PNM. S_{wr} and S_{or} are used as fitting parameters to match the capillary pressure data close to the end-points.
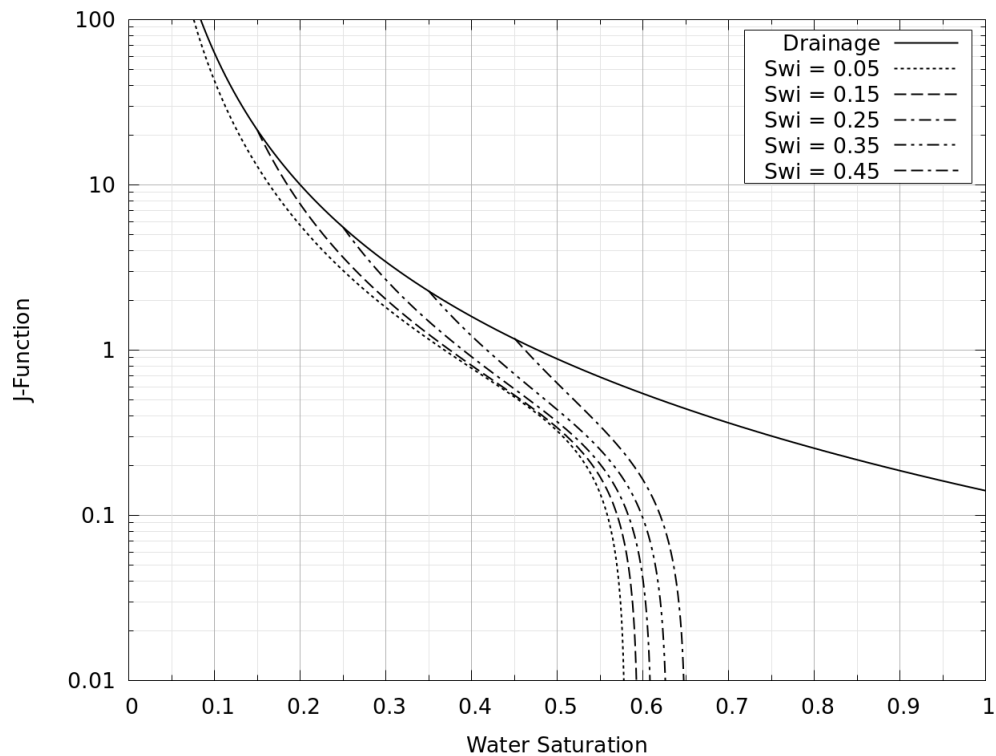
Figure 6.6: Primary drainage and imbibition J-function for water-wet conditions

The fitted parameters are given in Table 6.4. In the water-wet case c_o has small magnitude and c_w is large and comparable to the value from the drainage MICP data. The situation is reversed in the oil-wet case.

The J-functions are shown in Figures 6.6 and 6.7.

The initial water saturation in the model is determined by a capillary-gravity equilibrium using the drainage J-function (Figure 6.6) assuming a receding contact angle of 0°. To validate the model, Figure 6.8 shows the calculated water saturation for Model B compared with the water saturation obtained from logging data from well 21/30-8. This shows that the model adequately reproduces the heterogeneity of the water saturation which is a function of porosity/permeability heterogeneity and height above the FWL.
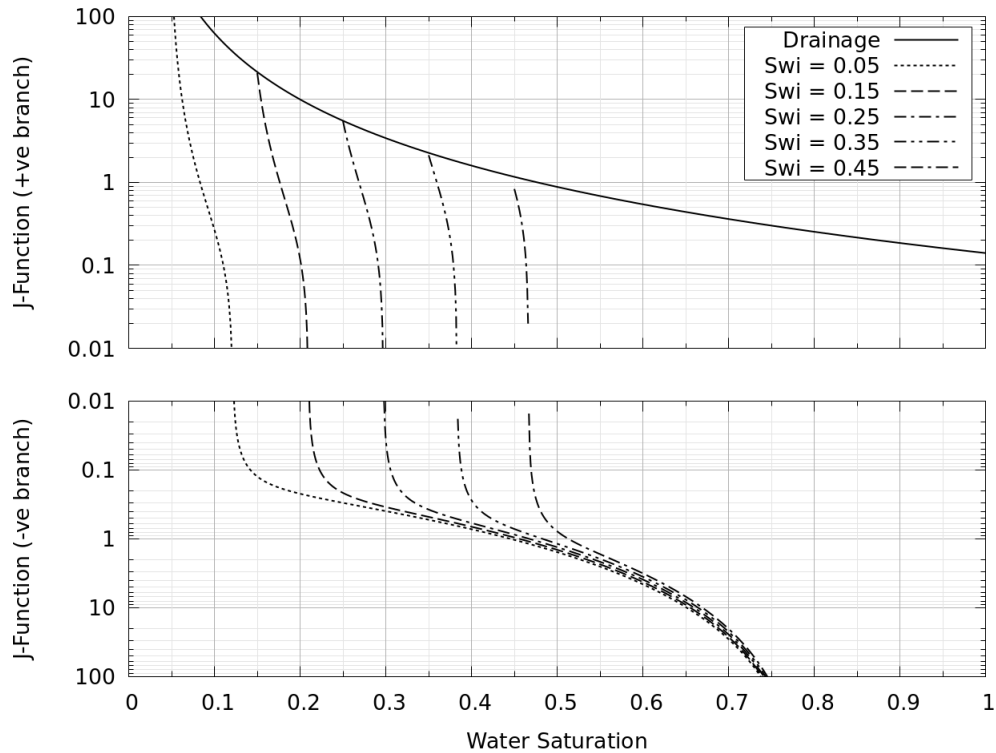
Figure 6.7: Primary drainage and imbibition J-function for oil-wet conditions

Table 6.4: Skjaeveland model parameters for oil-water capillary pressure under water-wet and oil-wet conditions

Direction	Wettability	S_{wi}	S_{wr}	S_{or}	c_w	b_w	c_o	b_o
Drainage	Water-wet	-	0.0	0.0	0.141	2.65	0.0	0.0
Imbibition	Water-wet	0.05	0.012	0.375	0.071	2.65	-0.0095	2.65
Imbibition	Water-wet	0.15	0.045	0.350	0.063	2.65	-0.0089	2.65
Imbibition	Water-wet	0.25	0.091	0.325	0.054	2.65	-0.0080	2.65
Imbibition	Water-wet	0.35	0.156	0.300	0.048	2.65	-0.0074	2.65
Imbibition	Water-wet	0.45	0.244	0.275	0.039	2.65	-0.0065	2.65
Imbibition	Oil-wet	0.05	0.046	0.2	0.00022	2.65	-0.117	2.65
Imbibition	Oil-wet	0.15	0.137	0.2	0.00035	2.65	-0.108	2.65
Imbibition	Oil-wet	0.25	0.225	0.2	0.00063	2.65	-0.100	2.65
Imbibition	Oil-wet	0.35	0.310	0.2	0.00132	2.65	-0.091	2.65
Imbibition	Oil-wet	0.45	0.388	0.2	0.00360	2.65	-0.082	2.65

6.2 Homogeneous Wettability Modelling

Figures 6.9 to 6.11 show the results from the three models for the homogeneous water-wet case, the homogeneous oil-wet case plus a third case utilising the oil-wet relative permeability and the water-wet capillary pressure curves. The reason for considering this third case is to help understand the differences between the water-wet and oil-wet cases.
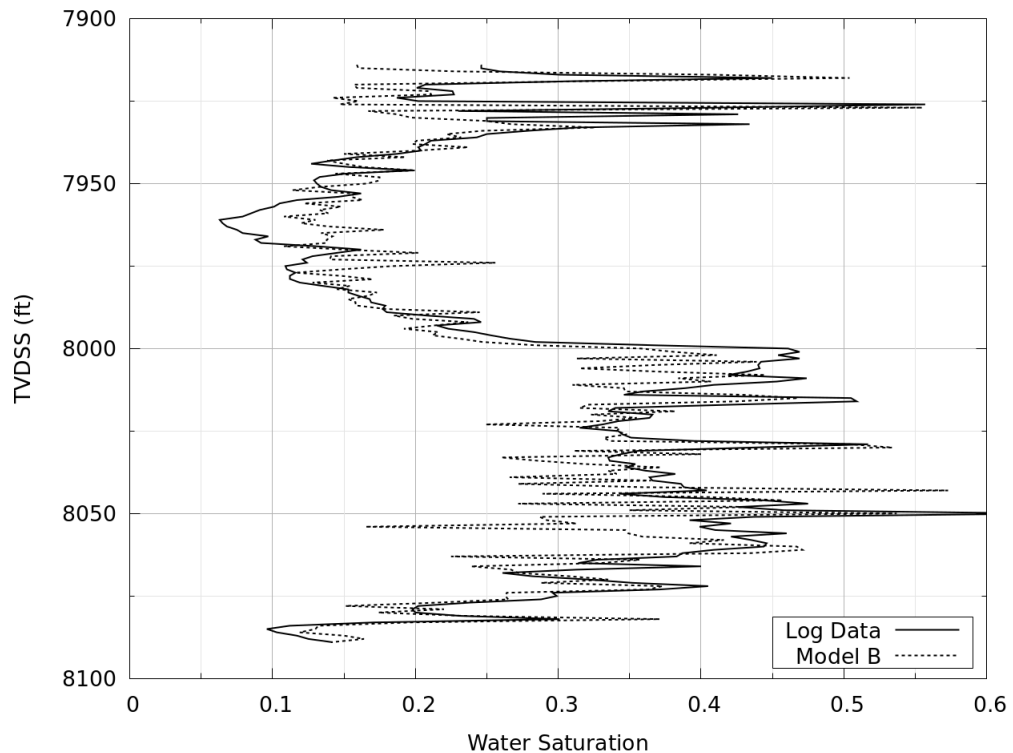
Figure 6.8: Initial water saturation for Model B compared with logged water saturation from well 21/30-8

The results are plotted against cumulative pore volume injection. To put this in perspective, the cumulative water injection in the Guillemot A field to date is less than 0.5 pore volumes and, at current injection rates, it will take at least a further 20 years to reach a cumulative injection of 1 pore volume.

All three model predict earlier water breakthrough for the oil-wet case and an extended tail of oil production at high watercut. For water-wet conditions, the water breakthough is delayed but the watercut rises more rapidly and the tail production is less. These results are consistent with conventional observations of oil-wet versus water-wet behaviour in core flooding experiments (Salathiel, 1973; Anderson, 1987c).

However, the difference between water-wet and oil-wet conditions are greater for the more heterogeneous Models B and C. In particular, the cross-over point, where the oil recovery from the oil-wet case exceeds that from the water-wet case, is significantly delayed (from 0.64 pore volume injection to greater than 1.0).

The third case, with oil-wet relative permeability and water-wet capillary pressure curves, shows that the effect of including the oil-wet capillary pressure is to bring forward the water breakthrough time and decrease the oil recovery. Whereas the effect of including the oil-wet relative permeability
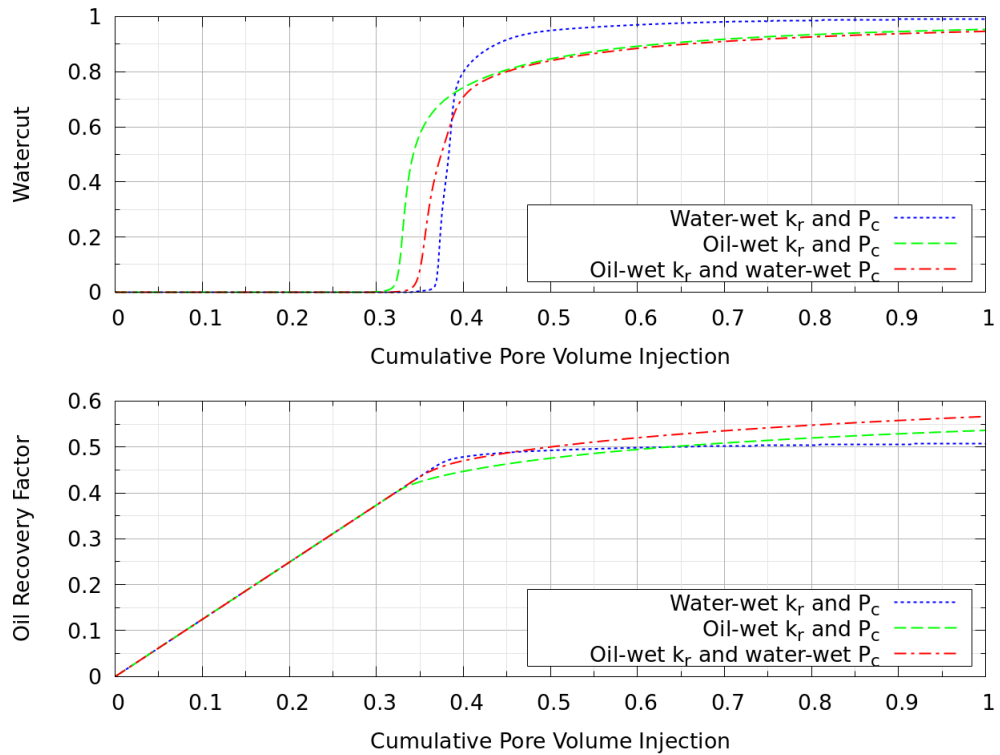
Figure 6.9: Model A results for homogeneous wettability cases
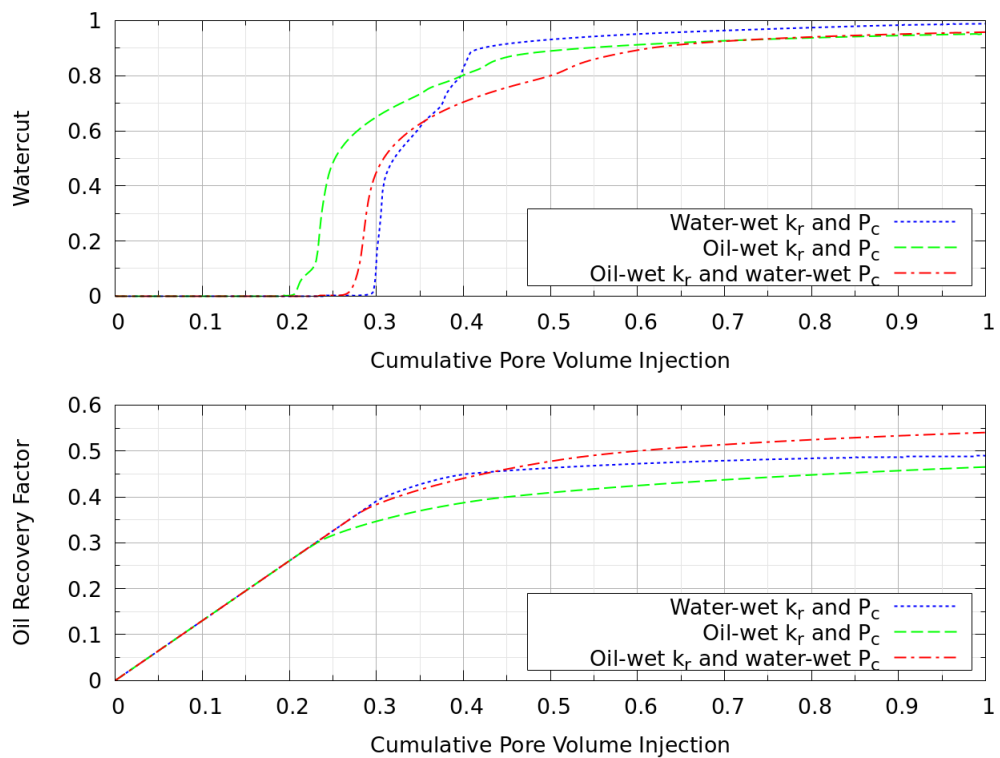
Figure 6.10: Model B results for homogeneous wettability cases

is to decrease the watercut after breakthrough. In the more heterogeneous Models B and C, the effects of changing relative permeability and capillary
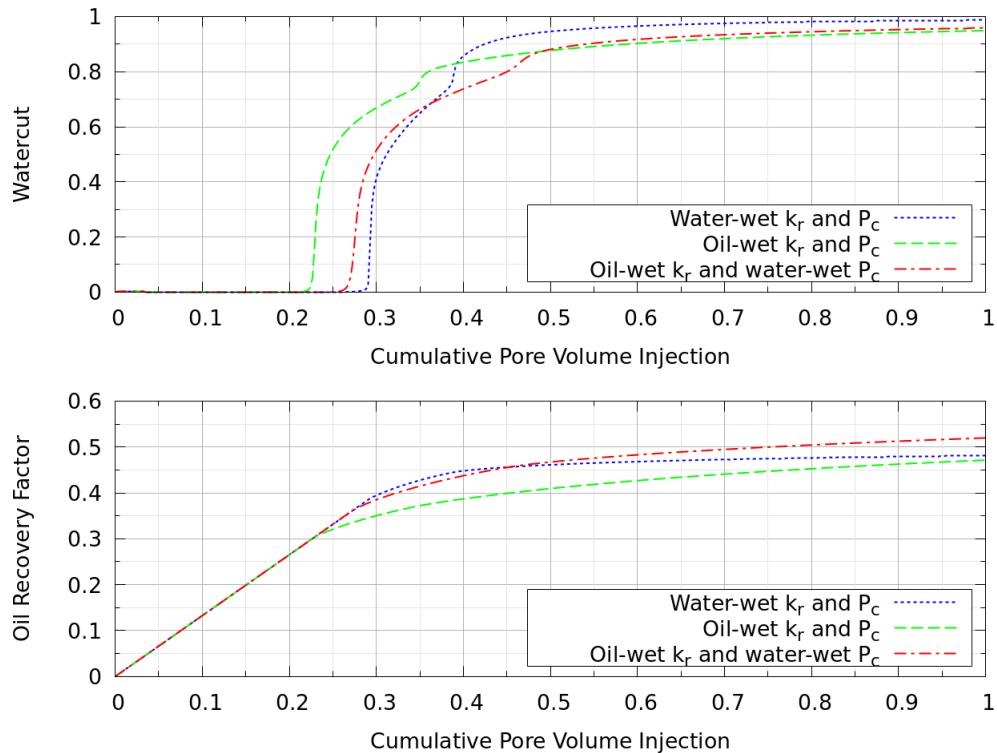
Figure 6.11: Model C results for homogeneous wettability cases

pressure are comparable whilst the relative permeability is more significant in Model A.

Figures 6.12 and 6.13 show the waterflood pattern after 0.25 pore volume injection for the three models in the water-wet and oil-wet cases (injection is from left to right). Note that models B and C in the oil-wet case are producing circa 50% watercut at this point.

It is clear that the low permeability intervals, particularly the Lower Fulmar, are better swept in the water-wet case. This is because water imbibes into these areas as they have a high positive capillary pressure. In contrast, the low permeability areas are poorly swept in the oil-wet case because they have a large negative capillary pressure and the high permeability areas are well swept because the residual oil saturation is low. This is consistent with capillary force barriers observed in oil-wet reservoirs (Namba and Hiraoka, 1995; Muneta et al., 2004).

In the oil-wet case the underlying permeability heterogeneity has a strong influence on the waterflood pattern, particularly in Model C (Figure 6.13 bottom). Not only is the recovery a function of wettability, but the large scale distribution of the remaining oil at any intermediate time is also a function of wettability.
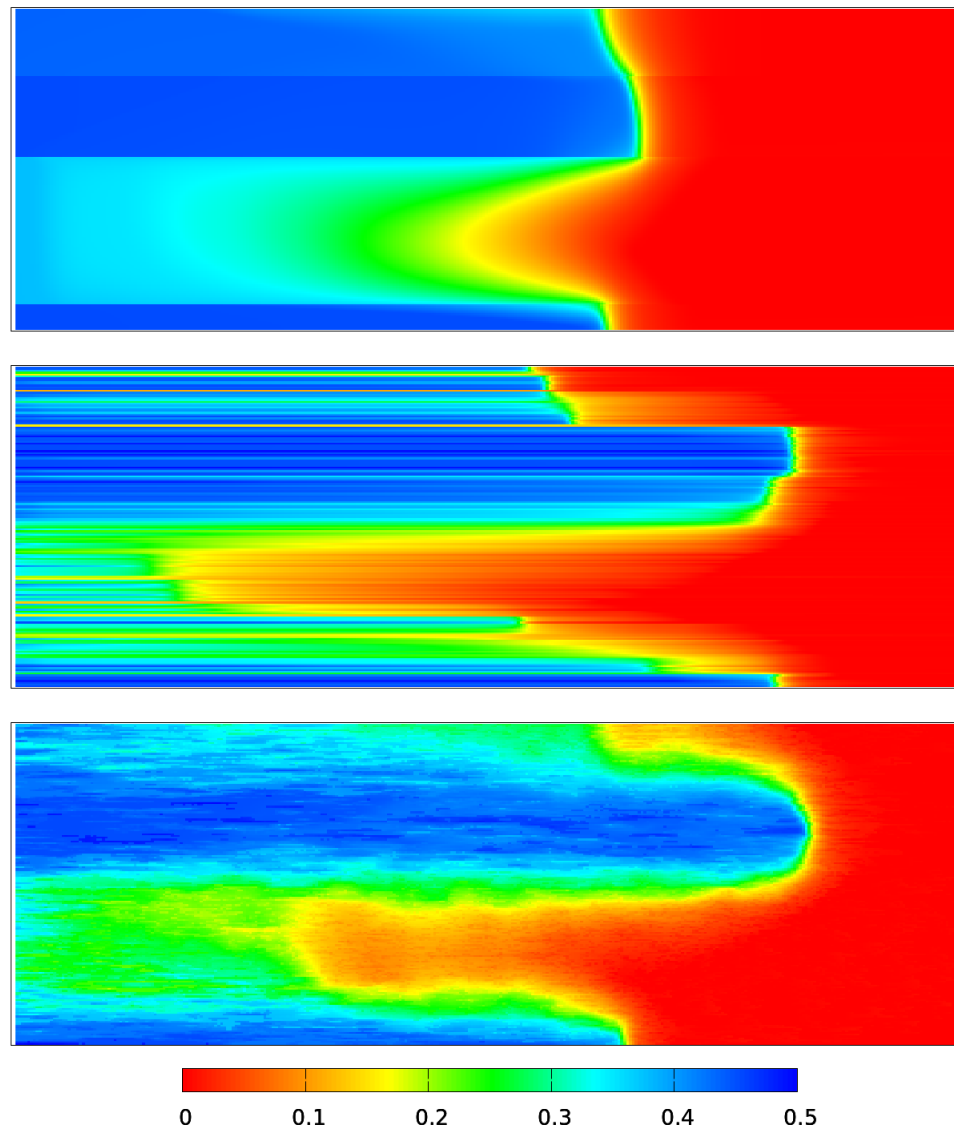
Figure 6.12: Change in water saturation after cumulative injection of 0.25 pore volumes for water-wet conditions, top: model A, middle: model B, bottom: model C

6.3 Heterogeneous Wettability Modelling

Three heterogeneous wettability scenarios have been considered.

Random wettability case assumes the wettability is distributed at random with no correlation with any other property.

High permeability oil wet (HPOW) case assumes that areas with permeability greater than 20 mD are oil-wet and areas less than 20 mD are water-wet.

Low permeability oil wet (LPOW) case assumes that areas with permeab-
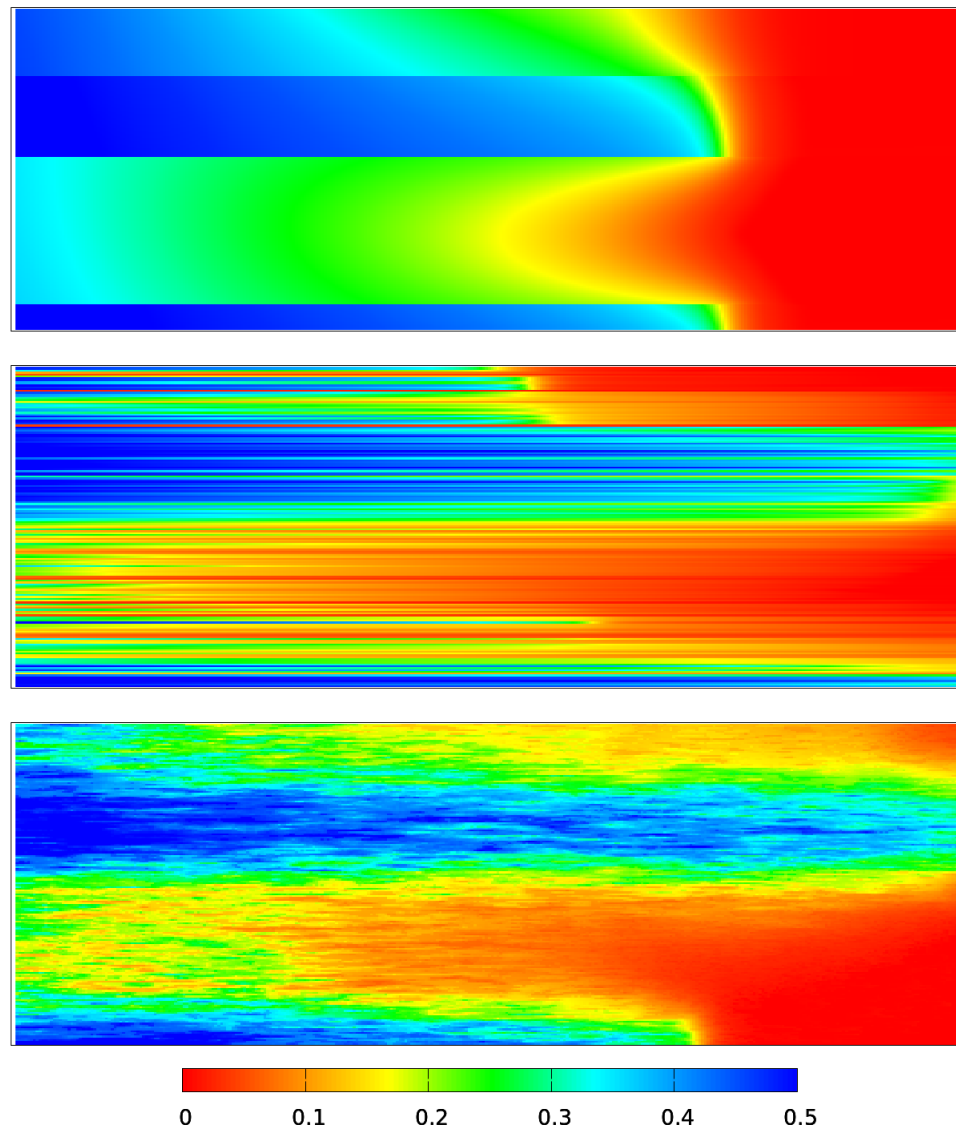
Figure 6.13: Change in water saturation after cumulative injection of 0.25 pore volumes for oil-wet conditions, top: model A, middle: model B, bottom: model C

ility less than 20 mD are oil-wet and areas greater than 20 mD are water-wet.

The threshold of 20 mD in the HPOW and LPOW cases was chosen because this is approximately the median permeability in Model B.

Figures 6.14 to 6.16 show the results from the three models where the random wettability case has half of the model water-wet and half oil-wet. Figure 6.17 shows the oil recovery as a function of the fraction of the reservoir which is water wet for random wettability cases. Also show on this figure are the results from the HPOW and LPOW cases. Figure 6.18 shows the average residual oil saturation for the same models.

As expected, the HPOW case has the highest recovery for all models. The high permeability areas have a low residual oil saturation and the low permeability areas benefit from capillary imbibition of water.

Of particular interest is the fact that the random wettability cases yield lower recovery than the water-wet and oil-wet cases. Furthermore, the oil recovery as a function of the water-wet fraction (Figure 6.17) exhibits a minimum which is actually lower than the LPOW case. This is in contrast to the microscale observation that mixed and fraction wettability yield higher recovery than strong water and oil wettability (Jadhunandan and Morrow, 1995; McDougall and Sorbie, 1993).

Figure 6.15 shows that the water breakthrough time in the random wettability case is very similar to the HPOW case and subsequently the watercut behaviour is similar to the LPOW case. This observation suggests that the random distribution of wettability both inhibits flooding of the lower permeability areas and accelerates water movement in the high permeability areas. This is supported by the waterflood patterns for model C shown in Figure 6.19.
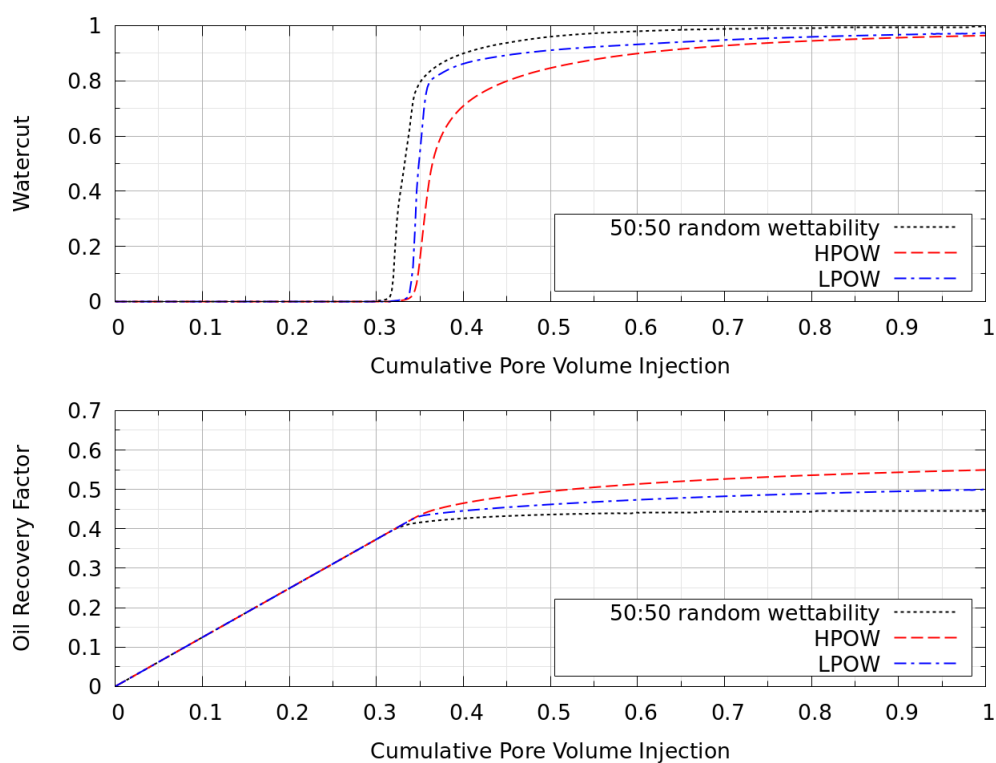
Figure 6.14: Model A results for heterogeneous wettability cases
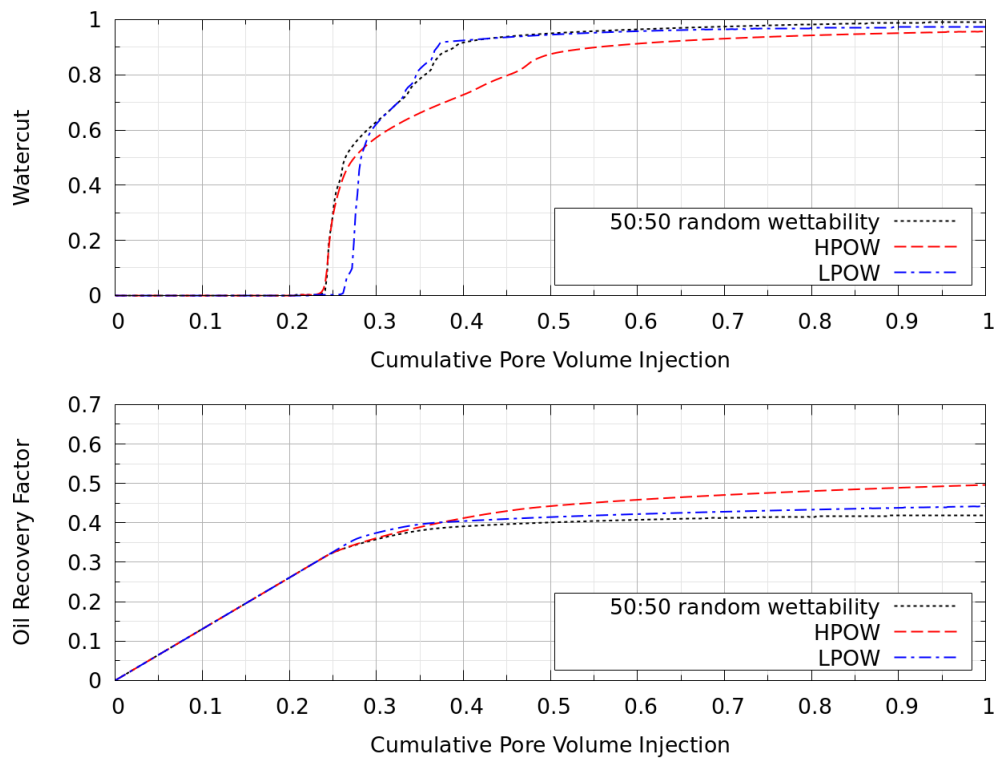
Figure 6.15: Model B results for heterogeneous wettability cases
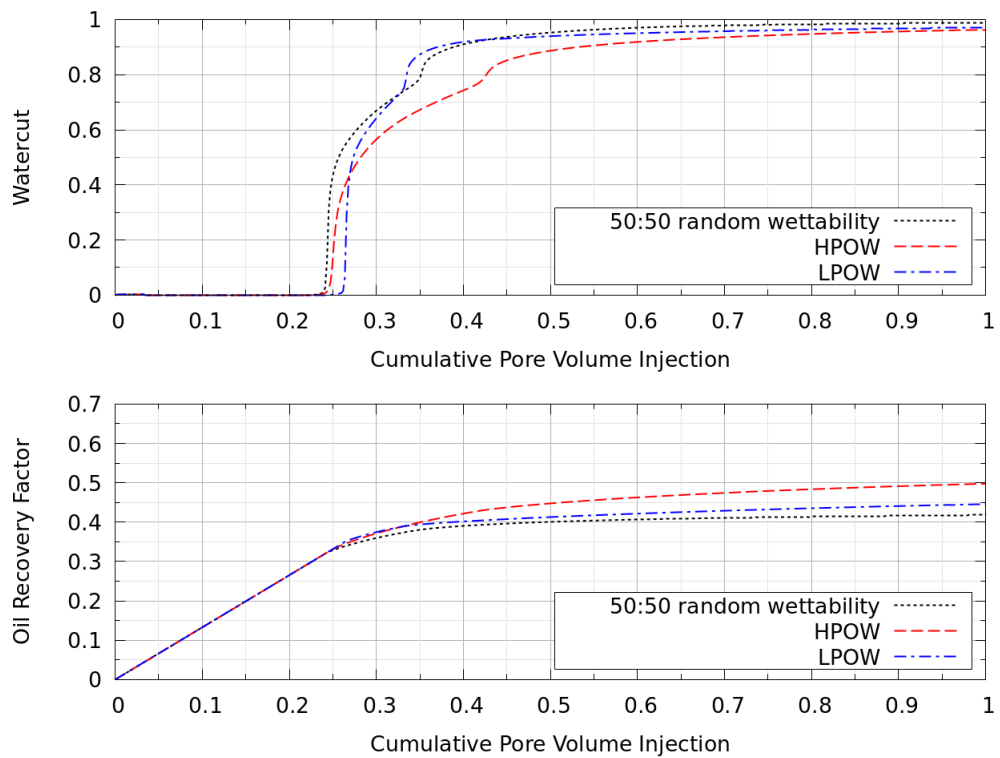
Figure 6.16: Model C results for heterogeneous wettability cases
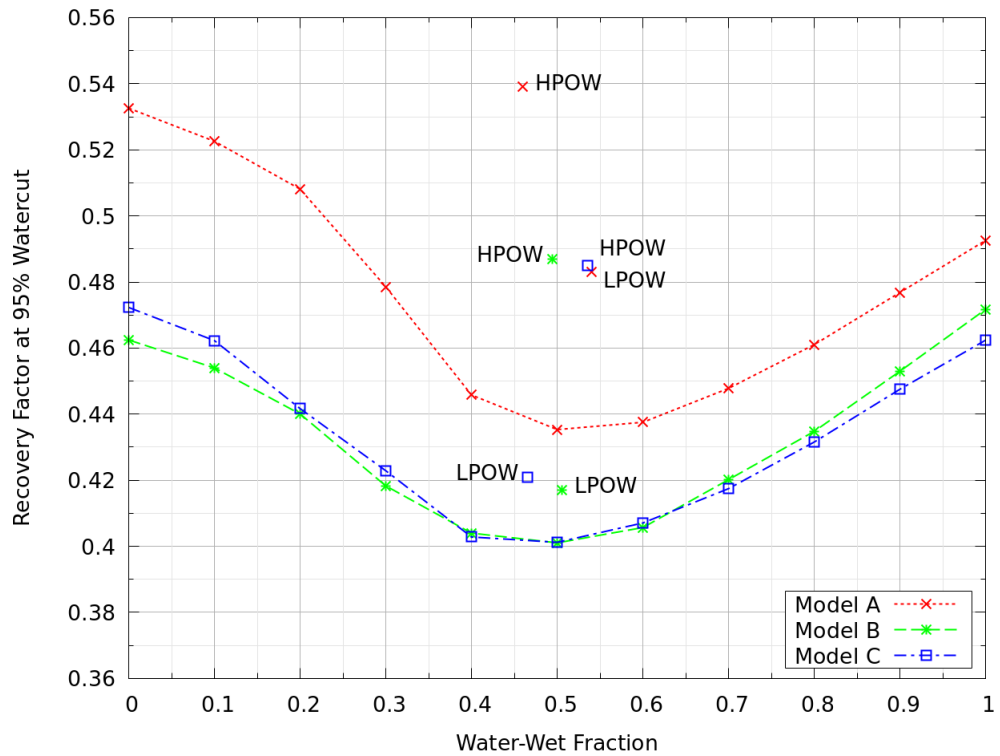
Figure 6.17: Oil recovery at 95% watercut as a function of water-wet reservoir fraction showing random wettability, HPOW and LPOW cases
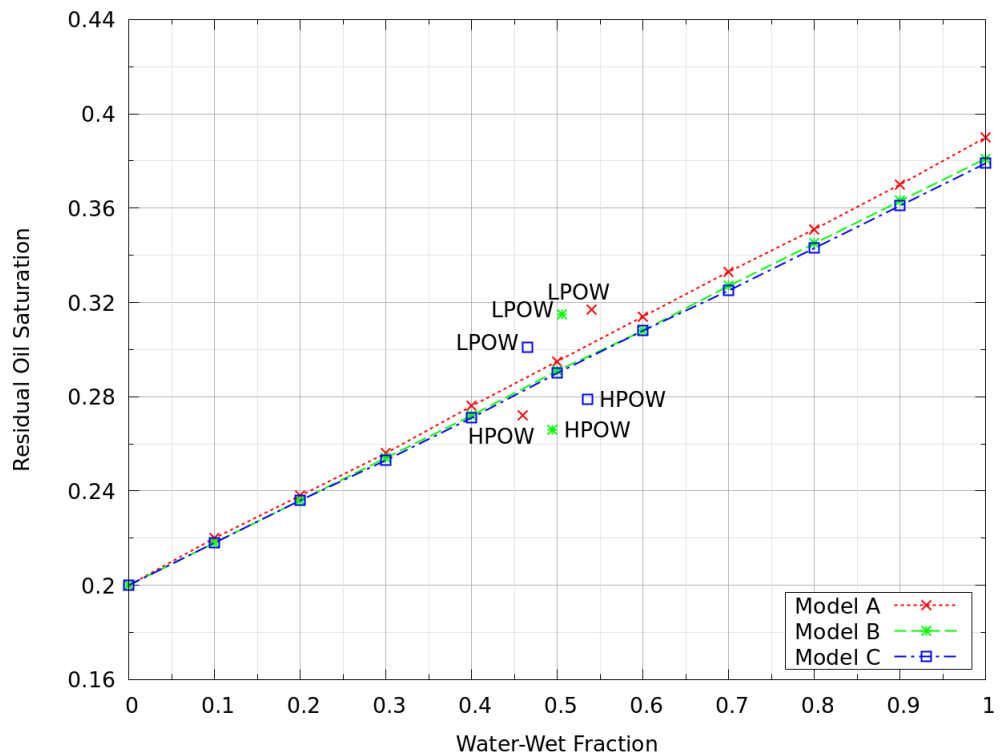
Figure 6.18: Pore volume weighted average residual oil saturation as a function of water-wet reservoir fraction showing random wettability, HPOW and LPOW cases
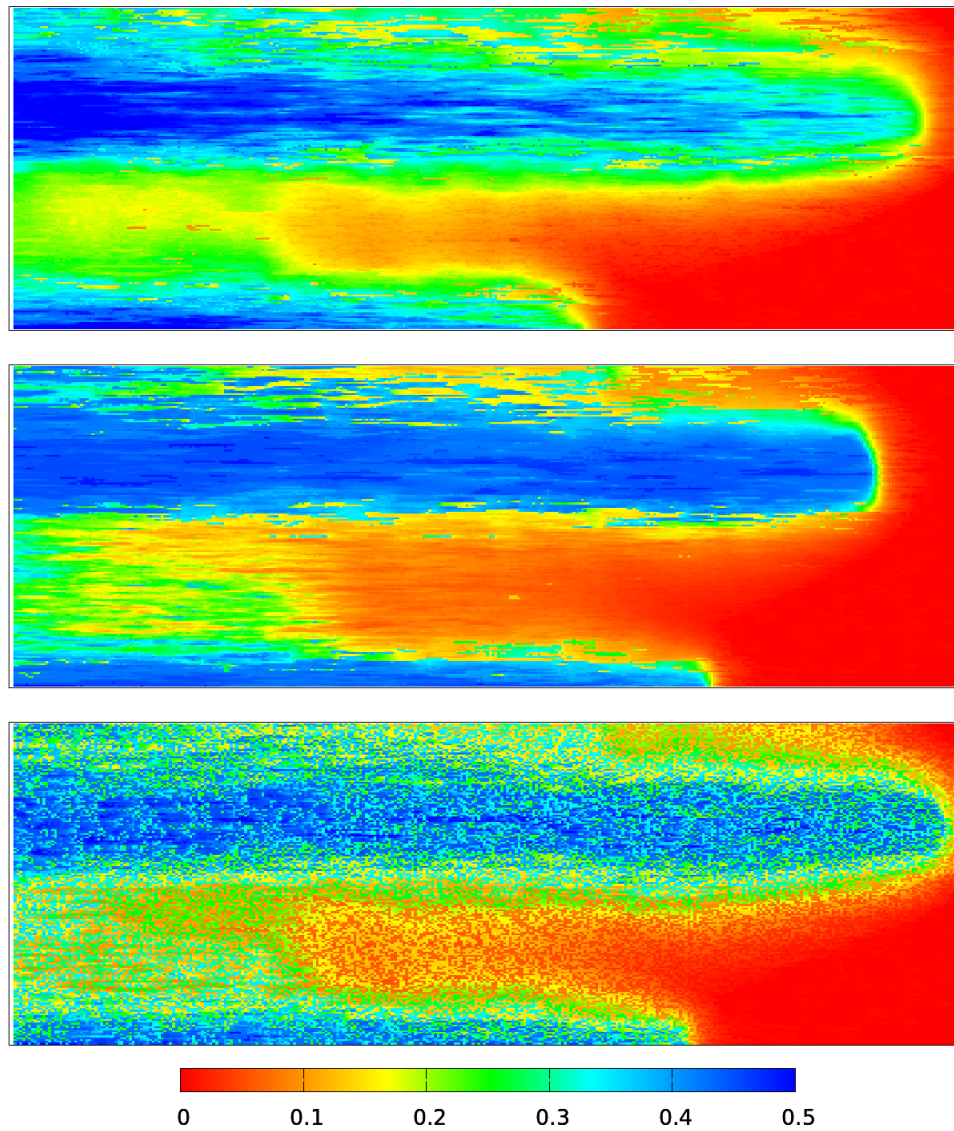
Figure 6.19: Change in water saturation after cumulative injection of 0.25 pore volumes for model C, top: HPOW case, middle: LPOW case, bottom: 50:50 random wettability

Chapter 7

Conclusions

But the Cat keeps his side of the bargain too. He will kill mice, and he will be kind to Babies when he is in the house, just as long as they do not pull his tail too hard. But when he has done that, and between times, and when the moon gets up and night comes, he is the Cat that walks by himself, and all places are alike to him.

— Rudyard Kipling, Just So Stories

7.1 Summary

Understanding multiphase flow in natural porous media is important for several engineering applications such as optimising recovery from oil reservoirs, planning CCS projects and managing fresh water aquifers. Imaging and modelling at the pore scale can improve our understanding of the physics, but complex systems with a wide range of pore sizes remain a challenge because of the combined effect of limited resolution and limited field of view of imaging technologies.

Multiscale SEM and µCT imaging techniques have been used to image the pore space geometry and topology of ten sandstone samples from the Guillemot A field and five from the Vanguard field. These sandstones were buried to depths of around 8000-9000 ft and subjected to multiple diagenetic processes which has resulted in complex pore spaces with a wide range of pore sizes.

Established techniques were used to filter and segment the SEM and µCT images of the selected samples to discriminate the pore space and the rock

matrix.

The pore space of the samples was characterised from 2D and 3D imaging information to quantify the pore size and pore coordination number distributions. The pore space was divided into a set of connected elements each of which is characterised by an inscribed radius, volume and shape factor. The methodology was validated by calculating the single phase permeability from 2D/3D images and FRF from 3D images and comparing with measured data. The characterisation displays differences firstly between 2D and 3D images and secondly between images of different resolution. To better compare 2D and 3D characterisation, a random series of 2D cross-sections were extracted from a set of 3D µCT volumes and the key statistical parameters compared.

A stochastic algorithm has been developed to generate pore networks in 2D and 3D based on statistical information. The stochastic algorithm has a recursive process that naturally fits into multiscale pore structure hierarchies and naturally leads to large pores having high coordination and smaller pores having lower coordination. The algorithm starts at the largest pore size and progressively adds smaller elements in a process that honours the connectivity function and honours the mean and SD of the pore coordination as a function of radius. The algorithm does not randomly distribute pore elements in space, rather the largest elements are randomly distributed and the smaller pore elements are positioned next to larger elements and linked to them in order to honour the connectivity information.

To illustrate and validate the stochastic algorithm, a suite of models was generated and the calculated permeability and FRF compared with measured data. Multiphase properties capillary pressure, RI and relative permeability were also generated from the stochastic models using quasi-static PNM and compared against measured data from the Guillemot A and Vanguard fields.

Relative permeability and capillary pressure functions were generated for the Guillemot A field from stochastic pore networks. The flow functions were used in a continuum field scale reservoir simulation model to examine the impact of different wettability assumptions and the effect of wettability heterogeneity.

7.2   Conclusions

- The SEM images acquired in this work have higher resolution, better definition of microporosity, better signal to noise ratio and greater field of view in comparison with the µCT images.

- The porosity from analysis of SEM and µCT images is generally in agreement with the macroporosity estimated from capillary pressure data from the core plug samples.

- Despite the combination of multiple complex diagenetic processes influencing the pore space architecture, the pore size distributions and coordination number distributions show some regular character that can be represented by empirical models.

- Although there are differences between the depositional environments for the Guillemot A and Vanguard sands, the pore architectures display common features which are most likely a consequence of the regularisation from the multiple diagenetic processes which have strongly affected both fields.

- The pore size distributions can be fitted to modified power law (Pareto) distributions with an exponential cut-off at large radii. The scaling index, parameter α, from high resolution 2D image analysis varies from approximately 1.2 to 1.6. In contrast, the scaling index from 3D µCT image analysis varies from approximately 2 to 3.

- The frequency distribution of coordination numbers follows an exponential model where $\Pr(Z) \propto exp(-aZ)$ and the constant a is in the range 0.5 to 0.7 for 2D image analysis and 0.4 to 0.6 for 3D image analysis.

- For a given pore size, the coordination number is approximately normally distributed. The mean and standard deviation of the coordination number are power law functions of the pore radius where the scaling exponent varies from approximately 0.3 to 0.5 for 2D image analysis and from 0.5 to 0.9 for 3D image analysis.

- The shape factor of pore elements is approximately normally distributed with a mean of circa 0.06 and a SD close to 0.01 for all samples analysed. The shape factor distribution is not substantially different between 2D and 3D image analyses and therefore it can be estimated directly from 2D imaging.

- Image resolution has a strong effect on both the pore size and coordination number distributions. The pore size distribution r_0 parameter is primarily controlled by image resolution. The coordination number of larger pores is a function of the smallest resolvable pore and the mean coordination number as a function of pore radius increases uniformly for higher resolution images.

- The single phase permeability estimated from 2D SEM imaging shows fair agreement with laboratory measured data. The samples which have poor agreement are most likely explained by core plug heterogeneity and/or damage to the samples during preparation.

- The single phase permeability and FRF calculated from µCT images show good agreement with measured data although there is some variation between the X, Y and Z directions not consistent with the expected anisotropy. The directional variation is greater for low porosity samples, suggesting that the µCT images do not capture REVs.

- Relative permeability calculated from the µCT images displays some differences between X, Y and Z directions. The poorer connected and lower porosity samples have lower relative permeability and greater variation between directions.

- Analysis of random 2D sections extracted from 3D volumes shows that the 3D pore size scaling index, α, is approximately 25% higher than the 2D scaling index. The analysis also shows that the r_1 parameter controlling the exponential cut-off of the distribution is approximately 25% lower from the 3D analysis than from the 2D analysis.

- Analysis of random 2D sections extracted from 3D volumes shows that the mean 3D coordination number for a given radius is related to the mean 2D coordination number for the same radius. Based on the samples analysed here, the relationship between 3D and 2D mean coordination numbers is a power law with a scaling exponent of 1.5.

- 3D pore size and coordination number distributions can be estimated from 2D imaging data for isotropic porous media.

- Realistic pore networks can be constructed from a stochastic algorithm using statistical information from 2D imaging such as SEM. In principle, this allows high resolution information from SEM to be incorporated into pore networks plus multiple stochastic realisations and networks

with arbitrary domain sizes can be generated to overcome the limitations of μCT imaging.

- The WPSL construction is an attractive model for porous media because there is a natural relation between pore element size and coordination number. The recursive process also naturally fits into multiscale pore structure hierarchys.

- Stochastic pore networks based on imaging information from the Guillemot A field reproduce a realistic range of single phase permeability and FRF commensurate with the ranges observed in the Guillemot A field. This suggests that the stochastic algorithm reproduces realistic 3D connectivity of the pore space.

- Relative permeability calculated from stochastic pore networks has good agreement with relative permeability from the plug 44 μCT network but poorer agreement with the lower porosity and more poorly connected samples.

- Relative permeability from PNM has fair agreement with measured imbibition data from the Guillemot A field assuming that the reservoir is oil-wet. The comparison with the drainage relative permeability from the Vanguard field is poorer potentially because these samples are lower porosity.

- Both μCT networks and stochastic pore networks show that relative permeability is lower for more poorly connected and lower porosity systems.

- Field scale modelling of waterflooding shows that wettability and its heterogeneity have a significant impact on oil recovery and distribution of remaining oil. In particular, imbibition capillary pressure has a significant effect if the reservoir has large permeability/porosity heterogeneity.

- A heterogeneous wettability distribution can result in lower oil recovery than homogeneous oil-wet or homogeneous water-wet assumptions for the same permeability/porosity reservoir.

- Pore scale imaging and modelling provides valuable reservoir characterisation information which can be incorporated into reservoir scale simulation modelling.

7.3   Further Work

- This project has examined samples from two North Sea sandstone reservoirs. It would be beneficial to apply the same techniques to other samples from different depositional environments, reservoirs with more or less heterogeneity, different rock type (e.g. chalk, limestone) and samples that are less heavily cemented or diagenetically influenced. This would confirm the observed trends and conclusions regarding the pore space characterisation. In particular, the identified relationships between 2D and 3D characterisation should be confirmed by further analysis.

- Legacy SCAL data from the Guillemot A and Vanguard fields were used in this project. However, some discrepancies between model predictions and laboratory measurements have been highlighted, particularly for relative permeability and there is some suspicion about the reliability of the SCAL data. Ideally, some better quality controlled and more reliable relative permeability data should be obtained for comparison with the PNM.

- This project used quasi-static PNM which is computationally efficient and permits large networks to be simulated, however there are some known deficiencies with quasi-static models, particularly with imbibition in oil-wet media. Dynamic PNM techniques have been developed by a number of other workers to address some of these deficiencies by incorporating viscous effects. The networks generated here should be investigated with dynamic PNM to see if this improves the match to measured data, particularly for imbibition.

- The stochastic pore network algorithm is not ideal in all cases and could be improved. In particular, the connectivity function is not always honoured at small radii where the connectivity is very high and a large number of links need to be inserted into the model. Adding further connectivity where the connectivity is already high is not expected to have a significant impact, however this should be investigated further and the issue resolved.

- Stochastic modelling sensitivities were investigated in this project to try and identify the impact of pore space characterisation parameters on relative permeability behaviour. This was not entirely successful as only qualitative trends could be identified. Further work could be

performed to identify the key parameters (e.g. porosity, connectivity, tortuosity and pore size distribution). A problem with the methodology is the variability due to different stochastic realisations of the same model; which can be addressed using models with larger domains and/or taking the average of multiple realisations. This needs to be examined in more detail and an optimal solution identified.

- In this project, multiphase flow functions derived from PNM were used in reservoir simulation modelling. The assumptions of homogeneity and the dominance of capillary forces should be scrutinised further. In general, the upscaling of multiphase flow functions from pore scale to the grid block scale is an important subject that warrants further investigation.

Appendix A

Guillemot A Field Data

Porosity was measured by helium porosimeter, permeability was measured by nitrogen permeameter and the data were Klinkenberg corrected by the laboratory (Fyfe, 1979; Roberts, 1982, 1983a; Kirk, 1984).

Formation resistivity factor (FRF) was measured at ambient temperature and a confining pressure of 100 bars using a synthetic formation brine (Cornwall, 1984a; Roberts, 1983b).

Air-brine capillary pressure was measured at ambient temperature conditions using the porous plate method with humidified nitrogen and a synthetic formation brine (Cornwall, 1984a). Resistivity index was measured in conjunction with the air-brine capillary pressure. When an equilibrium saturation was reached at an applied pressure, the sample was removed from the porous plate cell and the electrical resistance measured.

Figures A.4 and A.5 show lines for specific values of the Archie parameters m and n, where the electrical resistivity of a brine saturated porous medium is given by (Archie, 1942):

$$R = \frac{aR_w}{\phi^m S_w^n} \tag{A.1}$$

Mercury injection capillary pressure (MICP) was measured on whole core plug samples at ambient temperature (Van Benten, 1980a,b; Roberts, 1983b).

Figures A.6, A.7 and A.8 show the J-function (Leverett, 1941) including the contact angle (Rose and Bruce, 1949):

$$J = \frac{P_c}{\sigma \cos \theta} \sqrt{\frac{k}{\phi}} \tag{A.2}$$

Using the assumptions:

- Mercury: $\sigma = 486$ dyn/cm and $\theta = 139°$.

- Air-brine: $\sigma = 72$ dyn/cm and $\theta = 0°$.

Imbibition oil-water relative permeability was measured by a state method using a synthetic formation brine and a refined mineral oil. Cornwall (1984a) states that the core plugs were restored state. This typically means that they were oil saturated and stored at reservoir temperature for circa 40 days to restore the in-situ reservoir wettability (Anderson, 1986a). However, there are no details about the conditions and duration of this process. The relative permeability was measured at ambient temperature and a confining pressure of 300 psi by simultaneously injecting water and oil at controlled rates and monitoring the pressure difference across the core. The saturation was assumed to have reached a steady state condition when the pressure differential was stable for an extended period of time.

Table A.1: SCAL plug samples used for steady state imbibition relative permeability measurements

Well	Plug Sample	Zone	Helium Porosity	Permeability (mD)
21/30-8	29	Upper Fulmar	28.1%	179
21/30-8	70	Middle Fulmar	20.5%	29
21/30-8	157	Lower Fulmar	25.7%	133
21/30-8	233	Skagerrak	25.4%	375
21/30-8	369	Skagerrak	17.5%	61

Wettability was measured by the Amott test (Amott, 1959) at ambient pressure and temperature conditions using fresh state core plugs with a synthetic formation brine and depolarised kerosene (Cornwall, 1984b).
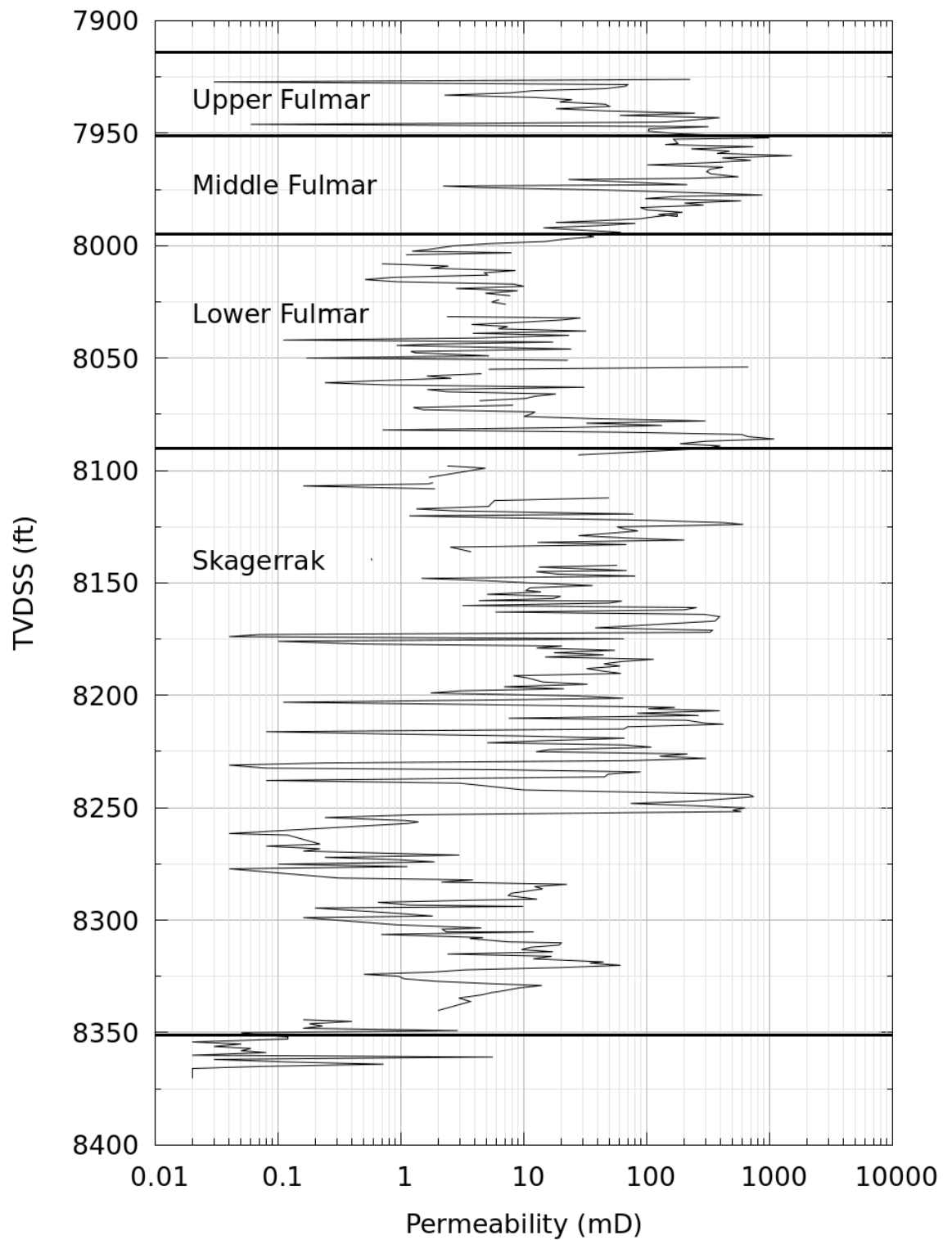
Figure A.1: Permeability vs depth: core plug data from well 21/30-8
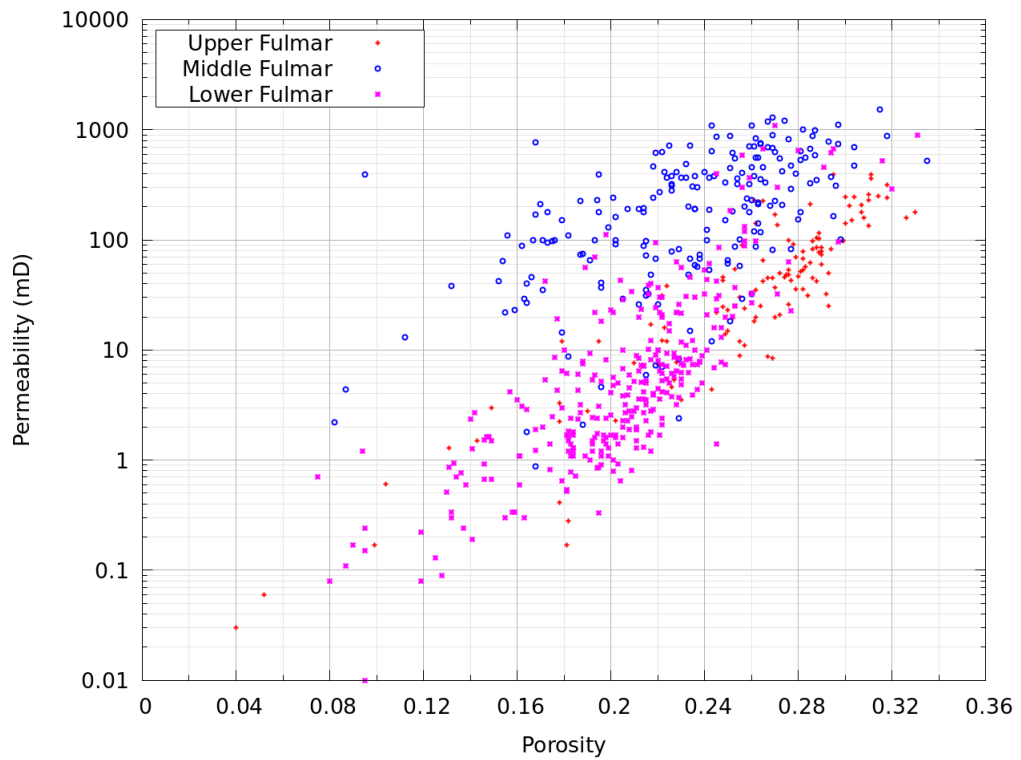
Figure A.2: Core permeability versus porosity for Fulmar samples
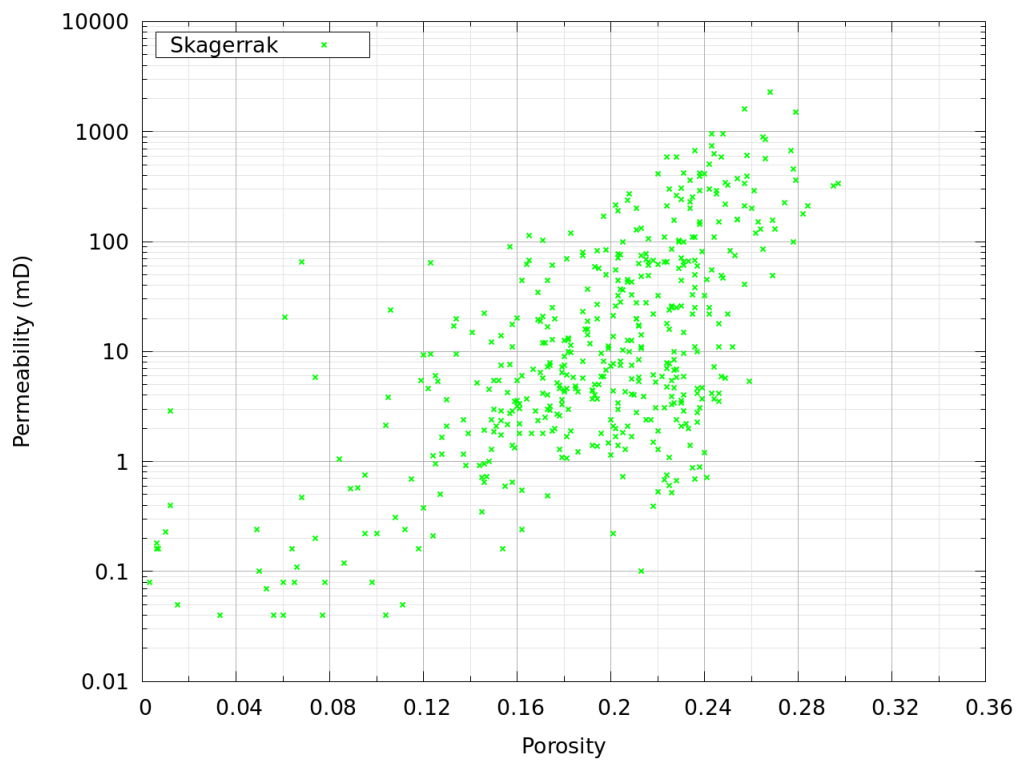
Figure A.3: Core permeability versus porosity for Skagerrak samples
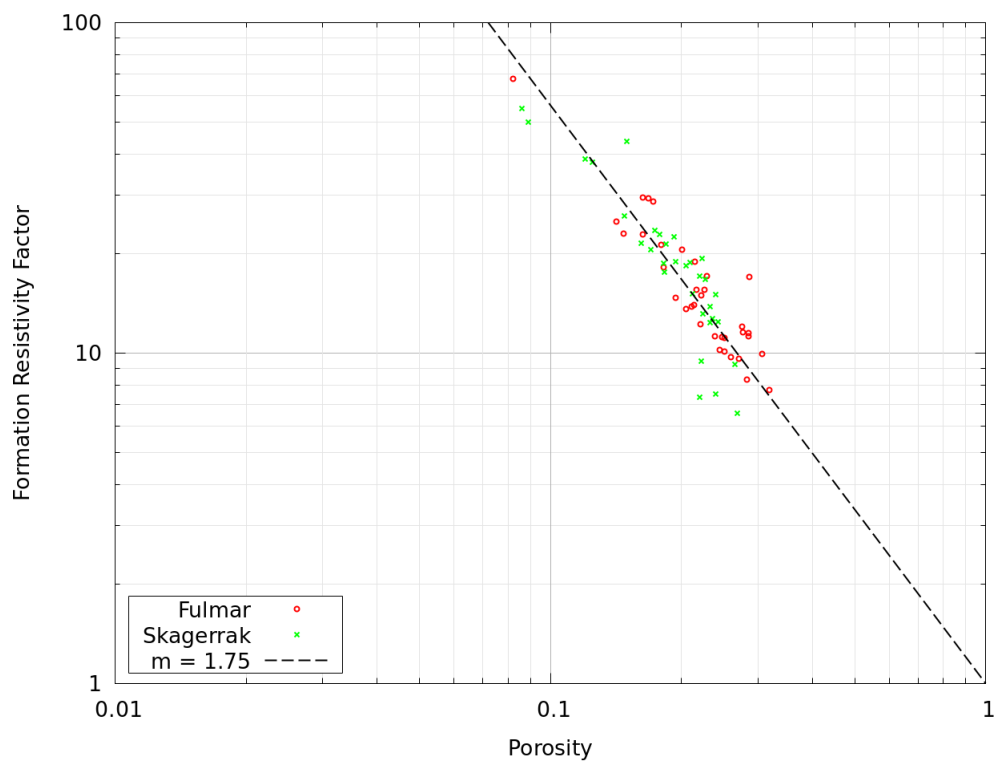
Figure A.4: Formation resistivity factor versus porosity
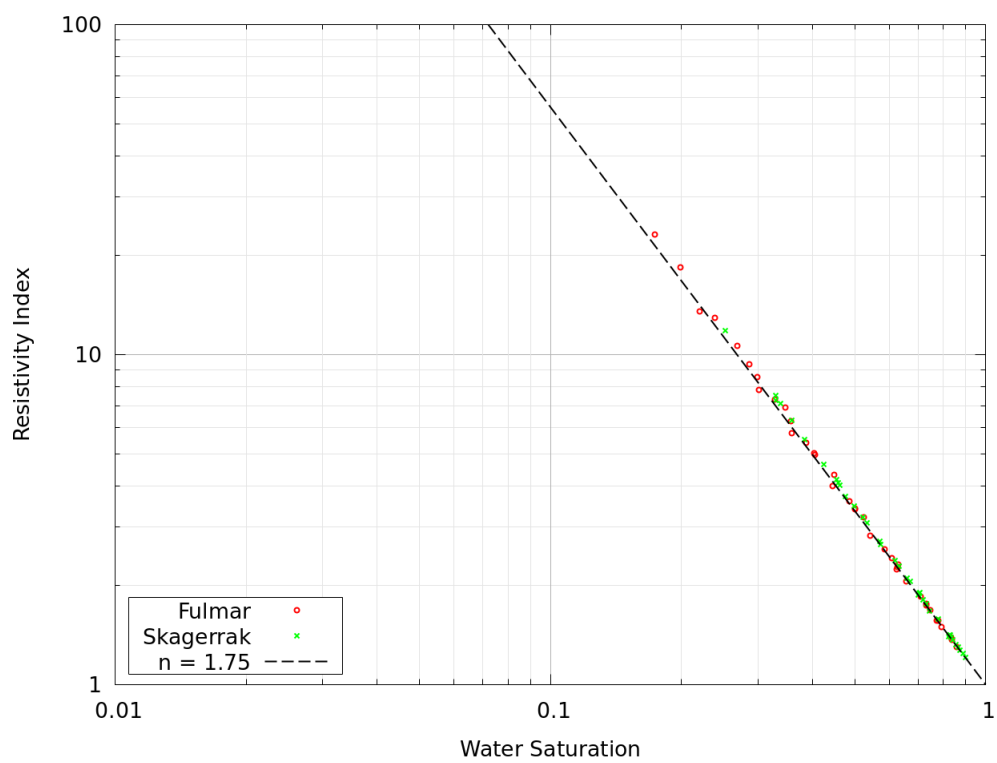
Figure A.5: Resistivity index versus water saturation
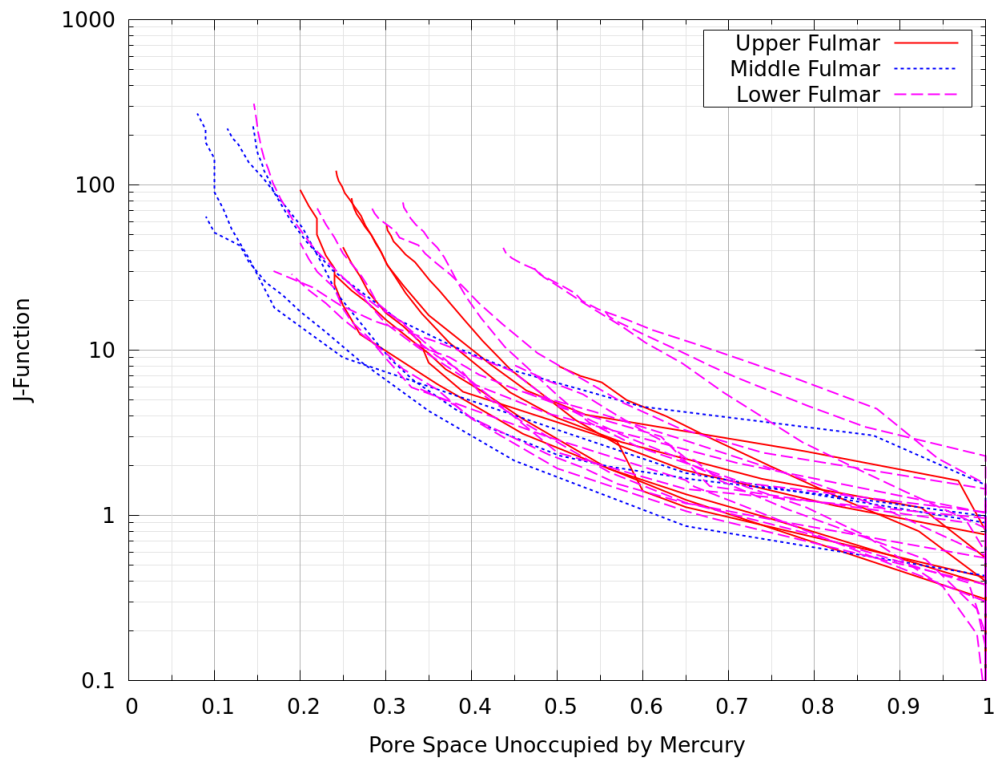
Figure A.6: MICP data for Fulmar sand core plug samples
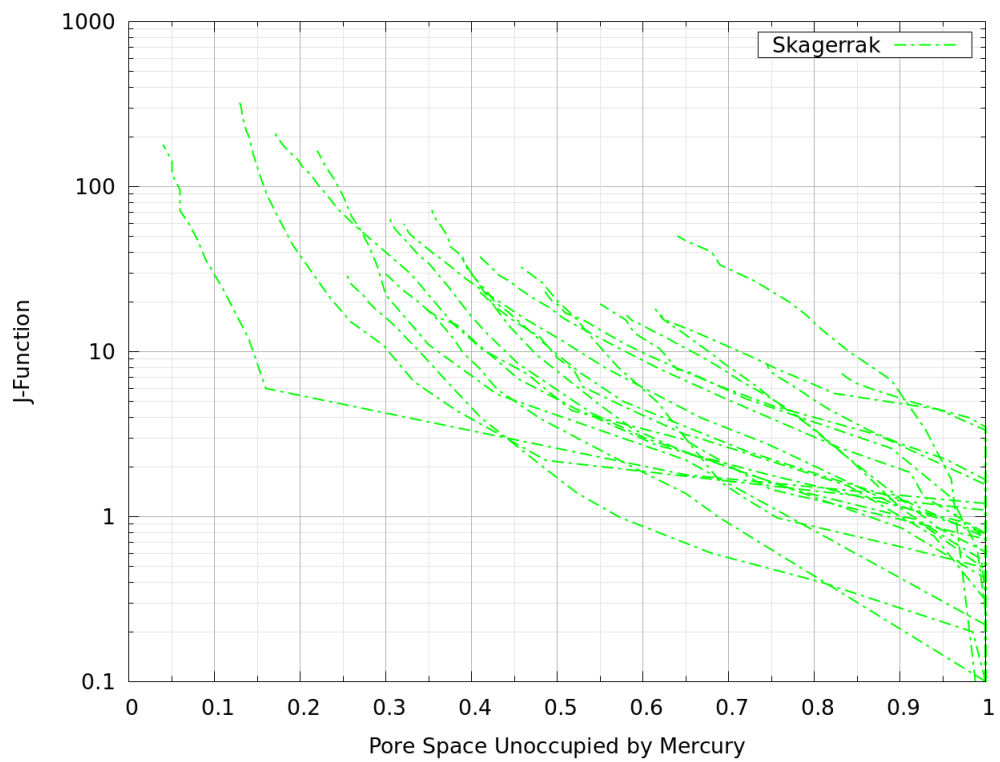
Figure A.7: MICP data for Skagerrak sand core plug samples
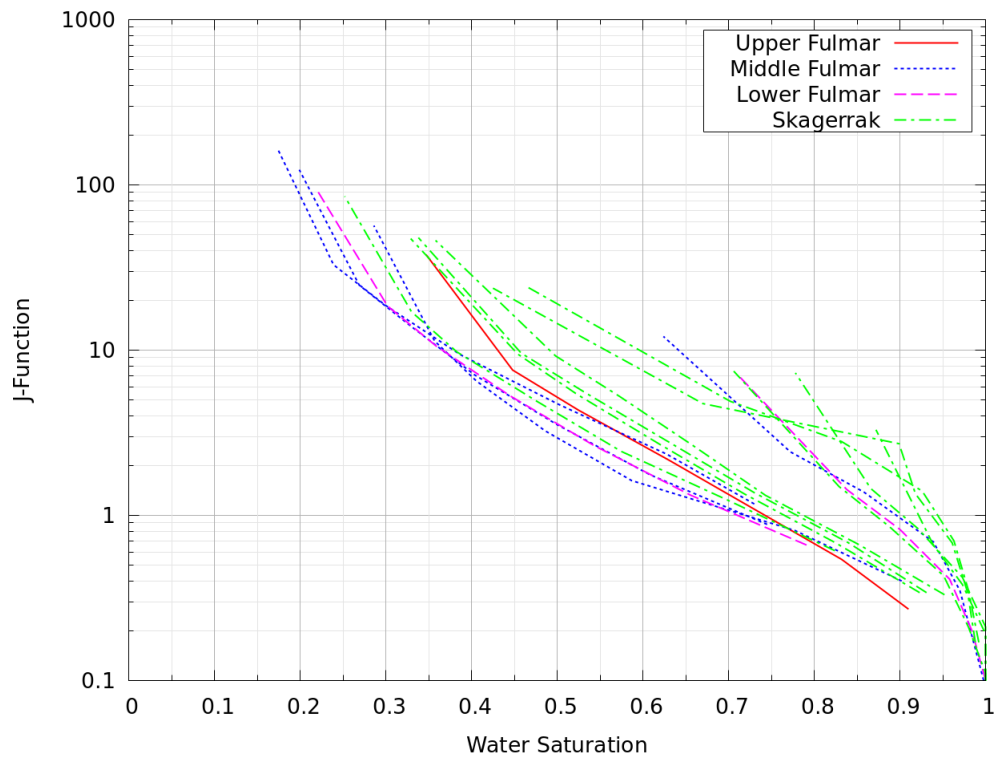
Figure A.8: Air-brine capillary pressure data
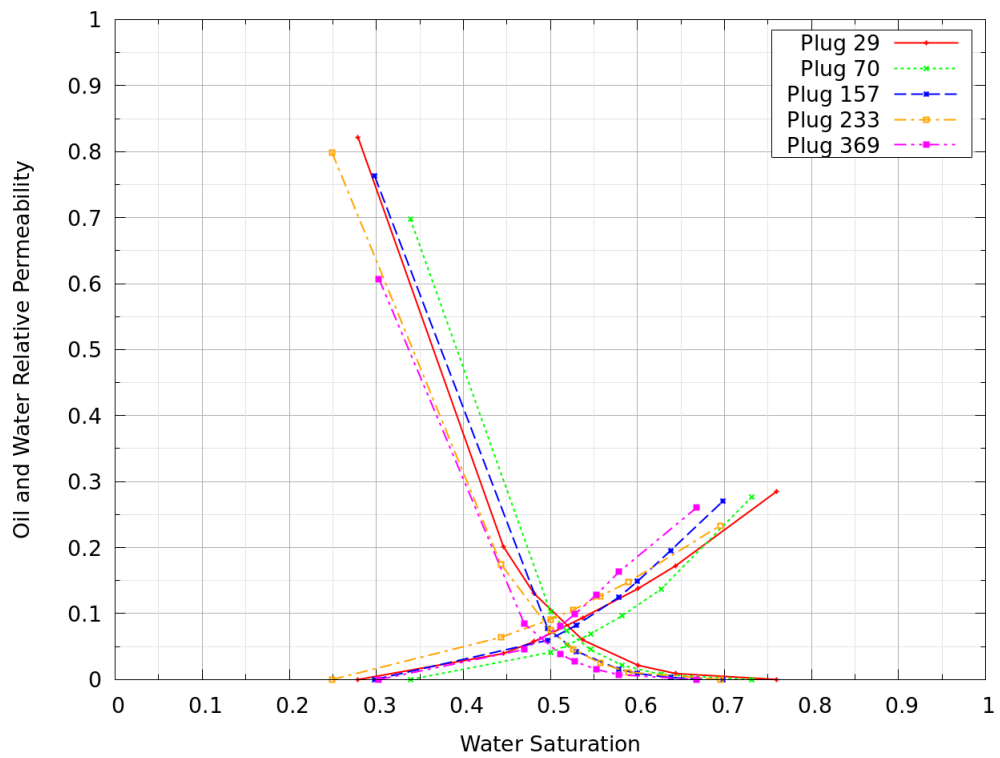
Figure A.9: Oil-water relative permeability imbibition direction
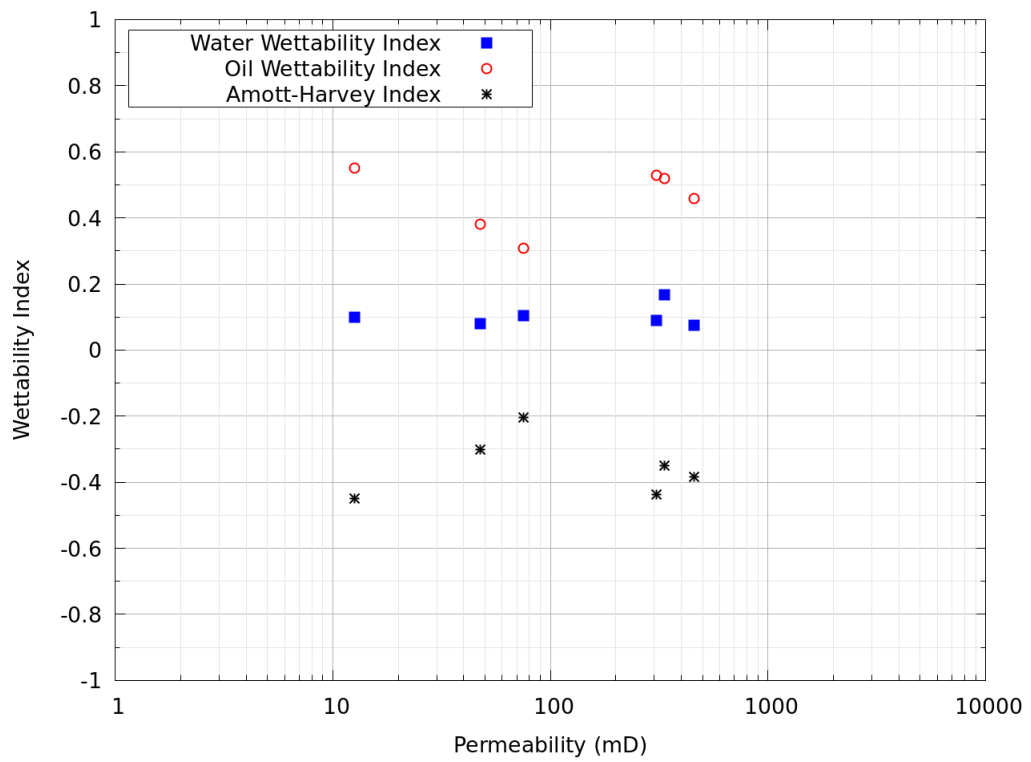
Figure A.10: Amott wettability indices as a function of permeability
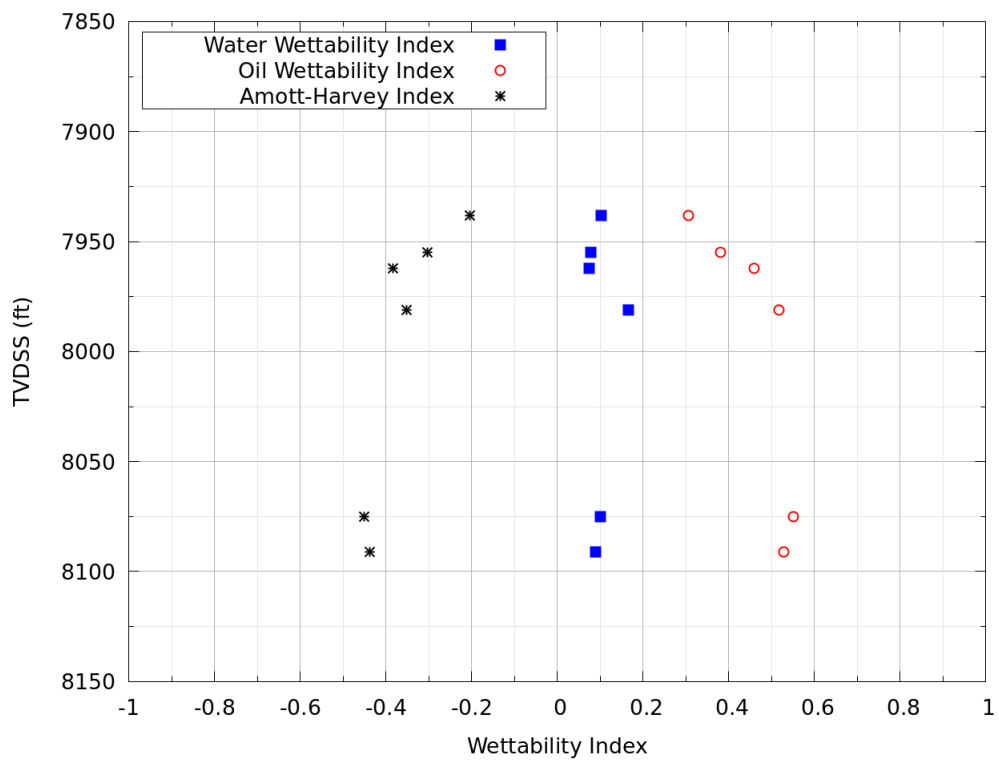
Figure A.11: Amott wettability indices as a function of depth

Appendix B

Vanguard Field Data

Porosity was measured by helium porosimeter, permeability was measured by nitrogen permeameter and the data were Klinkenberg corrected by the laboratory (Sutherland, 1984; Norrie, 1987, 1988a,b; Wyber, 1988; Williams, 1991).

Formation resistivity factor (FRF) was measured at ambient temperature and pressure using a synthetic formation brine (Maeso, 1988; Houston, 1989).

Air-brine capillary pressure was measured at ambient temperature conditions using the porous plate method with air and a synthetic formation brine (Lynn, 1985; Maeso, 1988; Houston, 1989). Resistivity index was measured in conjunction with the air-brine capillary pressure.

Figures B.4 and B.5 show lines for specific values of the Archie parameters m and n (Equation A.1).

Mercury injection capillary pressure (MICP) was measured on whole core plug samples at ambient temperature (Maeso, 1988).

Figures B.6 and B.7 show the Leverett J-function (Equation A.2) assuming:

- Mercury: $\sigma = 486$ dyn/cm and $\theta = 139°$.

- Air-brine: $\sigma = 72$ dyn/cm and $\theta = 0°$.

Drainage gas-water relative permeability was measured by a steady state method using nitrogen and a synthetic formation brine (Houston, 1989). The core plugs were cleaned using a cold-solvent flushing procedure using first toluene and then methanol. A synthetic formation brine was then injected into the plugs to miscibly displace the methanol. The relative permeability

was measured at ambient temperature and a confining pressure of 200 psi by simultaneously injecting gas and brine at controlled rates and monitoring the pressure differential across the core. The saturation was assumed to have reached a steady state condition when the pressure differential was stable for an extended period of time.

Table B.1: SCAL plug samples used for steady state drainage relative permeability measurements

Well	Plug Sample	Zone	Helium Porosity	Permeability (mD)
49/16-Q5	2C	B	20.8%	98
49/16-Q5	3C	B	18.4%	46
49/16-Q5	7C	C	23.3%	107
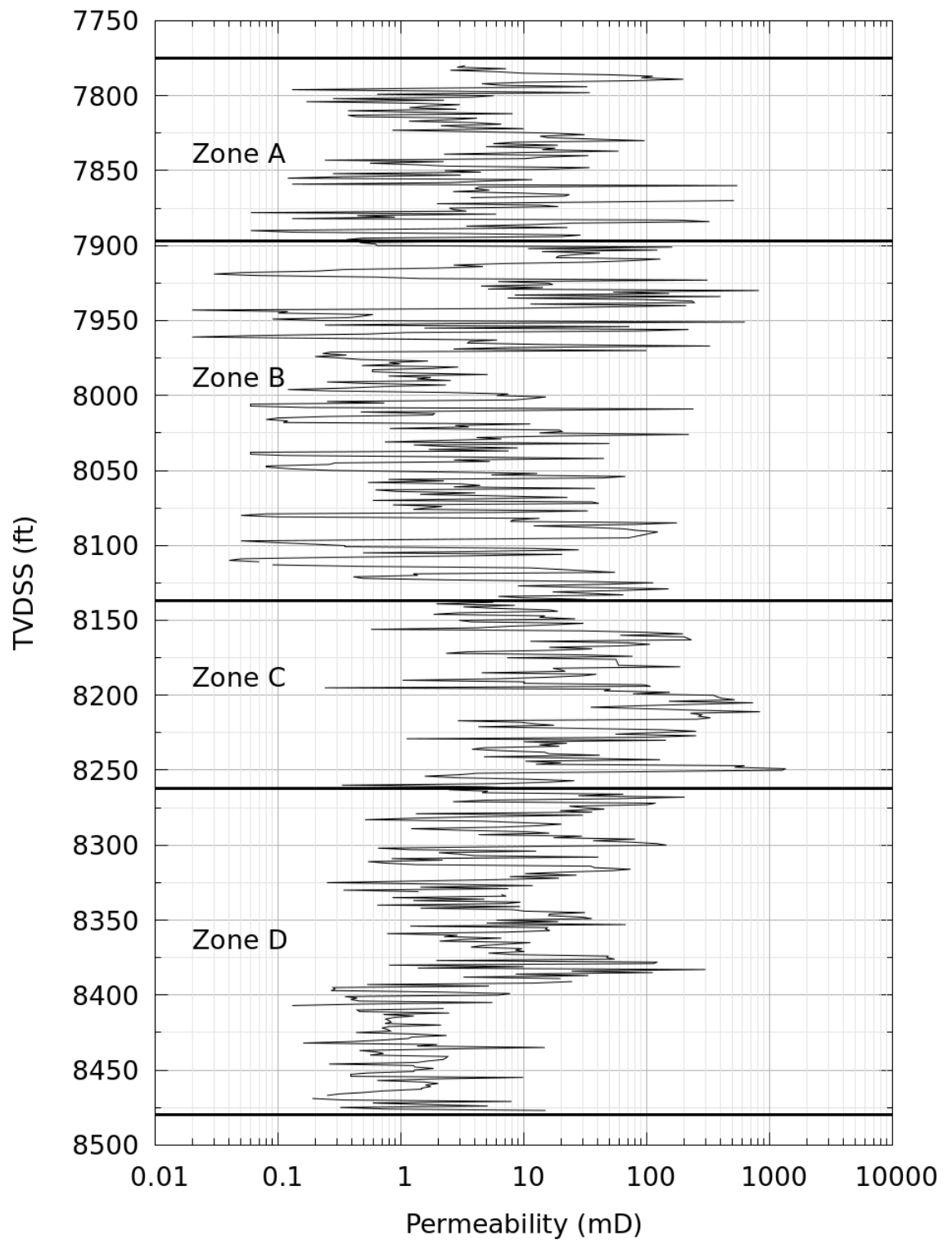
Figure B.1: Permeability vs depth: core plug data from well 49/16-Q3
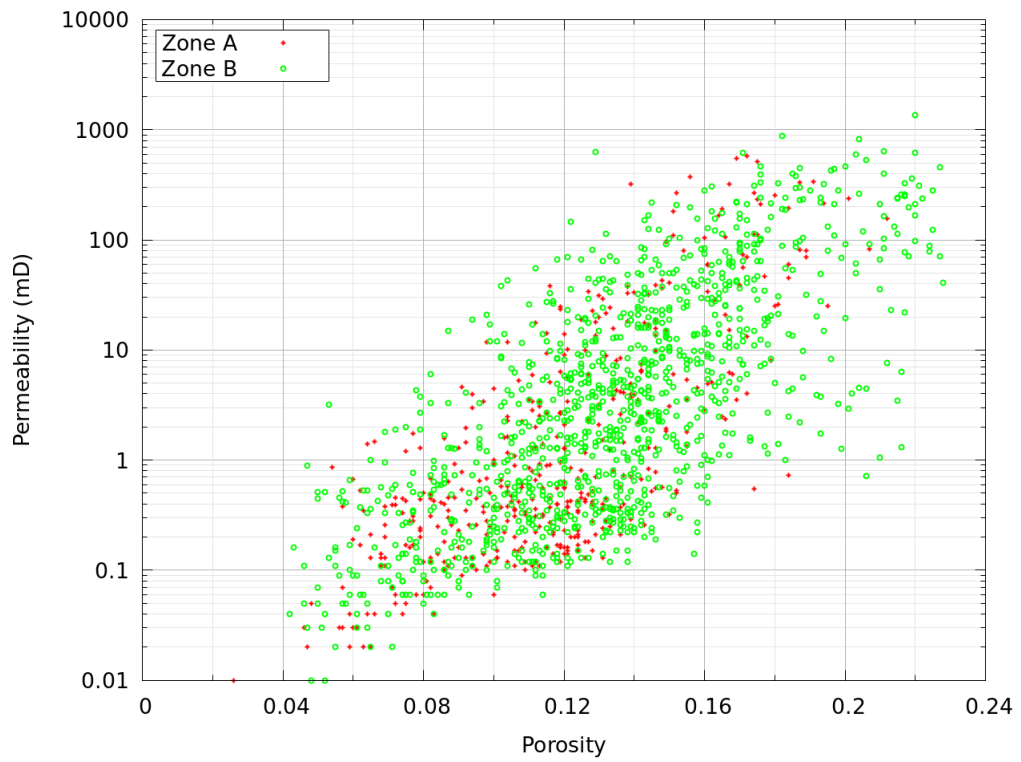
Figure B.2: Core permeability versus porosity for Zones A and B
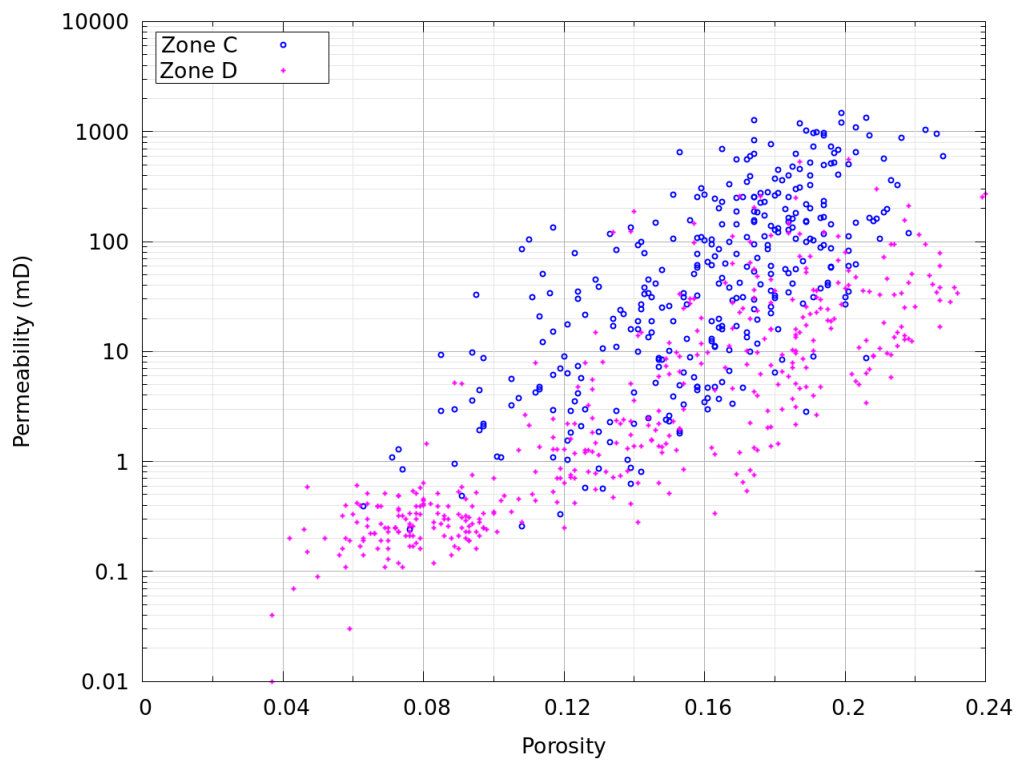
Figure B.3: Core permeability versus porosity for Zones C and D
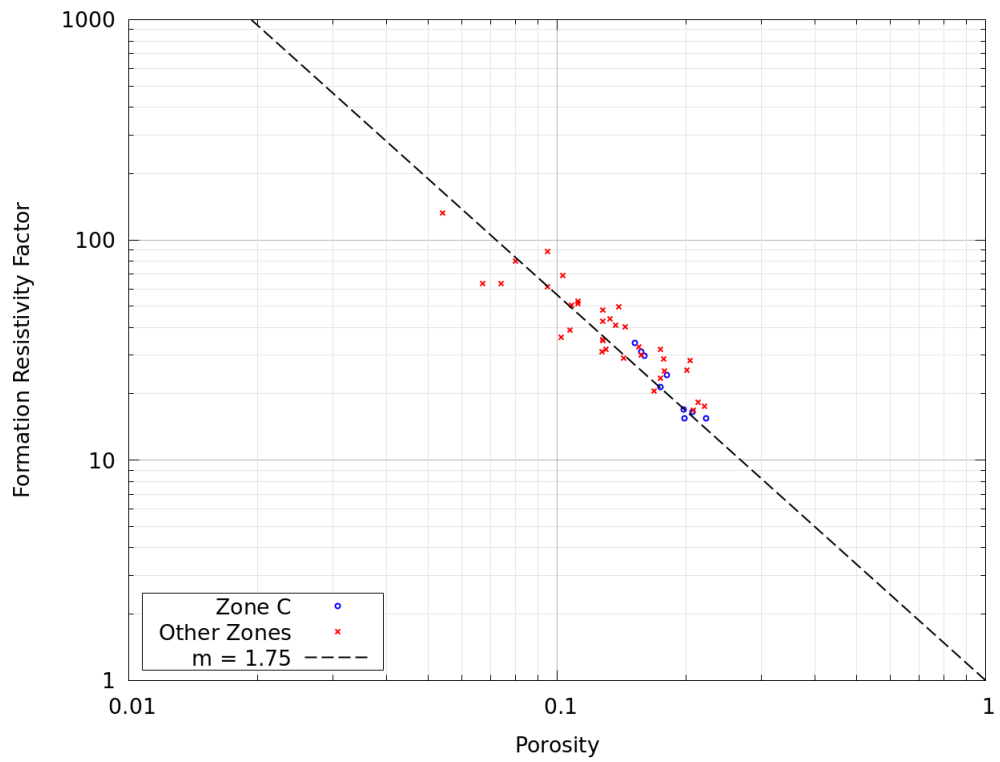
Figure B.4: Formation resistivity factor versus porosity
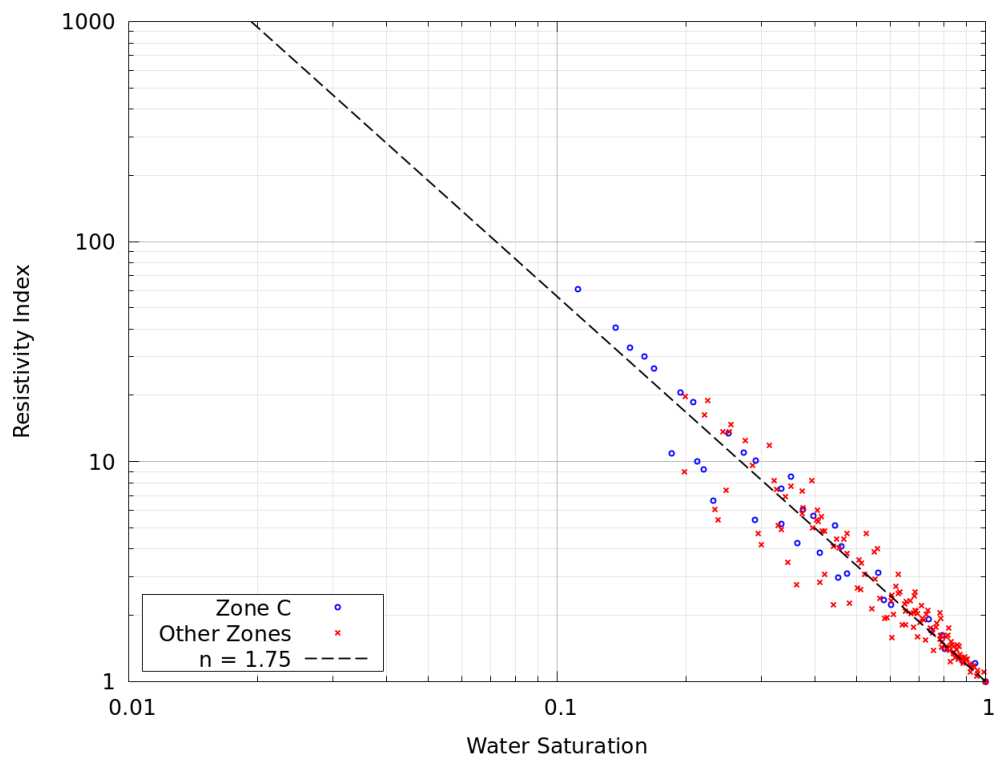
Figure B.5: Resistivity index versus water saturation
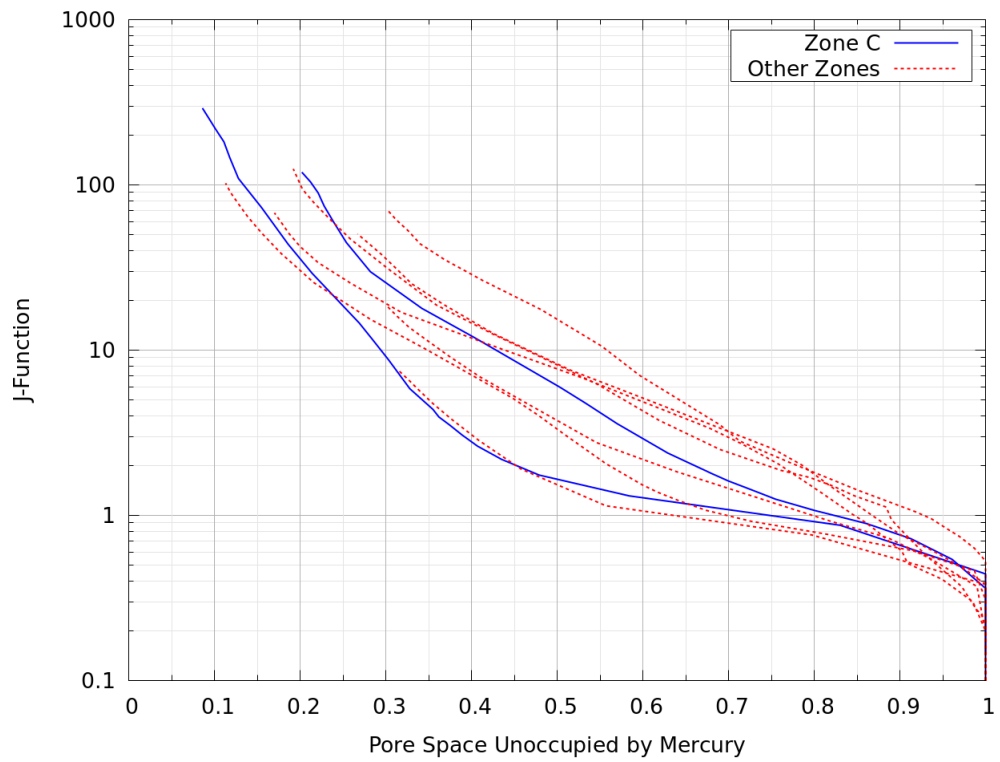
Figure B.6: MICP data
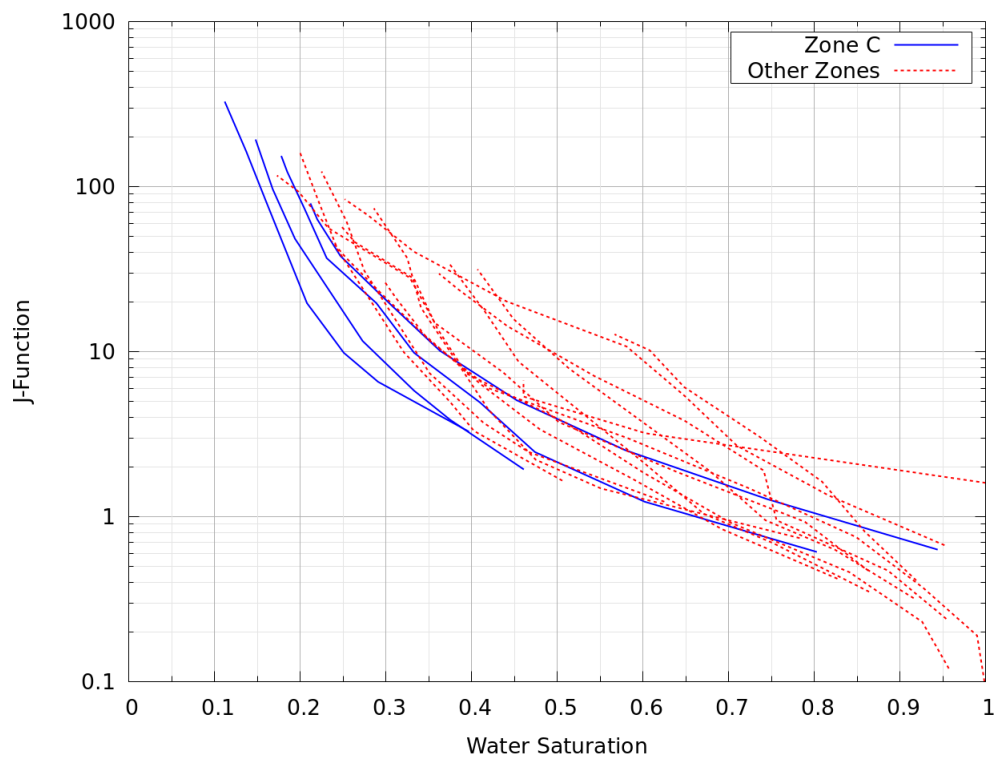
Figure B.7: Air-brine capillary pressure data
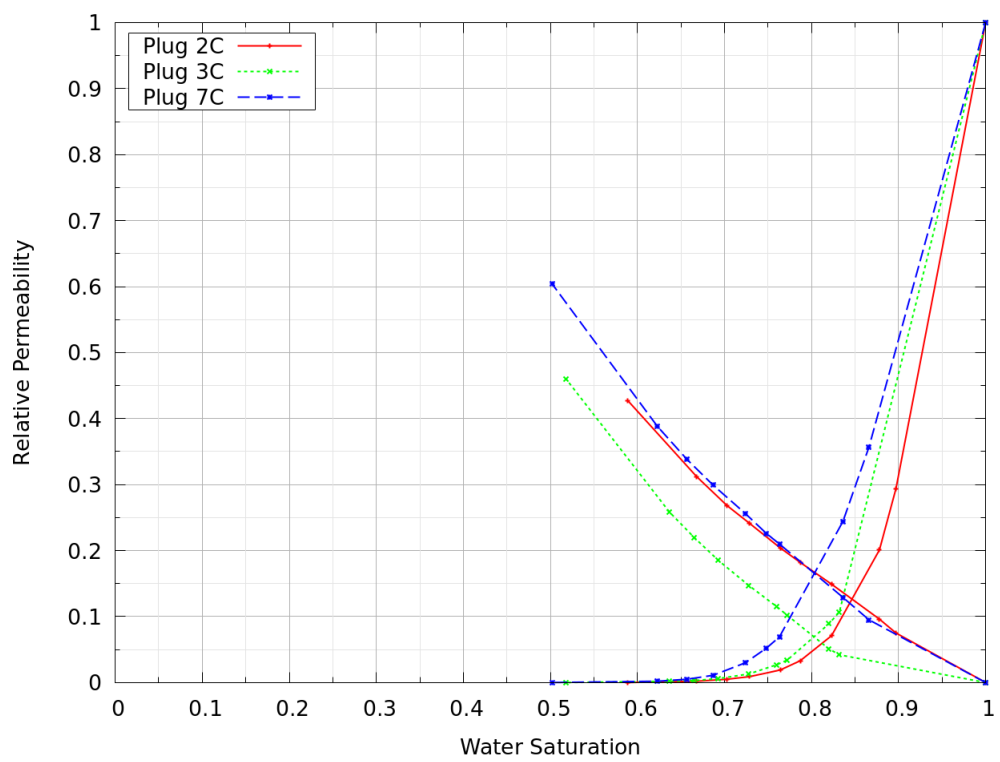
Figure B.8: Gas-water relative permeability drainage direction

Appendix C

Imagenet Software Manual

C.1   Overview

C.1.1   Introduction

Imagenet is a program to perform manipulation of images and pore networks. Images may be 2D or 3D, colour (RGB) or greyscale. Pore networks are defined by a spatial domain containing nodes and bonds with properties such as radius, volume and shape factor. Pore networks can be 2D or 3D. Images and networks may be defined within the program, imported from files and exported to files.

Imagenet reads an input text file containing a set of keyword commands and writes an output file containing the results.

The keywords are processed sequentially in the order they appear in the input file. Any order of keywords is possible although some possibilities do not make sense. Keywords can be repeated as many times as necessary. All keywords are optional, none are compulsory.

C.1.2   Program Execution

Read the input file 'FILE.INP' and write to standard output:

```
imagenet FILE.INP
```

Read the input file 'FILE.INP' and write to the output file 'FILE.OUT':

```
imagenet FILE.INP FILE.OUT
```

Read the input file 'FILE.INP' and write to the output file 'FILE.OUT':

```
imagenet FILE
```

C.1.3   Input Data Format

Keywords consist of an ampersand "&" followed by the keyword name, then the data terminated by a forward slash "/". The data consists of a set of name-value pairs. Each name-value is a variable name, followed by an equals sign "=" followed by the value to be assigned.

Here is an example of a keyword which creates an image:

```
&IMAGE
 NAME = ’A1’
 NX = 640 NY = 400 NZ = 1 NC = 3
/
```

This is another example which imports an image from a png file:

```
&IMAGE_IMPORT
 PNG = ’image1.png’
/
```

Whitespace in the form of spaces, tabs and newlines may be used freely to aid readability. However, the ampersand "&" at the beginning of the keyword must be at the <u>start</u> of a line.

Comments may be inserted using an exclamation mark "!". The comment continues up to the end of the line.

Real numbers (REAL) can be entered in all common formats e.g. 23.5, 18.8923, 42.0E+3.

Integers (INTE) similarly e.g. 0, 23, -6.

Character strings (CHAR) indicating image names, file names etc should be surrounded by single quotes "''".

Arrays can be input either as a list of values separated by spaces or using an array index in round brackets "(" and ")".

This sets five elements of the array:

```
 Z = 0.1 0.15 0.35 0.25 0.15
```

This sets the third element only (other elements are defaulted):

```
 Z(3) = 0.35
```

C.1.4 Images

Multiple images may be created or imported and processed at one time. The number of images is only limited by the available computer memory. Each image has a unique name so it can be referenced in later keywords.

Keywords that create new images have the variable NAME. The default NAME is 'image_N' where N is an integer sequence number (1 for the first image created, 2 for the second, etc.).

Keywords that operate on existing images have the variable IMAGE. The default IMAGE is "image_N" where N is an integer equal to the last image created.

Images may have up to 3 dimensions and any extent in X, Y or Z. 2D images are usually specified in the XY plane (NZ = 1) but it is possible to define 2D images in the XZ or YZ planes.

The pixel (voxel) data are stored with 8 bits per channel i.e. values range from 0 to 255. A greyscale image has 1 channel and a colour image has 3 channels for RED, GREEN and BLUE values. Alpha (transparency) channels are not supported.

Some keywords require colours to be specified as a character string. This can either be a simple word such as 'BLACK' or a more general format which permits any possible colour to be specified. This general format consists of a hash "#" followed by one or three 2-digit hexadecimal values. One hexadecimal value is required for a greyscale image and three for a colour (RGB) image. The table below shows the recognised colour names and their hexadecimal string equivalents.

Colour Name	RGB Hexadecimal	Greyscale Hexadecimal	Colour Name	RGB Hexadecimal	Greyscale Hexadecimal
BLACK	#000000	#00	GREY10	#191919	#19
WHITE	#FFFFFF	#FF	GREY20	#333333	#33
RED	#FF0000	-	GREY30	#4C4C4C	#4C
GREEN	#00FF00	-	GREY40	#6A6A6A	#6A
BLUE	#0000FF	-	GREY50	#7F7F7F	#7F
YELLOW	#FFFF00	-	GREY60	#959595	#95
CYAN	#00FFFF	-	GREY70	#B3B3B3	#B3
MAGENTA	#FF00FF	-	GREY80	#CCCCCC	#CC
			GREY90	#E6E6E6	#E6

Some keywords have the CHANNEL variable. For a greyscale image, CHANNEL should be VALUE or defaulted. For a colour image, CHANNEL can be one of RED, GREEN, BLUE, HUE, SATURATION, VALUE, INTENSITY or CHROMA.

VALUE = max(RED,GREEN,BLUE).

SATURATION = 255*(1-min(RED,GREEN,BLUE)/max(RED,GREEN,BLUE)).

INTENSITY = average(RED,GREEN,BLUE).

CHROMA = max(RED,GREEN,BLUE)-min(RED,GREEN,BLUE).

C.1.5   Probability Distributions

Probability distribution functions (PDFs) may be defined for use in later network keywords. A PDF is defined either by an analytical model or by a tabulation of the cumulative probability and the corresponding value of the independent variable.

Multiple PDFs may be created and used in one program run. Each PDF has a unique name. The default NAME is 'pdf_N' where N is an integer sequence number (1 for the first created, 2 for the second, etc.).

For keywords that operate on PDFs, the default PDF is "pdf_N" where N is an integer equal to the last pdf created.

C.1.6   Pore Networks

Multiple networks may be created or imported and processed at one time. The number of networks is only limited by the available computer memory. Each networks has a unique name so it can be referenced in later keywords.

For keywords that create networks, the default NAME is 'net_N' where N is an integer sequence number (1 for the first network created, 2 for the second, etc.).

For keywords that operate on existing networks, the default NETWORK is "net_N" where N is an integer equal to the last network created.

A pore network is defined by: (i) a domain or extent (DX, DY, DZ) in the three spatial dimensions, (ii) an array of nodes, and (iii) an array of bonds.

Each node has a position in space (X, Y, Z), a radius, a shape factor, a pore volume, a clay volume and a set of bonds.

Each bond has a pair of linked nodes, a radius, a shape factor, a volume, a clay volume, a total length, a bond length, a node_1 length and a node_2 length.

C.1.7   Units

Input and output units are as follows:

Quantity	Unit
Length	m
Area	m^2
Volume	m^3

Permeability is reported in m^2 and mD.

C.2   Keyword Summary

C.2.1   General Keywords

&ECHO Turn on echoing of the input data to the output.

&NOECHO Turn off echoing of the input data to the output.

&INCLUDE Include the contents of another file in the input data.

&RANDOM Control the random number generator.

&END End processing of the input data.

C.2.2   Basic Image Keywords

&IMAGE Create a new image.

&IMAGE_DELETE Delete an image.

&IMAGE_IMPORT Import an image from a file.

&IMAGE_EXPORT Export an image to a file.

C.2.3   Image Analysis Keywords

&IMAGE_INFO Display information about an image.

&IMAGE_STATISTICS Display statistics of an image.

&IMAGE_CLUSTER Perform cluster analysis on an image.

C.2.4   Image Editing Keywords

&IMAGE_TO_GREY Convert a colour (RGB) image to a greyscale image.

&IMAGE_TO_RGB Convert a greyscale image to a colour (RGB) image.

&IMAGE_CROP Crop an image.

&IMAGE_EXTRACT Extract all or part of an image into a new image.

&IMAGE_INSERT Insert a copy of one image into another existing image.

&IMAGE_RESHAPE Reshape an image or permute the subscript indices.

&IMAGE_SCALE Scale an image.

&IMAGE_THRESHOLD Apply thresholds to an image.

&IMAGE_OTSU Segment an image using Otsu's method.

&IMAGE_GMM Segment an image using a Gaussian Mixture Model.

&IMAGE_CONTRAST Enhance the contrast of an image.

&IMAGE_FILTER Apply a noise reduction or smoothing filter to an image.

&IMAGE_DETREND Remove low frequency spatial trends from an image.

&IMAGE_TRANSLATE Edit an image to translate one set of colours to another.

&IMAGE_DIFF Analyse the differences between two images.

&IMAGE_DRAW Draw a line, box, circle or sphere on an image.

&IMAGE_EDM Calculate the Euclidean Distance Map for an image.

&IMAGE_ERODE Erode an image using a circle or sphere structuring element.

&IMAGE_DILATE Dilate an image using a circle or sphere structuring element.

&IMAGE_OPENING Perform opening (erosion followed by dilation) on an image.

&IMAGE_CLOSING Perform closing (dilation followed by erosion) on an image.

&IMAGE_DECLUSTER Edit an image to remove clusters less than a given size.

&IMAGE_DOWNSCALE Downscale an image.

C.2.5   Probability Distribution Function Keywords

&PDF Create a new probability distribution.

&PDF_DELETE Delete a probability distribution.

&PDF_INFO Print information about a probability distribution.

&PDF_OUTPUT Output a tabular form of a PDF.

C.2.6   General Network Keywords

&NET Create a new network.

&NET_DELETE Delete a network.

&NET_IMPORT Import a network from _Node and _Link files.

&NET_EXPORT Export a network to _Node and _Link files.

C.2.7 Network Creation and Editing Keywords

&NET_FROM_IMAGE Extract a network from a 2D or 3D image.

&NET_CUBIC Create a regular cubic lattice network.

&NET_LATTICE Create a network from a weighted stochastic lattice algorithm.

&NET_EXTRACT Extract all or part of one network into a new network.

&NET_INSERT Insert a copy of one network into another existing network.

&NET_EDIT Edit network node and bond properties.

&NET_CLEAN Clean a network.

&NET_RESHAPE Rescale the network domain and/or permute the coordinate axes.

&NET_FLOWDIR Redefine inlet and outlet bonds to a given flow direction.

C.2.8 Network Analysis Keywords

&NET_INFO Output basic information about a network.

&NET_STATISTICS Output statistical information for a network.

&NET_PSD Output the pore size distribution.

&NET_CHECK Check the consistency of a network.

&NET_PERMEABILITY Calculate single phase permeability.

&NET_RESISTIVITY Calculate single phase resistivity.

&NET_TORTUOSITY Calculate the tortuosity of a network.

&NET_RADIUS Output tables of node and bond properties vs radius.

&NET_OUTPUT Output tables of nodes and bonds.

&NET_COORDINATION Output coordination number vs radius and frequency.

&NET_SHAPE_FACTOR Output shape factor vs radius and frequency.

&NET_CONNECTIVITY Output the topological connectivity function.

&NET_CLUSTER Analyse disconnected network clusters.

&NET_SUBGRID Analyse sub-areas of a network.

C.3   Keyword Detailed Description

C.3.1   General Keywords

&ECHO &NOECHO

These keywords may be used to turn on and off the echoing of the input data to the output file. By default, the echo is on. There are no variables for these keywords.

Example

```
&NOECHO /
```

&INCLUDE

Include the contents of another file in the input data.

Name	Type	Number	Description
FILE	CHAR	1	File name

FILE must be specified, there is no default. The name may specify a file in the current directory, a relative pathname or an absolute pathname.

Example

Include the file "data1.INP" in the current directory.

```
&INCLUDE FILE = 'data1.INP' /
```

&RANDOM

Control the random number generator.

Name	Type	Number	Description
SEED	INTE	1	Random number seed

SEED must be zero or a positive integer. The default value is 1. If SEED is zero, then the kernel random number generator will be used which gives non-repeatable results i.e. a different random number sequence for each execution of the program. If SEED is positive, then this integer will be used to seed the random number generator. This gives repeatable results for subsequent program executions.

&END

End processing of the input.

Anything after this keyword will be ignored. There are no variables for this keyword.

C.3.2   Basic Image Keywords

&IMAGE

Create a new image.

Name	Type	Number	Description
NAME	CHAR	1	Image name
NC	INTE	1	Number of channels in the image
NX	INTE	1	Number of pixels in the X-direction
NY	INTE	1	Number of pixels in the Y-direction
NZ	INTE	1	Number of pixels in the Z-direction
DATA	INTE	NC*NX*NY*NZ	Image data

The default image NAME is "image_N" where N is an integer sequence number (1 for the first image created, 2 for the second etc.).

NC is the number of channels in the image which must be 1 or 3. The default is NC = 1. A greyscale image has 1 channel. A colour image has 3 channels for RED, GREEN and BLUE values.

The size (number of pixels) in the image is specified with NX, NY and NZ. The defaults are NX = 1, NY = 1 and NZ = 1.

2D images are usually specified in the XY plane (NZ = 1), but it is possible to define 2D images in the XZ or YZ planes.

DATA defines the image data with an array of decimal integers. Each value should be in the range 0 to 255 inclusive. The values are ordered with the channel cycling fastest followed by the X, Y and Z indices in that order. The default is to fill the entire image with WHITE (value 255). DATA is limited to a maximum of 10000 values.

Example

Create a 2D greyscale image with 600x400 pixels. All pixels will be white. The name of the image will be "image_1" if this is the first image created.

```
&IMAGE NX = 600 NY = 400 /
```

&IMAGE_DELETE

Delete an image.

Name	Type	Number	Description
IMAGE	CHAR	1	Image name

All data for the image are deleted from memory.

&IMAGE_IMPORT

Import an image from a file.

Name	Type	Number	Description
NAME	CHAR	1	Image name
PAM	CHAR	1	Name of PAM file
PPM	CHAR	1	Name of PPM file
PLAIN_PPM	CHAR	1	Name of plain PPM file
PNG	CHAR	1	Name of PNG file
TIFF	CHAR	1	Name of TIFF file
TXT	CHAR	1	Name of text file
DAT	CHAR	1	Name of data file
UDAT	CHAR	1	Name of unformatted data file
FILTER	CHAR	1	Filter program to use for PNG and TIFF output
NC	INTE	1	Number of channels in the image
NX	INTE	1	Number of pixels in the X-direction
NY	INTE	1	Number of pixels in the Y-direction
NZ	INTE	1	Number of pixels in the Z-direction

The format of the file is determined by giving a filename to one of the following variables:

PAM Portable arbitrary map (a Netpbm format)

PPM Portable pixmap (a Netpbm format)

PLAIN_PPM Plain portable pixmap (a Netpbm format)

PNG Portable network graphics

TIFF Tagged image file format

TXT ASCII text file

DAT Binary data file

UDAT File containing a single unformatted Fortran record

TXT, DAT and UDAT are very basic file formats which simply contain the pixel data written into the file. The values are ordered with the channel cycling fastest followed by the X, Y and Z indices in that order. These file formats do not store any information about the image size or number of channels. Therefore, this information must be supplied with the NC, NX, NY and NZ variables. NC is the number of channels in the image which must be 1 or 3. The default is NC = 1. The size (number of pixels) in the image is specified with NX, NY and NZ. The defaults are NX = 1, NY = 1 and NZ = 1.

If a PNG or TIFF file is specified, then a filter program is used to convert the file to PAM format. The default filter is "convert" which is part of the ImageMagick software suite. The name of the filter can be changed with FILTER.

If the file contains a 2D image then it will be imported into the XY plane with NZ = 1.

The PPM, PLAIN_PPM and PNG can only store 2D images.

The PAM, TIFF, TXT, DAT and UDAT formats can store 3D images.

If a TIFF file contains multiple images then they must all be the same size and they will be imported into multiple layers to create a single 3D image.

&IMAGE_EXPORT

Export an image to a file.

Name	Type	Number	Description
IMAGE	CHAR	1	Name of image
PAM	CHAR	1	Name of PAM file
PPM	CHAR	1	Name of PPM file
PLAIN_PPM	CHAR	1	Name of plain PPM file
PNG	CHAR	1	Name of PNG file
TIFF	CHAR	1	Name of TIFF file
TXT	CHAR	1	Name of text file
DAT	CHAR	1	Name of data file
UDAT	CHAR	1	Name of unformatted data file
FILTER	CHAR	1	Filter program to use for PNG and TIFF output
IX	INTE	2	Pixel X-indices
JY	INTE	2	Pixel Y-indices
KZ	INTE	2	Pixel Z-indices
NX	INTE	1	Number of pixels to export in the X-direction
NY	INTE	1	Number of pixels to export in the Y-direction
NZ	INTE	1	Number of pixels to export in the Z-direction

The supported file formats are the same as for the &IMAGE_IMPORT keyword.

Part of an image can be saved using the IX, JY, KZ, NX, NY and NZ variables.

IX(1) and IX(2) specify the range of X-direction pixel indices to export. The defaults are IX(1) = 1 and IX(2) = IX(1)+NX-1. NX is the size of the saved image in the X-direction which is equal to the number of pixels exported from the source image. The default is NX = NXS-IX(1)+1 where NXS is the X-direction size of the source image. IX(2) takes priority over NX. If both IX(2) and NX are specified then NX will be ignored.

JY(1) and JY(2) specify the range of Y-direction pixel indices to export, analogous to IX(1) and IX(2).

KZ(1) and KZ(2) specify the range of Z-direction pixel indices to export, analogous to IX(1) and IX(2).

C.3.3 Image Analysis Keywords

&IMAGE_INFO

Display information about an image.

Name	Type	Number	Description
IMAGE	CHAR	1	Image name

Example

```
&IMAGE_INFO
 IMAGE = 'New_Image'
/
```

&IMAGE_STATISTICS

Display statistics of an image.

Name	Type	Number	Description
IMAGE	CHAR	1	Image name
CHANNEL	CHAR	1	Name of a channel

If CHANNEL is specified for an RGB image, then additional statistics for the specified channel will be output.

Example

```
&IMAGE_STATISTICS
 IMAGE = 'New_Image'
 CHANNEL = 'VALUE'
/
```

&IMAGE_CLUSTER

Perform cluster analysis on an image.

Name	Type	Number	Description
IMAGE	CHAR	1	Image name
COLOUR	CHAR	1	Analyse pixels of this colour
LADJACENT	INTE	1	Adjacency level
ICLUSTER	INTE	3	Clusters to output: LOWER, UPPER, STRIDE

The algorithm identifies clusters of connected pixels of the same colour given by COLOUR. The default COLOUR is BLACK.

Two pixels of the same colour will be assigned to the same cluster if they are adjacent, where the definition of "adjacent" is controlled by LADJACENT.

LADJACENT = 1 means diagonal neighbours are not considered (each pixel is adjacent to 4 others in 2D and 6 others in 3D).

LADJACENT = 2 means some diagonal neighbours are considered (each pixel is adjacent to 8 others in 2D and 18 others in 3D).

LADJACENT = 3 means all diagonal neighbours are considered (each pixel is adjacent to 8 others in 2D and 26 others in 3D).

Higher values of LADJACENT will result in a smaller number of larger clusters because more possible adjacent neighbours are considered. The default is LADJACENT = 1.

The output consists of a table showing the number of clusters of each size starting with the smallest followed by a list of clusters.

ICLUSTER controls the output of the list of clusters. ICLUSTER(1) is the first cluster; ICLUSTER(2) is the last cluster and ICLUSTER(3) is an integer stride. The default is ICLUSTER = 1 N 100, where N is the total number of clusters identified in the image.

Example

Perform cluster analysis of white pixels and print a table of the first 500 clusters.

```
&IMAGE_CLUSTER
 COLOUR = 'WHITE'
 LADJACENT = 2
 ICLUSTER = 1 500 1
/
```

C.3.4   Image Editing Keywords

&IMAGE_TO_GREY

Convert a colour (RGB) image to a greyscale image.

Name	Type	Number	Description
IMAGE	CHAR	1	Image name
CHANNEL	CHAR	1	Channel to use for the greyscale

CHANNEL specifies the channel to use for the greyscale image. The default CHANNEL is VALUE.

&IMAGE_TO_RGB

Convert a greyscale image to a colour (RGB) image.

Name	Type	Number	Description
IMAGE	CHAR	1	Image name

All three channels in the RGB image will be set equal to the greyscale value of the original image.

&IMAGE_CROP

Crop an image.

Name	Type	Number	Description
IMAGE	CHAR	1	Image name
IX	INTE	2	Pixel X-indices
JY	INTE	2	Pixel Y-indices
KZ	INTE	2	Pixel Z-indices
NX	INTE	1	Number of pixels in cropped image in X-direction
NY	INTE	1	Number of pixels in cropped image in Y-direction
NZ	INTE	1	Number of pixels in cropped image in Z-direction

IX(1) and IX(2) specify the range of X-direction pixel indices to remain uncropped. The defaults are IX(1) = 1 and IX(2) = IX(1)+NX-1. NX is the size of the cropped image in the X-direction. The default is NX = NXS-IX(1)+1 where NXS is the X-direction size of the source image. IX(2) takes priority over NX. If both IX(2) and NX are specified then NX will be ignored.

JY(1) and JY(2) specify the range of Y-direction pixel indices to export, analogous to IX(1) and IX(2).

KZ(1) and KZ(2) specify the range of Z-direction pixel indices to export, analogous to IX(1) and IX(2).

&IMAGE_EXTRACT

Extract all or part of an image into a new image.

Name	Type	Number	Description
IMAGE	CHAR	1	Name of existing source image
NAME	CHAR	1	Name of new image to create
IX	INTE	2	Pixel X-indices
JY	INTE	2	Pixel Y-indices
KZ	INTE	2	Pixel Z-indices
NX	INTE	1	Number of pixels to extract in the X-direction
NY	INTE	1	Number of pixels to extract in the Y-direction
NZ	INTE	1	Number of pixels to extract in the Z-direction

IX(1) and IX(2) specify the range of X-direction pixel indices to extract. The defaults are IX(1) = 1 and IX(2) = IX(1)+NX-1. NX is the size of the new image in the X-direction which is equal to the number of pixels extracted from the source image. The default is NX = NXS-IX(1)+1 where NXS is the X-direction size of the source image. IX(2) takes priority over NX. If both IX(2) and NX are specified then NX will be ignored.

JY(1) and JY(2) specify the range of Y-direction pixel indices to exptract, analogous to IX(1) and IX(2).

KZ(1) and KZ(2) specify the range of Z-direction pixel indices to extract, analogous to IX(1) and IX(2).

The number of channels in the new image will be the same as in the source image.

&IMAGE_INSERT

Insert a copy of one (source) image into another (target) image.

Name	Type	Number	Description
IMAGE	CHAR	1	Name of source image to copy from
TARGET	CHAR	1	Name of target image to insert into
IX	INTE	1	X-direction insertion point
JY	INTE	1	Y-direction insertion point
KZ	INTE	1	Z-direction insertion point

TARGET is the target image into which a copy of the source image will be placed. TARGET must be specified, there is no default.

IX, JY and KZ specify the pixel coordinates of the insertion point of pixel (1,1,1) from the source image. The remaining pixels from the source image will be copied into the offset pixel positions. If the target image is too small to accept the entire source image, then the additional data will not be copied. The defaults are IX = 1, JY = 1 and KZ = 1.

&IMAGE_RESHAPE

Reshape an image or permute the subscript indices.

Name	Type	Number	Description
IMAGE	CHAR	1	Image name
SX	INTE	1	Number of pixels in the X-direction in the new image
SY	INTE	1	Number of pixels in the Y-direction in the new image
SZ	INTE	1	Number of pixels in the Z-direction in the new image
ORDER	CHAR	1	Order of the original image axes in the new image

Either {SX,SY,SZ} or ORDER must be given.

If SX, SY and SZ are given, then the product SX*SY*SZ must equal the total number of pixels in the input image. In this case, the image is reshaped to the new extents. Note that the order of storage of the pixel data is unchanged.

If ORDER is given, then it must be a 3-character string containing a permutation of 'XYZ'. This specifies the order of the original axes in the new image.

Example

Swap X and Y (columns and rows) in an image.

```
&IMAGE_RESHAPE
 ORDER = 'YXZ'
/
```

&IMAGE_SCALE

Scale an image.

Name	Type	Number	Description
IMAGE	CHAR	1	Image name
COARSEN	INTE	3	Image coarsening in X, Y and Z directions
REFINE	INTE	3	Image refinement in X, Y and Z directions

Either COARSEN or REFINE must be given.

If COARSEN is given, then a coarser image is created with fewer pixels by taking the arithmetic mean of the pixel channel values.

If REFINE is given, then a finer image is created with more pixels by subdividing each pixel in the original image. In this case, no smoothing or interpolation is performed.

Example

Coarsen a 2D image by averaging 2x2 groups into one pixel.

```
&IMAGE_SCALE COARSEN = 2 2 1 /
```

&IMAGE_THRESHOLD

Apply thresholds to an image.

Name	Type	Number	Description
IMAGE	CHAR	1	Image name
CHANNEL	CHAR	1	Name of a channel
VLT	INTE	1	Threshold value - less than
VLE	INTE	1	Threshold value - less than or equal to
VGT	INTE	1	Threshold value - greater than
VGE	INTE	1	Threshold value - greater than or equal to
PLT	REAL	1	Threshold probability - less than
PLE	REAL	1	Threshold probability - less than or equal to
PGT	REAL	1	Threshold probability - greater than
PGE	REAL	1	Threshold probability - greater than or equal to
SET	CHAR	1	Set pixels defined by the threshold equal to this colour

CHANNEL specifies the channel to analyse for a colour (RGB) image. The default CHANNEL is VALUE.

The threshold value can be specified with one of {VLT, VLE, VGT, VGE}. The different key names indicate how the threshold is to be interpreted (see Examples).

Alternatively, a threshold can be computed to meet a target probability specified with one of {PLT, PLE, PGT, PGE}. In this case, the probability must be between zero and one and the different key names indicate how the threshold is to be interpreted. Note that the threshold must be an integer; therefore the target probability may not be met exactly.

If SET is give, it must specify a single colour which is used change all pixels which meet the threshold.

Examples

Change all pixels less than value 23 to BLACK then change all pixels greater than or equal to 23 to WHITE.

```
&IMAGE_THRESHOLD VLT = 23 SET = 'BLACK' /
&IMAGE_THRESHOLD VGE = 23 SET = 'WHITE' /
```

Calculate the threshold of the RED channel required to meet a target probability of 25%, then set all pixels less than the threshold to BLACK.

```
&IMAGE_THRESHOLD PLT = 0.25 CHANNEL = 'RED' SET = 'BLACK' /
```

&IMAGE_OTSU

Segment an image using the multi-level Otsu method.

Name	Type	Number	Description
IMAGE	CHAR	1	Image name
CHANNEL	CHAR	1	Name of a channel
NK	INTE	1	Number of classes
SET	CHAR	6	Set thresholded pixels equal to these colours
IT	INTE	5	Initial guess for the thresholds

The multi-level Otsu method segments an image into NK classes with NK-1 thresholds. The classes are chosen to maximise the inter-class variance.

For a colour (RGB) image, CHANNEL indicates which channel to use for the analysis. The default CHANNEL is VALUE.

NK is the number of classes. NK must be greater than or equal to 2 and less than or equal to 6. The default value of NK is 2.

SET is a list of NK colours which are assigned to the classes defined by the thresholds. If SET is not given, then the thresholds are calculated but the image is not changed.

IT specifies a list of NK-1 values which are taken as initial estimates of the thresholds. Each threshold must lie in the interval (0,255) and no two should be the same. The algorithm starts at the given thresholds and searches for the maximum of the inter-class variance using a steepest ascent process. This process is usually very fast but it may converge to a local maximum.

If IT is not given, then a comprehensive search is performed to maximise the inter-class variance. This process is guaranteed to find the global maximum, but it may be very slow for a large number of classes.

Examples

Segment an image into two classes. Set all pixels below the threshold to BLACK and all pixels above the threshold to WHITE.

```
&IMAGE_OTSU
 NK = 2 SET = 'BLACK' 'WHITE' /
```

Segment an image into 5 classes defined by 4 thresholds. Start from the given thresholds.

```
&IMAGE_OTSU
 IMAGE = 'image_1'
 NK = 5 IT = 51 102 153 204
 SET = 'RED' 'YELLOW' 'GREEN' 'CYAN' 'BLUE'
/
```

&IMAGE_GMM

Segment an image using a Gaussian Mixture Model (GMM)

Name	Type	Number	Description
IMAGE	CHAR	1	Image name
CHANNEL	CHAR	1	Name of a channel
NK	INTE	1	Number of classes
SET	CHAR	6	Set thresholded pixels equal to these colours
ALPHA	REAL	6	Initial guess for the component weights
XMU	REAL	6	Initial guess for the component means
XSIGMA	REAL	6	Initial guess for the component standard deviations
VMIN	REAL	1	Minimum pixel value
VMAX	REAL	1	Maximum pixel value

A Gaussian Mixture Model segments an image into NK classes with NK-1 thresholds based on decomposing the distribution of pixel values into a set of Gaussian distributions. The parameters of the Gaussian distributions are calculated using a non-linear least-squares Gauss-Newton algorithm. This algorithm is not guaranteed to find the global optimim and the results can depend on the starting point.

For a colour (RGB) image, CHANNEL indicates which channel to use for the analysis. The default CHANNEL is VALUE.

VMIN and VMAX specify the range of pixel values used to calculate the minimisation objective function i.e. the sum of the squares of the residuals. It is usually best to exclude the tails of the distribution because these are not important and/or difficult to match. The defaults are VMIN = 1 and VMAX = 254.

NK is the number of classes or Gaussian components. NK must be greater than or equal to 2 and less than or equal to 6. The default value of NK is 2.

ALPHA provides an initial guess for the component weights. Each component weight should lie between 0 and 1 but the sum of the weights is not necessarily 1. The default is to set the initial value of each weight to 1/NK.

XMU provides an initial guess for the component means. Each mean must lie in the interval (VMIN,VMAX) and no two should be the same. The default is to start by spreading out the means uniformly over the interval.

XSIGMA provides an initial guess for the component standard deviations. The default is to set the initial standard deviation of each component to 127/NK.

The thresholds are equal to the channel values where the GMM component probability densities are equal.

SET is a list of NK colours which are assigned to the classes defined by the thresholds. If SET is not given, then the thresholds are calculated but the image is not changed.

&IMAGE_CONTRAST

Enhance the contrast of an image.

Name	Type	Number	Description
IMAGE	CHAR	1	Image name
VMIN	INTE	1	Pixel value to be mapped to 0
VMAX	INTE	1	Pixel value to be mapped to 255
PMIN	REAL	1	Cumulative probability of VMIN
PMAX	REAL	1	Cumulative probability of VMAX

The image contrast will be increased by linearly scaling the pixel values from the interval (VMIN,VMAX) to the interval (0,255). For colour (RGB) images, the same scaling is applied to all channels which preserves the colour hue.

If VMIN is defaulted, then it is calculated from the cumulative probability PMIN. The default value of PMIN is 0.01.

If VMAX is defaulted, then it is calculated from the cumulative probability PMAX. The default value of PMAX is 0.99.

Examples

Increase the contrast of an image using the default settings.

```
&IMAGE_CONTRAST
/
```

Increase the contrast of an image, excluding the lower 5% and the upper 10% of the pixel value distribution.

```
&IMAGE_CONTRAST
 PMIN = 0.05
 PMAX = 0.90
/
```

&IMAGE_FILTER

Filter an image.

Name	Type	Number	Description
IMAGE	CHAR	1	Image name
TYPE	CHAR	1	Type of filter
S	INTE	1	Size of filter window
V	INTE	1	Value range for bilateral filter

TYPE must be one of MEDIAN, MEAN, GAUSSIAN or BILATERAL. The general effect of all filters is to smooth or reduce noise in the image. For a colour (RBG) image, each channel is processed separately.

S is the size of the filter window which must be an odd integer. For example, S = 3 creates a 3x3 filter window (9 pixels) for a 2D image and a 3x3x3 filter window (27 pixels) for a 3D image. Larger values of S will have greater smoothing or noise reduction effect. S = 1 limits the window to one pixel which will have no effect.

The MEDIAN filter replaces each pixel value with the median value of the pixels within the filter window.

The MEAN filter replaces each pixel value with the mean value of the pixels within the filter window.

The GAUSSIAN filter effectively convolves the image with a 2D or 3D Gaussian function. The filter replaces each pixel value with the weighted mean of the pixels within the filter window, where the weighting factors are calculated from a Gaussian function of the distance of each pixel from the central target pixel. The standard deviation of the Gaussian function is (S+1)/4 which results in the weighting factors being close to zero at the edges of the window. Note that the weighting factors are first calculated and then normalised to sum to unity.

The BILATERAL filter is an extension of the GAUSSIAN filter which attempts to preserve edge detail. The filter computes the weighting factors from the product of a Gaussian distance function and a Gaussian function of the difference in the pixel values (RED, GREEN and BLUE for a colour image). The standard deviation of the second Gaussian function is given by the parameter V. If the difference in pixel values is small (large) compared with V, then those pixels have a high (low) weighting factor. This effectively averages over pixels which have a similar value to the target pixel which tends to preserve detail where there are large changes over short distances (i.e. at the edges of image features).

Example

Filter a 2D image using the edge-preserving bilateral filter with a 5x5 filter window and a value range of 20.

```
&IMAGE_FILTER
  TYPE = 'BILATERAL' S = 5 V = 20
/
```

&IMAGE_DETREND

Remove low frequency spatial trends from an image.

Name	Type	Number	Description
IMAGE	CHAR	1	Image name
S	INTE	1	Size of filter window
XDEGREE	INTE	1	Degree of polynomial in X-direction
YDEGREE	INTE	1	Degree of polynomial in Y-direction
ZDEGREE	INTE	1	Degree of polynomial in Z-direction

Low frequency trends are removed from the image by fitting a polynomial function to a coarse scale average of the image. For a greyscale image, the grey level intensity is used for the average and for a colour (RGB) image, the VALUE channel is used. The fitted polynomial is then subtracted from each of the image channels.

S is the size of the window used to create the coarse scale average which must be a positive integer. For example, S = 5 creates a 5x5 window (25 pixels) for a 2D image and a 5x5x5 window (125 pixels) for a 3D image. The default value of S is 10.

XDEGREE, YDEGREE and ZDEGREE specify the polynomial degree in each of the X, Y and Z directions. By default these are all zero; therefore at least one of them should be specified with a positive value. Typically they should be in the range 0-3. There is no limit to the polynomial degree in any of X, Y or Z, but using high order polynomials often results in over-fitting; therefore polynomial orders higher than 3 should be used with caution. The polynomial will also contain XY, XZ and YX terms if both component degrees are greater than zero.

The output consists of a table of the polynomial coefficients and a table of the coarse scale image pixels.

Example

Remove a linear trend from a 2D image.

```
&IMAGE_DETREND
 S = 15
 XDEGREE = 1
 YDEGREE = 1
/
```

&IMAGE_TRANSLATE

Edit an image to translate one set of colours into another set.

Name	Type	Number	Description
IMAGE	CHAR	1	Image name
FROM	CHAR	256	Names of source colours
TO	CHAR	256	Names of target colours

FROM and TO are lists of up to 256 colours. The image will be edited to change each colour in the FROM list into the corresponding colour in the TO list. Each pixel is examined once and the translation performed if it matches one of the colours in the FROM list. The TO list may contain a permutation of the colours in the FROM list.

Examples

Swap BLACK and WHITE. Other pixels are unchanged.

```
&IMAGE_TRANSLATE
 FROM = 'BLACK' 'WHITE'
 TO  = 'WHITE' 'BLACK'
/
```

&IMAGE_DIFF

Analyse the differences between two images.

Name	Type	Number	Description
NAME	CHAR	1	Name of new image to create
IMAGES	CHAR	2	Image names
COLOURS	CHAR	9	List of colours to analyse
SCALE	REAL	1	Scale differences by this factor

IMAGES(1) and IMAGES(2) are the two images to be analysed. These must be given; there are no defaults. The two images must be the same size and have the same number of channels. The output consists of a table showing the numbers of pixels which are the same and different in the two images.

If NAME is given, then a new image is created with the difference between the input images scaled by the factor SCALE. NAME = 127+SCALE*(IMAGES(1)-IMAGES(2)).

The factor 127 means that identical pixels in IMAGES(1) and IMAGES(2) will be mid-grey in the new image. The default SCALE is 1.0 which means that differences greater than 127 will be 0 (black) or 255 (white) in the new image.

COLOURS specifies a list of up to 9 colours to analyse. A table is output showing the differences between the two input images for each pixel colour.

&IMAGE_DRAW

Draw a line, box, circle or sphere on an image.

Name	Type	Number	Description
IMAGE	CHAR	1	Image name
LINE	INTE	6	Draw a line from I1,J1,K1 to I2,J2,K2
BOX	INTE	6	Draw a box over I1 to I2, J1 to J2, K1 to K2
CIRCLE	INTE	4	Draw a circle radius R, centre I,J,K
DIR	CHAR	1	Plane of the circle. 'X', 'Y' or 'Z'
SPHERE	INTE	4	Draw a sphere radius R, centre I,J,K
COLOUR	CHAR	1	Colour to draw
FILL	INTE	1	Fill the shape. 0 = No, 1 = Yes

LINE requires 6 integers. The first 3 are the coordinates of the start point and the second three are the coordinates of the end point.

BOX draws a rectangle in 2D or a cuboid in 3D. The first two integers are the extent of the box in the x-direction. The second two are the extent in the y-direction. The last two are the extent in the z-direction.

CIRCLE requires 4 integers. The first is the radius and the last three are the coordinates of the centre. The plane of the circle is given by DIR.

SPHERE requires 4 integers. The first is the radius and the last three are the coordinates of the centre.

FILL = 1 means that the box, circle or sphere will be filled with COLOUR. The default is FILL = 0 which draws the outline only.

Example

Draw a filled black sphere with radius 10 pixels and centre (8,12,16).

```
&IMAGE_DRAW
 SPHERE = 10 8 12 16
 COLOUR = 'BLACK'
 FILL = 1
/
```

&IMAGE_EDM

Calculate the Euclidean distance map (EDM) of an image.

Name	Type	Number	Description
IMAGE	CHAR	1	Image name
COLOUR	CHAR	1	Analyse pixels of this colour
SCALE	REAL	1	Colour level per unit distance
CHANNEL	CHAR	1	Channel to use for the map
RIDGE	CHAR	1	Colour for the EDM ridge

The algorithm calculates the Euclidean distance from each pixel of colour COLOUR to the nearest pixel of a different colour. The default COLOUR is BLACK.

If CHANNEL is specified, then the given channel of the target pixels will be modified to encode the Euclidean distance using the scale factor SCALE. In particular, the channel of each pixel is assigned the value SCALE*EDM. CHANNEL must be GREY or VALUE for a greyscale image. CHANNEL must be RED, GREEN, BLUE or VALUE for a colour (RGB) image.

If SCALE is defaulted, then the scale factor will be calculated from SCALE = 255/MAX(EDM), where MAX(EDM) is the maximum value of the Euclidean distance map over the whole image.

If RIDGE is specified, then pixels on the ridge of the Euclidean distance map will be changed to this colour.

Example

Calculate the Euclidean distance for the black pixels in image A_1, put the results in the red channel multiplied by a scale factor of 10 and colour the ridge pixels blue.

```
&IMAGE_EDM
 IMAGE = 'A1'
 COLOUR = 'BLACK'
 CHANNEL = 'RED'
 SCALE = 10.0
 RIDGE = 'BLUE'
/
```

&IMAGE_ERODE

Erode an image using a circle or sphere structuring element.

Name	Type	Number	Description
IMAGE	CHAR	1	Image name
COLOUR	CHAR	1	Analyse pixels of this colour
SET	CHAR	1	Change eroded pixels to this colour
S	REAL	1	Radius of erosion in pixels

The algorithm calculates the Euclidean distance from each pixel of colour COLOUR to the nearest pixel of a different colour. The default COLOUR is BLACK.

Pixels which have Euclidean distance less than S are changed to the colour given by SET. The default SET is WHITE.

S is the radius of the erosion in pixels and must be given (there is no default).

For a 2D image, the pixels are effectively eroded using a circular structuring element of radius S. For a 3D image, the pixels are effectively eroded using a spherical structuring element of radius S.

&IMAGE_DILATE

Dilate an image using a circle or sphere structuring element.

Name	Type	Number	Description
IMAGE	CHAR	1	Image name
COLOUR	CHAR	1	Analyse pixels of this colour
SET	CHAR	1	Change dilated pixels to this colour
S	REAL	1	Radius of erosion in pixels

The algorithm calculates the Euclidean distance from each pixel not of colour COLOUR to the nearest pixel of colour COLOUR. The default COLOUR is BLACK.

Pixels which have Euclidean distance less than S are changed to the colour given by SET. The default SET is WHITE.

S is the radius of the dilation in pixels and must be given (there is no default).

For a 2D image, the pixels are effectively dilated using a circular structuring element of radius S. For a 3D image, the pixels are effectively dilated using a spherical structuring element of radius S.

&IMAGE_OPENING

Perform opening (erosion followed by dilation) on an image.

Name	Type	Number	Description
IMAGE	CHAR	1	Image name
COLOUR	CHAR	1	Analyse pixels of this colour
SET	CHAR	1	Change eroded pixels to this colour
S	REAL	1	Radius of erosion in pixels

The opening operation removes small features of colour COLOUR, changing them to colour SET. The algorithm consists of two steps:

- Pixels of colour COLOUR are eroded with radius S and eroded pixels changed to colour SET.

- Pixels of colour COLOUR are dilated with radius S and dilated pixels changed to colour COLOUR.

S is the radius of the erosion and dilation in pixels and must be given (there is no default).

&IMAGE_CLOSING

Perform closing (dilation followed by erosion) on an image.

Name	Type	Number	Description
IMAGE	CHAR	1	Image name
COLOUR	CHAR	1	Analyse pixels of this colour
SET	CHAR	1	Change dilated pixels to this colour
BACK	CHAR	1	Change eroded pixels to this colour
S	REAL	1	Radius of dilation and erosion in pixels

The closing operation removes small features of colour BACK, changing them to colour COLOUR. The algorithm consists of two steps:

- Pixels of colour COLOUR are dilated with radius S and dilated pixels changed to colour SET.

- Pixels of colour COLOUR are eroded with radius S and eroded pixels changed to colour BACK.

If SET is not given, the default is COLOUR.

S is the radius of the dilation and erosion in pixels and must be given (there is no default).

&IMAGE_DECLUSTER

Edit an image to remove clusters less than or equal to a given size.

Name	Type	Number	Description
IMAGE	CHAR	1	Image name
COLOUR	CHAR	1	Analyse pixels of this colour
SET	CHAR	1	Change small clusters to this colour
LADJACENT	INTE	1	Adjacency level
S	INTE	1	Critical cluster size

The algorithm identifies clusters of connected pixels of the same colour given by COLOUR. The default COLOUR is BLACK.

Two pixels of the same colour will be assigned to the same cluster if they are adjacent, where the definition of "adjacent" is controlled by LADJACENT.

LADJACENT = 1 means diagonal neighbours are not considered (each pixel is adjacent to 4 others in 2D and 6 others in 3D).

LADJACENT = 2 means some diagonal neighbours are considered (each pixel is adjacent to 8 others in 2D and 18 others in 3D).

LADJACENT = 3 means all diagonal neighbours are considered (each pixel is adjacent to 8 others in 2D and 26 others in 3D).

Higher values of LADJACENT will result in a smaller number of larger clusters because more possible adjacent neighbours are considered. The default is LADJACENT = 1.

The critical cluster size is given by S. Clusters containing S pixels or less will be removed by changing those pixels to another colour given by SET.

Example

Remove clusters of 10 or fewer black pixels by changing them to white.

```
&IMAGE_DECLUSTER
 S = 10
 COLOUR = 'BLACK'
 SET = 'WHITE'
/
```

&IMAGE_DOWNSCALE

Downscale an image.

Name	Type	Number	Description
IMAGE	CHAR	1	Name of image to downscale
IMAGE_COARSE	CHAR	1	Coarse training image
IMAGE_FINE	CHAR	1	Fine training image
COLOURS	CHAR	2	Colours of each state
SYMMETRY	INTE	1	Allow for symmetry, 0 = No, 1 = Yes
PX	REAL	8192	Transition matrix

The downscaling algorithm will be applied to IMAGE. Currently, only 2D images in the XY-plane can be downscaled. The result will be an image with exactly twice the resolution in X an Y directions.

IMAGE should be a binary image which contains only two pixel values given by COLOURS. The default colours are BLACK and WHITE.

The training images are IMAGE_COARSE and IMAGE_FINE. These should also be binary images containing only two pixel values. IMAGE_FINE must be exactly twice the resolution of IMAGE_COARSE in X and Y directions. These images are used to calculate the transition probability matrix.

SYMMETRY = 1 means that probabilities for symmetric states are combined. This is the default. SYMMETRY = 0 means don't combine probabilities for symmetric states.

Optionally, all or part of the probability matrix can be entered manually with PX. This is rank-2 array ordered with the fine scale 2x2 state index cycling fastest and the coarse scale 3x3 state index cycling slowest.

Example

Downscale image A1 using training images T1 and T2. All images are binary containing only BLACK and WHITE pixels.

```
&IMAGE_DOWNSCALE
 IMAGE = 'A1'
 IMAGE_COARSE = 'T2'
 IMAGE_FINE = 'T2'
/
```

C.3.5   Probability Distribution Function Keywords

&PDF

Create a new probability distribution.

Name	Type	Number	Description
NAME	CHAR	1	PDF name
SCALE	CHAR	1	LINEAR scale or LOG scale
XC	REAL	1	Constant value
XMIN	REAL	1	Minimum value
XMAX	REAL	1	Maximum value
XMU	REAL	1	Mean value
XSIGMA	REAL	1	Standard deviation
XALPHA	REAL	1	Scale power
XN	REAL	1	Powerlaw cut-off exponent
TABLE	REAL	998	Tabulated pdf

The type of probability distribution is determined by the key names XC, XMIN, XMAX, XMU, XSIGMA, XALPHA and XN.

SCALE can be 'LINEAR' or 'LOG and determines whether the distribution is linear or logarithmic in the independent variable. The default SCALE is 'LINEAR'.

If XC is given, this specifies a constant equal to the given value. In this case, the probability density is a Dirac delta function and the cumulative probability is a step function.

If XMU is given, the pdf is a (possibly truncated) normal (Gaussian) distribution. XMU and XSIGMA specify the parameters of the distribution. If the distribution is not logarithmic and not truncated, then XMU is the mean and XSIGMA is the standard deviation. The default value of XSIGMA is 1.0. Optionally, the distribution can be truncated by specifying the minimum and/or the maximum with XMIN and XMAX. If SCALE = 'LOG' then the distribution is log-normal.

If XMAX and XMIN are given without XMU, then the pdf is a uniform distribution between the given minimum and maximum. If SCALE = 'LOG' then the distribution is log-uniform.

If XALPHA is given, this specifies the scaling exponent. The pdf is a powerlaw model with an exponential cut-off controlled by XN. The minimum is given by XMIN and maximum XMAX.

TABLE indicates a tabulated pdf and is followed by a table of numbers. The first column is the cumulative probability increasing from 0.0 to 1.0. The second column contains the values of the independent variable. If SCALE = 'LINEAR' the table is interpolated linearly. If SCALE = 'LOG' the table is interpolated using the logarithm of the independent variable.

Example

Create a pdf with the name "x1". The distribution is Gaussian with a mean

of 55.0 and a standard deviation of 12.0.

```
&PDF
 NAME = 'x1'
 XMU = 55.0
 XSIGMA = 12.0
/
```

&PDF_DELETE

Delete a pdf.

Name	Type	Number	Description
PDF	CHAR	1	PDF name

All data for the pdf are deleted from memory.

&PDF_INFO

Display information about a PDF.

Name	Type	Number	Description
PDF	CHAR	1	PDF name

&PDF_OUTPUT

Output a tabular form of a PDF.

Name	Type	Number	Description
PDF	CHAR	1	PDF name
XMIN	REAL	1	Minimum value of the independent variable
XMAX	REAL	1	Maximum value of the independent variable
DX	REAL	1	Incremental value of the independent variable
DP	REAL	1	Incremental probability
SCALE	CHAR	1	LINEAR scale or LOG scale

The output is a tabulation of the pdf irrespective of whether the pdf is a tabular type or an analytical model.

Either DX or DP must be specified.

If DX is specified then a table is output with the cumulative probability as a function of the independent variable. The independent variable ranges from XMIN to XMAX in increments of DX. If SCALE = LOG or SCALE is not given and the PDF has a log-scale, then the table is a geometric progression with a common factor of DX. In this case DX must be greater than 1.

IF DP is specified then table is output with the independent variable as a function of the cumulative probability. The cumulative probability ranges from 0 to 1 in increments of DP. In this case SCALE has no effect.

C.3.6 General Network Keywords

&NET

Create an new (empty) network.

Name	Type	Number	Description
NAME	CHAR	1	Network name
DX	REAL	1	Domain X-direction size
DY	REAL	1	Domain Y-direction size
DZ	REAL	1	Domain Z-direction size

An empty network contains no nodes or bonds but serves as a container for later operations such as &NET_INSERT and &NET_EXTRACT.

DX, DY and DZ must be specified, there are no defaults.

Example

```
&NET
 NAME = 'net1'
 DX = 100.0E-6
 DY = 100.0E-6
 DZ = 100.0E-6
/
```

&NET_DELETE

Delete a network.

Name	Type	Number	Description
NETWORK	CHAR	1	Network name

All data for the network are deleted from memory.

&NET_IMPORT

Import a network from _Node and _Link files.

Name	Type	Number	Description
NAME	CHAR	1	Network name
ROOT	CHAR	1	File root name
BINARY	INTE	1	0 = text files, 1 = binary files
CASE	CHAR	1	UPPER or LOWER

_Node files contain the network node data and _Link files contain the network bond data.

The rootname of the files must be specified with ROOT. The actual file names and the expected number of files depend on the BINARY and CASE settings as shown in the following table:

	BINARY=0	BINARY=1
CASE= UPPER	ROOT_Node1.DAT ROOT_Node2.DAT ROOT_Link1.DAT ROOT_Link2.DAT	ROOT_Node.BIN ROOT_Link.BIN
CASE= LOWER	ROOT_node1.dat ROOT_node2.dat ROOT_link1.dat ROOT_link2.dat	ROOT_node.bin ROOT_link.bin

The defaults are BINARY = 0 and CASE = 'UPPER'.

&NET_EXPORT

Export a network to _Node and _Link files.

Name	Type	Number	Description
NAME	CHAR	1	Network name
ROOT	CHAR	1	File root name
BINARY	INTE	1	0 = text files, 1 = binary files
CASE	CHAR	1	UPPER or LOWER

The rootname of the files must be specified with ROOT.

The file names and the number of files generated depend on the BINARY and CASE settings (see &NET_IMPORT).

The defaults are BINARY = 0 and CASE = 'UPPER'.

C.3.7 Network Creation and Editing Keywords

&NET_FROM_IMAGE

Extract a network from a 2D or 3D image.

Name	Type	Number	Description
NAME	CHAR	1	Network name
IMAGE	CHAR	1	Image name
COLOUR	CHAR	1	Colour representing pore space
XPIXEL	REAL	1	Size of one pixel/voxel
ALPHA	REAL	1	Parameter controlling node overlap
BETA	REAL	1	Parameter controlling bond length
LAMBDA	REAL	1	Parameter controlling bond creation
DIR	CHAR	1	Direction of flow 'X', 'Y', 'Z' or ' '
BALLS	CHAR	1	Colour to use for circles or spheres
LINKS	CHAR	1	Colour to use to draw links
EDGES	CHAR	1	Colour to use to draw node boundaries

COLOUR specifies the colour of pixels representing pore space. All other pixels are assumed to be solid matrix. The default COLOUR is BLACK.

XPIXEL specifies the pixel or voxel size. All pixels (voxels) are assumed to be square (cubic).

ALPHA is the parameter controlling overlap of the inscribed circles or spheres defining pore nodes. The default value is 1.25.

BETA is a parameter controlling the length of bonds. The total bond length is equal to the distance between nodes (centre to centre). The bond length is then set equal to BETA multiplied by the total bond length. Finally, bond node_1 and node_2 lengths are scaled by 1-BETA such that their sum plus the bond length is equal to the total bond length. The default value is BETA = 0.5.

LAMBDA is a parameter controlling the creation of bonds between nodes. In 2D, a bond is created between two nodes if the interface length is greater than LAMBDA times the harmonic mean of the node diameters. In 3D, a bond is created between two nodes if the interface area is greater than LAMBDA times the harmonic mean of the circular areas. Where the circular area of an node is π multiplied by the square of its radius. The default value is LAMBDA = 0.5.

DIR specifies the direction of flow which can be 'X', 'Y', 'Z' or ' ' i.e. none. The latter will result in no inlet or outlet bonds. Otherwise, an inlet (outlet) bond will be created for a node if it has one or more pixels in the inlet (outlet) face.

BALLS, LINKS and EDGES can be used to edit the image to illustrate the network. Each variable defines a colour to be used for the respective features. The default is not to draw anything.

&NET_CUBIC

Create a regular cubic lattice network.

Name	Type	Number	Description
NAME	CHAR	1	Network name
NX	INTE	1	Number of nodes in X-direction
NY	INTE	1	Number of nodes in Y-direction
NZ	INTE	1	Number of nodes in Y-direction
DIR	CHAR	1	Direction of flow
LT	REAL	1	Total bond length
ZMEAN	REAL	1	Mean coordination number
NODE_R	CHAR	1	PDF for node radius
BOND_R	CHAR	1	PDF for bond radius
NODE_G	CHAR	1	PDF for node shape factor
BOND_G	CHAR	1	PDF for bond shape factor

NX, NY and NZ specify the number of lattice nodes in each direction. The total number of network nodes will be NX*NY*NZ.

LT is the lattice spacing equal to the total bond length (node centre to node centre).

ZMEAN can be used to adjust the average coordination number. The default is ZMEAN = 6. If ZMEAN is less than 6, then bonds are deleted at random to achieve the target. ZMEAN cannot be greater than 6.

Node and bond radii and shape factors are defined by randomly sampling PDFs specified with NODE_R, BOND_R, NODE_G and BOND_G.

DIR specifies the direction of flow which can be 'X', 'Y' or 'Z'. Inlet (outlet) bonds will be created for the nodes which are in the lattice plane closest to the inlet (outlet).

&NET_LATTICE

Create a network from a weighted stochastic lattice algorithm.

Name	Type	Number	Description
NAME	CHAR	1	Network name
DX	REAL	1	Domain X-direction size
DY	REAL	1	Domain Y-direction size
DZ	REAL	1	Domain Z-direction size
NNODE	INTE	1	Number of nodes
ZR	REAL	2997	Table of Zmean and Zstdev vs radius
NODE_R	CHAR	1	PDF for node radius
BOND_R	CHAR	1	PDF for bond radius
NODE_G	CHAR	1	PDF for node shape factor
BOND_G	CHAR	1	PDF for bond shape factor
LRATIO	REAL	1	Ratio of LMAX to RMAX
LMAX	REAL	1	Side length of largest squares
DIR	CHAR	1	Direction of flow 'X', 'Y' or 'Z'

DX, DY and DZ must be specified, there are no defaults.

NNODE specifies the number of nodes to create. The default is NNODE = 1.

ZR should be followed by a table with three columns. The first column is node radius. The second column is the mean coordination number and the third column is the standard deviation of the coordination number. The table is used to calculate the target coordination number of each node. The table is interpolated in the logarithm of the node radius.

The nodes and bonds are constructed to honour the node radius and bond radius PDFs given by NODE_R and BOND_R.

The shape factors are randomly sampled from the PDFs NODE_G and BOND_G.

LRATIO specifies the ratio of the side length of a square to the largest node radius assigned to that square. The default is LRATIO = 2.

LMAX specifies the side length of the largest square. The default value is LRATIO*RMAX where RMAX is the largest radius possible from NODE_R or BOND_R. Note that DX, DY and DZ should normally be integer multiples of LMAX otherwise the domain will not be completely filled. Therefore it is best to set LMAX explicitly and not rely on the default.

DIR specifies the direction of flow which can be 'X', 'Y' or 'Z'. Inlet (outlet) bonds will be created for the nodes in the lattice positions bordering the inlet (outlet) face.

&NET_EXTRACT

Extract all or part of one network into another network.

Name	Type	Number	Description
NAME	CHAR	1	Name of new network
NETWORK	CHAR	1	Name of existing network
XI	REAL	2	Lower and upper limit of X-dimension to extract
YJ	REAL	2	Lower and upper limit of Y-dimension to extract
ZK	REAL	2	Lower and upper limit of Z-dimension to extract
DIR	CHAR	1	Direction of flow in new network
ALPHA	REAL	1	Parameter controlling inlet/outlet bonds

A new network is created by extracting all of the nodes and bonds within a box-shaped sub-domain of the existing network.

The sub-domain is specified with XI, YJ and ZK. The size of the new network will be DX = XI(2)-IX(1), DY = YJ(2)-YJ(1) and DZ = ZK(2)-ZK(1).

Inlet and outlet bonds in the source network will not be copied into the new network. Rather, new inlet and outlet bonds will be defined from DIR and ALPHA.

DIR specifies the direction of flow which can be 'X', 'Y', 'Z' or ' ' i.e. none. The latter will result in no inlet or outlet bonds.

ALPHA is a parameter controlling the creation of inlet and outlet bonds. In particular, an inlet (outlet) bond will be created for a node if the distance from the centre of the node to the inlet (outlet) face is less than ALPHA times the node radius. The default is ALPHA = 1.25.

&NET_INSERT

Insert a copy of one network into another existing network.

Name	Type	Number	Description
NAME	CHAR	1	Network name
TARGET	CHAR	1	Name or target network
X	REAL	1	X-direction insertion point
Y	REAL	1	Y-direction insertion point
Z	REAL	1	Z-direction insertion point
EXTRA_BONDS	INTE	1	Flag for extra bonds
ALPHA	REAL	1	Parameter controlling extra bonds

The source network, NAME, is copied into the TARGET network. TARGET must be specified, there is no default.

X, Y and Z specify the coordinates in the target domain of the insertion point of the origin of the source network.

Existing nodes and bonds in the target network are unaffected. In particular, there is no overlap check. Therefore, it is possible for the resulting network to have overlapping nodes.

If EXTRA_BONDS = 0 then no additional bonds will be created to link the nodes in the source network with existing nodes in the target network. This is the default.

ALPHA is a parameter controlling the creation of bonds between the source and target networks if EXTRA_BONDS > 1. A bond will be created between two nodes if the distance between the node centres is less than ALPHA times the sum of the node radii. The default is ALPHA = 1.25.

If EXTRA_BONDS = 1 then the nodes along the faces of the source network are checked and bonds with the target network are created if the criterion above is satisfied.

If EXTRA_BONDS = 2 then all nodes in the source network are checked and bonds with the target network are created if the criterion above is satisfied. This involves checking every potential pair of nodes which can be very time consuming if the networks are large.

&NET_EDIT

Edit network node and bond properties.

Name	Type	Number	Description
NAME	CHAR	1	Network name
NODE_R	CHAR	1	PDF for node radius
NODE_G	CHAR	1	PDF for node shape factor
NODE_V	CHAR	1	PDF for node volume
NODE_VC	CHAR	1	PDF for node clay volume
BOND_R	CHAR	1	PDF for bond radius
BOND_G	CHAR	1	PDF for bond shape factor
BOND_V	CHAR	1	PDF for bond volume
BOND_VC	CHAR	1	PDF for bond clay volume
BOND_LT	CHAR	1	PDF for bond total length
BOND_LB	CHAR	1	PDF for bond length
BOND_L1	CHAR	1	PDF for bond node_1 length
BOND_L2	CHAR	1	PDF for bond node_2 length
ORDER	INTE	1	1 = maintain existing order of arrays

This keyword enables any network node or bond property to be redefined by sampling a probability distribution. All controls are optional. If a PDF is not given for a particular property, then that property remains unchanged.

The default is ORDER = 0. In this case, each specified PDF is randomly sampled to assign the appropriate node or bond properties. In general, this results in new properties unrelated to the existing ones.

If ORDER = 1, then the existing magnitude order is maintained within each modified array. Each specified PDF is randomly sampled, the results are sorted and the smallest value is assigned to the node/bond which has the smallest existing value of the property, the second smallest is assigned to the node/bond with the second smallest existing value etc. This makes it possible to stretch or shift the distribution of a property whilst maintaining the existing magnitude relationship between the nodes or bonds.

&NET_CLEAN

Clean a network.

Name	Type	Number	Description
NAME	CHAR	1	Network name
ISOLATED_NODES	INTE	1	1 = remove isolated nodes
DEAD_ENDS	INTE	1	1 = remove dead ends
LOOP_BONDS	INTE	1	1 = remove loop bonds
DUAL_BONDS	INTE	1	1 = remove dual bonds
ISOLATED_SUBNETS	INTE	1	1 = remove isolated subnets

The default for all option is 0.

ISOLATED_NODES = 1 removes any nodes with coordination = 0.

DEAD_ENDS = 1 removes any nodes with coordination = 1.

LOOP_BONDS = 1 removes any bonds which link a node directly to itself.

DUAL_BONDS = 1 removes any duplicate bonds i.e. bonds linking two nodes which are already directly linked by another bond. In this case, the volume of the deleted bond is added to the the other bond.

ISOLATED_SUBNETS = 1 removes any clusters of nodes and bonds which are isolated i.e. not connected to the inlet or the outlet.

&NET_RESHAPE

Rescale the domain and/or permute the coordinate axes of a network.

Name	Type	Number	Description
NAME	CHAR	1	Network name
SX	REAL	1	Scale factor X-direction
SY	REAL	1	Scale factor Y-direction
SZ	REAL	1	Scale factor Z-direction
ORDER	CHAR	1	Order of the original axes in the new network

Variables SX, SY and SZ enable the network domain and the position of all nodes to be scaled in the X, Y and Z directions respectively. In general, this will change the gross volume and therefore the porosity. Negative values of SX, SY or SZ are possible, in which case the domain is reversed. In all cases the inlet and outlet bonds remain unchanged, hence reversing the domain will also reverse the direction of flow. The defaults are SX = 1, SY = 1 and SZ = 1.

If ORDER is given, then it must be a 3-character string containing a permutation of 'XYZ'. This specifies the order of the original coordinate axes in the new network. The default is ORDER = 'XYZ'.

&NET_FLOWDIR

Redefine inlet and outlet bonds to a given flow direction.

Name	Type	Number	Description
NAME	CHAR	1	Network name
DIR	CHAR	1	Flow direction
ALPHA	REAL	1	Parameter controlling inlet/outlet bonds
REVERSE	INTE	1	1 = reverse inlet and outlet

The algorithm proceeds by deleting all inlet and outlet bonds and then re-defining them based on DIR and ALPHA.

DIR specifies the direction of flow which can be 'X', 'Y', 'Z' or ' ' i.e. none. The latter will result in no inlet or outlet bonds.

ALPHA is a parameter controlling the creation of inlet and outlet bonds. In particular, an inlet (outlet) bond will be created for a node if the distance from the centre of the node to the inlet (outlet) face is less than ALPHA times the node radius. The default is ALPHA = 1.25.

REVERSE enables the inlet and outlet to be reversed. The default is REVERSE = 0 which results in the inlet at X = 0, Y = 0 or Z = 0 and the outlet at X = DX, Y = DY or Z = DZ. REVERSE = 1 means the inlet becomes the outlet and vice versa.

C.3.8   Network Analysis Keywords

&NET_INFO

Output basic information about a network.

Name	Type	Number	Description
NETWORK	CHAR	1	Network name

The output consists of three tables. The first shows nodes and bonds with numbers, porosity and pore volume. The second shows minimum, mean and maximum properties for nodes. The third shows minimum, mean and maximum properties for bonds.

&NET_STATISTICS

Display statistical information about a network.

Name	Type	Number	Description
NETWORK	CHAR	1	Network name

The output consists of four tables. The first two contain probability distributions of node and bond properties. The last two contain the Pearson correlation coefficients of node and bond properties.

&NET_PSD

Output the pore size distribution.

Name	Type	Number	Description
NETWORK	CHAR	1	Network name

Nodes and bonds are tabulated separately.

&NET_CHECK

Check the consistency of a network.

Name	Type	Number	Description
NETWORK	CHAR	1	Network name

The following checks are performed:

- nodes are inside the domain

- node and bond radii > 0

- node and bond shape factor > 0 and shape factor < 0.1

- bond lengths ≥ 0

- node volume > 0

- bond volume ≥ 0

- node and bond clay volume ≥ 0

- inlet nodes are close (less than 10% of model length) to the inlet face

- outlet nodes are close (less than 10% of model length) to the outlet face

- inlet nodes are connected to pseudo-node -1

- outlet nodes are connected to pseudo-node 0

- node and bond connections are consistent

&NET_PERMEABILITY

Calculate single phase permeability of a network.

Name	Type	Number	Description
NETWORK	CHAR	1	Network name
RADIUS	INTE	1	1 = output table of permeability vs radius

The permeability is determined by calculating the hydraulic conductivity of all nodes and bonds and formulating a system of simultaneous equations for the pressure at each node. Parts of the network which are isolated from the inlet and outlet would lead to a singular matrix and therefore an initial connectivity analysis is performed to remove any such isolated clusters from the system of equations. If the connectivity analysis shows there is no connected path from the inlet to the outlet then the permeability is zero.

The system of equations is solved using a conjugate gradient algorithm with an incomplete Cholesky factorisation pre-conditioner. The number of conjugate gradient iterations is reported by "IICCG =". The total inlet and outlet fluxes are computed and the relative flux error reported by "UERR =".

The permeability follows from the total flux by applying Darcy's law. This calculation requires the cross-sectional area perpendicular to the direction of flow. The direction of flow is determined from a heuristic algorithm that examines the location of inlet and outlet nodes. If the direction of flow cannot be determined then the permeability cannot be calculated.

If RADIUS = 1 then two additional tables are output showing the permeability for the reduced network containing nodes and bonds less than and greater than a given radius respectively.

&NET_RESISTIVITY

Calculate single phase electrical resistivity (formation factor) of a network.

Name	Type	Number	Description
NETWORK	CHAR	1	Network name

The electrical resistivity is determined in an analogous way to the single phase permeability calculation except that electrical conductivity is used rather than hydraulic conductivity.

The additional comments under &NET_PERMEABILITY also apply here.

If RADIUS = 1 then two additional tables are output showing the formation factor for the reduced network containing nodes and bonds less than and greater than a given radius respectively.

&NET_TORTUOSITY

Calculate the tortuosity of a network.

Name	Type	Number	Description
NETWORK	CHAR	1	Network name
COND	CHAR	1	'H' or 'E'
NP	INTE	1	Number of particles to simulate

The tortuosity of a network is determined by tracking a large number of particles from the inlet to the outlet and calculating the average path length divided by the length of the model.

A particle starts at the inlet. At each node the probability of the particle moving through each of the connected bonds is proportional to the bond flux. Bonds which have negative flux (i.e. flow towards the node) are discounted, the remaining probabilities are normalised and one bond is chosen at random. The particle continues until it reaches the outlet.

COND specifies the conductivity used to calculate the flux. COND = 'H' uses the hydraulic conductivity. COND = 'E' uses the electrical conductivity. The default is 'H'.

NP is the number of particles to simulate. The default is 100.

&NET_RADIUS

Output tables of node and bond properties vs radius.

Name	Type	Number	Description
NETWORK	CHAR	1	Network name

The output consists of four tables containing average properties of nodes and bonds as a function or radius.

&NET_OUTPUT

Output tables of node and bond properties.

Name	Type	Number	Description
NETWORK	CHAR	1	Network name
INODE	INTE	3	Nodes to output: LOWER, UPPER, STRIDE
IBOND	INTE	3	Bonds to output: LOWER, UPPER, STRIDE

INODE and IBOND control the range of nodes and bonds which are output. The default is to output all nodes and all bonds.

&NET_COORDINATION

Output coordination number frequency and coordination number vs radius.

Name	Type	Number	Description
NETWORK	CHAR	1	Network name

The output consists of two tables. The first contains the frequency distribution of coordination numbers. The second contains the minimum, mean, maximum and standard deviation of the coordination number as a function of node radius. Inlet and outlet bonds are not included in the coordination number counts.

&NET_SHAPE_FACTOR

Output shape factor frequency and shape factor vs radius.

Name	Type	Number	Description
NETWORK	CHAR	1	Network name

The output consists of three tables. The first contains the frequency distribution of shape factor. The second contains the minimum, mean, maximum and standard deviation of the shape factor as a function of node radius. The third contains the minimum, mean, maximum and standard deviation of the shape factor as a function of bond radius.

&NET_CONNECTIVITY

Output the topological connectivity function.

Name	Type	Number	Description
NETWORK	CHAR	1	Network name

The output consist of two tables of the connectivity as a function of network elements greater than and less than a given radius respectively.

&NET_CLUSTER

Analyse disconnected network clusters.

Name	Type	Number	Description
NETWORK	CHAR	1	Network name
ICLUSTER	INTE	3	Clusters to output: LOWER, UPPER, STRIDE

The algorithm identifies the disconnected clusters of nodes and bonds i.e. parts of the network which are disconnected from each other.

The output consists of up to three tables. The first shows clusters connected and disconnected to the inlet and outlet. The second shows the number of clusters of each size.

The third table lists individual clusters and is not generated by default. It can be generated by specifying a range of clusters with ICLUSTER. ICLUSTER(1) is the first cluster; ICLUSTER(2) is the last cluster and ICLUSTER(3) is an integer stride.

&NET_SUBGRID

Analyse sub-areas of a network.

Name	Type	Number	Description
NETWORK	CHAR	1	Network name
L	INTE	3	Number of divisions of each dimension X, Y and Z

The algorithm divides the network domain into L(1) x L(2) x L(3) sub-areas, counts the number of nodes in each sub-area and then outputs a table of the number of sub-areas containing a given number of nodes. The default value of L is 2.

Bibliography

Adler, P., Jacquin, C., and Quiblier, J. (1990). Flow in simulated porous media. *International Journal of Multiphase Flow*, 16(4):691 – 712.

Agbalaka, C., Dandekar, A., Patil, S., Khataniar, S., and Hemsath, J. (2008). SPE 114496 The Effect of Wettability on Oil Recovery: A Review. *SPE Asia Pacific Oil and Gas Conference and Exhibition*, pages 1–13.

Akpokodje, M., Melvin, A., Churchill, J., Burns, S., Morris, J., S., K., Wakefield, M., and Ameerali, R. (2017). Regional study of controls on reservoir quality in the Triassic Skagerrak Formation of the Central North Sea. *Proceedings of the 8th Petroleum Geology Conference*, pages 125–146.

Al-Kharusi, A. S. and Blunt, M. J. (2007). Network extraction from sandstone and carbonate pore space images. *Journal of Petroleum Science and Enginering*, 56:219–231.

Al Mansoori, S., Itsekiri, E., Iglauer, S., Pentland, C., Bijeljic, B., and Blunt, M. (2010). Measurements of non-wetting phase trapping applied to carbon dioxide storage. *International Journal of Greenhouse Gas Control*, 4(2):283 – 288.

Al-Raoush, R. and Willson, C. (2005). Extraction of physically realistic pore network properties from three-dimensional synchrotron x-ray microtomography images of unconsolidated porous media systems. *Journal of Hydrology*, 300(1):44 – 64.

AlRatrout, A., Raeini, A. Q., Bijeljic, B., and Blunt, M. J. (2017). Automatic measurement of contact angle in pore-space images. *Advances in Water Resources*, 109:158 – 169.

Alyafei, N. and Blunt, M. J. (2016). The effect of wettability on capillary trapping in carbonates. *Advances in Water Resources*, 90:36 – 50.

Amott, E. (1959). SPE 1167 Observations Relating to the Wettability of Porous Rock. *Trans AIME*, 216.

Anderson, W. (1986a). SPE13932 Wettability Literature Survey - Part 1: Rock/Oil/Brine Interactions and the Effects of Core Handling on Wettability. *Journal of Petroleum Technology*.

Anderson, W. (1986b). SPE13933 Wettability Literature Survey - Part 2: Wettability Measurement. *Journal of Petroleum Technology*.

Anderson, W. (1987a). SPE15271 Wettability Literature Survey - Part 4: The Effects of Wettability on Capillary Pressure. *Journal of Petroleum Technology*.

Anderson, W. (1987b). SPE16323 Wettability Literature Survey - Part 5: The Effects of Wettability on Relative Permeability. *Journal of Petroleum Technology*.

Anderson, W. (1987c). SPE16471 Wettability Literature Survey - Part 6: The Effects of Wettability on Waterflooding. *Journal of Petroleum Technology*.

Angert, P. and Begg, S. (1993). SPE 26081 Modeling the Effect of Imbibition Capillary Pressure in Heterogeneous Porous Media: Waterflood Recoveries of the Romeo Interval, Prudhoe Bay Field. *Presented at SPE Western Regional Meeting, Anchorage, Alaska, U.S.A.*

Angulo, R., Alvarado, V., and Gonzalez, H. (1992). SPE 23695 Fractal Dimensions from Mercury Intrusion Capillary Tests. *Second SPE Latin American Petroleum Engineering Conference, Caracas, Venezuela*, SPE 23695:255–263.

Anovitz, L. and Cole, D. (2015). Characterisation and analysis of porosity and pore structures. *Reviews in Mineralogy and Geochmeistry*, 80:61–164.

Arand, F. and Hesser, J. (2017). Accurate and efficient maximal ball algorithm for pore network extraction. *Computers and Geosciences*, 101(January):28–37.

Archie, G. (1942). The Electrical Resistivity Log as an Aid in Determining Some Reservoir Characteristics. *Trans AIME*, 146.

Arief, I. H., Xue, L., and Lomeland, F. (2016). SPE 180059 Solutions to the Curve Fitting Problem of Mathematical Correlation and SCAL Data. *Presented at the SPE Bergen One Day Seminar, Bergen, Norway, 20 April*.

Arns, J., Robins, V., Sheppard, A., Sok, R., Pinczewski, W., and Knackstedt, M. (2004). Effect of network topology on relative permeability. *Transport in Porous Media*, 55(1):21–46.

Bakke, S. and Øren, P.-E. (1997). SPE 35479 3-D Pore-Scale Modelling of Sandstones and Flow Simulations in the Pore Networks. *SPE Journal*, 2(02):136–149.

Barabasi, A. and Albert, R. (1999). Emergence of scaling in random networks. *Science*, 286:509–512.

Barker, J. W. and Thibeau, S. (1997). A Critical Review of the Use of Pseudorelative Permeabilities for Upscaling. *SPE Reservoir Engineering*, 12(02):138–143.

Bauer, D., Youssef, S., Fleury, M., Bekri, S., Rosenberg, E., and Vizika, O. (2012). Improving the estimations of petrophysical transport behavior of carbonate rocks using a dual pore network approach combined with computed microtomography. *Transport in Porous Media*, 94(2):505–524.

Bauer, D., Youssef, S., Han, M., Bekri, S., Rosenberg, E., Fleury, M., and Vizika, O. (2011). From computed microtomography images to resistivity index calculations of heterogeneous carbonates using a dual-porosity pore-network approach: Influence of percolation on the electrical transport properties. *Phys. Rev. E*, 84:011133.

Beckingham, L., Peters, C., Um, W., Jones, K., and Lindquist, W. (2013). 2D and 3D Imaging Resolution Trade-offs in Quantifying Pore Throats for Prediction of Permeability. *Advances in Water Resources*, 62:1–12.

Békri, S., Laroche, C., and Vizika, O. (2005). SCA2005-35 Pore network models to calculate transport and electrical properties of single or dual-porosity rocks. *International Symposium of the Society of Core Analysts, Toronto*.

Berg, S., Armstrong, R., and Wiegmann, A. (2018). Gildehauser sandstone http://www.digitalrocksportal.org/projects/134.

Berg, S., Rücker, M., Ott, H., Georgiadis, A., van der Linde, H., Enzmann, F., Kersten, M., Armstrong, R., de With, S., Becker, J., and Wiegmann, A. (2016). Connected pathway relative permeability from pore-scale imaging of imbibition. *Advances in Water Resources*, 90:24 – 35.

Bieniek, A. and Moga, A. (2000). An efficient watershed algorithm based on connected components. *Pattern Recognition*, 33(6):907–916.

Biswal, B., Manwart, C., Hilfer, R., Bakke, S., and Øren, P. (1999). Quantitative analysis of experimental and synthetic microstructures for sedimentary rock. *Physica A: Statistical Mechanics and its Applications*, 273(3):452 – 475.

Biswal, B., Øren, P., Held, R., Bakke, S., and Hilfer, R. (2007). Stochastic multiscale model for carbonate rocks. *Phys Rev E Stat Nonlin Soft Matter Phys*, 75(6):061303.

Biswal, B., Øren, P., Held, R., Bakke, S., and Hilfer, R. (2009). Modeling of multiscale porous media. *Image Analysis and Stereology*, 28(1):23–34.

Blair, S., Berge, P., and Berryman, J. (1993). Two-point correlation functions to characterize microgeometry and estimate permeabilities of synthetic and natural sandstones. *U.S. Department of Energy, Office of Scientific and Technical Information*.

Blunt, M. (1997). SPE 38435 Pore Level Modeling of the Effects of Wettability. *Society of Petroleum Engineers Journal*, 2:494 – 510.

Blunt, M. (2017). *Multiphase Flow in Permeable Media a Pore-Scale Perspective*. Cambridge University Press.

Blunt, M., King, M., and Scher, H. (1992). Simulation and theory of two-phase flow in porous media. *Physical Review A*, 46(12):7680–7699.

Blunt, M. J. (2001). Flow in porous media - Pore-network models and multiphase flow. *Current Opinion in Colloid and Interface Science*, 6(3):197–207.

Blunt, M. J., Bijeljic, B., Dong, H., Gharbi, O., Iglauer, S., Mostaghimi, P., Paluszny, A., and Pentland, C. (2013). Pore-scale imaging and modelling. *Advances in Water Resources*, 51:197–216.

Blunt, M. J., Jackson, M. D., Piri, M., and Valvatne, P. H. (2002). Detailed physics, predictive capabilities and macroscopic consequences for pore network models of multi-phase flow. *Advances in Water Resources*, 25:1069–1089.

Bodla, K. K., Garimella, S. V., and Murthy, J. Y. (2014). 3D reconstruction and design of porous media from thin sections. *International Journal of Heat and Mass Transfer*, 73:250–264.

Boever, W. D., Derluyn, H., Loo, D. V., Hoorebeke, L. V., and Cnudde, V. (2015). Data-fusion of high resolution X-ray CT, SEM and EDS for 3D and pseudo-3D chemical and structural characterization of sandstone. *Micron*, 74:15 – 21.

Borgefors, G. (1984). Distance transformations in arbitrary dimensions. *Computer Vision, Graphics, & Image Processing*, 27(3):321–345.

Bosl, W., Dvorkin, J., and Nur, A. (1998). A study of porosity and permeability using a lattice boltzmann simulation. *Geophysical Research Letters*, 25:1475–1478.

Brooks, R. and Corey, A. (1964). Hydraulic Properties of Porous Media. *Hydrology Papers No. 3, Colorado State University, Fort Collins, Colorado, USA*.

Bryant, S. and Cade, C. (1992). Permeability Prediction from Geological Models. *ECMOR III - 3rd European Conference on the Mathematics of Oil Recovery*.

Bryant, S. L., Mellor, D. W., and Cade, C. A. (1993). Physically representative network models of transport in porous media. *AIChE Journal*, 39(3):387–396.

Buckley, J., Liu, Y., and Monsterleet, S. (1998). SPE 37230 Mechanisms of Wetting Alteration by Crude Oils. *SPE Journal*, 3(01):54–61.

Buckley, J., Liu, Y., Xie, X., and Morrow, N. (1997). SPE 35366 Asphaltenes and Crude Oil Wetting - The Effect of Oil Composition. *SPE Journal*, 2(02):107–119.

Bultreys, T., Boever, W. D., Hoorebeke, L. V., and Cnudde, V. (2015a). A Multi-Scale, Image-Based Pore Network Modeling Approach To Simulate Two-Phase Flow in Heterogeneous Rocks. *International Symposium of the Society of Core Analysts, St. John's Newfoundland and Labrador, Canada*.

Bultreys, T., De Boever, W., and Cnudde, V. (2016a). Imaging and image-based fluid transport modeling at the pore scale in geological materials: A practical introduction to the current state-of-the-art. *Earth-Science Reviews*, 155:93–128.

Bultreys, T., Van Hoorebeke, L., and Cnudde, V. (2015b). Multi-scale, micro-computed tomography-based pore network models to simulate drainage in heterogeneous rocks. *Advances in Water Resources*, 78:36–49.

Bultreys, T., Van Hoorebeke, L., and Cnudde, V. (2016b). Simulating secondary waterflooding in heterogeneous rocks with variable wettability using an image-based, multiscale pore network model. *Water Resources Research*, 52(9):6833–6850.

Burns, F. E., Burley, S. D., Gawthorpe, R. L., and Pollard, J. E. (2005). Diagenetic signatures of stratal surfaces in the Upper Jurassic Fulmar Formation, Central North Sea, UKCS. *Sedimentology*, 52(6):1155–1185.

Cannon, S. J. C. and Gowland, S. (1996). Facies controls on reservoir quality in the Late Jurassic Fulmar Formation, Quadrant 21, UKCS. *Geology of the Humber Group; Central Graben and Moray Firth, UKCS.*, 114(114):215–233.

Carman, P. (1956). *Flow of gases through porous media*. Butterworths Scientific.

Caudle, B., Slobod, R., and Brownscombe, E. (1951). Further Developments in the Laboratory Determination of Relative Permeability. *Trans. AIME*, 192:145–150.

Chen, S. and Doolen, G. D. (1998). Lattice Boltzmann Method. *Annual Review of Fluid Mechanics*, 30:329–364.

Clelland, W. and Fens, T. (1991). SPE 20920 Automated Rock Characterization with SEM/Image-Analysis Techniques. *SPE Formation Evaluation*, pages 437–443.

Cnudde, V. and Boone, M. (2013). High-resolution X-ray Computed Tomography in Geosciences: A Review of the Current Technology and Applications. *Earth-Science Reviews*, 123:1 – 17.

Coelho, D., Thovert, J.-F., and Adler, P. M. (1997). Geometrical and transport properties of random packings of spheres and aspherical particles. *Phys. Rev. E*, 55:1959–1978.

Cook, J., Goodwin, L., and Boutt, D. (2011). Systematic diagenetic changes in the grain-scale morphology and permeability of a quartz-cemented quartz arenite. *AAPG Bulletin*, 95(6).

Cornwall, C. (1984a). Special Core Analysis Studies for Shell UK Exploration and Production, Well 21/30-8. Technical Report SC 8354, Redwood Corex Services Ltd.

Cornwall, C. (1984b). Special Core Analysis Studies for Shell UK Exploration and Production, Well 21/30-8. Technical Report SC 8401, Redwood Corex Services Ltd.

Courtier, J. and Riches, H. (2003). The V-Fields, Blocks 49/16, 49/21, 48/20a, 48/25b, UK North Sea. *United Kingdom Oil and Gas Fields Commemorative Millennium Volume, Geological Society Memoir No. 20*, pages 861–870.

Craig, F. (1971). *The Reservoir Engineering Aspects of Waterflooding*. Society of Petroleum Engineers of AIME.

Crocker, M. and Marchin, L. (1988). SPE 14885 Wettability and Adsorption Characteristics of Crude Oil Asphaltene and Polar Fractions. *Journal or Petroleum Technology*.

Dillard, L. A. and Blunt, M. J. (2000). Development of a pore network simulation model to study nonaqueous phase liquid dissolution. *Water Resources Research*, 36(2):439–454.

Dixit, A., Buckley, J., McDougal, S., and Sorbie, K. (1998). Core Wettability: Should IAH Equal IUSBM? *Presented at The International Symposium of the Society of Core Analysts The Hague, Netherlands*.

Dixit, A., Buckley, J., McDougal, S., and Sorbie, K. (2000). Empirical Measures of Wettability in Porous Media and the Relationship Between them Derived from Pore-Scale Modelling. *Transport in Porous Media*, 40(1).

Dixit, A., McDougal, S., Sorbie, K., and Buckley, J. (1999). SPE 54454 Pore Scale Modelling of Wettability Effects and Their Influence on Oil Recovery. *SPE Reservoir Evaluation and Engineering*, 2(1).

Donaldson, E. and Alam, W. (2008). *Wettability*. Gulf Publishing Company.

Donaldson, E. and Crocker, M. (1977). Review of Petroleum Oil Saturation and its Determination. Technical Report BERC/RI-77/15, US DOE, Bartlesville Energy Research Center, New York, NY.

Donaldson, E., Thomas, R., and Lorenz, P. (1969). SPE 2338 Wettability Determination and its Effect on Recovery Efficiency. *SPE Journal*, pages 13–20.

Dong, H. and Blunt, M. J. (2009). Pore-network extraction from micro-computerized-tomography images. *Physical Review E - Statistical, Nonlinear, and Soft Matter Physics*, 80(3):1–11.

Dubey, S. and Doe, P. (1993). SPE 22598 Base Number and Wetting Properties of Crude Oils. *SPE Reservoir Engineering*, 8(03):195–200.

Dullien, F., Allsop, H., MacDonald, I., and Chatzis, I. (1990). Wettability and Immiscible Displacement in Pembina Cardium Sandstone. *J. Can. Pet. Technol.*, 29(63).

Eibenberger, E., Borsdorf, A., Wimmer, A., and Hornegger, J. (2008). Edge-Preserving Denoising for Segmentation in CT-images. *Bildverarbeitung für die Medizin 2008: Algorithmen, Systeme, Anwendungen Proceedings des Workshops*, pages 257–261.

Elkhoury, J., Shankar, R., and Ramakrishnan, T. (2019). Resolution and Limitations of X-Ray Micro-CT with Applications to Sandstones and Limestones. *Transport in Porous Media*, 129(1):413–425.

Evans, D., Graham, C., Armour, A., and Bathurst, P. (2002). *Millennium Atlas: Petroleum Geology of the Central and Northern North Sea*. The Geological Society.

Fenwick, D. and Blunt, M. (1998). SPE 38881 Network Modelling of Three-Phase Flow in Porous Media. *SPE Annual Technical Conference and Exhibition, San Antonio, Texas, USA*.

Finney, J. (2016). Finney packing of spheres http://www.digitalrocksportal.org/projects/47.

Finney, J. and Bernal, J. D. (1970). Random packings and the structure of simple liquids. i. the geometry of random close packing. *Proc. R. Soc. Lond.*, 319(1539):479–493.

Firoozabadi, A. and Ramey, H. (1988). Surface Tension of Water-Hydrocarbon Systems at Reservoir Conditions. *Jour. Cdn. Pet. Tech.*

Fischer, U. and Celia, M. A. (1999). Prediction of relative and absolute permeabilities for gas and water from soil water retention curves using a pore-scale network model. *Water Resources Research*, 35(4):1089–1100.

Flannery, B., Deckman, H., Roberge, W., and D'Amico, K. (1987). Three-dimensional X-ray Microtomography. *Science*, 237(4821):1439–1444.

Fouard, C., Cassot, E., Malandain, G., Mazel, C., Prohaska, S., Asselot, D., Westerhoff, M., and Marc-Vergnes, J. P. (2004). Skeletonization by Blocks for Large 3D Datasets: Application to Brain Microcirculation. *2nd IEEE International Symposium on Biomedical Imaging: Nano to Macro*, 1:89–92 Vol. 1.

Fredrich, J., Lakshtanov, D., Lane, N., Liu, E., Natarajan, C., Ni, D., and Toms, J. (2014). SPE 170752 Digital Rocks: Developing an Emerging Technology Through to a Proven Capability Deployed in the Business. *SPE Annual Technical Conference and Exhibition held in Amsterdam, The Netherlands*.

Fullwood, D., Niezgoda, S., and Kalidindi, S. (2008). Microstructure reconstructions from 2-point statistics using phase-recovery algorithms. *Acta Materialia*, 56(5):942 – 948.

Fyfe, C. (1979). Core Analysis Report for Shell, Well 21/25-2 North Sea. Technical Report SCA505, Core Laboratories.

Garing, C., de Chalendar, J., Voltolini, M., Ajo-Franklin, J., and Benson, S. (2017). Pore-scale capillary pressure analysis using multi-scale x-ray micromotography. *Advances in Water Resources*, 104:223–241.

Glennie, K. W. and Armstrong, L. A. (1991). The Kittiwake Field, Block 21/18, UK. North Sea. *United Kingdom Oil and Gas Fields 25 years Commemorative Volume. Geol. Soc. Memoir No. 14*, 14(14):339–346.

Golparvar, A., Zhou, Y., Wu, K., Ma, J., and Yu, Z. (2018). A comprehensive review of pore scale modeling methodologies for multiphase flow in porous media. *Advances in Geo-Energy Research*, 2:418–440.

Gostick, J. T. (2017). Versatile and efficient pore network extraction method using marker-based watershed segmentation. *Phys Rev E*, 96:023307.

Gowland, S. (1996). Facies characteristics and depositional models of highly bioturbated shallow marine siliciclastic strata: an example from the fulmar formation (late jurassic), uk central graben. *Geology of the Humber Group; Central Graben and Moray Firth, UKCS.*, 114:185–214.

Hamon, G. (2000). SPE 63144 Field-Wide Variations of Wettability. *Presented at the SPE Annual Technical Conference and Exhibition Dallas, Texas, USA*.

Hasanabadi, A., Baniassadi, M., Abrinia, K., Safdari, M., and Garmestani, H. (2016). 3D microstructural reconstruction of heterogeneous materials from 2D cross sections: A modified phase-recovery algorithm. *Computational Materials Science*, 111:107 – 115.

Hassan, M., Hassan, M., and Pavel, N. I. (2010). Scale-free network topology and multifractality in a weighted planar stochastic lattice. *New Journal of Physics*, 12.

Hazlett, R. D. (1997). Statistical characterization and stochastic modeling of pore networks in relation to fluid flow. *Mathematical Geology*, 29(6):801–822.

Herman, G. T. (2009). *Fundamentals of Computerized Tomography, Image Reconstruction from Projections*. Springer.

Hilfer, R., Armstrong, R., Berg, S., Georgiandis, A., and Ott, H. (2015). Capillary saturation and desaturation. *Physical Review E*, 92(6):063023.

Hilfer, R. and Zauner, T. (2011). High-precision synthetic computed tomography of reconstructed porous media. *Phys Rev E*, 84.

Hilfer, R., Zauner, T., Lemmer, A., and Biswal, B. (2012). Synthetic micro-computed tomograms https://www.icp.uni-stuttgart.de/microct/dl.php.

Homberg, U., Baum, D., Wiebel, A., Prohaska, S., and Hege, H.-C. (2014). Definition, extraction, and validation of pore structures in porous materials. *Topological Methods in Data Analysis and Visualization III: Mathematics and Visualization*, pages 235–248.

Houston, I. (1989). Special Core Analysis Study for Conoco (UK) Ltd, Well 49/16-Q05. Technical Report SC 8855, Corex Services.

Howell, J., Flint, S., and Hunt, C. (1996). Sedimentological aspects of the Humber Group (Upper Jurassic) of the South Central Graben, UK North Sea. *Sedimentology*, 43(1):89–114.

Huang, J., Cavanaugh, T., and Nur, B. (2013a). An Introduction to SEM Operational Principles and Geologic Applications for Shale Hydrocarbon Reservoirs. *AAPG Memoir 102*, pages 1–6.

Huang, Z. and Chau, K. (2008). A new image thresholding method based on gaussian mixture model. *Applied Mathematics and Computation*, 205(2):899–907.

Huang, Z., Chen, J., Xue, H., Wang, Y., Wang, M., and Deng, C. (2013b). Microstructural characteristics of the cretaceous qingshankou formation shale, songliao basin. *Petroleum Exploration and Development*, 40(1):61 – 68.

Iassonov, P., Gebrenegus, T., and Tuller, M. (2009). Segmentation of X-ray computed tomography images of porous materials: A crucial step for characterization and quantitative analysis of pore structures. *Water Resources Research*, 45(9).

Idowu, N. and Blunt, M. (2008). IPTC 12292 Pore-scale modelling of rate effects in waterflooding. *Presented at the International Petroleum Technology Conference, Kuala Lumpur, Malaysia*.

Jackson, M., Valvatne, P., and Blunt, M. (2002). SPE 77543 Prediction of Wettability Variation and its Impact on Waterflooding Using Pore- to Reservoir-Scale Simulation. *SPE Annual Technical Conference and Exhibition, San Antonio, Texas, USA*.

Jadhunandan, P. and Morrow, N. (1995). SPE 22597 Effect of Wettability on Waterflood Recovery for Crude-Oil/Brine/Rock Systems. *SPE Reservoir Engineering*, 10(01):40–46.

Jerauld, G. and Rathmell, J. (1997). SPE 28576 Wettability and Relative Permeability of Prudhoe Bay: A Case Study in Mixed-Wet Reservoirs. *SPE Reservoir Engineering*, 12(01):58–65.

Jiang, Z., van Dijke, M., Geiger, S., Kronbauer, D., Mantovani, I., and Fernandes, C. (2013a). SPE 1660001 The Impact of Spatial Correlation of Microporosity on Fluid Flow in Carbonate Rocks. *SPE Reservoir Characterisation and Simulation Conference and Exhibition, Abu Dhabi, UAE*.

Jiang, Z., van Dijke, M. I. J., Sorbie, K. S., and Couples, G. D. (2013b). Representation of multiscale heterogeneity via multiscale pore networks. *Water Resources Research*, 49(9):5437–5449.

Jiang, Z., van Dijke, M. I. J., Wu, K., Couples, G. D., Sorbie, K. S., and Ma, J. (2012). Stochastic Pore Network Generation from 3D Rock Images. *Transport in Porous Media*, 94(2):571–593.

Jiang, Z., Wu, K., Couples, G., van Dijke, M. I. J., Sorbie, K. S., and Ma, J. (2007). Efficient extraction of networks from three-dimensional porous media. *Water Resources Research*, 43(12):1–17.

Jivkov, A. P., Hollis, C., Etiese, F., McDonald, S. A., and Withers, P. J. (2013). A novel architecture for pore network modelling with applications to permeability of porous media. *Journal of Hydrology*, 486:246–258.

Johnson, H., MacKay, T., and Stewart, D. (1986). The Fulmar Oil-field (Central North Sea): Geological Aspects of its Discovery, Appraisal and Development. *Marine and Petroleum Geology*, 3(2):99–125.

Journel, A. G. (1986). Constrained interpolation and qualitative information — the soft kriging approach. *Mathematical Geology*, 18(3):269–286.

Ju, Y., Zheng, J., Epstein, M., Sudak, L., Wang, J., and Zhao, X. (2014). 3D Numerical Reconstruction of Well-Connected Porous Structure of Rock using Fractal Algorithms. *Computer Methods in Applied Mechanics and Engineering*, 279:212–226.

Kashib, T. and Srinivasan, S. (2006). A probabilistic approach to integrating dynamic data in reservoir models. *Journal of Petroleum Science and Engineering*, 50(3):241–257.

Katz, A. and Thompson, A. (1987). A quantitative prediction of permeability in porous rock. *Physical Review B*, 34:8179–8181.

Keehm, Y., Mukerji, T., and Nur, A. (2004). Permeability Prediction from Thin Sections: 3D Reconstruction and Lattice Boltzmann Flow Simulation. *Geophysical Research Letters*, 31(4).

Killins, C., Nielsen, R., and Calhoun, J. (1953). Capillary Desaturation and Imbibition on Porous Rocks. *Producers Monthly*, 18(2):30–39.

Kirk, J. (1984). Conventional Core Analysis for Shell UK Exploration and Production, Well 21/30-8. Technical Report CC 412/84, Redwood Corex Services Ltd.

Klise, K. A., Moriarty, D., Yoon, H., and Karpyn, Z. (2016). Automated contact angle estimation for three-dimensional x-ray microtomography data. *Advances in Water Resources*, 95:152 – 160. Pore scale modeling and experiments.

Kovscek, A., Wong, H., and Radke, C. (1993). SPE 24880 A Pore-Level Scenario for the Development of Mixed Wettability in Oil Reservoirs. *Presentation at the 67th SPE Annual Technical Conference and Exhibition, Washington, DC, USA*.

Kyte, J. and Naumann, V. (1961). SPE 55 Effect of Reservoir Environment on Water-Oil Displacements. *SPE Journal*, 13(6):579–582.

Lahann, R., Ferrier, J., and Corrigan, S. (1993). Reservoir Heterorgeneity in the Vanguard Field UKCS. *Advances in Reservoir Geology, Geological Society Special Publication No. 69*, pages 33–56.

Lai, J., Wang, G., Cao, J., Xiao, C., Wang, S., Pang, X., Dai, Q., He, Z., Fan, X., Yang, L., and Qin, Z. (2018). Investigation of pore structure and petrophysical property in tight sandstones. *Marine and Petroleum Geology*, 91:179–189.

Land, C. (1968). SPE 1942 Calculation of Imbibition Relative Permeability for Two and Three Phase Flow from Rock Properties. *SPE Journal*, 8(2):149–156.

Latief, F., Biswal, B., Fauzi, U., and Hilfer, R. (2010). Continuum reconstruction of the pore scale microstructure for fontainebleau sandstone. *Physica A: Statistical Mechanics and its Applications*, 389(8):1607–1618.

Leverett, M. (1941). Capillary Behaviour in Porous Solids. *Trans AIME*, 142.

Li, K. (2004). SPE 89429 Theoretical Development of the Brooks-Corey Capillary Pressure Model from Fractal Modeling of Porous Media. *Proceedings of SPE/DOE Symposium on Improved Oil Recovery*.

Liang, Y., Hu, P., Wang, S., Song, S., and Jiang, S. (2019). Medial axis extraction algorithm specializing in porous media. *Powder Technology*, 343:512–520.

Liao, P., Chen, T., and Chung, P. (2001). A fast algorithm for multilevel thresholding. *J. Inf. Sci. Eng.*, 17:713–727.

Lindquist, W. B., Lee, S.-M., Coker, D. A., Jones, K. W., and Spanne, P. (1996). Medial axis analysis of void structure in three-dimensional tomographic images of porous media. *Journal of Geophysical Research: Solid Earth*, 101(B4):8297–8310.

Liu, H., Kang, Q., Leonardi, C. R., Schmieschek, S., Narváez, A., Jones, B. D., Williams, J. R., Valocchi, A. J., and Harting, J. (2016). Multiphase lattice Boltzmann simulations for porous media applications. *Computational Geosciences*, 20(4):777–805.

Lomeland, F., Ebeltoft, E., and Thomas, W. (2005). SCA2005-32 A New Versatile Relative Permeability Correlation. *Presented at the International Symposium of the Society of Core Analysts held in Toronto, Canada, August*.

Lynn, J. (1985). Special Core Analysis Report 3240184-84 for Conoco (UK) Ltd, Well 49/16-10. Technical Report 3240184-84, Erco Petroleum Services Inc.

Maeso, C. (1988). Special Core Analysis Study Conoco (UK) Ltd V-Field Study. Technical Report C2/152, Robertson Group Plc.

Manwart, C., Torquato, S., and Hilfer, R. (2000). Stochastic reconstruction of sandstones. *Phys. Rev. E*, 62:893–899.

Masalmeh, S., Jing, X., Roth, S., Wang, C., Dong, H., and Blunt, M. (2015). SPE 177572 Towards Predicting Multi-Phase Flow in Porous Media Using Digital Rock Physics: Workflow to Test the Predictive Capability of Pore-Scale Modeling. *Presentation at the Abu Dhabi International Petroleum Exhibition and Conference*.

Mason, G. and Morrow, N. (1991). Capillary behavior of a perfectly wetting liquid in irregular triangular tubes. *Journal of Colloid and Interface Science*, 141(1):262 – 274.

Mattila, K., Puurtinen, T., Hyvaluoma, J., Surmas, R., Myllys, M., Turpeinen, T., Robertsen, F., Westerholm, J., and Timonen, J. (2016). A prospect for computing in porous materials research: Very large fluid flow simulations. *Journal of Computational Science*, 12:62 – 76.

McCaffery, F. and Bennion, D. (1974). The Effect of Wettability on Two-Phase Relative Permeabilitiies. *Journal of Canadian Petroleum Technology*, 13(4).

McCain, W. (1991). SPE 18571 Reservoir Fluid Property Correlations - State of the Art. *SPE Reservoir Engineering*.

McDougall, S. and Sorbie, K. (1993). SPE 25271 The Prediction of Waterflood Performance in Mixed-Wet Systems from Pore-Scale Modelling and Simulation. *Presented at the 12th SPE Symposium on Reservoir Simulation held in New Orleans, LA, USA*.

McNeil, B., Shaw, H., and Rankin, A. (1995). Diagenesis of the Rotliegend Sandstones in the V-Fields, Southern North Sea: a Fluid Inclusion Study. *The Geochemistry of Reservoirs, Geological Society Special Publication No. 86*, pages 125–139.

Meakin, P. and Tartakovsky, A. M. (2009). Modeling and simulation of pore-scale multiphase fluid flow and reactive transport in fractured and porous media. *Reviews of Geophysics*, 47(3):1–47.

Mehmani, A., Milliken, K., and Prodanović, M. (2019). Predicting flow properties in diagenetically-altered media with multi-scale process-based modeling: A wilcox formation case study. *Marine and Petroleum Geology*, 100:179–194.

Mehmani, A. and Prodanović, M. (2014). The effect of microporosity on transport properties in porous media. *Advances in Water Resources*, 63:104 – 119.

Morad, S., Al-Ramadan, K., Ketzer, J., and DeRos, L. (2010). The impact of diagenesis on the heterogeneity of sandstone reservoirs: A review of the role of depositional fades and sequence stratigraphy. *AAPG Bulletin*, 94(8):1267–1308.

Morgan, J. and Gordon, D. (1970). SPE2588 Influence of Pore Geometry on Water-Oil Relative Permeability. *JPT*, pages 1199–1208.

Morrow, N., Lim, H., and Ward, J. (1986). SPE 13215 Effect of Crude Oil Induced Wettability Changes on Oil Recovery. *SPE Formation Evaluation*, 281(2).

Morrow, N. R. (1990). SPE 21621 Wettability and Its Effect on Oil Recovery. *Journal of Petroleum Technology*, 42(12):1476–1484.

Mosser, L., Dubrule, O., and Blunt, M. (2017). Reconstruction of three-dimensional porous media using generative adversarial neural networks. *Phys. Rev. E*, 96:043309.

Mosser, L., Dubrule, O., and Blunt, M. (2018). Stochastic reconstruction of an oolitic limestone by generative adversarial networks. *Transport in Porous Media*, 125(1):81–103.

Munawar, M. J., Lin, C., Cnudde, V., Bultreys, T., Dong, C., Zhang, X., De Boever, W., Zahid, M. A., and Wu, Y. (2018). Petrographic characterization to build an accurate rock model using micro-CT: Case study on low-permeable to tight turbidite sandstone from Eocene Shahejie Formation. *Micron*, 109(March):22–33.

Muneta, Y., Mubarak, M., Alhassani, H., and Arisaka, K. (2004). SPE 88711 Formulation of Capillary Force Barriers in Moderately Oil-Wet Systems and their Application to Reservoir Simulation. *Presented at SPE Abu Dhabi International Exhibition and Conference, Abu Dhabi, UAE*.

Namba, T. and Hiraoka, T. (1995). SPE 29773 Capillary Force Barriers in a Carbonate Reservoir Under Waterflooding. *Presented at the SPE Middle East Oil Show, Bahrain*.

Naraghi, M. E., Spikes, K., and Srinivasan, S. (2017). SPE 180489 3D Reconstruction of Porous Media From a 2D Section and Comparisons of Transport and Elastic Properties. *SPE Reservoir Evaluation & Engineering*, 20(02):342–352.

Norrie, A. (1987). Final Core Analysis Report for Conoco (UK) Ltd, Well 49/16-Q02. Technical Report APS 056, Aberdeen Petroleum Services.

Norrie, A. (1988a). Final Core Analysis Report for Conoco (UK) Ltd, Well 49/16-Q03. Technical Report APS 061, Aberdeen Petroleum Services.

Norrie, A. (1988b). Final Core Analysis Report for Conoco (UK) Ltd, Well 49/16-Q04. Technical Report APS 064, Aberdeen Petroleum Services.

Okabe, H. and Blunt, M. (2005a). Prediction of Permeability for Porous Media Reconstructed Using Multiple-Point Statistics. *Physical Review E*, 70:066135.

Okabe, H. and Blunt, M. J. (2005b). Pore space reconstruction using multiple-point statistics. *Journal of Petroleum Science and Engineering*, 46(1-2):121–137.

Okabe, H. and Blunt, M. J. (2007). Pore space reconstruction of vuggy carbonates using microtomography and multiple-point statistics. *Water Resources Research*, 43(12):3–7.

Øren, P., Bakke, S., and Arntzen, O. (1998). SPE52052 Extending predictive capabilities to network models. *SPE Journal*.

Øren, P. E. and Bakke, S. (2002). Process based reconstruction of sandstones and prediction of transport properties. *Transport in Porous Media*, 46(2-3):311–343.

Otsu, N. (1979). A threshold selection method from gray-level histograms. *IEEE Trans. Sys., Man., Cyber.*, 9(1):62–66.

Owens, W. and Archer, D. (1971). SPE 3034 The Effect of Rock Wettability on Oil-Water Relative Permeability Relationships. *Journal Petroleum Technology*, pages 873–878.

Pak, T., Butler, I., Geiger, S., van Dijke, M., Jiang, Z., and Surmas, R. (2016). Multiscale pore network representation of heterogeneous carbonate rocks. *Water Resources Research*, 52:5433–5441.

Paterson, M. (1983). The Equivalent Channel Model for Permeability and Resistivity in Fluid-Saturated Rock: A Re-appraisal. *Mechanics of Materials*, 2(4):345 – 352.

Patzek, T. W. (2001). Verification of a Complete Pore Network Simulator of Drainage and Imbibition. *SPE Journal*, 6(02):144–156.

Pei, H., Zhang, G., Ge, J., Jin, L., and Liu, X. (2011). Analysis of microscopic displacement mechanisms of alkaline flooding for enhanced heavy-oil recovery. *Energy and Fuels*, 25.

Pentland, C., Tanino, Y., Iglauer, S., and Blunt, M. (2013). SPE 133798 Capillary Trapping in Water-Wet Sandstones: Coreflooding Experiments and Pore-Network Modeling. *Presented at the SPE Annual Technical Conference and Exhibition, Florence, Italy*.

Pilotti, M. (2000). Reconstruction of clastic porous media. *Transport in Porous Media*, 41(3):359–364.

Pittman, E. and Thomas, J. (1979). SPE 7550 Some Applications of Scanning Electron Microscopy to the Study of Reservoir Rocks. *Journal of Petroleum Technology*.

Politis, M. G., Kikkinides, E. S., Kainourgiakis, M. E., and Stubos, A. K. (2008). A hybrid process-based and stochastic reconstruction method of porous media. *Microporous and Mesoporous Materials*, 110(1):92–99.

Pritchard, M. (1991). The V-Fields, Blocks 49/16, 49/21, 48/20a, 48/25b, UK North Sea. *United Kingdom Oil and Gas Fields 25 Years Commemorative Volume, Geological Society Memoir No. 14*, pages 497–502.

Prodanovic, M., Esteva, M., Hanlon, M., Nanda, G., and Agarwal, P. (2015). Digital Rocks Portal: a sustainable platform for imaged dataset sharing, translation and automated analysis. In *AGU Fall Meeting Abstracts*, volume 2015, pages MR43A–02.

Prodanović, M., Lindquist, W., and Seright, R. (2006). Porous structure and fluid partitioning in polyethylene cores from 3d x-ray microtomographic imaging. *Journal of Colloid and Interface Science*, 298(1):282 – 297.

Prodanović, M., Mehmani, A., and Sheppard, A. (2015). Imaged-based multiscale network modelling of microporosity in carbonates. *Geological Society, London, Special Publications*, 406(1):95–113.

Pyrcz, M. and Deutsch, C. (2014). *Geostatistical Reservoir Modelling, Second Edition*. Oxford University Press.

Rabbani, A., Ayatollahi, S., Kharrat, R., and Dashti, N. (2016). Estimation of 3-D pore network coordination number of rocks from watershed segmentation of a single 2-D image. *Advances in Water Resources*, 94:264–277.

Rabbani, A., Jamshidi, S., and Salehi, S. (2014). An automated simple algorithm for realistic pore network extraction from micro-tomography images. *Journal of Petroleum Science and Engineering*, 123:164–171.

Ramstad, T. (2018). Bentheimer micro-CT with waterflood http://www.digitalrocksportal.org/projects/172.

Ramstad, T., Berg, C., and Thompson, K. (2019). Pore-scale simulations of single- and two-phase flow in porous media: Approaches and applications. *Transport in Porous Media*.

Ramstad, T., Idowu, N., Nardi, C., and Øren, P.-E. (2012). Relative Permeability Calculations from Two-Phase Flow Simulations Directly on Digital Images of Porous Rocks. *Transp Porous Med*, 94:487–504.

Ramstad, T., Øren, P.-E., and Bakke, S. (2010). SPE 124617 Simulation of Two-Phase Flow in Reservoir Rocks Using a Lattice Boltzmann Method. *SPE Annual Technical Conference and Exhibition, New Orleans 4-7 October*.

Raoof, A. and Hassanizadeh, S. M. (2010). A new method for generating pore-network models of porous media. *Transport in Porous Media*, 81(3):391–407.

Reed, S. (2005). *Electron Microprobe Analysis and Scanning Electron Microscopy in Geology*. Cambridge University Press.

Roberts, J. (1982). Conventional Core Analysis for Shell UK Exploration and Production, Well 21/30-3. Technical Report 311 91247, Core Laboratories.

Roberts, J. (1983a). Conventional Core Analysis for Shell UK Exploration and Production, Well 21/25-3. Technical Report SCA859, Core Laboratories.

Roberts, J. (1983b). Special Core Analysis Study for Shell UK Exploration and Production, Well 21/25-3. Technical Report UKSCAL 311-82340, Core Laboratories.

Roberts, J. N. and Schwartz, L. M. (1985). Grain consolidation and electrical conductivity in porous media. *Phys. Rev. B*, 31:5990–5997.

Robertson, C., Rapach, J., Grant, N., and Smith, M. (1992). SPE 25047 The history of horizontal wells in the V-Fields. *European Petroleum Conference Cannes, France*.

Robin, M., Rosenberg, E., and Fassi-Fihri, O. (1995). SPE 22596 Wettability Studies at the Pore Level: a New Approach by use of Cryo - SEM. *SPE Formation Evaluation*, pages 11 – 19.

Rose, W. and Bruce, W. (1949). Evaluation of Capillary Character in Petroleum Reservoir Rock. *Trans AIME*, 186.

Roth, S., Biswal, B., Afshar, G., Held, R., Øren, P.-E., Berge, L., and Hilfer, R. (2011). Continuum-based rock model of a reservoir dolostone with four orders of magnitude in pore sizes. *AAPG Bulletin*, 95(6):925–940.

Roth, S., Li, D., Dong, H., and Blunt, M. (2012). SCA2012-02 Numerical Pore-Network Fusion to Predict Capillary Pressure and Relative Permeability in Carbonates. *International Symposium of the Society of Core Analysts, Aberdeen, Scotland, UK*.

Ruspini, L. C., Lindkvist, G., Bakke, S., Alberts, L., Carnerup, A. M., and Øren, P. E. (2016). SPE 180268 A Multi-Scale Imaging and Modeling Workflow for Tight Rocks. *SPE Low Perm Symposium*, pages 5–6.

Ruzyla, K. (1986). SPE 13133 Characterization of Pore Space by Quantitative Image Analysis. *SPE Formation Evaluation*.

Sahimi, M. (2011). *Flow and Transport in Porous Media and Fractured Rock, Second Edition*. Wiley-VCH.

Salathiel, R. (1973). SPE 4104 Oil Recovery by Surface Film Drainage in Mixed Wettability Rocks. *Journal or Petroleum Technology*.

Santiago, A. (2008). Multiscaling of porous soils as heterogeneous complex networks. *Nonlinear Processes in Geophysics*, pages 893–902.

Schlüter, S., Sheppard, A., Brown, K., and Wildenschild, D. (2014). Image processing of multiphase images obtained via X-ray microtomography: A review. *Water Resources Research*, 50(4):3615–3639.

Sebborn, L. (1983). Reservoir Fluid Study for Shell UK Exploration and Production Well: 21/25-3. Technical Report RFLA 830069, Core Laboratories.

Serra, J. (1983). *Image Analysis and Mathematical Morphology*. Academic Press, Inc.

Shams, M., El-Banbi, A., and Khairy, M. (2013). SPE 164658 Effect of Capillary Pressure on the Numerical Simulation of Conventional and Naturally Fractured Reservoirs. *Presented at SPE North Africa Technical Conference and Exhibition, Cairo, Egypt*.

She, F. H., Chen, R. H., Gao, W. M., Hodgson, P. D., Kong, L. X., and Hong, H. Y. (2009). Improved 3D thinning algorithms for skeleton extraction. *DICTA 2009 - Digital Image Computing: Techniques and Applications*, pages 14–18.

Sheppard, A., Latham, S., Middleton, J., Kingston, A., Myers, G., Varslot, T., Fogden, A., Sawkins, T., Cruikshank, R., Saadatfar, M., Francois, N., Arns, C., and Senden, T. (2014). Techniques in helical scanning, dynamic imaging and image segmentation for improved quantitative analysis with x-ray micro-ct. *Nuclear Instruments and Methods in Physics Research Section B*, 324:49 – 56.

Sheppard, A. P., Sok, R. M., and Averdunk, H. (2005). Improved pore network extraction methods. *Proc. Int. Symp. Soc. Core Anal. Toronto, Canada*.

Sheppard, A. P., Sok, R. M., Averdunk, H., Robins, V. B., and Ghous, A. (2006). Analysis of Rock Microstructure Using High Resolution X-ray Tomography. *Proc. Int. Symp. Soc. Core Anal. Trondheim, Norway*.

Silin, D. and Patzek, T. (2006). Pore space morphology analysis using maximal inscribed spheres. *Physica A*, 371:336–360.

Skjaeveland, S., Siqveland, L., Kjosavik, A., Hammervold, W., and Virnovsky, G. (1998). SPE 39497 Capillary Pressure Correlation for Mixed-Wet Reservoirs. *SPE India Oil and Gas Conference, New, Delhi, India*.

Sorbie, K. and Skauge, A. (2011). Can Network Modelling Predict Two-Phase Flow Functions? *Presented at The International Symposium of the Society of Core Analysts Austin, Texas, USA*.

Soulaine, C., Gjetvaj, F., Garing, C., Roman, S., Russian, A., Gouze, P., and Tchelepi, H. (2016). The impact of sub-resolution porosity of x-ray microtomography images on the permeability. *Transport in Porous Media*, 113(1):227–243.

Spiteri, E., Juanes, R., Blunt, M., and Orr, F. (2008). SPE 96448 A New Model of Trapping and Relative Permeability Hysteresis for All Wettability Characteristics. *SPE Journal*.

Stewart, D. J. (1986). Diagenesis of the Shallow Marine Fulmar Formation in the Central North Sea. *Clay Minerals*, 21(4):537–564.

Stewart, S. A. and Clark, J. A. (1999). Impact of salt on the structure of the Central North Sea hydrocarbon fairways. *Petroleum Geology of Northwest Europe: Proceedings of the 5th Conference*, pages 179–200.

Strebelle, S. (2002). Conditional Simulation of Complex Geological Structures Using Multiple-Point Statistics. *Mathematical Geology*, 34(1):1–21.

Sukop, M. and Thorne, D. (2006). *Lattice Boltzmann Modeling: An Introduction for Geoscientists and Engineers*. Springer.

Sutherland, W. (1984). Final Core Analysis Report, Well 49/16-10. Technical Report 1075, Erco Petroleum Services Inc.

Tahmasebi, P. (2018). *Multiple Point Statistics: A Review*, pages 613–643. Springer International Publishing, Cham.

Tahmasebi, P., Hezarkhani, A., and Sahimi, M. (2012). Multiple-point geostatistical modeling based on the cross-correlation functions. *Computational Geosciences*, 16(3):779–797.

Tahmasebi, P. and Kamrava, S. (2018). Rapid multiscale modeling of flow in porous media. *Phys Rev E*, 98:052901.

Tahmasebi, P. and Sahimi, M. (2012). Reconstruction of three-dimensional porous media using a single thin section. *Phys Rev E*, 85.

Tanino, Y. and Blunt, M. J. (2013). Laboratory investigation of capillary trapping under mixed-wet conditions. *Water Resources Research*, 49(7):4311–4319.

Taylor, T. R., Kittridge, M. G., Winefield, P., Bryndzia, L. T., and Bonnell, L. M. (2015). Reservoir quality and rock properties modeling - Triassic and Jurassic sandstones, greater Shearwater area, UK Central North Sea. *Marine and Petroleum Geology*, 65:1–21.

Thompson, A., Katz, A., and Raschke, R. (1987). SPE16794 Estimation of Absolute Permeability From Capillary Pressure Measurements. *Presented at the SPE Annual Technical Conference and Exhibition Dallas, Texas, USA*.

Thompson, K., Wilson, C., White, C., Nyman, S., Bhattacharya, J., and Reed, A. (2005). SPE 95887 Application of a New Grain-Based Reconstruction Algorithm to Microtomography Images for Quantitative Characterization and Flow Modeling. *SPE Annual Technical Conference and Exhibition, Dallas, Texas, USA*.

Thomson, P.-R., Aituar-Zhakupova, A., and Hier-Majumder, S. (2018). Image segmentation and analysis of pore network geometry in two natural sandstones. *Frontiers in Earth Science*, 6:58.

Tomasi, C. and Manduchi, R. (1998). Bilateral filtering for gray and color images. *ICCV*, 98:839–846.

Treiber, L. and Owens, W. (1972). A Laboratory Evaluation of the Wettability of Fifty Oil-Producing Reservoirs. *Society of Petroleum Engineers Journal*, 12(06):531–540.

Tsakiroglou, C. D. (2012). A multi-scale approach to model two-phase flow in heterogeneous porous media. *Transport in Porous Media*, 94(2):525–536.

Valvatne, P. H. (2004). *Predictive Pore-Scale Modelling of Multiphase Flow*. PhD thesis, Imperial College London.

Valvatne, P. H. and Blunt, M. J. (2004). Predictive pore-scale modeling of two-phase flow in mixed wet media. *Water Resources Research*, 40(7):1–21.

Valvatne, P. H., Piri, M., Lopez, X., and Blunt, M. J. (2005). Predictive Pore-Scale Modeling of Single and Multiphase Flow. *Transport in Porous Media*, 58(1-2):23–41.

Van Benten, J. (1980a). Investigation of Cores from Well 21/25-2 UK, Part II Petrophysical Properties of Core Samples. Technical Report RKTR.80.120, Shell Exploratie en Produktie Laboratorium, Rijswijk, The Netherlands.

Van Benten, J. (1980b). Investigation of Cores from Well 21/30-3 UK, Part II Petrophysical Properties of Core Samples. Technical Report RKTR.82.351, Shell Exploratie en Produktie Laboratorium, Rijswijk, The Netherlands.

van Lingen, P., Bruining, J., and van Kruijsdijk, C. (1996). SPE 30782 Capillary Entrapment Caused by Small-Scale Wettability Heterogeneities. *SPE Reservoir Engineering*, 11(2):93–99.

Varslot, T., Kingston, A., Myers, G., and Sheppard, A. (2011). High-resolution helical cone-beam micro-CT with theoretically-exact reconstruction from experimental data. *Medical Physics*, 38(10):5459–5476.

Verri, I., Della Torre, A., Montenegro, G., Onorati, A., Duca, S., Mora, C., Radaelli, F., and Trombin, G. (2017). Development of a digital rock physics workflow for the analysis of sandstones and tight rocks. *Journal of Petroleum Science and Engineering*, 156.

Vogel, H. J. and Roth, K. (2001). Quantitative morphology and network representation of soil pore structure. *Advances in Water Resources*, 24(3-4):233–242.

Walsh, J. B. and Brace, W. F. (1984). The effect of pressure on porosity and the transport properties of rock. *Journal of Geophysical Research*, 89(B11):9425–9431.

Warren, E. and Smalley, P. (1994). Part 1: Compendium of North Sea Oil and Gas Fields. *Geological Society, London, Memoirs*, 15(1):3–77.

Welton, J. (2003). *SEM Petrology Atlas, Methods is Exploration Series No.4*. American Association of Petroleum Geologists.

Wendell, D., Anderson, W., and Meyers, J. (1987). Restored-State Core Analysis for the Hutton Reservoir. *SPE Formation Evaluation*, 2(04):509–517.

Werth, C. J., Zhang, C., Brusseau, M. L., Oostrom, M., and Baumann, T. (2010). A review of non-invasive imaging methods and applications in contaminant hydrogeology research. *Journal of Contaminant Hydrology*, 113(1):1 – 24.

Wildenschild, D. and Sheppard, A. P. (2013). X-ray imaging and analysis techniques for quantifying pore-scale structure and processes in subsurface porous medium systems. *Advances in Water Resources*, 51:217 – 246.

Williams, G. (1991). Final Core Analysis Report for Conoco (UK) Ltd, Well 49/16-Q06. Technical Report APS 131, Aberdeen Petroleum Services.

Wolcott, J. and Groves, F. (1996). SPE 25194 The Influence of Crude-Oil Composition on Mineral Adsorption and Wettability Alteration. *Presented at the SPE International Symposium on Oilfield Chemistry held in New Orleans, LA, USA*.

Wu, K., Jiang, Z., Ma, J., Couples, G., van Dijke, M., and Sorbie, K. (2011). SCA2011-36 Multiscale Pore System Reconstruction and Integration. *International Symposium of the Society of Core Analysts, Austin, Texas, USA*.

Wu, K., Nunan, N., Crawford, J. W., Young, I. M., and Ritz, K. (2004). An efficient Markov chain model for the simulation of heterogeneous soil structure. *Soil Science Society of America Journal*, 68(2):346–351.

Wu, K., van Dijke, M. I. J., Couples, G. D., Jiang, Z., Ma, J., Sorbie, K. S., Crawford, J., Young, I., and Zhang, X. (2006). 3D Stochastic Modelling of Heterogeneous Porous Media: Applications to Reservoir Rocks. *Transport in Porous Media*, 65(3):443–467.

Wu, Y., Lin, C., Ren, L., Yan, W., An, S., Chen, B., Wang, Y., Zhang, X., You, C., and Zhang, Y. (2018). Reconstruction of 3D porous media using multiple-point statistics based on a 3D training image. *Journal of Natural Gas Science and Engineering*, 51(November 2017):129–140.

Wu, Y., Tahmasebi, P., Lin, C., Munawar, M., and Cnudde, V. (2019a). Effects of micropores on geometric, topological and transport properties of pore systems for low-permeability porous media. *Journal of Hydrology*, 575:327–342.

Wu, Y., Tahmasebi, P., Lin, C., Zahid, M., Dong, C., Golab, A., and Ren, L. (2019b). A comprehensive study on geometric, topological and fractal characterizations of pore systems in low-permeability reservoirs based on SEM, MICP, NMR, and X-ray CT experiments. *Marine and Petroleum Geology*, 103:12–28.

Wyber, G. (1988). Final Core Analysis Report for Conoco (UK) Ltd, Well 49/16-Q05. Technical Report APS 083, Aberdeen Petroleum Services.

Xiong, Q., Baychev, T. G., and Jivkov, A. P. (2016). Review of pore network modelling of porous media: Experimental characterisations, network constructions and applications to reactive transport. *Journal of Contaminant Hydrology*, 192:101–117.

Yakubo, K. and Koroak, D. (2011). Scale-free networks embedded in fractal space. *Physical Review E - Statistical, Nonlinear, and Soft Matter Physics*, 83(6).

Yan, J., Plancher, H., and Morrow, N. (1997). Wettability Changes Induced by Adsorption of Asphaltenes. *SPE Production & Facilities*, 12(04):259–266.

Yao, J. and Al., E. (2013). Upscaling of Carbonate Rocks From Micropore Scale To Core Scale. *Journal for Multiscale Computational Engineering*, 11(5)(January):497–504.

Yeong, C. L. Y. and Torquato, S. (1998). Reconstructing Random Media I and II. *Physical Review E*, 58(1):224–233.

Youssef, S., Rosenberg, E., Gland, N., Bekri, S., and Vizika, O. (2007). Quantitative 3D Characterisation of the Pore Space of Real Rocks : Improved micro-CT Resolution and Pore Extraction Methodology. *International Symposium of the Society of Core Analysts*, pages 1–13.

Zhang, F., Wang, Y.-s., Gao, C.-y., Si, S.-c., and Xu, J.-q. (2008). An improved parallel thinning algorithm with two subiterations. *Optoelectronics Letters*, 4(1):69–71.

Zhang, P., Lee, Y., and Zhang, J. (2019). A review of high-resolution X-ray computed tomography applied to petroleum geology and a case study. *Micron*, 124.

Zhang, T. Y. and Suen, C. Y. (1988). A modified fast parallel algorithm for thinning digital patterns. *Pattern Recognition Letters*, 7(2):99–106.

Zhao, X., Blunt, M. J., and Yao, J. (2010). Pore-scale modeling: Effects of wettability on waterflood oil recovery. *Journal of Petroleum Science and Engineering*, 71(3):169 – 178.

Zhou, W., Apkarin, R., Wang, Z., and Joy, D. (2006). Fundamentals of Scanning Electron Microscopy. In *Scanning Electron Microscopy for Nanotechnology*, chapter 1. Springer.